



THE UNIVERSITY *of* EDINBURGH

This thesis has been submitted in fulfilment of the requirements for a postgraduate degree (e.g. PhD, MPhil, DClinPsychol) at the University of Edinburgh. Please note the following terms and conditions of use:

This work is protected by copyright and other intellectual property rights, which are retained by the thesis author, unless otherwise stated.

A copy can be downloaded for personal non-commercial research or study, without prior permission or charge.

This thesis cannot be reproduced or quoted extensively from without first obtaining permission in writing from the author.

The content must not be changed in any way or sold commercially in any format or medium without the formal permission of the author.

When referring to this work, full bibliographic details including the author, title, awarding institution and date of the thesis must be given.

Development of a Numerical and
Experimental Framework to Understand
and Predict the Burning Dynamics of
Porous Fuel Beds

Mohamad El Houssami

A thesis submitted for the degree of
Doctor of Philosophy



THE UNIVERSITY
of EDINBURGH

2016

Development of a Numerical and
Experimental Framework to Understand
and Predict the Burning Dynamics of
Porous Fuel Beds

by

Mohamad El Houssami

This thesis has been supervised by

Dr. R.M. Hadden

Prof. A. Simeoni

The examining committee was integrated by

Prof. A. Trouvé

Dr. S. Welch

Declaration

This thesis and the work described within have been completed solely by Mohamad El Houssami at the BRE Centre for Fire Safety Engineering at the University of Edinburgh, under the supervision of Dr Rory M. Hadden and Prof Albert Simeoni. Where others have contributed or other sources are quoted, references are given.

Mohamad El Houssami

September 2016

Abstract

Understanding the burning behaviour of litter fuels is essential before developing a complete understanding of wildfire spread. The challenge of predicting the fire behaviour of such fuels arises from their porous nature and from the strong coupling of the physico-chemical complexities of the fuel with the surrounding environment, which controls the burning dynamics. In this work, a method is presented to accurately understand the processes which control the burning behaviour of a wildland fuel layer using numerical simulations coupled with laboratory experiments. Simulations are undertaken with ForestFireFOAM, a modification of FireFOAM that uses a Large Eddy Simulation solver to represent porous fuel by implementing a multiphase formulation to conservation equations (mass, momentum, and energy). This approach allows the fire-induced behaviour of a porous, reactive and radiative medium to be simulated. Conservation equations are solved in an averaged control volume at a scale sufficient to contain both coexisting gas and solid phases, considering strong coupling between the phases. Processes such as drying, pyrolysis, and char combustion are described through temperature-dependent interaction between the solid and gas phases. Different sub-models for heat transfer, pyrolysis, gas combustion, and smouldering have been implemented and tested to allow better representation of these combustion processes. Numerical simulations are compared with experiments undertaken in a controlled environment using the FM Global Fire Propagation Apparatus. Pine needle beds of varying densities

and surface to volume ratios were subject to radiative heat fluxes and flows to interrogate the ignition and combustion behaviour. After including modified descriptions of the heat transfer, degradation, and combustion models, it is shown that key flammability parameters of mass loss rates, heat release rates, gas emissions and temperature fields agree well with experimental observations. Using this approach, we are able to provide the appropriate modifications to represent the burning behaviour of complex wildland fuels in a range of conditions representative of real fires. It is anticipated that this framework will support larger-scale model development and optimisation of fire simulations of wildland fuels.

Lay Summary

It is important to understand the fire behaviour of vegetation found in the forest to develop accurate computer models that can predict wildfire spreads. The challenge of understanding the fire behaviour of such fuels arises from the porous nature of the fuel itself and from the complex interaction between the fuel and its surrounding environment. In this thesis, a method is presented to accurately quantify the coupling between processes using numerical simulations. These simulations are undertaken using advanced computational and mathematical techniques that allow representing a porous fuel bed undergoing physical and chemical processes such as drying, degrading, and burning. Representation of these processes are compared to experiments conducted in a controlled laboratory environment using a standard apparatus called the FM Global Fire Propagation Apparatus. Using this approach, we were able to assess the performance of the numerical model and to determine the potential source of errors, which cannot be measured during large scale fires.

Acknowledgements

This opportunity started with Dominique Morvan's lectures on turbulent flows during my Masters, during which I discovered a passion for fluid mechanics and numerical modelling. His trust and his constant support were essential even before starting this Ph.D. Moreover, I would like to thank him for his co-supervision, his impact on my thesis, and finally for introducing me to my mentor Albert Simeoni.

Words cannot express my gratitude to Albert for taking me through this incredible intercontinental journey and for being a good friend, a knowledgeable advisor, and a wise mentor. I thank him for everything we have been through, for teaching me consciously and unconsciously about wildfires, physics, science, Corsica, and life in general. I appreciate all his contribution of time, ideas, and efforts to make my Ph.D. experience productive and stimulating. The joy and enthusiasm he has for his research was contagious and motivational for me. I am also thankful for the excellent example he has provided and for showing the way.

I would also like to express my sincere gratitude to Rory Hadden for all his input and his efforts to supervise my thesis during the final year. It was a pleasure working together, I hope that we will continue interacting on further projects.

This work was financed by the University of Edinburgh, and was granted access to the HPC resources of Aix Marseille Université, financed by the project

Equip@Meso (ANR-10-EQPX-29-01) of the program "Investissements d'Avenir" supervised by the French Agence Nationale pour la Recherche.

This long journey has surely impacted me in many ways, not only through the knowledge and skills that I have developed, but also by the support and the interaction with remarkable scientists around the world. The help of Aymeric Lamorlette has been essential to this work, many thanks for initiating the development of ForestFireFOAM, for all the long discussions, and for letting me pick your brain! Special thanks to Alexander Filkov and for sharing his unique Russian input. I am glad that we were able to meet on several occasions, spasibo!

My sincere acknowledgments also go to FM Global Fire Research team for generously inviting me and for providing assistance in the development of ForestFireFOAM. Thanks to Sergey Dorofeev, Yi Wang, Marcos Chaos, Prateep Chatterjee, and Ankur Gupta for their personal contribution. Thanks to Ning Ren for the early car rides during snowy times! Last but not least, special thanks to Karl Meredith for his precious support, for debugging the code, and for helping me everyday during my stay in Norwood. I would like to thank Nicholas Skowronski, Kenneth Clark, Michael Gallagher, and the New Jersey Forest Service for hosting us and for the fruitful teamwork on instrumenting and conducting prescribed fires. It has been a pleasure staying in the Pine Barrens every year.

Special thanks to Jan Christian Thomas and to Eric Mueller, my enduring colleagues in the Wildfire Team and sons of the "Simeoni Clan". It has been a pleasure being part of the team. Thanks for supporting me at all times from the 1st day in Worcester, to the last day in Edinburgh via St. Petersburg, New Jersey, Coimbra, and Portland. Thanks to Michal Krajcovic for simply being the best laboratory manager and for his constant support. Thanks to Paolo Pironi for all his daily help in the laboratory and for cheering me up with the best coffee

in Edinburgh. Thanks to the legendary Juan Hidalgo Medina, for all the long discussions, his motivation, and foremost for being a good friend, I wish him the best in his new life in Australia. Thanks to Stephen Welch, Luke Bisby, and Ricky Carvel for all their support. Thanks to all the Doctors and soon to be Doctors that made my days in John Muir Building unforgettable: Martyn, Emma, Ieuan, Ben, Liming, Jamie, Nikolai, Felix, Simon, Doug, Holly, Agustin, Praveen, Maluk, Brian, Zaid, Daryan, Mohamad, Emran, Xu, Farian, Alastair, SORCHA, Francesca, Ida, and Kate. With you, the Fire Group became my family and John Muir Building my home.

A special thought to Majed, Cornelius, Lydia, Sreeni, Hamed, Haejun, Young-Geun, Sari, A.J., Jim, David, Wayne, and to all my friends in the USA. I would also like to thank Kamila, Mel, David, Jérémi, and all the Basketball and Karate friends I made in Scotland. Many thanks to Alessandro, Octo, Bastien, Orel, Clems, Val, Libera, Mandou, Yas, Omar, and to my family in France who constantly cheered me up during the toughest times. I gratefully acknowledge Catriona for proofreading my thesis, Zaid and Nikolai for printing the final version.

To my Grandparents, thank you for your unconditional love and support. Thanks to my grandma Em-Rachid, who left us while I was far away. Your love and kindness will always remain with me.

Last but not least, this PhD would not have been successfully completed without the unshakable support and belief in my dreams offered by my Mathilde, my father, and my mother. Your achievements have always been my inspiration.

It doesn't matter how beautiful your theory is, it doesn't matter how smart you are. If it doesn't agree with experiment, it's wrong.

Richard P. Feynman

Contents

Declaration	v
Abstract	vii
Lay Summary	ix
Acknowledgements	xi
Contents	xv
List of Tables	xix
List of Figures	xxi
List of Acronyms	xxv
Nomenclature	xxxix
1 Overview of Wildfire Science History	1
1.1 Impact of Wildfires	1
1.1.1 Climate Change	3
1.1.2 Anthropogenic Activity	6
1.1.3 Wildfires in the Mediterranean Basin	7
1.1.4 Wildfires in North America	9
1.1.5 Wildland Urban Interface	11
1.2 A Spectrum of Complexities in Wildfires	14
1.2.1 Climate Patterns	16
1.2.2 Fire Weather	18
1.2.3 Plume Dynamics	20
1.2.4 Terrain Effects	22
1.2.5 Effects of Moisture	22
1.3 Summary of Progress in Wildland Fire Behaviour	24
1.3.1 How It Started	24
1.3.2 Scaling Problem	25
1.3.3 Fire Modelling	45
1.4 Purpose of the Thesis	60

2	Experimental and Numerical Techniques	65
2.1	Introduction	65
2.2	Physico-Chemical Properties	66
2.2.1	Morphology	67
2.2.2	Surface to Volume Ratio	68
2.2.3	Specific Heat Capacity	68
2.2.4	Density	69
2.2.5	Chemical Composition	69
2.3	Laboratory Scale Experimental Setup	72
2.3.1	Fire Propagation Apparatus	73
2.3.2	Fourier Transform Infra-Red	78
2.3.3	Spectral Analysis	81
2.4	The Multiphase Approach	82
2.5	Numerical Setup	88
2.5.1	Turbulence Modelling	88
2.5.2	Direct Numerical Simulation	90
2.5.3	Reynolds Averaged Navier Stokes	90
2.5.4	Large Eddy Simulation	91
2.5.5	Mesh Generation	91
2.5.6	Boundary Conditions	96
2.5.7	Solvers	101
2.5.8	Parallelisation	103
2.6	Conclusion	105
3	Submodelling	107
3.1	Heat Transfer in Porous Beds	108
3.1.1	Radiative Heat Transfer	108
3.1.2	Convective Heat Transfer	116
3.2	Pine Needle Degradation	124
3.2.1	Evaporation Process	124
3.2.2	Pyrolysis Process	125
3.2.3	Charring Process	127
3.3	Reactive Flow Modelling	127
3.3.1	Flow and turbulence	127
3.3.2	Flaming Combustion	133
3.3.3	Smouldering Combustion	136
3.4	Conclusions	141

4	Results and Discussions	145
4.1	Introduction	145
4.2	Natural Convection	146
4.2.1	Burning Characteristics	146
4.2.2	Flaming Time	146
4.2.3	Mass Loss	148
4.2.4	Heat Release Rate	153
4.2.5	Low Heat Flux	155
4.2.6	Pitch Pine vs White Pine	157
4.3	Forced Flow	160
4.3.1	Burning Characteristics	160
4.3.2	Flaming Time	163
4.3.3	Mass Loss	165
4.3.4	Heat Release rate	172
4.3.5	Gas Emission	176
4.4	Conclusion	177
5	Conclusion	181
	Appendices	189
A	Spectral Analysis Configuration	189
B	Mathematical demonstration for density equation in the solid phase	193
C	Boundary Conditions	195
D	Extension to Live Needles	197
E	Charring Effect on the Surface to Volume Ratio	207
	References	211

List of Tables

1.1	Different time scales influencing a fire	16
1.2	Mass fractions of the degradation gases	32
2.1	Summary of species properties	69
2.2	Constitutional analysis of Mediterranean species	72
2.3	Ultimate analysis of three pine species	72
2.4	Flow fluxes supplied by the FPA	76
2.5	Summary of bulk densities and porosities	78
2.6	Main differences between large and small scale eddies in a turbulent flow	89
2.7	Chosen boundary conditions for pressure and velocity	97
3.1	Difference between solid and gas phase temperatures	119
3.2	Convective heat transfer coefficients	122
3.3	Mass fractions of pyrolysis products released from pitch pine needles before ignition	125
3.4	JANAF coefficients for $\text{CHO}_{0.65}$	135
4.1	Percentage of energy released by flaming and smouldering during experiments and simulations for all bulk densities	155
4.2	Percentage of energy released by flaming and smouldering during experiments and simulations for all bulk densities at HF	173
D.1	Conditioning and properties of live needles	198

List of Figures

1.1	Global fire map	2
1.2	April 2016 temperature departures from average	4
1.3	Burnt area in Alaska	5
1.4	Evolution of the number of fires in MB	9
1.5	Scenes from McMurray fire	11
1.6	Example of intermix and interface WUI	12
1.7	Structures lost to wildfires during 1999-2011	13
1.8	Methodology for exposure scale	14
1.9	Fire location during Black Saturday fire	15
1.10	Illustration from El Niño and La Niña	17
1.11	Image of a fire whirl	18
1.12	Pyrocumulonimbus cloud	19
1.13	Firebrands crossing over a fuel break	20
1.14	Plume dominated fire	21
1.15	Wind driven fire	21
1.16	Seasonal variations in live foliar moisture content	23
1.17	Experimental scales used in wildland fire studies	26
1.18	Measured quantities at different scales.	27
1.19	Correlation between mass loss and forest fuel composition.	29
1.20	Representation of steady smouldering	33
1.21	Absorptivity measurements for six species	36
1.22	Pictures of the flame in visible and infrared ranges	39
1.23	Spectral intensity emitted in the flame	40
1.24	Gas consumption and production for different conditions	41
1.25	Significant large scale experimental studies in wildland fires.	44
1.26	Experimental burning campaign for cured grassland	45
1.27	WFDS simulation of a burning Douglas fir	47
1.28	Firestar simulation of a fuel break	49
1.29	FIRETEC simulation of field-scale wildfire spread	50
1.30	Comparison between simulated and experimental ROS	52
1.31	Crown fire ROS curve as a function of wind speed	53
1.32	Fire danger meter disk	57
1.33	Structure of the Canadian Fire Weather Index system	58

2.1	Dead pitch pine needle	67
2.2	Dead pitch and white pine needles	68
2.3	Overview of the FPA	75
2.4	Experimental setup for temperature measurement	76
2.5	K-type thermocouple	77
2.6	Pitch pine needle samples with different masses	77
2.7	Gasmet DX-4000 gas analyser and sampling system	79
2.8	FTIR sampling position in the FPA	79
2.9	Alternative FTIR sampling position in the duct	80
2.10	Illustration of the multiphase approach	83
2.11	Numerical simulation of a turbulent flow	92
2.12	Computational domain	93
2.13	Zoom on the computational domain	93
2.14	Mesh convergence test: mass loss in a cell	95
2.15	Mesh convergence test: gas phase temperature in a cell	95
2.16	View factor calculation for a wedge-shaped groove	98
2.17	Influence of the RTE discretisation on the heat flux estimation . .	101
2.18	ForestFireFOAM scaling on the Mésocentre cluster	104
3.1	Extinction coefficient measurement for different heat fluxes	110
3.2	Spectral emissivity/absorptivity of dead pitch pine	112
3.3	Effective absorptivity of dead pitch pine	113
3.4	Temperature profile before ignition using Eq. 3.12	117
3.5	Temperature profile before ignition for pitch pine (25 kW/m ²) . .	120
3.6	Temperature profile before ignition for pitch pine (50 kW/m ²) . .	121
3.7	Convective heat transfer coefficient estimation for forced flow . . .	122
3.8	Calculated temperature using different convective heat transfer coefficients	123
3.9	Flow field velocity and vectors inside and around the fuel sample .	129
3.10	Measured and simulated air velocity using drag force estimation for spheres	130
3.11	Drag force coefficient estimation using different submodels	131
3.12	Measured and simulated air velocity using pseudofluid model (23 kg/m ³)	132
3.13	Measured and simulated air velocity using pseudofluid model (40 kg/m ³)	133
3.14	Computed specific heat capacities using JANAF tables	135
4.1	Temperature field before ignition and during flaming (NF)	147
4.2	Flaming time for different bulk density of pitch pine (NF)	147
4.3	Experimental and simulated mass loss in NF	149
4.4	Mass loss rates for pitch pine of different bulk densities (NF) . . .	151
4.5	Maximum mass loss rates for different bulk densities (NF)	152
4.6	Heat release rates of pitch pine for different bulk densities (NF) .	154
4.7	Normalised mass loss rates of pitch pine at 25 kW/m ² (NF) . . .	156

4.8	Normalised mass loss rate for white pine (NF)	158
4.9	Heat release rate for white pine (NF)	159
4.10	Pitch pine needles burning in the FPA	161
4.11	Temperature field during flaming (HF)	161
4.12	Simulated solid temperatures (HF)	162
4.13	Measured and simulated flaming times for all inlet flows	164
4.14	Flame structure	165
4.15	Experimental and simulated mass loss (HF)	166
4.16	Simulated rate of evaporation, pyrolysis, and char oxidation (HF)	167
4.17	Mass loss rates for different bulk densities (HF)	168
4.18	Averaged mass loss rates during flaming	169
4.19	Averaged mass loss rates after flameout	171
4.20	Measured and simulated heat release rates (HF)	173
4.21	Averaged heat release rates during flaming (HF)	174
4.22	Averaged heat release rates after flameout	175
4.23	Measured and simulated CO and CO ₂ production (HF)	177
A.1	Spectral reflectivity measurement systems	191
A.2	pine needle arrangement in spectral analysis	192
C.1	Boundary conditions	196
D.1	Simulated mass loss of live needles	200
D.2	Simulated mass loss in one cell	200
D.3	Measured and simulated heat release rates for live needles	201
D.4	Measured and simulated average heat release rates for live needles	203
D.5	Measured and simulated peak heat release rates for live needles	203
E.1	pine needle representation with char pores	208
E.2	Simulated mass loss with alternative char oxidation model	209

List of Acronyms

CDG	Carbon Dioxide Generation
CFD	Computational Fluid Dynamics
CFL	Courant-Fredrichs-Lewy
CPU	Central Processing Unit
CSIRO	Commonwealth Scientific and Industrial Research Organization
DIC	Diagonal Incomplete Cholesky
DILU	Diagonal Incomplete-LU
DNS	Direct Numerical Simulation
DOM	Discrete Ordinate Method
DSC	Differential Scanning Calorimetry
EDC	Eddy Dissipation Concept
EFB	Eruptive Fire Behaviour
FDS	Fire Dynamics Simulator
FF	FireFOAM
FFDM	Forest Fire Danger Meter
FMC	Fuel Moisture Content
FPA	Fire Propagation Apparatus
FTIR	Fourier Transform Infra-Red
FVM	Finite Volume Method
FWI	Fire Weather Index
GAMG	Geometric-Algebraic Multi-Grid

HF	High Flow
HKM	Hybrid Kinetic Method
HRR	Heat Release Rate
ISI	Initial Spread Index
LAD	Leaf Area Density
LDA	Laser Doppler Anemometry
LES	Large Eddy Simulation
LF	Low Flow
LFL	Lower Flammability Limit
LFMC	Live Foliar Moisture Content
MB	Mediterranean basin
MLR	Mass Loss Rate
MPI	Message Passing Interface
NF	No Flow
NIST	National Institute of Standard and Technology
OC	Oxygen Consumption
OF	OpenFOAM
PBiCG	Preconditioned Bi-Conjugate Gradient
PCG	Preconditioned Conjugate Gradient
PIV	Particle Image Velocimetry
RANS	Reynolds Averaged Navier Stokes
ROS	Rate of Spread
RTE	Radiative Transfer Equation
SGS	Sub-Grid Scale
SVR	Surface to Volume Ratio
TGA	Thermogravimetric Analysis

TNF	Turbulent Nonpremixed Flames
TVD	Total Variation Diminishing
WALE	Wall Adapting Local Eddy
WFDS	Wildland Urban Interface Fire Dynamics Simulator
WRF	Weather Research and Forecasting
WUI	Wildland Urban Interface

Nomenclature

Symbol	Description
a_D	Thermal diffusivity
Bi	Biot number
c	Speed of light
C_o	Courant number
C, C'	Convective heat transfer constants
C_D	Drag force coefficient
C_{EDC}, C_{diff}	EDC model coefficients
C_p	Specific heat capacity
D	Equivalent diameter
d_γ	Pore diameter
E	Energy activation
F	Drag force
F_{1-2}	View factor
Fo	Fourier number
Gr	Grashof number
h_p	Plancks constant
h_{conv}	Convective heat transfer coefficient
Hu	Humidity
I	Spectral Intensity
J	Irradiance
K	Thermal conductivity
k_b	Boltzmann constant
$K_{pyr}, K_{char}, K_{vap}$	Pre-exponential factors for pyrolysis, char oxidation, and evaporation
k_{SGS}	Sub grid scale kinetic energy
L	Characteristic length scale
m_0	Initial mass
m, m', n, n'	Convective heat transfer coefficient constants
n_γ	Number of pore per unit volume
Nu	Nusselt number
P	Pressure
Pr	Prandtl number
$Q_\pm^{(s)}$	Energy balance source term

$Q_{conv}Q_{rad}$	Convective and radiation heat transfer source terms
q_{FPA}, q_{surf}	Imposed and corrected heat fluxes
q_{net}	Net energy received by the solid fuel
R	Ideal gas constant
Re	Reynolds number
s	Stoichiometric O ₂ /C mass ratio
S	Speedup
t	Time
T, T_s	Gas and solid phase temperatures
T_r	Radiation source temperature
U	Velocity
V	Volume
x	Sample thickness
Y	Mass fraction

Greek symbols

α_{char}	Char absorptivity
α_{eff}	Effective absorptivity
α_{flam}	Effective absorptivity from flame
α_g	Gas phase volume fraction (porosity)
α_s	solid phase volume fraction
α_{sg}	Fraction between solid and gas phases
β	Buoyancy
β_{char}	Char correction factor
γ	Fraction
Δ	LES filter size
Δh	Heat of reaction
ϵ	Dissipation rate
η	Kolmogorov length scale
θ	Angle size
λ	Wavelength
μ	Dynamics viscosity
ν	Kinematic viscosity
ρ	Density
σ	StefanBoltzmann constant
σ_s	Surface to volume ratio (SVR)
σ_0	Extinction coefficient
ϕ	Split function
φ	Mass fraction multiplied by the density
ω	Mass rate

Subscripts and superscripts

<i>b</i>	Bulk
<i>c</i>	Graphite
<i>comb</i>	Combustion
<i>conv</i>	Convection
<i>cr</i>	Critical
<i>disc</i>	Discretisation
<i>eff</i>	Effective
<i>F</i>	Fuel
<i>flam</i>	Flaming
<i>G</i>	Gas phase
<i>H</i>	High
<i>L</i>	Low
<i>m</i>	Molecular
<i>rad</i>	Radiation
<i>S</i>	Solid phase
<i>SGS</i>	Sub Grid Scale
<i>surf</i>	Surface
<i>t</i>	Turbulent
<i>TH</i>	Thermally heated
<i>vap</i>	Evaporation
ϕ	Azimuthal angle
θ	Polar angle
<i>2D</i>	2 Dimensions

Chapter 1

Overview of Wildfire Science History

1.1 Impact of Wildfires

Definition of *wildfire*:

noun [C]

A large, destructive fire that spreads quickly over woodland or brush ([Oxford Dictionary, 2010](#)). Also referred to as *wildland fire*, *forest fire*, or *bush fire*.

This chapter is a general overview of the problem of wildfires. General issues such as observations, tendencies, and global occurrences are reviewed. We will then present the complexities of the fundamental science which drives wildfires, highlighting the main historical breakthroughs that have resulted in the attainment of today's state of the art knowledge. We will present the different

approaches taken to investigate the problem, their advantages, and limitations. Finally, we will lay out our approach to this problem and what we want to achieve.

Based on satellite emissions of burned areas, it is estimated that 3.5 to 4.4 million km² were burned every year on average over the period 2000-2007 (Tansey et al., 2008), representing nearly 3.4 % of Earth total vegetation area (Rochoux, 2014). This trend is confirmed by the fire maps in Fig. 1.1, produced by MODIS, detecting fire locations over ten-day periods (Giglio et al., 2003; Davies et al., 2004). But this is not new fire has occurred in Earth's ecosystems ever since

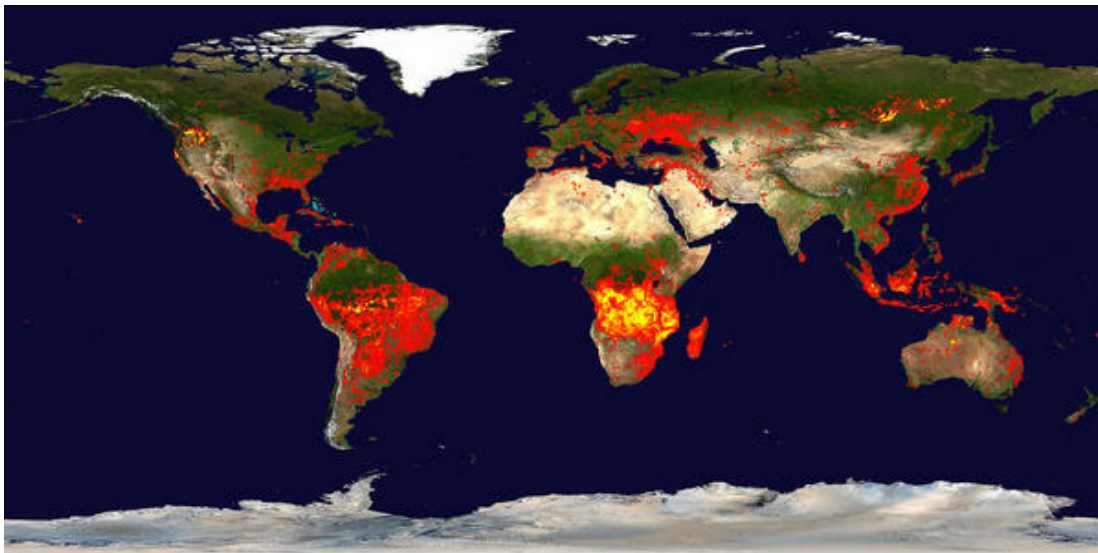


Figure 1.1: Global fire map, averaged over 19/08/2015 - 28/08/2015. Each coloured dot indicates a location where MODIS detected at least one fire during the compositing period. Colour ranges from red where the fire count is low to yellow where number of fires is large. Credit: MODIS

the terrestrial atmosphere became sufficiently oxygenated for combustion to take place with the presence of lightning and other ignition sources (Falkowski, 2005; Glasspool and Scott, 2010; Belcher et al., 2010). Today, the most fire-prone

ecosystems are grasslands, savannahs, Mediterranean shrubland, and boreal* forests ([Bond et al., 2004](#)). In recent years, changes have been observed in wildfire behaviour. The drivers of this change are complex and range from climate change to anthropogenic activity. These are discussed in the sections below.

1.1.1 Climate Change

Climate is known to be a key driver of wildfire occurrences in an ecosystem. Climate is defined by the average weather and its variability over a given time period (around 30 years) and results from numerous non-linear processes and interactions between the atmosphere, the hydrosphere, the biosphere, and the geosphere ([Sommers et al., 2011](#)). In 1896, Arrhenius established a correlation between human-induced emissions of greenhouse gas and the average temperature at the Earth's surface ([Arrhenius, 1896](#)). He estimated that variations in the amount of carbon dioxide in the atmosphere could greatly influence the heat budget of the Earth. Using the best data available to him, he performed a series of calculations on the temperature effects of increasing and decreasing amounts of carbon dioxide in the Earth's atmosphere. He predicted that the temperature of the Arctic regions would rise about 8°C, if the carbonic acid increased 2.5 to 3 times its present value ([Arrhenius, 1896](#)). More recently, it has been recorded that the first decade of the 21st century (2001-2010), was the warmest decade in the 130-year record of global temperature ([NASA](#)). According to NASA's Goddard Institute for Space Studies, the global temperature of each month in 2016 was warmer than the average for each month from 1951 to 1980 for land and sea, which is used as a baseline. January was 1.13°C hotter than the baseline for previous Januaries ([NASA](#)). Similarly, an excess of 1.34°C was measured in

*The boreal region stretches across the Northern Hemisphere through Alaska, Canada, Scandinavia, and Russia.

February, 1.28°C in March, and 1.11°C in April (Fig. 1.2). So far, April 2016 was the seventh consecutive warmest month on record for earth (NASA).

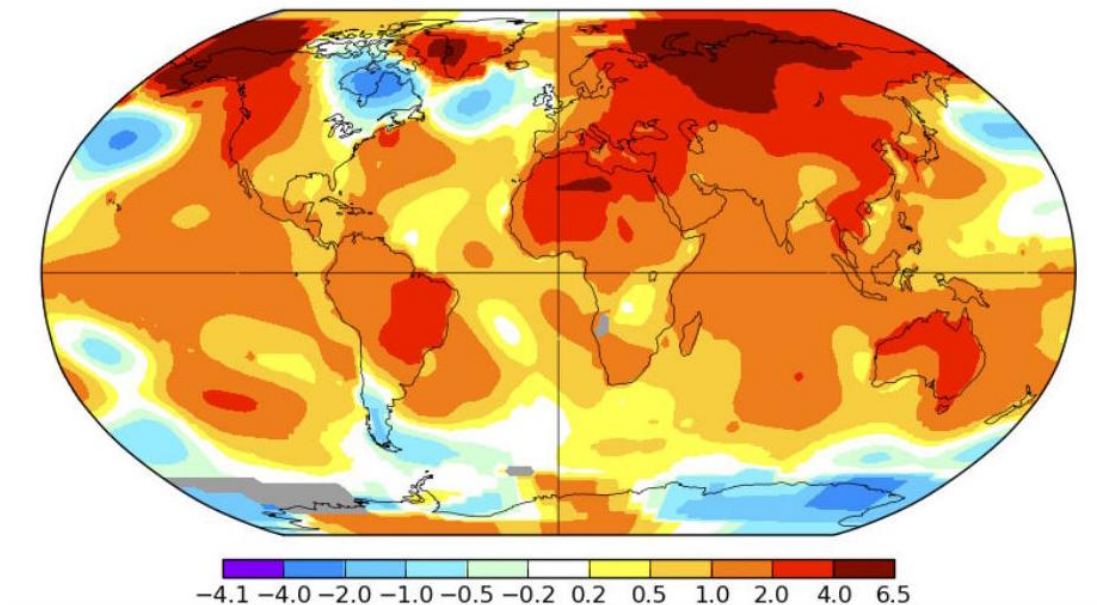


Figure 1.2: April 2016 Temperature departures from average, in degrees Celsius, relative to 1951-1980 average. Brown/blue contours correspond to temperatures most above/below April averages. Credit: NASA/GISS

In addition, many indicators show that future global temperatures will be warmer than current levels and that drought will be more prevalent. This will likely lead to longer fire seasons and will increase the potential for wildfire activity, and these events are likely to be more extreme and damaging. Although the exact consequences climate change will have on wildfire regimes are not well understood, the general consensus is that fires will be larger, more frequent and more severe (Flannigan et al., 2000).

One technique that is used to understand how future climate change will affect fire behaviour is to study the history of fire in the earth system. Fire history

records how climate, humans and other factors have shaped fire regimes in the past, and helps us understand how climate change may modify fire regimes in the future. Paleoclimatology and palaeoecology studies show fires have been an active part of ecosystems since the first plants evolved. Throughout this time period, the global mean temperature, oxygen concentration, and CO₂ concentrations have been different from the levels recorded today. Consequently, as the global climate changes, the number of uncontrolled fires is expected to increase in many worldwide regions (Fried et al., 2004; Niu and Zhai, 2012; Nijhuis, 2012). Although it is difficult to explicitly link climate change to wildfire occurrences, there are several notable cases which show changes in fire behaviour in recent years. The 2007 Anaktuvuk River Fire was an unusually large fire that occurred in the tundra of the Alaskan Arctic (Hu et al., 2010). This fire burned 1,039 km² of the tundra on Alaskas North slope (Fig. 1.3), which had not been disturbed by fire for more than 3,000 years (Hu et al., 2010). The fire burned deeply into organic peat soils releasing enough carbon into the atmosphere to offset all of the carbon taken up by the entire arctic tundra biome over the past quarter-century (Groffman et al., 2014). This shows that the effects of wildfires are not limited to threats to ecosystems but can offer positive feedback into climate change processes as CO₂ released from ancient carbon stocks will result in further warming.

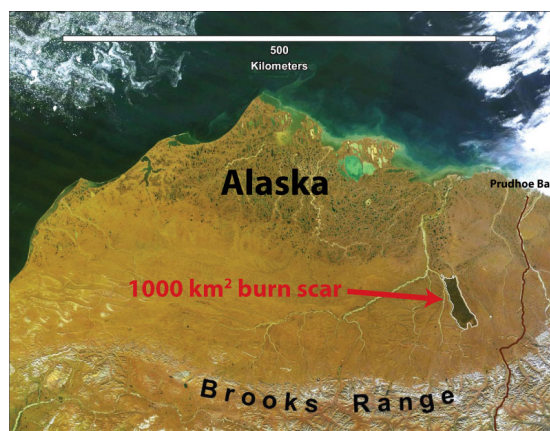


Figure 1.3: Burnt area after Anaktuvuk River fire in Alaska. Credit: MODIS

1.1.2 Anthropogenic Activity

In addition to climate change impact, there have been direct human influences on wildfire behaviour. These range from government policies of wildfire fighting to commercial interests and forest agriculture. Throughout most of the 20th century governments (in particularly the USA) enforced a forest fire exclusion policy. This policy meant that almost all wildfires were actively suppressed. The reasoning behind this was to protect ecosystems, people and property from the effects of wildfires (Keane et al., 2002). The consequence of this was that accumulation of surface biomass increased substantially. This has been linked to increased occurrences of fires exceeding historical size, and resulting in unprecedented social and economic challenges (Keane et al., 2002). Indeed, the changes in wildfire severity depend on pre-suppression activities, fire suppression strategies, human settlement patterns, the degree of climate change, and how these factors affect vegetation type and fuel loading (Fried et al., 2004).

As well as direct fire management strategies, unbalanced forest management practices have also made the forests more vulnerable to catastrophic fires. For instance, in New Mexico, man-made tree plantations are strongly vulnerable to fire because they are much denser than naturally occurring forest. Consequently, they consume more water from the soil and increase the availability of dry above-ground fuel leading to a more fire-prone system (Groffman et al., 2014). Globalisation has allowed new species to be introduced into ecosystems which are not well adapted to them. For instance Portugal is among the countries that have the largest areas of planted *Eucalyptus globulus* in the world (Águas et al., 2014). This species is native to Australia and was introduced to Portugal in the middle of the 19th century mostly for paper production. It is now the

most widespread tree species on the Portuguese mainland, representing 26 % (8,120 km²) of its forest cover (Radich, 2007; ICNF, 2013). Moreover, eucalypt stands are highly flammable in comparison to other forest systems in Portugal and Europe (Xanthopoulos et al., 2012; Águas et al., 2014). As a result, Portugal has the largest percentage of burnt forest area in Europe and one of the largest in the world (FAO, 2010; JRC, 2012). The result is that wildfires are a major threat to sustainable, economic forest management in this country.

1.1.3 Wildfires in the Mediterranean Basin

Many civilisations have evolved in the Mediterranean basin (MB) (e.g. Mesopotamian, Egyptian, Phoenician, Greek, Roman, and Arab), with many political conflicts, changes in land ownership, migrations and other influences that generated numerous socioeconomic and land-use changes. Over the years, These changes have resulted in the burning and cutting of non-arable lands, as well as cultivation of arable areas, creating a vast array of strongly human-modified landscapes. A large proportion of Mediterranean landscapes include terraced slopes, built for agricultural purposes a long time ago then abandoned (urban migration, over exploitation...). The result of all this is that current Mediterranean landscapes are very far from being wild, except for parts of Corsican forests, which are considered to be the only remaining pieces of primal forests in Europe (Rossi et al., 2013). In the MB, the most fire-sensitive ecosystems are the pine woodlands (Pausas et al., 2008). This is evidenced by the crown fire regimes which have been observed in the last few decades and reduced fire intervals occurring in mountain zones that were not traditionally subject to this type of fires. Although pine trees reproduce relatively fast (<10 years) (Ne’eman et al., 2004), in some areas they have been repeatedly burnt with fire intervals shorter than the time they need to

produce a seed bank (15-20 years). Hence, many early pine woodlands are being taken over by shrubland (Baeza et al., 2007).

The number of forest fires in Europe has been increasing in recent years (Fig. 1.4), and is affecting sub-Mediterranean mountain areas where fires were uncommon in the past. These ecosystems are often populated by species lacking post-fire regeneration mechanisms (e.g. *Pinus nigra*, *Pinus sylvestris*). Some of these woodlands have survived a long history of surface fires but are rapidly being reduced due to the change to crown fire regimes (Rodrigo et al., 2004). The increase of large crown fires in these sub-Mediterranean areas is not only affecting the vegetation but also other biodiversity components (Arnan et al., 2006). Pines grow naturally in many places in the MB. However, most current MB pine woodlands have been favoured or even planted by humans. For many years, the traditional forest policy in the MB, usually based on European models, has been to plant monospecific pine woodlands (Pausas et al., 2004). Some of these pine woodlands are very flammable as they consist of dense stands of pine species with branches all along the main stem (e.g. *Pinus halepensis*, *Pinus brutia*), and are subject to few silvicultural treatments, thus facilitating large and intense crown fires.

As a stating example in Europe, throughout the summer of 2007 (June to September), Greece was ravaged by wildfires that killed 84 people. The most dangerous and intense fires occurred on the 23rd of August, expanding rapidly and raging out of control until the 27th of August. The last fires were extinguished on September the 3rd in the outskirts of Athens. High temperatures, including three consecutive heat waves of over 40°C and severe drought, were recorded during this season. From the end of June to early September, over 3,000 forest fires were

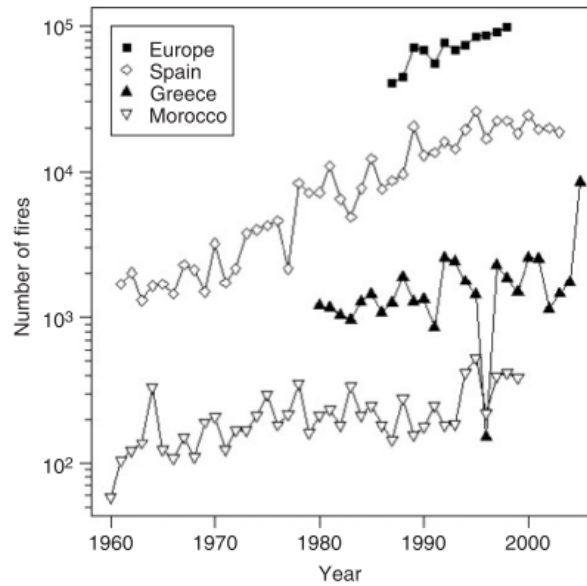


Figure 1.4: Evolution of the number of fires during the last decades in Spain, Morocco, Greece and Europe. (Pausas et al., 2008)

recorded with a total of 271,000 ha of pine forest, olive grove, brush, and farmland destroyed (Rosenfeld, 2011).

1.1.4 Wildfires in North America

In North America, the pre-colonial ecosystem is considered wilder than in the MB even with Native American intervention and fire practices. The fire suppression policy operated in the USA during the 19th and 20th centuries was the origin of an important switch in fire regimes. In some places, the fire return interval increased from 2,000 years to 10-40 years (evaluated from projections) (Sommers et al., 2011). These changes in wildfire behaviour had unanticipated ecological consequences. A cascade of compositional and structural changes took place in open lands such as grasslands, savannahs, and woodlands where closed-canopy forests were formed, and led to the replacement of fire-dependent plants by shade-tolerant, fire-sensitive vegetation.

In 1910, the Great Fire (Big Blowup or Big Burn) occurred in Idaho and Montana, burned 1 million ha, and caused 87 casualties (Sommers et al., 2011). This fire is considered to be one of the most devastating wildfires in US history as it affected urban properties and had a significant social impact. As a result of this fire, the first steps in fire monitoring began to take place. The incident also revealed the need for fire behaviour understanding, which led to the development of many other technologies that form the basis of our current understanding of wildfires. In the first four months of 2016 there were 15,485 wildfires in the USA, compared to 15,327 fires that occurred in the first four months of 2015. However, in 2016 wildfires burned 600,000 ha, compared with 128,000 ha in 2015 (III, 2016). The 2015 fire season set a new record for the number of acres burned in the United States. Between the 1st of January and the 30th December, 2015, there were 68,151 wildfires, which burned 4.1 million ha (NIFC, 2016). The previous record was set in 2006 at 3.9 million ha. In total, over the 20-year period (from 1995 to 2015), fires, including wildfires, accounted for 1.5 % of insured catastrophes losses, totalling about \$6.0 billion (III, 2016).

More recently, the Fort McMurray wildfire became the most expensive catastrophe in Canada's history with losses potentially reaching C\$9.4 billion (\$7.3 billion) according to analysts (Dmitrieva, 2016). This fire burnt 400,000 ha in the first three days and destroyed more than 1,600 structures in Fort McMurray (Fig. 1.5). Almost 90,000 people left the city causing two fatalities during evacuations (Todd, 2016). Wotton et al. (2010) predicted an increase in overall fire occurrence across Canada of 25 % by 2030 and 75 % by the end of the century. Hence, understanding the impact of climate change on forest fire activity is important for understanding long-term change in forests, as well as the size, and the potential emissions from terrestrial carbon stocks (Flannigan et al., 2009). Throughout the managed forests of Canada, most fires are suppressed and kept to a very small size. 3 % of the

fires that escape lead to an area burned >200 ha and account for over 97 % of the area burned (Stocks et al., 2002).



Figure 1.5: Scenes from McMurray fire (16 km south of the city) (Credit: J. Hayward)

1.1.5 Wildland Urban Interface

Since the 1980's, fire managers, government officials, and the public began to accept the importance of the role of fire in the ecosystem and how to better accommodate this natural phenomenon. Living with fire requires solving a complexity of issues including Wildland Urban Interface (WUI), public safety, property protection, impacts of smoke, and advanced fire management skills. The front line between wildfires and the built environment is the WUI. People living in the WUI are at substantial risk from the health and property loss consequences of wildfires. Indeed, the occurrence of massive fires at a growing WUI overwhelms fire fighting resources and induces huge socio-economic losses. Two types of WUI are existent, interface WUI, where the wildland is adjacent to housing developments, and intermix WUI, where houses and the wildland intermingle (see Fig. 1.6) (Stein et al., 2013).

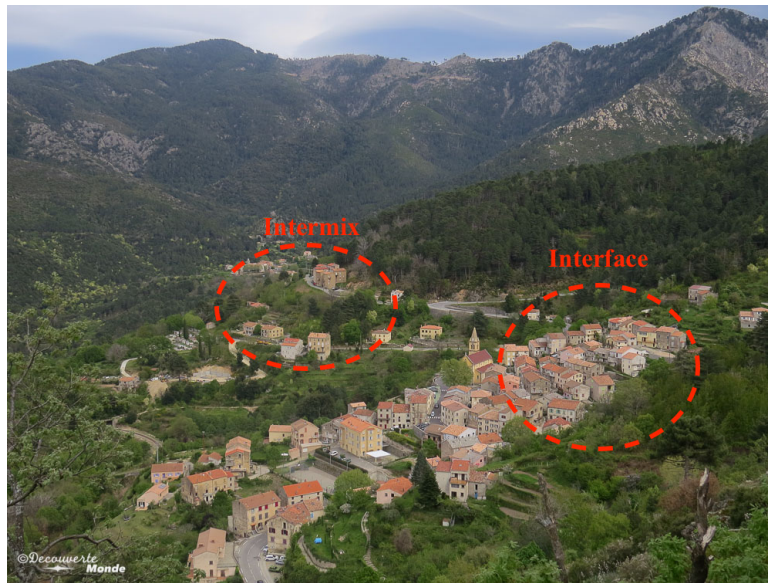


Figure 1.6: Example of intermix and interface WUI in a Corsican village (Credit: Découverte Monde)

This problem is widely seen in the USA, where the cost of WUI fires was estimated to be more than \$4 billion during the 1990's (Hammer et al., 2007). In the 2000's, the WUI area on the USA West Coast increased by 11 % to nearly 53,000 km² and the number of housing units at the WUI was around 6.9 million. It is estimated that the WUI continues to increase by more than 15 % every 10 years (Hammer et al., 2007). In 2011 alone, more than 3 million hectares in the WUI burned, causing 15 deaths and property losses greater than \$1.9 billion (Fig. 1.7) (Grossman et al., 2014). The challenge keeps escalating, as people continue to relocate from urban to rural areas thereby expanding the WUI.

The main threats from these wildfires are the ignition of structures creating urban conflagrations, and managing the evacuation of the public. Further details on the complexity of this growing problem are fully described in a National Institute of Standard and Technology (NIST) report (Maranghides and Mell, 2012) in which the need for a WUI-hazard scale assessment is outlined. The report identifies that direct fire and firebrand exposure are the leading cause

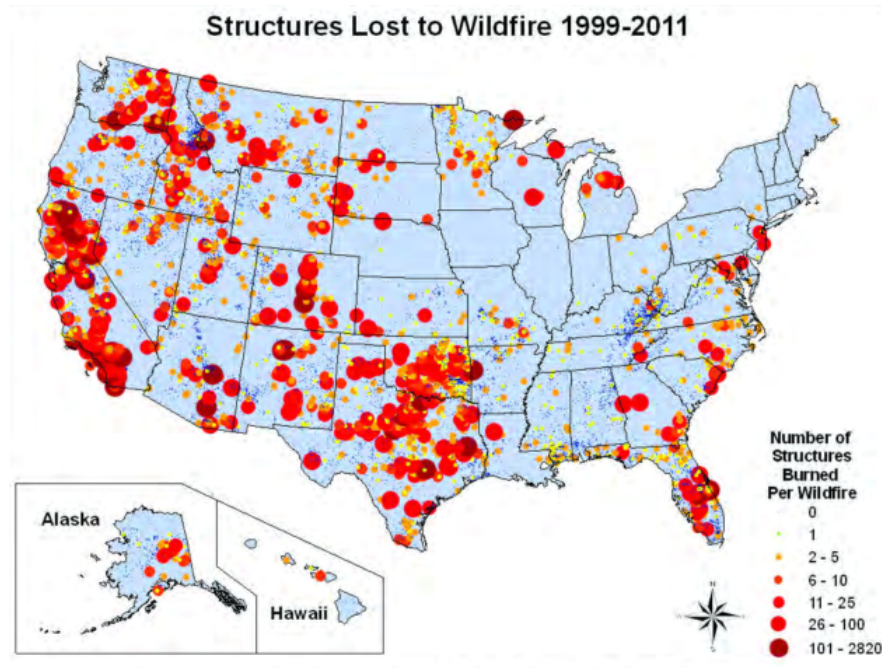


Figure 1.7: Structures lost to wildfire in 1999-2011 period (Credit: US-FS)

of ignition of structures in the WUI. Figure 1.8 illustrates the fire and ember exposure matrix developed by NIST for wildland fuels (Maranghides and Mell, 2012). The exposure matrix is developed using three terrain categories (flat, steep slope, and ravine), three wind categories (no wind, low, and high wind), and four fuel categories (homogeneous surface fuels, inhomogeneous surface fuels, inhomogeneous shrubs and low vegetation, and canopied forest) (Fig. 1.8). This approach is designed to quantify the fire and ember exposure with particular application to improve building codes and standards, supporting the design and maintenance guidelines of ignition resistant structures in the WUI (Maranghides and Mell, 2012).

This problem is also prevalent in other parts of the world. For instance, in Australia the highest single loss of life event was the result of bushfires (Teague et al., 2010). On the 7th of February 2009, the Black Saturday fire started in south-eastern Australia and burnt over 450,000 ha during three weeks, resulting in 173 human fatalities (Fig. 1.9). The Kilmore East fire was the most significant

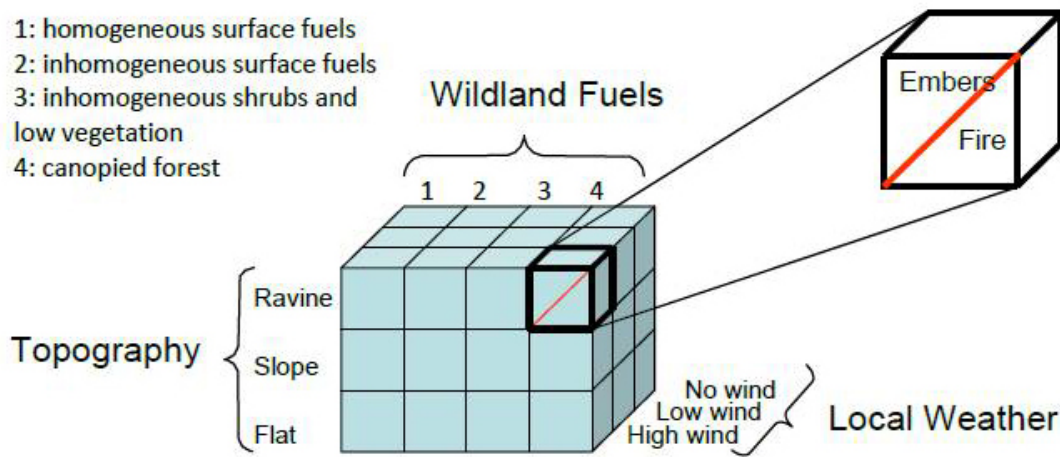


Figure 1.8: Methodology for exposure scale. Credit: NIST

of these fires. In fewer than 12 hours, 100,000 ha burned and 2,200 buildings were destroyed, accounting for 70 % of the fatalities. The fire was driven by an unfortunate combination of extreme conditions: very high temperatures, very low fuel moisture, and high wind. The fire was characterised by intense short range firebrands that increased spotting fires in addition to the very high rate of spread, ranging between 68 and 153 m/min and with an average fireline intensity of 88 MW/m. For comparison, 20 m of the fireline is equivalent to a heat release of 1,760 MW, which is comparable to the net power produced by a nuclear power plant ($\sim 1,500$ MW) (WNA, 2016).

1.2 A Spectrum of Complexities in Wildfires

The main challenges in understanding and predicting wildfire behaviour arise from the variability and numerous possible combinations of important factors that influence a fire regime. Those are associated with the ecosystem characteristics and climate patterns. The fire regime can be impacted through changes in

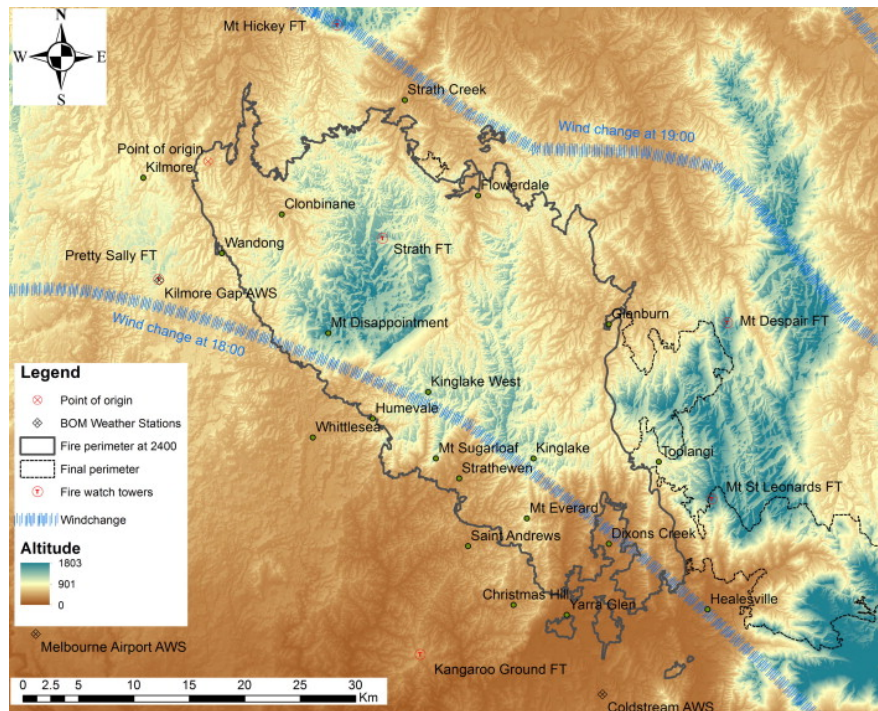


Figure 1.9: General fire location with topography, Bureau of Meteorology Automatic Weather Station (AWS) locations, and wind change isochrones (Cruz et al., 2012)

weather, ignition and fuel, hence affecting the three time scales as described in Table 1.1 (Sommers et al., 2011):

At a short time scale the local weather conditions influence the burning dynamics by affecting fuel conditions and the related heat transfer mechanisms. On medium time scales meteorological variables can influence the abundance of fine fuels (defined as grass, pine needles, tree moss, twigs and other fuels with a diameter less than 6.35 mm), the frequency of lightning ignitions, and the duration of a fire season. On a large scale, fire regimes can be influenced by climate through the alteration of net primary productivity, vegetation composition, structure, fuel loading, and decomposition across a landscape.

Table 1.1: Different time scales influencing a fire

Time scale	Cause	Consequences
Short (hours to days)	Local weather conditions	Burning dynamics
		Heat transfer
		Combustion
Medium (weeks to months)	Meteorological variables	Fuel abundance
		Lightning ignitions
		Fire season duration
Large (years to decades)	Climate	Fire regime

1.2.1 Climate Patterns

Wildfires are also affected by the variability of the atmosphere/ocean climate patterns in many areas of the world (Sommers et al., 2011). For instance, the cyclic anomalies of the surface temperature on a large scale of oceans, such as the El Niño Southern Oscillation (ENSO) in the Pacific Ocean, can drastically affect air-sea interactions and consequently have a significant indirect influence on wildfire occurrence (NOAA, 2016). ENSO combines both El Niño and La Niña and has a frequency ranged between 2 and 7 years. El Niño events can be described by a warming of the ocean surface in the central and eastern tropical Pacific Ocean. The low-level surface winds, which normally blow from east to west along the equator, weaken, or in some cases, reverse direction (NOAA, 2016). Furthermore, it has been proved that ENSO contributed to drought in Africa and Asia and to precipitations in Northern plains in North America (Siegert et al., 2001; Kitzberger et al., 2001). In other areas, El Niño events coincide with above-average cool season precipitation and increased moisture availability to plants during the growing season (Kitzberger et al., 2001). Other consequences of an El Niño event are drought and bush fires in Australia and in Southern Asia,

severe drought in Southern Africa and consequently an increase of fire occurrence in these regions (Sommers et al., 2011).

On the other hand, La Niña corresponds to the cooling of the ocean surface in the central and eastern tropical Pacific Ocean (Fig. 1.10). The normal easterly winds along the equator become even stronger. Typically, large fires are recorded in Southwest USA during La Niña events. In some regions, the transition between El Niño and La Niña conditions can exacerbate fire behaviour. El Niño conditions enhance the production of fine fuel that is then dried by La Niña conditions, creating favourable conditions for wildfire spread (Kitzberger et al., 2001).

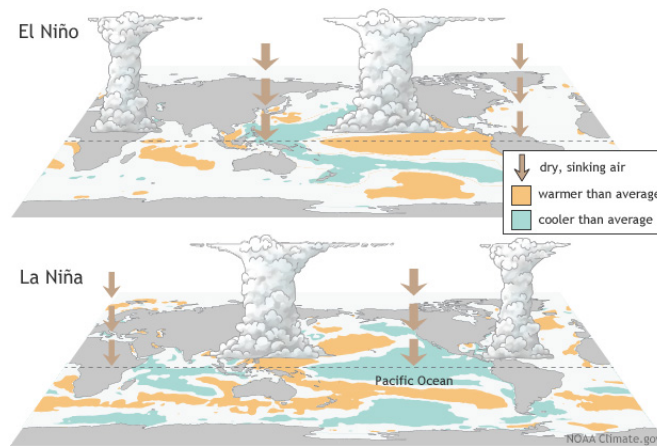


Figure 1.10: Illustration from El Niño and La Niña (Credit: (NOAA, 2016))

In addition to the effects on precipitation, such strong weather patterns make an important contribution to critical fire weather via the production of strong winds such as Foehn winds or Santa Anna winds along the Pacific Coast of the USA (Sommers et al., 2011). These winds bring changes in moisture and high temperature conditions towards the fire and can produce unexpected changes in its behaviour. Such instabilities in the air can amplify the vertical growth of a smoke plume over a large fire by enhancing the strength of the updrafts and increasing the combustion rates by supplying more oxygen. As the height and strength of the smoke plume increases, the potential for fire whirls (Fig. 1.11) and dust devil

occurrence also increases (Seto and Clements, 2011). The resulting fire whirls can reach up to 3 km in diameter and velocities can exceed 50 m/s. This extreme fire behaviour poses a significant threat to firefighting activity. Additionally, these vortices can be produced in a wildfire by the shear of the wind flow above the ground. This mechanism produces horizontally oriented vortices that can be tilted by the fires buoyant flow (Emmons, 1965).



Figure 1.11: Image of a fire whirl. (Credit: KSWB)

1.2.2 Fire Weather

Under strong wind conditions, strong convection plumes can reach several kilometres in altitude, promoting the development of pyrocumulonimbus* (Fig. 1.12) clouds that inject smoke and other combustion products into the lower stratosphere (Cruz et al., 2012).

Strong winds can also cause the ignition of spot fires at a distance of up to a dozen kilometres (Wells, 1968). The maximum spotting distance depends on the burning duration of firebrands (Tarifa et al., 1965; Albini, 1979). Thus, the

*A type of cumulonimbus cloud that forms above a source of heat, such as a wildfire.



Figure 1.12: Pyrocumulonimbus cloud observed 10 km outside of Fort McMurray, Canada. (Credit: Reuters)

spotting distance increases as the fire grows larger and the generated plume has more energy to carry large firebrands (Koo et al., 2010). Spotting can be classed into three categories based on distance and density distribution:

- Short-distance spotting, including ember showers (Manzello and Foote, 2014; El Houssami et al., 2016a) (Fig. 1.13).
- Medium-distance spotting (1,000-5,000 m) as a result of embers and firebrands being lofted into the convection column (Koo et al., 2010).
- Long-distance spotting ($>5,000$ m), which is less frequent because the transport of firebrands over such large distances requires upper level wind speeds in the order of 90-100 km/h (Koo et al., 2010; Cruz et al., 2012). Burning firebrands can easily ignite forest fuel, especially if it is dry, and the ignited recipient fuel can become another source of firebrands (Koo et al., 2010). Therefore, the conditions of the recipient fuel are critical and the criteria required for ignition due to firebrands are strongly related to weather conditions.



Figure 1.13: Image of firebrands crossing over a fuel break and igniting the other side (El Houssami et al., 2016a)

1.2.3 Plume Dynamics

The dynamics of the fire plume also affect fire behaviour, especially during extreme fires. The vertical acceleration of the flow inside the plume depends on the stability and wind profile of the atmosphere surrounding the plume. The most documented connection between extreme fire behaviour and plume dynamics is the concept of a plume-dominated or wind-driven fire. Generally, wind-driven fires are more predictable because the relationship between the rate of spread and the wind speed is approximately linear (Anderson, 1969). Essentially, wind speed provides an upper limit to the flame propagation speed, and an increase in wind can change the dominant mode of heat transfer between the flame and the fuel from radiation to convection (Beer, 1991). The competition between radiative and convective heat transfer modes in wildfire is still an open question. During a plume-dominated fire, the smoke plume is almost vertical, with little influence of horizontal wind on it. The most regularly observed characteristics of a fire plume are the updraft column, eddy vortices along the fire's head, and the winds blowing into the rear and sides of the fire at the ground (Byram, 1959a). Byram

characterized plume-dominated (Fig. 1.14) and wind-driven (Fig. 1.15) modes by referring to the power of the fire (P_f) and power of the wind (P_w), identifying them as the energy-criterion equations, where $P_f > P_w$ during extreme fire behaviour (Byram, 1959b). Such effects have great influences on fire propagation.



Figure 1.14: Plume dominated fire during Las Conchas Fire in New Mexico.
(credit: Creative commons)



Figure 1.15: Wind driven fire in Colorado near Pagosa Springs (Credit: NASA)

1.2.4 Terrain Effects

Fire behaviour is sensitive to the topography of the terrain. Topography is associated with terrain configuration, altitude, slope, and orientation, which directly impact a fire spread (Simeoni, 2013). Dupuy (1995) conducted fire spread experiments to study the effects of fuel load and slope on the rate of spread of different fuel beds. Similarly, Mendes-Lopes et al. (2003) combined the effects of slope and wind on the rate of spread and added the study of the flame characteristics (length, tilt angle and temperature). Viegas (2004) conducted mixed wind and slope experiments and obtained two-dimensional fire shapes. Viegas (2005, 2006) also introduced the notion of Eruptive Fire Behaviour (EFB) to describe the sudden increase of the rate of spread of fire propagation along a steep terrain. This phenomenon was observed many times in the field and resulted in catastrophic accidents resulting in firefighter fatalities (Viegas, 2005). Experimental investigations at laboratory scale have shown that the rate of spread increases by a factor 2.5, for a slope angle above 20° in comparison to the propagation on a flat terrain (Dupuy et al., 2011). This is mainly attributed to the increased contribution of the convective heat transfer. Other atmospheric processes such as channelling effects of upper level winds and flow accelerations over the crest of mountain ridges can also contribute to the EFB (Werth et al., 2011).

1.2.5 Effects of Moisture

The relative humidity is one of the most important factors in development of dangerous forest fires (Hofmann, 1923) and the moisture content of fuels is one of the dominant flammability drivers. Biomass fuels can absorb moisture from the atmosphere, a process that drastically modifies their physical and chemical

properties over time (Rochoux, 2014). As the Fuel Moisture Content (FMC) increases, more energy must be supplied to the fuel to generate a flammable mixture for ignition of moist fuel (McAllister et al., 2012). Jolly et al. (2014) analysed the Live Foliar Moisture Content (LFMC) over a year (see Fig. 1.16) and highlighted the phenomenon known as the Spring Dip in conifer live foliar moisture content. Low LFMC values were observed in old needles during the Spring Dip period and the highest recorded values were observed in new needles. By the end of the study period, old and new needles had similar foliar moisture contents, but new needle moisture content was consistently higher for both species. Foliar flammability followed the same trend as LFMC, reaching its period of highest flammability during the time of the lowest LFMC. However, the critical values of FMC are still not well quantified and depend on the nature of the fuel.

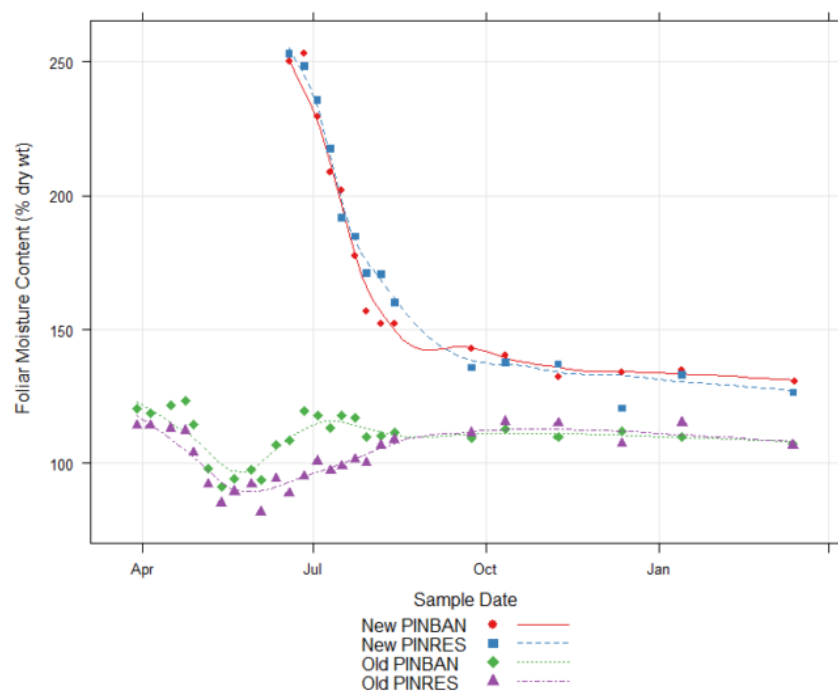


Figure 1.16: Seasonal variations in live foliar moisture content for red pine and Jack pine from April 2013 - April 2014 (Jolly et al., 2014).

1.3 Summary of Progress in Wildland Fire Behaviour

1.3.1 How It Started

Historically, fire prevention in forested areas received much less attention than preventing fires in urban settings (Williams, 1982). Indeed, the first attempts to understand wildland fires were founded by the US Forest Service about a century ago, which is relatively recent compared to other sciences (Show, 1919). This was following the devastating Peshtigo Fire in 1871 (Wells, 1968) and the Great Fire of 1910 (Pyne, 2008). Gisborne (1923, 1927, 1928) was one of the pioneers in the development of fire danger research that was based on observations. At that time, the number and the magnitude of fires were concerning for the Forest Service. Studying fire behaviour in wildland regions was driven by the needs of practitioners directly involved in wildland resource management. Those were mainly foresters, for whom preventing this natural phenomenon was key to protecting their assets (Sullivan, 2009c). This was followed by the development of a research programme in Canada (Wright, 1932). For most of the 20th century, any form of wildland fire was quickly suppressed for fear of uncontrollable and destructive consequences. In the 1960's, policies governing wildfire suppression changed due to ecological studies that recognized fire as a natural process necessary for the development of the ecosystem (Keane et al., 2002). In addition to the early work conducted in the USA, other countries became progressively involved in wildfire research, mainly through their forest services. Canada, Australia, Russia, as well as Mediterranean countries such as Spain, France, Portugal, and Greece have also made a significant impact on wildland fire research (Simeoni, 2013). Since the early 1990's, European Union countries have dedicated substantial funds towards wildland fire research,

resulting in a boom period for this field. This was followed by numerous studies investigating specific aspects of the wide range of problems in wildfires. The studies accomplished through the collection of data from real wildfires and from experiments mimicking the behaviour found in wildfires. For instance, experimental measurements of fire behaviour were conducted at field scale for grasslands (Cheney et al., 1993; Cheney and Gould, 1995; Marsdens-Smedley and Catchpole, 1995), shrublands (Viegas et al., 2002; Santoni et al., 2006; Morandini and Silvani, 2010), and forested environments (Vega et al., 1998; Stocks et al., 2004; Fernandes et al., 2009; Wotton et al., 2012; El Houssami et al., 2016a). Empirical knowledge has been extracted for specific conditions and applied to estimate the fire Rate of Spread (ROS) and the flame height. However, due to the experimental challenges, namely instrumentation limitations, unstable conditions, and testing variability, it is difficult to measure all the relevant quantities needed to make accurate temporal and spatial measurements at the resolution required to obtain statistically representative data with a reduced level of uncertainty.

1.3.2 Scaling Problem

The crucial challenge which inhibits understanding arises from the multiscale aspect of wildfires as described by Simard (1991). Multiple time (seconds to years) and length (m to thousands of km) scales are involved in a wildfire. Physical, chemical, biological, thermal, ecological, and environmental effects are all involved on different time and spatial scales but they are all interrelated during a fire. So far, wildfire problems have been tackled through the focus on specific aspects within one or two scales using experimental, theoretical, and/or analytical techniques, and by developing different tools for either operational, predictive, or scientific ends. Simeoni (2013) categorised the different experimental scales that

can be used to study wildland fires, going from the microscopic scale to the uncontrolled scales as shown in Fig. 1.17.

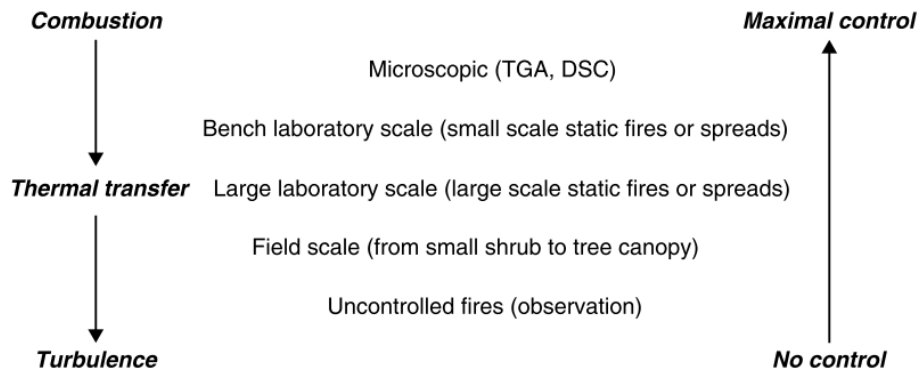


Figure 1.17: Different experimental scales used in wildland fire studies (Simeoni, 2013)

Maximal control over the experimental conditions is offered at the smallest scale. However, large scale experiments and especially real uncontrolled fires offer very little control over the conditions, which make measurements more difficult. Studies at different scales are necessary and complementary because some phenomena can only be observed (and measured) in one or two scales (Simeoni, 2013). Hence, it is difficult to verify if a phenomenon characterised in one scale is well represented at a different scale. Bridging the gap between scales remains one of the greatest problems encountered in fire science (Wickström and Göransson, 1992). An illustration of all the quantities that can be measured at each scale is presented in the Fig. 1.18. Quantities in red are all measurable at laboratory scale (microscopic, bench or large scale) and are all directly linked to physical or chemical properties of the fuel and their conditioning. As for the quantities written in blue, they can only be measured at a larger scale (laboratory large scale, in the field or during a wildfire). However, the latter often result from the combination of the former properties and quantities, in addition to the effect of turbulence. Hence, understanding the fundamentals behind the properties written

in red (and turbulence), will help understanding and describing the quantities written in blue.

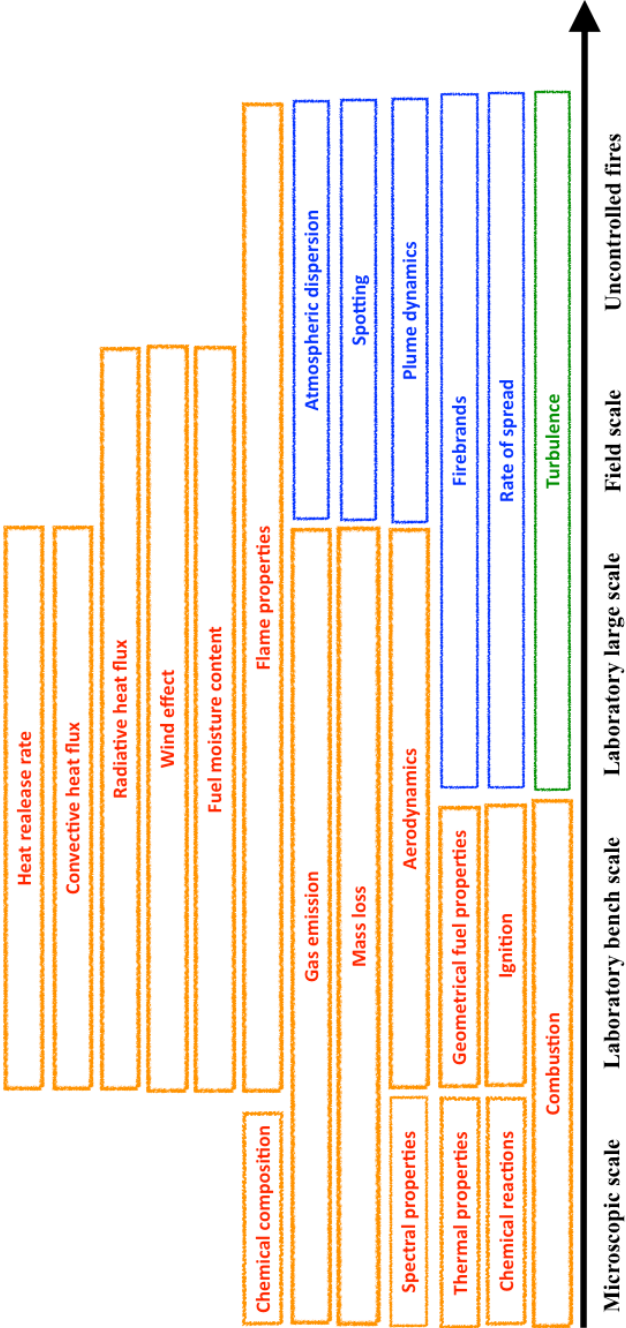


Figure 1.18: Measured quantities at different scales.

A broad description of the main advances made are presented below for each defined scale.

Microscopic scale

The microscopic scale includes processes such as chemical reactions, chemical characteristics of vegetation, the thermal degradation, and kinetics of combustion. Studies conducted at this scale helped to establish physical and chemical parameters that are used at other scales, such as calculating the total energy released by a fuel. Thermogravimetric Analysis (TGA) and Differential Scanning Calorimetry (DSC) have been used to characterise thermal degradation pathways and physical properties of heated vegetative fuel samples (10-1,000 μ m) (Di Blasi et al., 2001; Leroy et al., 2010). The aim of a DSC analysis is to measure the energy required to increase the temperature of a sample and to obtain thermo-kinetic parameters of the material (Leoni et al., 2003; Cancellieri et al., 2005; Leroy et al., 2006), whereas TGA consists of measuring the mass variation during a thermal cycle to evaluate the reaction rate (Font et al., 2009; Leroy et al., 2010). For slow heating rates several trends appear in a typical mass loss curve, which can be associated with the material components, as presented in Fig. 1.19, where the primary components of forest fuels are cellulose, hemicellulose, and lignin cells.

For a constant heating rate (β), an Arrhenius type equation can be obtained from TGA data to model the reaction rate (α) as a function of the temperature (T). It can be written as (Lautenberger, 2007):

$$\frac{d\alpha}{dT} = \frac{Z}{\beta} \exp\left(\frac{-E}{RT}\right) (1 - \alpha)^n \quad (1.1)$$

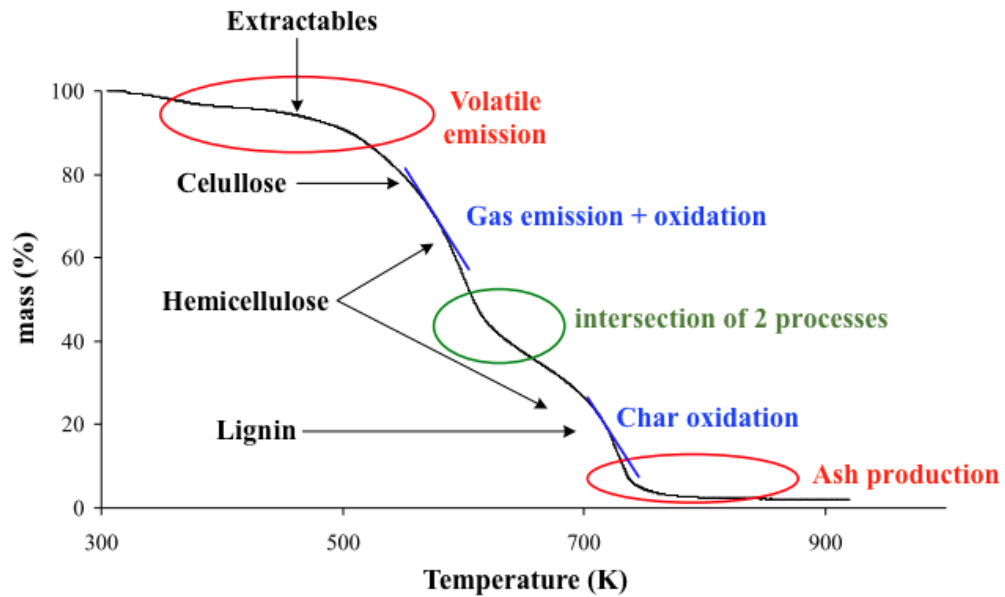


Figure 1.19: Correlation between mass loss and forest fuel composition. Extracted from (Leroy, 2007) in French

The three kinetic parameters, Z the pre-exponential factor, E the energy activation, and n the reaction order are known as the kinetic triplet and can be evaluated under the conditions tested in the TGA. However, when the heating rate is increased, the different peaks in the degradation rate merge and the characteristic reaction temperatures can become progressively higher. Furthermore, if temperatures are sufficiently high, significant degradation rates are simultaneously attained by all the components. This complexity means that the heating rate is generally kept low, which is very far from a real fire scenario where the temperature gradient can be in the range of hundreds of degrees per second. Other studies were conducted to obtain the best set of kinetic parameters for non-isothermal conditions and faster heating rates to be closer to real fire scenarios. Cancellieri et al. (2005) used an approach called Hybrid Kinetic Method (HKM) that includes isoconversional methods mixed with model-fitting methods (Pratap et al., 2007).

This approach allows a more accurate kinetic triplet to describe the fuel degradation (mass loss rate) to be found. Despite successful results, the model is limited by the natural physiology of the samples (thickness, size of leaves and branches) which strongly control the heat transfer during the preheating phase and ignition (Cancellieri et al., 2014). The limitations of extrapolating kinetic analysis are exposed when mixing the effects of chemistry with transport phenomena. This is why the sample size in TGA experiments is required to be small enough that the sample temperature can be considered to be equal to the temperature of the experimental atmosphere. In reality, the sample size is important for the heat and mass transfer processes in the kinetic analysis during pyrolysis and can cause spatial gradients of temperature leading to non-negligible effects of internal heat transfer or significant differences of temperatures between the sample and the surrounding environment. This is why the sample has to be small and have a small Biot number. This is a dimensionless parameter that provides a way to compare the internal thermal resistance of a solid to the boundary layer thermal resistance (Incropera and Dewitt, 1996). It is expressed as:

$$Bi = \frac{\chi L}{k} \quad (1.2)$$

where χ is the convection coefficient, k is the conductivity of the solid, and L is the characteristic length of the solid. In general, when the Biot number is small ($\ll 1$), the body is considered as thermally thin, meaning that the temperature field is uniform inside the body. When the Biot number is much larger than 1, thermal gradients within the the body will dominate the heat transfer.

The chemistry of the thermal degradation can also be understood by analysis of the gaseous products. This is usually undertaken by coupling flammability experiments with gas chromatography (Ormeño et al., 2009), or alternatively using Fourier Transform Infra-Red (FTIR) spectroscopy (Tihay and Gillard, 2010; Bartoli et al., 2011) to determine the nature and type of compounds evolved

during the thermal degradation. It is important to know the composition of gaseous pyrolysis products as this is what forms the flammable mixture with air required for flaming combustion. If the gases are released at a sufficient rate and a suitable ignition source is present, these can be ignited and the gas phase oxidation reactions may generate sufficient heat to cause the ignition of adjacent materials. As suggested by Fons (1946), wildfire propagation can be regarded as a succession of advancing ignition events which induce the displacement of the pyrolysis zone towards the unburnt region. Therefore, the study of pyrolysis is particularly useful for modelling purpose and the fuel hazard assessment. In a series of papers, Tihay et al. (2009a,b); Tihay and Gillard (2010) observed the differences in pyrolysis behaviour and gas composition between different plant species. Tihay et al. (2009a) found that the gas mixture is mainly composed of CO, CH₄, CO₂, and H₂O (Table 1.2). By contrast, other studies consider pyrolysis products to be carbon monoxide burning in air regardless of the vegetation species (Grishin, 1996; Morvan et al., 2006). Hence, a two step global mechanism including methane and carbon monoxide and assuming incomplete combustion of methane can give a better approximation of experimental temperatures and radiant heat fluxes for different fuel tested. However, the model can be more complex under turbulent conditions, which are more representative of a field scale fire. Overall, the thermal degradation chemistry must be explicitly considered in wildfire modelling since the combustion mechanism of the gas species influences the heat of combustion, flame radiation, and flame height, consequently the heat release rate and the heat flux (Tihay et al., 2009b).

Incomplete combustion can also arise from smouldering combustion. By definition, smouldering is a flameless form of combustion, deriving its heat from heterogeneous oxidation reactions occurring on the surface of a fuel (Ohlemiller, 2002). It is also an exothermic oxidation reaction that is self sustained. Smouldering is observed for many types of fuels, including coal (Beshty, 1978; Pironi et al., 2009;

Table 1.2: Mass fractions of the degradation gases released between 280 and 430°C for *P. pinaster* (PP), *P. halepensis* (PH), *P. laricio* (PL), *Erica arborea* (EA), *Cistus monspeliensis* (CM), and *Arbutus unedo* (AU), extracted from [Tihay et al. \(2009a\)](#)

Fuel	PP	PH	PL	EA	CM	AU
CO ₂	0.64	0.663	0.616	0.718	0.59	0.693
H ₂ O	0.089	0.07	0.074	0.047	0.138	0.084
CO	0.171	0.15	0.14	0.141	0.127	0.129
CH ₄	0.029	0.032	0.04	0.026	0.035	0.02
C ₂ H ₄	0.007	0.007	0.008	0.004	0.007	0.005
C ₂ H ₆	0.011	0.011	0.016	0.006	0.009	0.008
C ₃ H ₆	0.002	0.002	0.002	0.001	0.004	0.001
C ₃ H ₈	0.008	0.009	0.013	0.005	0.011	0.007
C ₄ H ₆	0.022	0.037	0.059	0.04	0.051	0.032
C ₄ H ₈	0.014	0.014	0.021	0.009	0.019	0.014
C ₄ H ₁₀	0.007	0.005	0.01	0.003	0.009	0.007
H ₂	0	0	0.001	0	0	0
O ₂	0	0	0	0	0	0

[Hasan et al., 2015](#)), peat ([Hadden, 2011](#); [Cancellieri et al., 2012](#)), soil contaminated with hydrocarbon liquids ([Pironi, 2009](#)), cellulosic materials ([Rogers and Ohlerniller, 1980](#)), polyurethane foams ([Hadden et al., 2014](#)), and wood products ([Swann et al., 2008](#); [Anca-Couce et al., 2012](#)). One characteristic that all these materials have in common is that they form a rigid char upon heating in the presence of oxygen. Once the char is formed by pyrolysis of the fuel, the oxidation is driven by the competition between oxygen supply and heat transfer that ultimately determines the characteristics of the smouldering reaction ([Torero, 1991](#)). This model is illustrated in Fig. 1.20.

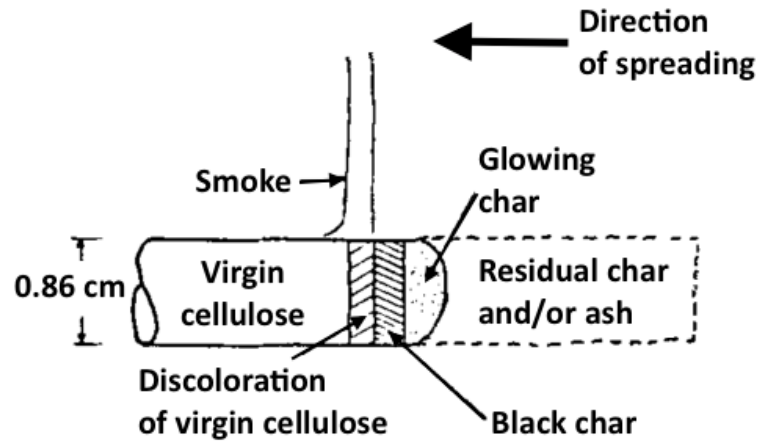


Figure 1.20: Representation of steady smouldering along a horizontal cellulose rod (Moussa et al., 1977)

Smouldering temperatures (approximately 600°C), reaction rates, and heat released (approximately 5 kJ/g-O_2) (Ohlemiller, 2002) are lower than for flaming combustion ($1,500^{\circ}\text{C}$ and 13 kJ/g-O_2) (Drysdale, 2011). These characteristics make smouldering propagations (which are of the order of 0.1 mm/s) about two orders of magnitude lower than the velocity of flame spread (Ohlemiller, 2002). From a chemical point of view, smouldering combustion is characteristically incomplete as the gaseous pyrolysis products are not fully oxidised, hence it emits toxic gas compounds at a higher yield than from flaming fires (Koppmann et al., 2005).

Bench laboratory scale

Most studies conducted at this scale focus on the flammability of a fuel (i.e. ignition, energy released, and flame characteristics) and the external conditions (i.e. flow, heat flux, and temperature). The term flammability refers to the ability of a fuel to ignite and sustain a fire. It consists of three components: ignitibility, sustainability, and combustibility (Anderson, 1970). Later, Tewarson and Pion

(1976) expanded this definition and described flammability using five quantifiable components: ignition, fire growth, burning intensity, generation of smoke and toxic compounds, and extinction. Proper evaluation of material flammability requires understanding of the pyrolysis process and the interactions with the flame. Many studies have looked at this issue regarding building materials (Quintiere, 1981; Quintiere and Harkleroad, 1984; Janssens, 1991; Wickman, 1992; Long et al., 1999). Ignition is obviously a critical process for the development of a fire as it is the phenomenon which leads to the initiation of a fire. It can be accurately defined as the initiation of a combustion reaction between the fuel and oxidizer followed by the establishment of the reaction through a balance between the energy generated by the combustion reaction and the heat lost from the reaction to the surroundings (Fernandez-Pello, 2011). There are many published reviews concerning fire ignition and its characterisation (Babrauskas, 2003; Quintiere, 2006; Torero, 2008). Related to forest fuel, Torero and Simeoni (2010) applied a one-dimensional model for the ignition of porous fuel to determine the effective thermal properties assuming that the fuel is thermally thin. The model was originally developed for solid fuels, but in contrast to those fuels, the thermal transfer through the porous bed is mainly due to radiation instead of conduction, thus radiation was linearised. It was found that the extension of ignition theory to porous fuels provides good results as long as the influence of the flow inside the fuel layer is negligible on both convective heat and mass transfer and pyrolysis gases dilution. When air flow is added, the porous fuel does not follow the same behaviour as for solid fuels due to changes in heat and mass transfer mechanisms. Thomas et al. (2011, 2014) worked on the extension of this model for flow conditions through the sample and for fuels with different physical and chemical properties. They described how convection cooling of a forced airflow influences the time to ignition and the transition between radiation and convection dominated heat transfer regimes depending on the external heat flux. Benkoussas et al. (2007) assessed the validity of the thermally-thin assumption

used in porous bed descriptions of wildland fire behaviour models and defined a radiative Biot number (Bi_{Rad}) as:

$$Bi_{Rad} = \frac{\epsilon Q_{ext} L}{k \Delta T} \quad (1.3)$$

with ϵ the surface emissivity, Q_{ext} , the external heat flux. They established that the transition occurs when $Bi=0.1$, regardless of the particle shape. Hence particles can be considered isothermal (thermally thin) for values of Biot number less than 0.1. [Lamorlette et al. \(2015\)](#); [Lamorlette and Candelier \(2015\)](#) also investigated the thermal behaviour of solid particles at ignition in attempting to theoretically separate the transition between thermally thick and thin behaviour when a sample is exposed to a radiant heat flux. They were able to describe the region where thermally thin and thick solutions overlap, allowing the use of models based on both assumptions with the same accuracy.

The physical characteristics of fuel elements or even the fuel bed bulk properties have a strong influence on the burning regime: geometrical properties such as thickness, surface to volume ratio or packing ratio can often dominate the fire behaviour. [Anderson \(1969\)](#) observed that the residence time associated with fire spread increases with particle thickness in porous beds but also that burning characteristics and flame depth are strongly controlled by the fuel particle size and the porosity of the bed. Similar behaviour was described by [Bartoli et al. \(2010\)](#), who demonstrated that permeability drives the burning dynamics in porous beds and that the energy released increases with permeability. It has also been shown that, for a given permeability, the fuel species have an influence on times to ignition and duration of flames. Several relationships and descriptions have been made to investigate the effects of permeability on flame height and temperatures ([Dupuy et al., 2003](#); [Ormeño et al., 2009](#)). The physical characteristics of forest fuels also influence the fuel radiative properties in two ways, which reflect fuel particle and bulk bed properties:

- Forest fuel emissivity/absorptivity is highly spectrally dependent. The transmissivity and reflectivity of different Mediterranean forest species were measured by [Monod et al. \(2009\)](#) in the near-infrared and mid-infrared ranges ($1,000$ to $6,000\text{ cm}^{-1}$) (see Fig. 1.21). The corresponding absorptivity was deducted from these measurements and was close to 1 between $1,000$ and $3,500\text{ cm}^{-1}$, whereas a drastic regression was observed above this value. These spectral variations were seen consistently regardless of the species. A total absorptivity was averaged for each species ranging between 0.84 and 0.93 . It was also found that the water content of the vegetation influences the absorptivity, as the same measurements were carried out on fresh and dry species.

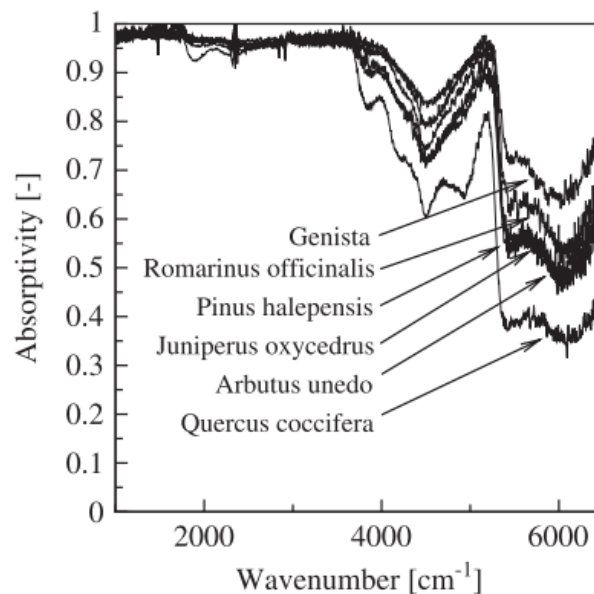


Figure 1.21: Absorptivity measurements for six species. Extracted from [Monod et al. \(2009\)](#)

Similarly, [Acem et al. \(2010\)](#) conducted another series of spectral analyses on Mediterranean live pine needles. A spectral average of the absorptivity and transmissivity were calculated over the entire range, resulting in 0.95 and 0.02 for the absorptivity and transmissivity, respectively. However,

significant variation was noticed in the absorptivity (from 0.6 to 1) in the near infrared showing dependence to the wavenumber.

- The extinction coefficient of an equivalent medium of forest fuel is usually estimated from De Mestre correlation as (NAS, 1961; De Mestre et al., 1989):

$$\sigma = \frac{nA}{4} \quad (1.4)$$

Where σ is the extinction coefficient (m^{-1}), n is the density (of leaves or fuel) located in the medium (number of leaves per m^3) and A is the total area of the considered vegetation element (m^2). This concept of equivalent medium involves an ensemble of vegetation elements considered as a whole, often assumed homogeneous, grey and non-scattering. A numerical study has been carried out by Monod et al. (2009) on the validity of De Mestre relationship often used when predicting the extinction coefficient of a vegetation medium. A mathematical justification has been found for this relationship. In the case of a medium made with purely absorbing leaves, the relationship gives very good results. When introducing realistic radiative properties for leaves, the relationship is less robust but can be easily corrected by multiplying with a correct value of the sum of absorptivity and reflectivity of the leaves. The study indicates that these correction factors are in the range of 0.94-0.98 depending on the species. Acem et al. (2009) developed analytical methods to estimate the effective extinction coefficient for vegetative medium of various leaf orientations, as an extension to De Mestre formulation for random leaf distributions. They have also developed a numerical tool based on using ray tracing methods to estimate the effective extinction coefficient for homogeneous leaf distribution in a tree that also works when heterogeneities are introduced.

Additionally, Boulet et al. (2011) measured the radiation emission from flames

and the corresponding absorption by vegetation. Strong emission peaks were distinguished due to the hot gases produced by the combustion in the gas but no emission by soot was observed at the scale used because the flames were not optically thick. Similarly, measurements of flame emission from burning vine branches and excelsior were carried out by Parent et al. (2010), where infrared imagery (Fig. 1.22) and FTIR spectrometry (Fig. 3.2) confirmed the large contribution of emission around $2,300\text{ cm}^{-1}$ by CO_2 , the important emission by H_2O , and weak contribution of soot. At around $7.83\text{ }\mu\text{m}$ ($1,277\text{ cm}^{-1}$), most of the flux was coming from the bottom of the picture due to the burning vegetation (Fig. 1.22b). This wavelength band is characteristic of water vapour emission produced by combustion. At around $4.45\text{ }\mu\text{m}$ ($2,247\text{ cm}^{-1}$), more radiation was emitted from flame than by the vegetation, which represents the contribution of CO_2 (Fig. 1.22c). At around $3.8\text{ }\mu\text{m}$ ($2,631\text{ cm}^{-1}$), soot was the only emission source in the flame area, but the signal was very low (Fig 1.22d and 3.2). Furthermore, the fuel embers contributed in a continuous way in the infrared range.

Indeed, flames from forest fuels are not usually considered very sooty at laboratory scale, but an estimation of the radiant fraction can be obtained. By assuming that the Heat Release Rate (HRR) of a fire is the addition of a convective and a radiant component, Tewarson (2004) demonstrated how to obtain the convective component in systems where heat losses are negligible, and was then able to calculate the radiant component by complementarity. He also indicated that the chemical, convective, and radiant HRR depend on the chemical structures of the materials and ventilation conditions. Among the fuels tested, Tewarson (2004) reported values for the radiant fraction of well ventilated fires of pine wood (29.8 %). This approach gives only an order of magnitude and comparison points for classification as the analysis is simplified. Morandini et al. (2013); Tihay et al. (2014) applied the same methodology to estimate the radiant fraction for the fire spread across pine needle beds in different configurations. They provided

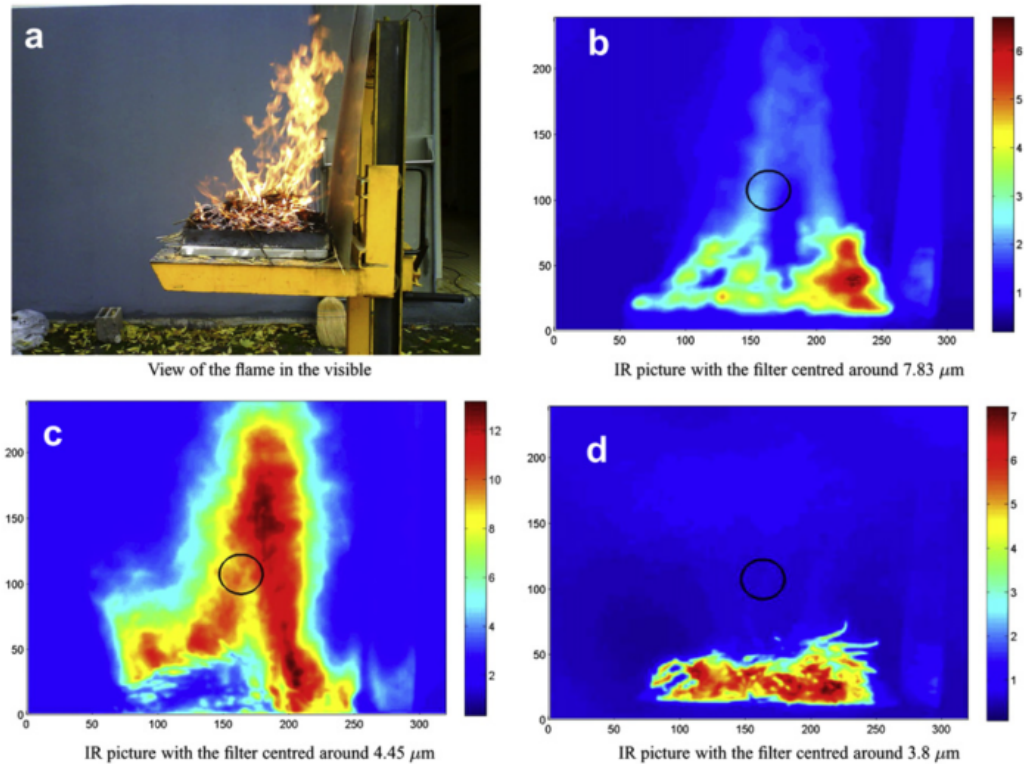


Figure 1.22: Pictures of the flame in a) the visible range and in the infrared around b) 7.83 μm c) 4.45 μm and d) 3.8 μm . Black circles correspond to areas viewed by the spectrometer. Extracted from Parent et al. (2010)

measurements of the **HRR** by Oxygen Consumption (**OC**) calorimetry, the fireline intensity, and the heat fluxes to calculate the combustion efficiency, the convective fraction, and then derived the radiant fraction. They also attempted to separate the radiant fraction due to the flame from the one due to ember radiation. This was done by calculating the radiant fraction due to the flames through radiant heat flux measurements and flame radiant power calculations. Then the contribution of embers to the radiation was obtained by deduction from the overall radiant fraction. This approach appears reasonable theoretically, however the way the heat flux gauge was positioned in these studies is highly controversial. In fact, the heat flux gauge was positioned in such a way that both embers and the flames

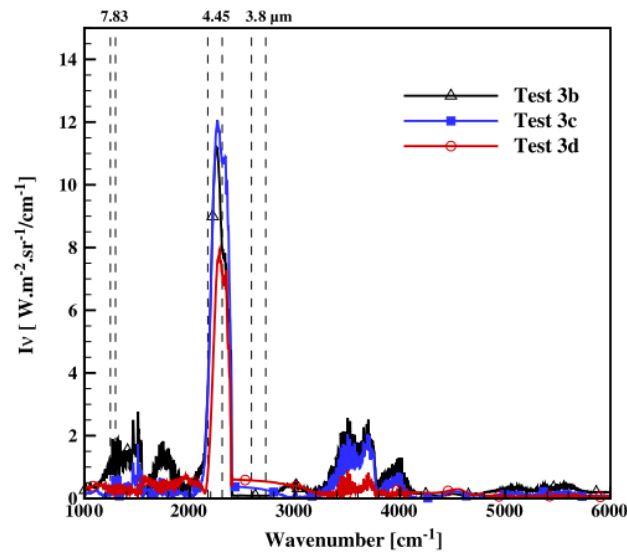


Figure 1.23: Spectral intensity emitted in the flame 10 cm above the burning vegetation. Extracted from [Parent et al. \(2010\)](#)

were apparent in the view field. Hence, the incident heat flux included the ember component in the calculation of the flame component.

Estimating the energy released during a fire is a main aspect of the flammability assessment. As the [HRR](#) is not a quantity directly measured, there is a considerable uncertainty regarding its quantification during a fire. The heat release rate is commonly assumed to be equal to the product between the mass loss rate and the higher heating values, which can lead to potential error in the determination of combustion efficiency of the fire. [Biteau et al. \(2008\)](#) conducted laboratory scale experiments to determine the [HRR](#) of pine needles (and other fuels) by means of calorimetry. He demonstrated that the [HRR](#) can hardly be obtained using [OC](#) and Carbon Dioxide Generation ([CDG](#)) ([Janssens and Parker, 1992](#)) calorimetry without specifically knowing the energy constants of the fuel for materials with complex combustion processes, because of the strong dependence of the calorimetric methods on the chemistry of the materials. However, [Schemel et al. \(2008\)](#) showed that calculating the [HRR](#) by means of calorimetry for pine

needles can be reinforced by the use of mass loss rate and by knowing the heat of combustion in well ventilated test conditions. Mass loss, [HRR](#), and gas concentration measurements were also presented in [Schemel et al. \(2008\)](#) for natural and forced flow condition. These results are shown in Fig. 1.24.

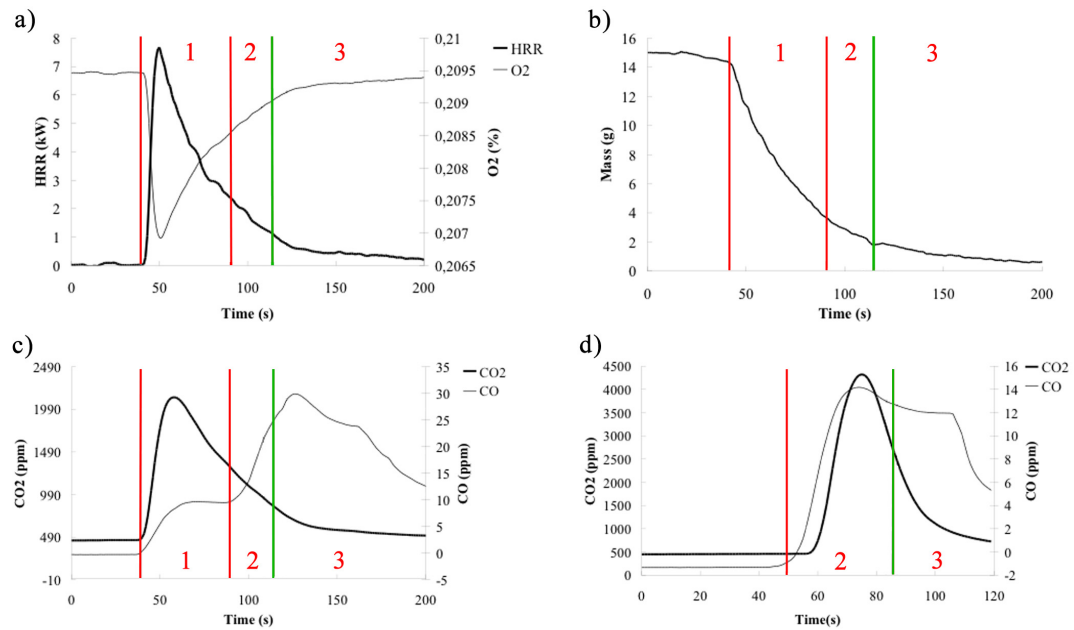


Figure 1.24: a) Mean oxygen consumption in natural flow conditions and HRR; b) Mass loss in natural flow conditions; c) Mean CO₂ and CO concentrations with natural flow; d) Mean CO₂ and CO concentrations with forced flow.

Figures 1.24a and b show the evolution of the [HRR](#) and mass loss for natural flow conditions during the burning of pine needles in the FPA. The vertical green lines represent flameout. Useful information can be extracted from these curves and three phases can be defined. During phase 1, which occurs just after ignition, only flaming is involved, and the [HRR](#) peaks (Fig. 1.24b). During phase 2, flaming and smouldering occur simultaneously, and finally during phase 3 (after flameout) only smouldering is observed. Fig. 1.24c and 1.24d present CO₂ and CO production under natural flow and forced flow, respectively. The differences in CO curves demonstrate the changing behaviour in the combustion process. CO concentration is a good indicator of the two stages of combustion

when correlated to visual observations. The first steep increase in Fig. 1.24c is due to the ignition of the sample. A steady production of CO follows, which corresponds to the flaming stage (phase 1) with a strong oxidation of CO in the flame. The consequent increase is due to the decrease of the flame and the initiation of smouldering combustion. The two processes overlap during this stage (phase 2). After flameout, CO production peaks due to the incomplete combustion due to smouldering (phase 3). Fig. 1.24d describes forced flow conditions. The CO₂ curve indicates a shorter time of combustion, and it is noticeable that the steady state has disappeared. This behaviour was mainly due to the additional oxygen supplied inside the fuel bed by the forced flow. Fig. 1.24c shows that smouldering is occurring mainly after flameout (phase 3) whereas Fig. 1.24d shows that flaming and smouldering are occurring simultaneously (phase 2).

Moreover, [Saâdaoui et al. \(2008\)](#) characterised the flow during the burning of a pine needle bed by measuring the gas velocity using Particle Image Velocimetry (PIV) to establish charts of velocity vectors in a region of the flow, and by Laser Doppler Anemometry (LDA) to measure two instantaneous velocity components at a point of the flow. These types of studies are important for understanding the role of the flow during a fire, which becomes greater during larger fires, where the fluid dynamics and the role of turbulence become more dominant as plumes are larger.

Large laboratory scale

Larger laboratory-scale experiments integrate coupled aspects and allow studying phenomena that do not appear at the small scale. These phenomena include the development of a turbulent flow along the fire front, fire acceleration, and large turbulent flames. [Simeoni \(2013\)](#) provides an exhaustive literature review concerning large scale experiments conducted in several laboratories around the

world. The experiments range from burning large fuel beds to single trees and allowed measurement of different quantities, typically the fire Rate of Spread (ROS). A selected number of noteworthy studies are listed in Fig. 1.25.

Field scale and uncontrolled fires

Numerous large scale experiments were conducted in controlled burnings over the last decades in different ecosystems including grasslands, shrubs and forests (Thomas, 1967; Cheney et al., 1993; Stocks et al., 2004). Such experiments provided remarkable indications regarding rate of spread, fireline intensity, and the direction of fires, wind effects, moisture content, heat transfer, wind fields and the properties of the fire front. For instance The Commonwealth Scientific and Industrial Research Organization (CSIRO) performed more than a hundred large-scale grass fire experiments in Australia (Fig. 1.26) to study the influence of fuel, weather and fire shape on fire spread and to develop statistical models (Cheney et al., 1993). Similarly, many empirical models were calibrated based on such experimental campaigns (Noble et al., 1980; Cheney et al., 1998; Fernandes et al., 2002; Gould et al., 2007).

Morandini and Silvani (2010) provided a literature review about the field scale experiment and their corresponding measured quantities. Additionally, they conducted experiments in live Mediterranean vegetation, in which they characterised two regimes. In a plume dominated regime, radiation heat transfer was dominant ahead of a fire front for higher fuel load. However, in wind driven regime for lower fuel loads, the flow was governed by inertial force due to the wind, and the fuel preheating was due to mixed radiative and convective heat transfer. The downside of such experiments is that the external parameters cannot be fully controlled (weather, terrain, fuel), as it is almost impossible to maintain repeatable conditions and to acquire full field measurements. While it is dangerous to

Measured quantities	Modified parameters	Tested material	Reference
ROS, intensity, flame height, length, mass loss	Wind speed, depth, packing ratio	Excelsior, sticks, and mixture	Catchpole et al. (1993)
ROS, fuel consumption, mass loss rate	Slope, fuel load	Pine needles	Dupuy (1995)
ROS	Particle size, fuel depth, packing ratio, FMC, wind speed	Pine needles and excelsior	Chatchpole et al. (1998)
ROS	Wind speed, slope	Pine needles	Viegas (2004)
ROS	Fuel depth, wind speed, slope, FMC	Chaparral	Weise et al. (2005)
Effective heat of combustion	FMC	Douglas Fir	Babrauskas (2006)
Firebrands (mass, diameter, size), mass loss, heat flux, temperature	Tree height	Douglas fir	Manzello et al. (2007) Mell et al. (2009)
Convective heat transfer, wind distribution, temperature, distance from ignition	Wind speed	Pine needle and excelsior	Anderson et al. (2010)
Radiative and convective heat transfer	Wind speed, burner (distance, temperature), fuel size	Wood shavings and pine needles	Frankman et al. (2010)
ROS, fuel consumption, flame residence time, temperate, flame geometry	Slope, fuel bed width	Pine needles	Dupuy et al. (2011)
Ignition probability, ignition time	FMC, fuel bed type, firebrand type	Eucalyptus bark and leaves, pine cones and needles	Viegas et al. (2014)
ROS, cumulative distance	Wind speed,	Eucalyptus and pine (leaves, twigs, bark)	Mulvaney et al. (2016)

Figure 1.25: Significant large scale experimental studies in wildland fires.



Figure 1.26: Experimental burning campaign (35 x 35m plots) for cured grassland in Australia. Different fire behaviours are observed in two simultaneous experimental fires by CSIRO. Extracted from (Cruz et al., 2015)

instrument real wildfires, it is always possible to monitor uncontrolled fire and to make observations during and after the fire, such as characterising the damage made from firebrand showers (Manzello and Foote, 2014).

1.3.3 Fire Modelling

During the last decades, many attempts at fire modelling were made using different approaches. With computational capabilities significantly increasing and becoming more accessible, many scientists developed numerical tools to either grasp the physical and chemical comprehension involved in fire dynamics, whereas other efforts were purely based on empirical knowledge that is derived from phenomenological and statistical descriptions of observed fires. Detailed reviews about the developments in fire spread modelling have been published (Weber, 1991; Pastor, 2003; Sullivan, 2009a,b,c). Based on the classification proposed by Weber (1991), there are three main types of models:

Physical models

Physical models are based on conservation principles of mass, momentum, energy and species. [Grishin \(1996\)](#) presented an extensive review of the work conducted in the USSR in the 1970's and 1980's, which was the cornerstone for physical fire modelling. A multiphase approach is defined in the work of [Grishin \(1996\)](#), which includes N-phases made of several solid phases and a gas phase. It allows the representation of different types of vegetation in an equivalent medium without having to model each single tree and particle individually. The multiphase approach implies that conservation equations are applied to both solid and gas phases, which are coupled through non linear heat and mass flux exchanges ([Grishin, 1996](#)). Since the 1990's, many other researchers worked on the improvement of the multiphase approach through the development of different codes, such as FireStar ([Morvan et al., 2006](#)), Wildland Urban Interface Fire Dynamics Simulator (WFDS) ([Mell, 2010](#)), and others ([Larini et al., 1998](#); [Zhou and Pereira, 2000](#); [Porterie et al., 2000, 2005](#); [Margerit and Sero-Guillaume, 2002](#)). A detailed review of these models is presented in ([Sullivan, 2009c](#)). These models combine advanced detailed physico-chemical models with a classical method of Computational Fluid Dynamics (CFD) to accurately describe fire dynamic processes. The system of averaged equations that are solved includes balances of mass, species, momentum, and energy for each species, as well as a Radiative Transfer Equation (RTE). The strong coupling between the solid and gas phases is represented by interface relationships. Mean flow advection, boundary effects, and buoyancy-induced flows are easily solved through Navier-Stokes equations, while fine-scale pyrolysis, radiation, chemistry, and combustion are sub-scale processes that are still under development.

- [WFDS](#) is an extension of Fire Dynamics Simulator ([FDS](#)), the former is a model developed to predict fire spread at the [WUI](#) ([Mell et al., 2007](#)). This

model is based on FDS's formulation of the equations of motion for buoyant flow, also referred to as the low Mach number combustion equations (Rehm and Baum, 1978). They describe the low speed motion of a gas driven by chemical heat release and buoyancy forces, simplifying equations describing the transport of mass, momentum, and energy for fire-induced flows. WFDS incorporates the multiphase approach and is designed to predict the progress of wildland fire for the intent of simulating WUI fires. Due to the relatively coarse scale of the resolved computational grids, detailed chemical kinetics and char oxidation are not included in the model. WFDS was confronted against measurements from experiments of individual Douglas fir tree burns in Mell et al. (2009) (Fig. 1.27). The model was successfully able to predict the mass loss rate and radiative heat flux. However, it was shown that further improvements are needed especially in the turbulence modelling of WFDS to better represent the interaction between the flow and vegetation, for individual trees or a canopy (Mueller, 2012; Mueller et al., 2014). This issue is important to model because it can affect the fire behaviour through a possible transition from a ground fire to a crown fire. This occurrence represents a critical condition in fire spread.

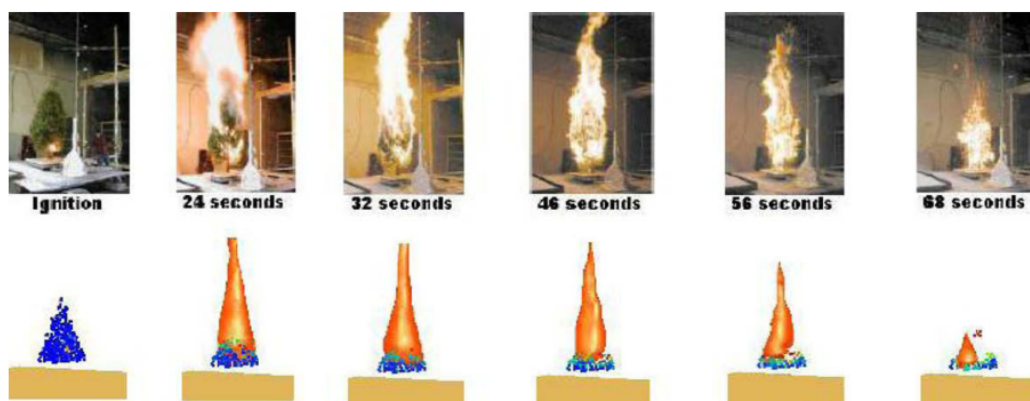


Figure 1.27: Experimental and simulated (WFDS) snapshots of the burning stages of a Douglas fir. Extracted from Mell et al. (2009)

- FireStar is a physical model developed by [Morvan and Larini \(2001\)](#); [Morvan and Dupuy \(2001\)](#) based on the multiphase approach. FireStar can potentially include an unlimited number of fuel types coexisting in an elementary control volume. It allows the representation of complex fuel mixing, such as in [Morvan and Dupuy \(2004\)](#), where complex Mediterranean fuel was modelled including live and dead components of shrub, grass, twigs and foliage. [Morvan and Dupuy \(2004\)](#) also proposed a re-normalisation group, $k-\epsilon$ turbulence model with an EDC concept for combustion to account for the coexistence between regions of turbulent (thermal plume) and laminar (near the ground) flows at flame scale and a pressure correction algorithm to couple the pressure with velocity. This study has confirmed the existence of two modes of wildfire spread that were proposed by [Pagni and Peterson \(1973\)](#), namely wind driven fires and plume dominated fires. In [Morvan et al. \(2009\)](#), the model was tested to reproduce experimental grassland fires, and a relatively good agreement was found. The numerical results also confirmed that a wind-aided line fire in a dry grassland can result in high ROS (>5 m/s) and very high intensity levels (>30 MW/m), representing extreme danger during a suppression or a prescribed burning operation. This study underlines the value of physical modelling tools to improve knowledge concerning wildfire behaviour where large scale experiments cannot be conducted. As an example, it is important to address the problem of the minimum width necessary to build a safe firebreak or a fuel break in the forest and in the WUI. [Morvan \(2015\)](#) also studied the thermal impact at different distances from a fire front in a shrub layer using FireStar. Predictions of the rate of spread, fire intensity, radiation heat flux, and temperature field allowed the efficiency of a firebreak to be assessed (Fig. 1.28). However, at this stage, physical modelling results cannot be trusted without experimental comparison ([Morvan, 2015](#)). Recent developments

in FireStar (FireStar3D) have allowed better estimation of the turbulent reacting flow in three dimensions (Meradji et al., 2016).

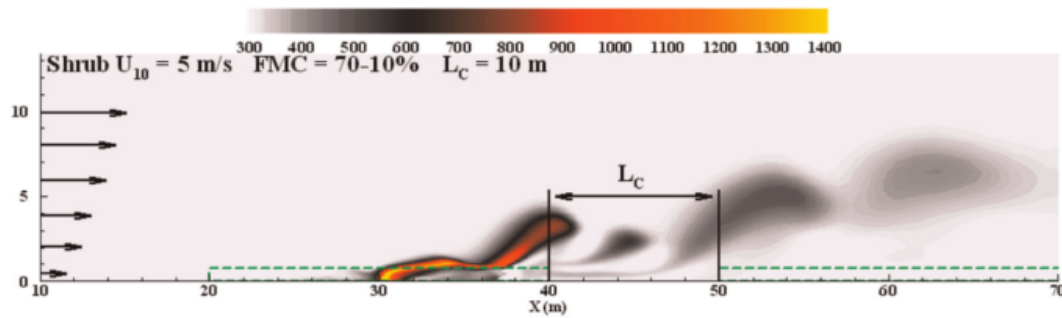


Figure 1.28: Configuration of a fuel break (L_c) in a Mediterranean shrubland. Extracted from Morvan (2015)

- FIRETEC (Linn, 1997) was developed at the Los Alamos National Laboratory in the USA, and is a three-dimensional model that employs a fully compressible gas transport formulation to represent the coupled interactions of heat release, heat transfer, and fluid mechanics (Linn et al., 2002). As the combustion and the solid fuel layer is strongly simplified, FIRETEC couples fire spread modelling with atmospheric modelling through an atmospheric model called HIGRAD (Reisner et al., 2000) for solving equations of high gradient flow. It is a very efficient way to describe fire spread in relation with the local flow around the fire (Fig. 1.29). However, the computational costs imply the use of supercomputing capacities to simulate a small wildland fire. Additionally, the model uses an ignition temperature criterion set at 500 K and a probability distribution function to determine the mean temperature in a control volume. Once ignition occurs, the evolution equations are used to track the solid and gas phase species.

WFDS and FIRETEC were confronted (Mell et al., 2005) over the experimental campaign reported by Cheney et al. (1993); Cheney and Gould (1995). It was

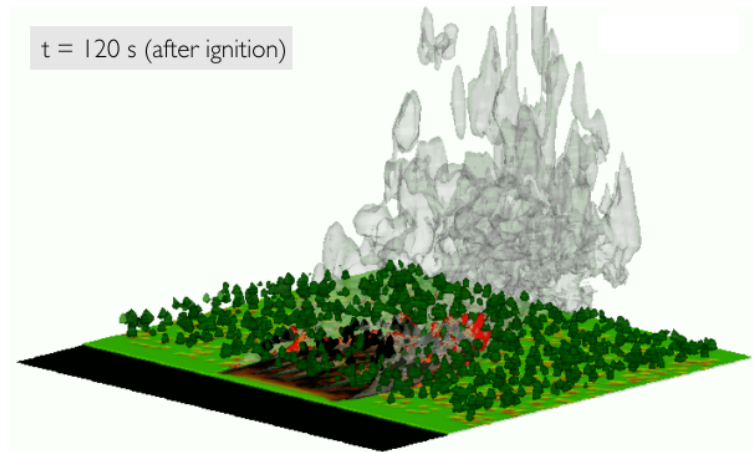


Figure 1.29: FIRETEC simulation of 20 m \times 50 m field-scale wildfire spread (Flagstaff, Arizona) in discontinuous fuel beds, 120 s after ignition. Colours on the horizontal plane represent the spatial variations in vegetation density, black indicating the absence of fuel and bright green indicating the 1 kg/m³ iso-contour (corresponding to a tall grass of 0.7 m depth). Dark green iso-surfaces indicate tree locations, while orange, red and grey iso-surfaces indicate regions of hot gases. Credit: (Linn et al., 2005).

found that the most significant difference in the results from the two models was that backing fires (spreading upwind) and flank fires are more likely to occur with **WFDS**. Field observations of backing fire behaviour suggest that they are less likely to survive at higher wind speeds, but this trend is less well reproduced by FIRETEC. However, it was noticed that FIRETEC requires significantly more computational resources to run, as the same simulation run with **WFDS** was 100 times faster.

Overall, FireStar and **WFDS** provide solutions not only for the fire but also for the atmosphere around the fire, as opposed to FIRETEC, which uses HIGRAD to provide atmospheric boundary conditions. Regarding radiation, FireStar solves the radiation transfer equation using the Discrete Ordinate Method (**DOM**), a transport equation for a finite number of discrete solid angles that can be used

over a wide range of optical thicknesses (Modest, 1993), while WFDS uses a Finite Volume Method (FVM) that solves the grey gas form of the radiation transfer equation in a participating medium (Raithby and Chui, 1990). The DOM is based on a Gauss-Legendre quadrature integration (i.e. a weighted sum at specified points within the domain of integration), which is not included in the FVM (in which all points are equidistant and weigh the same). These physical models deal with unsteady flows, and hence use defined methods of discretisation for partial differential equations. FIRETEC and WFDS are based on explicit solvers to reduce Central Processing Unit (CPU) time, while FireStar is based on an implicit solver, which provides more stability. In Meradji et al. (2016), numerical findings of FireStar3D were compared with experiments from Cheney et al. (1993, 1998), and results using an empirical model (MK5), a semi-empirical model (BEHAVE), 3D numerical models (FIRETEC, WFDS), and a 2D numerical model (FireStar). The evolution of the ROS with the wind speed measured at 10 m above ground is shown by Fig. 1.30.

For low to moderate velocities ($U \leq 6$ m/s), FireStar3D results compared well with experimental data and with other predictions, as a quasi-linear evolution of the ROS can be observed as a function of the velocity. For these values, a steady regime of fire propagation was reached in the simulations. For $6 \leq U \leq 8$ m/s, the results of the model remain consistent with the experiments and with other models, despite the large dispersion of the experimental measurements. For $U \geq 8$ m/s, FireStar3D and all the other models underestimate the ROS, except for FireStar (2D). In comparison between FireStar (2D) and FireStar3D, the former assumes a straight and unbounded pyrolysis front which allows a better prediction of the ROS at high wind speeds (10 m/s and 12 m/s), whereas, the 3D model assumes a short (50 m) ignition line. In return, the 2D model fails to account for the aerodynamic drag on the lateral border of the fire front that is primarily responsible for its curvature, which results in the overestimation of the ROS at low

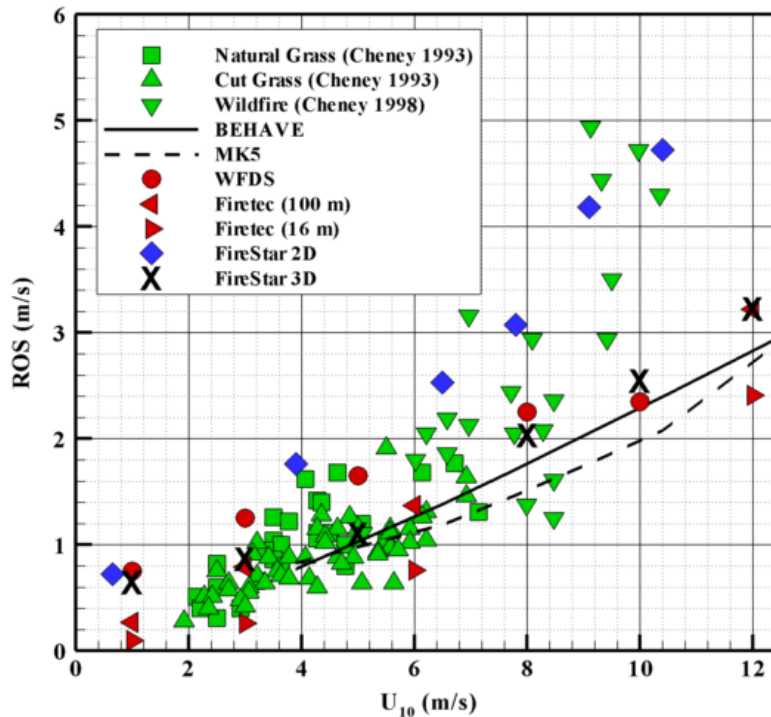


Figure 1.30: Rate of fire spread (ROS) through a uniform grassland obtained for different wind speeds measured at 10 m above ground. Extracted from Meradji et al. (2016)

to moderate wind speeds (Meradji et al., 2016). However, the issue of identifying the source of error in such complex, non linear, and coupled models is just as difficult as obtaining suitable data for testing the model (Sullivan, 2009c). On the other hand, comparison with real wildfires is very difficult because boundary conditions are rarely known and it is very dangerous to make measurements during a fire. Few studies have provided a level of detail necessary for testing physics-based models. Comprehensive time-histories of local fire spread are reported only in some cases (Cheney et al., 1993; Cheney and Gould, 1995; Santoni et al., 2006; Mueller et al., 2014). Often the variability of key dynamic parameters (wind speed) is not reported with respect to a single fire (Fernandes et al., 2009), which makes it difficult to compare with computed results and to verify which aspects can be validated.

In a recent study, [Hoffman et al. \(2015\)](#) evaluated crown fire spread rate using FIRETEC and [WFDS](#) and compared the results to a compilation of wildfire observations in North American forests ([Alexander and Cruz, 2006](#)). Over 80 % of the FIRETEC and [WFDS](#) predictions of crown fire rate of spread fell within the 95 % prediction bands of crown fire rate of spread provided in [Alexander and Cruz \(2006\)](#) (see Fig. 1.31).

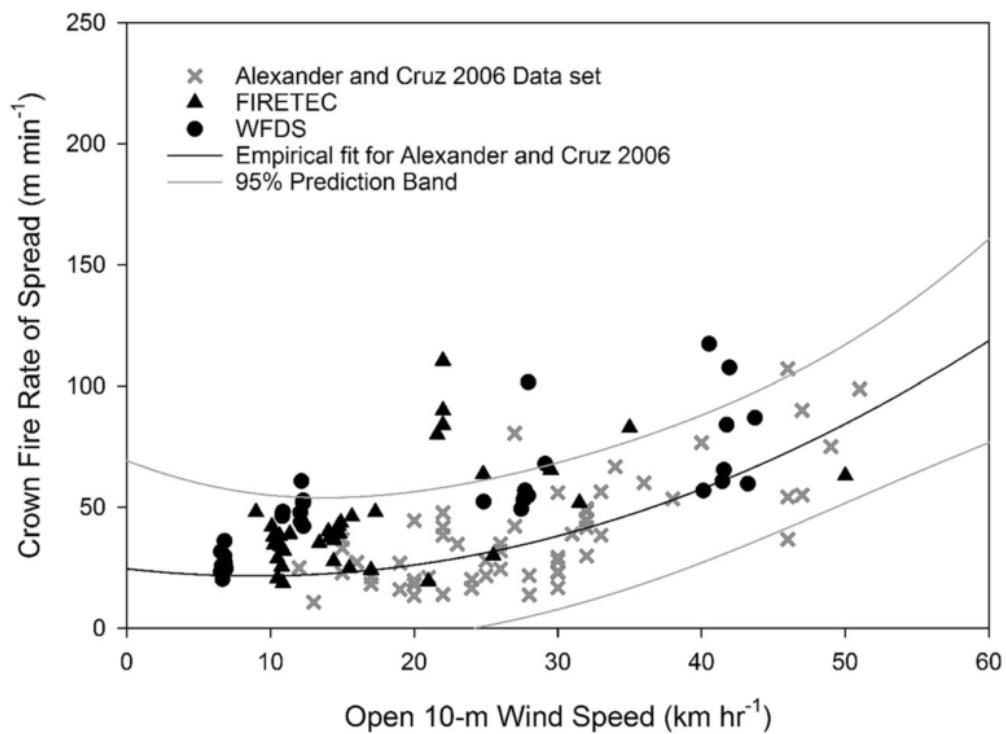


Figure 1.31: Crown fire ROS curve (black line) as a function of open 10-m wind speed with 95 % confidence intervals (gray lines). Extracted from [Hoffman et al. \(2015\)](#).

In cases where the two models were outside the predictive bounds, they appear to over-predict the crown fire rate of spread. As noted by [Alexander and Cruz \(2006\)](#), under-predictions have severe implications for public and firefighter safety and fire operations planning, while over-predictions can be dealt with. One important aspect that was discussed in [Hoffman et al. \(2015\)](#) is that the ability to test the model was limited by a lack of environmental and fuel data such as

errors associated with point-to-point. Hence, concurrent comparisons have not been estimated. This aspect is essential because the rate of spread predictions from detailed physics-based models are sensitive to small variations in both the spatial pattern of the fuels complex and assumptions regarding the atmosphere boundary layer (Linn et al., 2005). Therefore, this study recommended further assessment of detailed physics-based models. Particularly by providing additional data regarding spatial and temporal variability of key fuel and environmental characteristics (i.e. wind). Similarly, more information are needed for the heterogeneous nature of the rate of fire spread, beyond just the head-fire rate of spread, such as the rate of mass consumption, heat fluxes or fire depth through time for crown or surface fires at field-scales. Using new techniques such as remote sensing technologies (Skowronski et al., 2011) can be beneficial to quantify the pattern of surface and canopy fuel loading and could help in the assessment of both system and sub-level model behaviour. This step provides checks against incorrect conclusions, indicating if the model is conceptually consistent with reality, and identifying specific components of the model that need to be improved (Hoffman et al., 2015).

Semi-empirical models

Semi-empirical models are based on the principle of energy conservation but do not separate between the different types of heat transfer mechanisms and combustion reactions (Weber, 1991). This means that the energy produced by the fire is either transferred to the unburned fuel or lost to the ambient. Rothermel's model (Rothermel, 1972) is the most used of these models, where the rate of spread is a simple function of the heat flux from the fire, the fuel bulk density, a coefficient related to the amount of fuel, the heat necessary to ignite the fuel and correction factors for wind and slope. The different parameters are either obtained from fuel properties or derived from experiments mentioned earlier. The model is more

general than the empirical approach presented hereafter, and provides acceptable results in diverse configurations. However, it is challenged when applied to areas with a large variability of parameters, such as heterogeneous fuels like in the Mediterranean basin (Simeoni, 2016). Two other models based on Rothermel; Behave Plus (Anderson, 1969) and Farsite (Finney, 1998) are widely used by the US Forest Service to forecast fire propagation and to help forest manager. Using Lagrangian front tracking techniques, Behave Plus provides a quick estimation of the fire head rate of spread and Farsite extends Rothermel's model to two-dimensions along the ground by applying Huygens ellipse principle (Anderson et al., 1982). Despite being computationally very fast, they are limited by the simplified nature of the models. For instance, BEHAVE is not able to track the wind induced rate of spread variations, even in homogeneous vegetation. These models have been coupled to with large-scale meteorological models, such as in Clark et al. (2004). Others have attempted to optimise the input parameters using genetic algorithms (Abdalhaq et al., 2002). Later, Clark et al. (2004) model was coupled with a meteorological model named Weather Research and Forecasting (WRF) and forming WRF-Fire (Mandel et al., 2011; Kochanski et al., 2013; Coen et al., 2013). The atmospheric model was used to better account for time varying weather conditions, to describe the wind, and its effect on the fire spread rate and direction. Including more accurate meteorological conditions or optimized parameters can improve predictions but it will always be limited by the fire model (i.e. Rothermel's model), which is designed to fit the experimental conditions used during its development and where the description of the physics is simplified. More recently, Rochoux et al. (2013b,a) applied data assimilation techniques that integrate sensor observations with computational models to better accounts for modelling errors and to improve their predictions. Fire rate of spread is calculated using a fire propagation solver based on Rothermel's model, then it is corrected using measurements of the time-evolving fire front position. The model

was tested for grassland fires and the results indicate it can potentially increase the fire simulation accuracy of semi-empirical models.

Empirical models

Empirical models are primarily based on the statistical regression of several independent variables. They use simple correlations that relate the fire rate of spread to a set of statistically significant parameters without including any physical information. As an example, the McArthur Forest Fire Danger Meter (FFDM) first appeared in operational use in 1967 as the Mk 4 FFDM (McArthur, 1966, 1967; Noble et al., 1980). This meter brought together the results of over 800 experimental fires and wildfire observations into a simple system to determine the fire danger in forested areas of Australia. It provides an estimation of the fire rate of spread as a function of the Fuel Moisture Content (FMC), and fuel availability for fire spread in grasslands or Eucalypt forests. These models can be very efficient in places with homogeneous vegetation because the model parameters were calibrated from data collected in experimental fires or in well documented wildland fires in similar ecosystems and conditions. It works best during long, dry periods, when grasses are fully cured and when forest fuels do not contain residual moisture from recent rain and the maximum amount of fuel is available for combustion. The index is divided into five fire danger ratings (Low, Moderate, High, Very High, and Extreme) that represent the degree of difficulty of suppression. The equation for the forward rate of spread can be expressed as (Noble et al., 1980):

$$ROS = 0.0012FW \quad (1.5)$$

W represents the fuel weight and F is the fire danger index calculated from the following equation:

$$F = 1.25D \exp \left(\frac{T - H}{30} + 0.0234V \right) \quad (1.6)$$

with D being the drought factor, T the air temperature (degC), H the relative humidity (%), and V the average wind velocity. The rate of spread can be corrected in the presence of a slope (θ), such as:

$$ROS_{\theta} = R \exp(0.069\theta) \quad (1.7)$$

McArthurs model can also be expressed by fire danger meters, which are disks for which the alignment of the parameter values indicates the fire head rate of spread (Fig. 1.32). These meters are used daily by foresters and by most current operational fire spread prediction systems around the world.

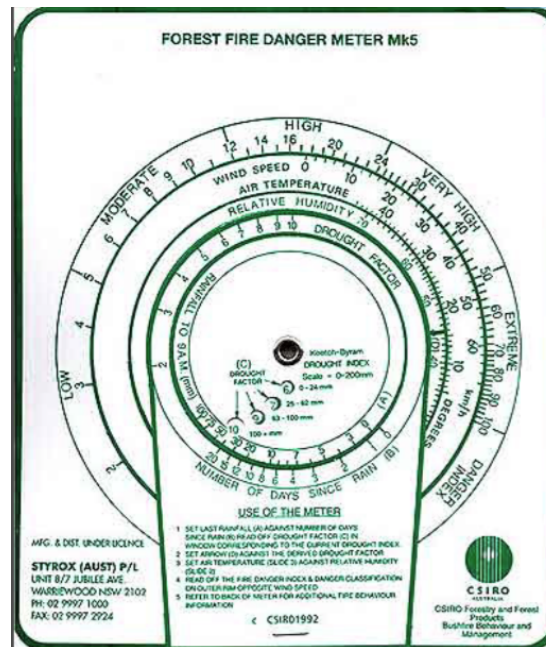


Figure 1.32: Typical fire danger meter disk (Credit CSIRO)

Similarly, a numerical rating in the Canadian fire danger rating system called

Fire Weather Index (**FWI**) was introduced by [Van Wagner \(1987\)](#) for estimating fire hazard. It is based on meteorological measurements of fire intensity in a standard fuel type (i.e. jack pine and lodgepole pine). The **FWI** is comprised of three fuel moisture codes, covering classes of forest fuel of different drying rates, and two indices that represent the rate of spread and the amount of available fuel ([Sommers et al., 2011](#)). Figure 1.33 illustrates the components of the **FWI** system. Calculation of the components is based on daily observations of temperature, relative humidity, wind speed, and 24-hour rainfall ([GOC, 2016](#)).

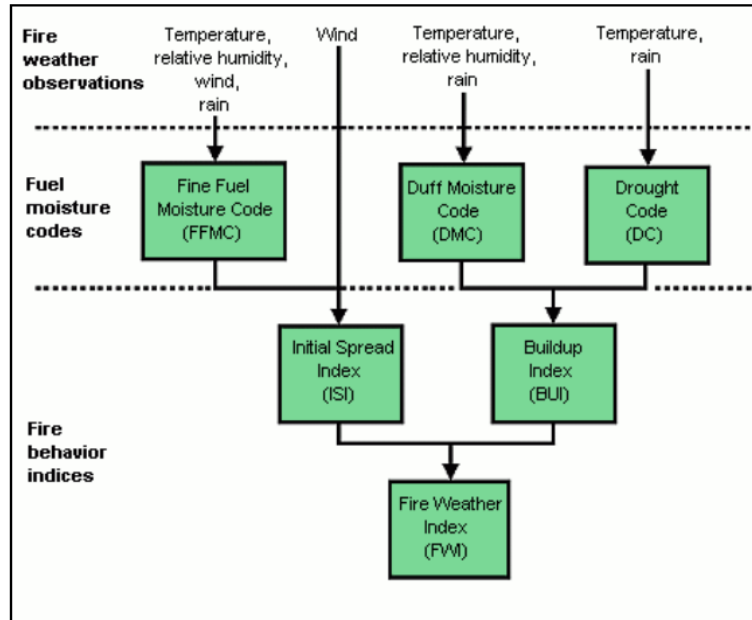


Figure 1.33: Structure of the Canadian Fire Weather Index system ([GOC, 2016](#))

The following equation provides the fire rate of spread in the **FWI**:

$$RSI = a [1 - \exp(-bISI)]^c \quad (1.8)$$

where a , b , and c are fuel-dependent factors that are divided in classes that are representative of Canadian ecosystems.

The Initial Spread Index (**ISI**) is expressed as:

$$ISI = 0.208 \exp(0.0504U_{10}) 91.9 \exp(-0.138FMC) \left(1 + \frac{FMC^{5.31}}{4.93} 10^7\right) \quad (1.9)$$

With U_{10} is the wind velocity at 10 m. These models are statistically derived to provide the rates of spread for a given range of fuel and weather conditions, and they must be used with care when the conditions differ from the ones used to derive the model. The main variables identified in many of these models are wind speed, temperature, and **FMC**. The method of incorporating the effect of these variables on the fire spread rate in a function influences the behaviour of the model. However, their domain of validity is limited to the experimental conditions during the original development and they must be used with care when the conditions differ from the ones used to derive the model. The Canadian **FWI** has been extended and adapted with success to other regions of the world for the local ecosystems.

As a concluding remark for this section, one must keep in mind that there is not one universal method of fire modelling suited for all scales mentioned earlier. Each method brings its advantages and disadvantages, and method selection depends on the level of complexity of the situation. As computational costs continue to decrease, many methods are becoming more widely available and with better performance. Using a more fundamental physical approach to explore fire spreads allows a more detailed analysis that will provide a better understanding of fire dynamics. Positively, this can deliver new types of simplified physical models, which would present a good compromise between simplicity and accuracy.

1.4 Purpose of the Thesis

Understanding the burning behaviour of forest fuels is essential for developing a complete understanding of wildfire spread. The main challenge arises from the porous nature of the fuels and its coupling with the transient surrounding environment, which strongly influences the heat transfer, degradation rates, and the burning dynamics. As it is impossible to maintain repeatable and fully controlled environments, and to monitor all the dynamics involved in field scale experiments, it becomes necessary to conduct studies at a scale small enough to maintain a controlled environment and large enough to relate to realistic conditions. Moreover, the problem of fire spread can be described as a series of local ignitions, which always begins at a relatively small scale.

The main goal of this study is to develop a fundamental understanding of fire phenomena involved in wildfires. Thus, the use of numerical models is essential for verifying our understanding. We have shown in this chapter the limitations of empirical and semi empirical models, and concluded that despite their success in providing useful operational tools, physical models are more appropriate for studying the elementary aspects in fire dynamics. Physical models are often used to study large fire propagations, in which many parameters and complex submodels are included to close the model (Grishin, 1996; Larini et al., 1998; Morvan et al., 2009). These closure models, or submodels, selected to represent degradation, heat transfer, combustion, and radiation, are applied to simulate large-scale wildfires in complex environments in order to estimate the ROS, flame height, and temperature fields (Porterie et al., 2000, 2005; Morvan and Dupuy, 2004; Mell et al., 2009; Morvan, 2015). However, these submodels have never been thoroughly pre-validated or verified to be well adapted to the fuel conditions and to the surrounding environment in which they are used. For instance, heat transfer models were developed in different contexts (Grishin,

1996), and aerodynamic properties were tested for simple geometries at ambient temperatures (Incropera and Dewitt, 1996). This is why it is necessary to establish a framework tailored to the development of fire modelling with the multiphase approach. It will allow us to study elementary aspects of the problem and to gradually move towards complexity (by changing the fuel or environmental properties). This methodology follows a building block approach to model development and facilitates a better understanding of forest fuel flammability and of its corresponding fire dynamics. This study includes well documented fire experiments that are conducted in a controlled environment, providing precise measurements for different fuel and ambient conditions, to quantify the influence of the parameters on the models numerical predictions. As these conditions change, some parameters and submodels in the numerical model are no longer valid and need to be replaced. This parametric study is often overlooked at larger scale due to the excessive uncertainties caused by the large variations of fuel properties (i.e. distribution, fuel moisture content), the unstable environment (i.e. wind gusts), and the strong coupling between submodels, which makes it impossible to pinpoint exactly which submodel is drifting. These submodel adjustments are endorsed by physical justifications and complemented with additional experiments or analyses. In addition, all the submodels domains of validity and limitations are exposed.

- In Chapter 2, a presentation of the experimental setup using the FM-Global Fire Propagation Apparatus (FPA) is provided for forest fuel samples made of pine needles. These tested fuel samples are characterised to quantify physical properties such as the surface to volume ratio, the specific heat capacity, and the density. In addition, a spectral analysis is conducted to measure the spectral behaviour (absorptivity and reflectivity) of pine needles at wavelengths relevant to radiation emitted from typical flames from the FPA heaters. Chemical gases released during thermal degradation are also

quantified using FTIR measurements in FPA. In the second part of the chapter, the mathematical formulation of the multiphase model is presented. This numerical approach is implemented in OpenFOAM ([OpenCFD Ltd.](#)) creating a new solver called ForestFireFOAM. It follows the same numerical structure as FireFOAM, a Large Eddy Simulation ([LES](#)) solver for fire purposes ([Wang et al., 2011](#)). A numerical domain and boundary conditions are carefully chosen using OpenFOAM numerical capabilities, matching the experimental conditions used in the FPA.

- Chapter 3 is dedicated to a detailed description of each submodel necessary to appropriately close the model and to physically represent the experimental conditions. The effective absorption coefficient for radiative heat transfer is investigated using finding from the spectral analysis. Additional experiments are performed for determining a representative extinction coefficient. Finally, heat transfer models are studied in natural convection and in forced flow to determine appropriate submodels that can be implemented in ForestFireFOAM. The ultimate goal of this chapter is to provide insight, limitations and physical justification for the submodels.
- Chapter 4 presents the comparison between numerical simulations and experimental measurements for various conditions, covering different flow conditions, porosities, species, and radiative heat fluxes. Measured and simulated quantities are mass loss, temperatures, flaming time, and heat release rate. Additionally, a comparison with preliminary experiments conducted with live needles is presented only as a proof of concept. Further recommendations on how to adjust the model are highlighted. It allows us to test the applicability of ForestFireFOAM outside the range of the initial development and to confirm that this framework is effective to extend fundamental knowledge to other wildland fire conditions.

This framework, with the appropriate modifications, will support the development

of large scale Computational Fluid Dynamics (CFD) modelling by providing inputs and indications for the necessary subscale modelling. Finally, as this work is mostly dedicated to improving our understanding of the mechanisms involved in wildfires, I conclude this section with the following quote:

Why bother with the science at all? [...] There is the generally justified hope that with an increased understanding will come an increased power to control. Are there trigger mechanisms in the process of spread of a fire which man with his small available energy could manipulate to affect in a major way the future course of a fire?

Emmons (1963)

Chapter 2

Experimental and Numerical Techniques

2.1 Introduction

Materials that are naturally found in the forest have wide ranges of physical and chemical characteristics that drive their flammability. As defined in Chapter 1, the term flammability refers to the ability of a certain fuel to ignite and sustain a fire, which includes a classification for ignition, fire growth, burning intensity, generation of smoke and toxic compounds, and extinction ([Tewarson and Pion, 1976](#)). As an application for wildland fuels, [Dimitrakopoulos and Papaioannou \(2001\)](#) tested typical Mediterranean species, and proposed four flammability classes that can be used as criteria in fuel hazard and wildland fire risk assessment for fire managers. It was found that species with a thorny structure (like thorny burnet) have higher lignin content, which is less flammable than cellulose, making them less flammable than other species. Species graded as moderately flammable such as Kermes oak and gum cistus have hard, leathery leaves with waxy or

hairy epidermis, which prevents rapid water loss from evapotranspiration. As for flammable species, they generally have high surface area to volume ratio, which facilitates water loss and heat absorption, and they also contain flammable volatile oils. These include pine needles, olive trees, cypress, some oak families, and heath. Finally, Laurel and Eucalyptus are considered as extremely flammable in Dimitrakopoulos classification because they are extremely rich in flammable volatile essential oils, which allows them to ignite easily.

Because pine needles are classified as flammable, and because they are abundantly present in forest fuel beds worldwide ([Westerling et al., 2006](#); [Pausas et al., 2008](#); [Han et al., 2015](#)), we conducted our numerical and experimental studies on pine needles only. However, the findings can easily be applied to other fuels as long as the physical and chemical properties are properly adjusted. Additionally, pine needles are well characterised in the literature, compared to other species. In this chapter, the physical and chemical properties of pine needles are presented. We will explain how pine needles were sampled and in which conditions they were tested, outlining all the experimental steps. Finally, in order to develop a better understanding of the phenomena involved in the fire dynamics of vegetative fuel, the multiphase approach and the numerical setup will be presented thoroughly. Using the parameters and the properties measured experimentally, the capacity of the model to provide an accurate mathematical representation of the experimental setup will be tested by using state of the art Computational Fluid Dynamics ([CFD](#)) techniques.

2.2 Physico-Chemical Properties

The most relevant physical and chemical properties of pine needles are presented and discussed in this section. Two distinct North American species were tested:

pitch pine (*Pinus rigida*) and white pine (*Pinus strobus*). Pitch pine is the most common species on the Atlantic Coastal Plain of the American continent. White pine is used for reforestation projects and landscaping in the same region, due to its rapid growth, and therefore it has the distinction of being one of the most widely planted American trees (Wendel, 1980). Both species were collected off the ground from the Silas Little Experimental Forest in New Lisbon, NJ, USA, and kept in paper bags. Care was taken to only collect the top layer of the litter so as not to include the duff layer. The needle stock was examined and cleared of any unwanted debris (other foliage, twigs, etc.). After collection, needles were dried in ambient air, which reduced the Fuel Moisture Content (FMC) to around 7-15 %. To prevent further degradation of the foliage, the needles were stored at laboratory conditions (typically 20°C and 45 % relative humidity).

2.2.1 Morphology

Pine needles naturally come in bundles (fascicles). The number of needles in a bundle can vary from species to species (generally 2, 3, 5 or 7). Pitch pine needles often grow in bundles of three (Fig. 2.1). The needles measure up to 15 cm long, with an average length of 11 cm white pine needles are smaller (7 to 11 cm), finer, and have five needles per fascicle (Fig. 2.2). Both pine species geometrical properties are listed in Table 2.1.

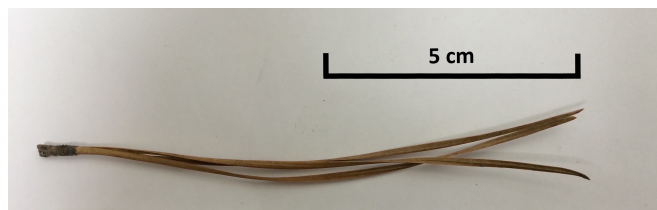


Figure 2.1: Dead pitch pine needle



Figure 2.2: Dead pitch pine needle (top) and white pine needle (bottom)

2.2.2 Surface to Volume Ratio

The Surface to Volume Ratio (**SVR**) was determined by making geometric measurements of the needles. Half cylinder and prism estimations were applied, similar to those proposed by [Moro \(2006\)](#). A larger **SVR** value indicates a finer fuel. This parameter is important for the upcoming analysis, since it has been observed that the **SVR** influences the burning rate and residence time ([Anderson et al., 1982](#)). Hence, by using two very different **SVR** (see Table 2.1), we will be able to evaluate the effect on the burning behaviour. Many other studies have been conducted on Mediterranean species with similar geometrical properties such as Aleppo pine (*Pinus halepensis*) ([Tihay et al., 2009b](#); [Jervis et al., 2011](#); [Simeoni et al., 2012](#)), and maritime pine (*Pinus pinaster*) ([Fernandes et al., 2009](#)). For instance, the **SVR** of Aleppo pine ($7,377 \text{ m}^{-1}$) has a comparable value to pitch pine ($7,295 \text{ m}^{-1}$).

2.2.3 Specific Heat Capacity

The Specific heat capacity (C_p) is the amount of heat needed to raise the temperature of one unit of mass by one degree. It was measured for both species using a standard Perkin-ElmerTM Model Differential Scanning Calorimetry (**DSC**) with sapphire as a reference (ASTM E1269). An average value was calculated

between ambient and 200°C as shown in Table 2.1. Both species have similar values to *Pinus pinaster* (2,017 J.kg⁻¹.K⁻¹) and slightly higher values than *Pinus halepensis* (1,827 J.kg⁻¹.K⁻¹) and *Pinus laricio* (1,868 J.kg⁻¹.K⁻¹) (Tihay, 2007).

Table 2.1: Summary of species properties

Species	Pitch pine (<i>Pinus rigida</i>)	White pine (<i>Pinus strobus</i>)
Density [kg/m ³]	607	621
SVR [m ⁻¹]	7,295	14,173
C _p [J/kg K]	2,069.7	2,090.4
FMC	0.07	0.07
Diameter [mm]	1.39	0.50

2.2.4 Density

The average density is calculated by immersing needles with a known mass (m_{needle}) in a known volume of liquid (V_{liquid}). Methanol is used as the liquid, because unlike water, it prevents bubble formation. The density can then be determined by measuring the total volume with the following equation (Thomas et al., 2014):

$$\rho = \frac{m_{needle}}{V_{total} - V_{liquid}} \quad (2.1)$$

The results of these measurements are presented in Table 2.1 for pitch and white pine needles.

2.2.5 Chemical Composition

It is necessary to assess the chemical composition of the fuel to better understand how it can influence flammability (Dimitrakopoulos and Papaioannou, 2001).

Most plants and wooden species are composed of three principal chemical components: cellulose, hemicellulose, and lignin, all of which are polymeric (Kollman and Côté, 1968). The nature and the proportions of each compound differ from species to species, seasonally, and depending on the maturity of the plant.

- Cellulose is the most abundant constituent of the plant cell wall. It is a macromolecule belonging to the family of β -D-glucans. Cellulose is a structural component that contributes to the high tensile strength of wood. Cellulose usually begins to thermally decompose at 300°C to form gases and tar (Di Blasi, 1998; Di Blasi et al., 2001).
- Hemicellulose is found in the plant cell walls, and it is composed of a variety of heteropolysaccharides representing 15 to 30 % of the dry mass. The role of hemicellulose is not clear in the plant physiology, but it is thermally sensitive as it starts degradation at around 250°C (Methacanon et al., 2003).
- Lignin is a parietal polymer that represents the second most abundant constituent of woody plants, such as trees and shrubs. It generally contributes to the rigidity in a plant. The molecular structure of lignin polymer depends on the botanical origin, age, tissue type, and other factors (Leroy, 2007). The thermal decomposition occurs slowly, starting at 250°C, but extends up to about 900°C. Lignin releases few volatiles, but it is the component responsible for most of the char produced (Orfão et al., 1999).
- In addition to the three major components, there are also extractives, such as terpenes (i.e. α -pinene, β -pinene, and limonene in pine species), polyphenols, and inorganic constituents (such as ash). These extractives are known to have important effects on the physical, chemical, and mechanical properties of a plant. They are responsible for the colour and the odour,

particularly when freshly cut. They usually represent 3 to 15 % of the total mass (Leroy, 2007).

Finally, water is stored within the structure in three different arrangements as described in Grishin et al. (2003); Luikov (1978); Romanovskii (1976):

- Chemically, at the molecular level, which possesses the highest energy of binding with a material.
- Physico-chemically by adsorption, osmotic*, and capillary moisture.
- Physico-mechanically where water takes the form of droplets and film moisture.

Chemical and physicochemical water is referred to as bound water and physico-mechanical moisture is called free water. All types of water (except for chemically bound) participate in the evaporation process (Romanovskii, 1976). Note that the density of bound water increases up to 2.5 g/cm^3 (for free water = 1 g/cm^3) (Lykov, 1968). Leroy (2007) conducted analyses on several Mediterranean forest species to determine the proportions of their constituents (Table 2.2). The species were: *Arbutus unedo* (AU), *Erica arborea* (EA), *Cistus monspeliensis* (CM), and *Pinus pinaster* (PP). However, only the latter is a pine species.

The total does not reach 100 % because the extractions were made separately and using independent procedures. Overall the amount of cellulose and lignin are similar for all species. The main differences can be observed in the proportions of hemicellulose and extractives. Tihay (2007); Tihay et al. (2009a) conducted ultimate analysis for *Pinus pinaster* (PP), *Pinus halpensis* (PH) and *Pinus laricio* (PL), among other forest species. The results for the pine needles are presented

*Osmosis is the diffusion of water across a permeable membrane

Table 2.2: Constitutional analysis of Mediterranean species (in %). Extracted from Leroy (2007)

Species	Cellulose	Lignin	Hemicellulose	Extractives	Total
AU	38.0	41.6	5.2	13.1	97.9
EA	40.7	39.7	13.6	5.8	99.8
CM	39.4	34.4	12.6	9.2	95.6
PP	38.3	38.9	5.1	12.9	95.2

in Table 2.3. The composition in C, H, and O of the samples are very similar. The main difference is the concentration of the ash contents, which can catalyse the decomposition of cellulose during combustion. With only a small variation between species, we can assume that the same chemical compounds are found in pitch pine and in white pine needles, in similar proportions.

Table 2.3: Ultimate analysis of three pine species. Extracted from Tihay (2007)

Species	Elements (in mass %)			
	C	H	O	Ash
PP	50.64	6.76	41.53	1.07
PH	48.64	6.84	39.36	5.16
PL	50.11	6.84	42.5	0.55

2.3 Laboratory Scale Experimental Setup

An experimental campaign conducted at laboratory scale is presented in this section. The majority of the tests are conducted in the FM-Global Fire Propagation Apparatus (FPA), which is thoroughly presented, as well as the measurements relevant to our analysis. Additional tests used to complement the measurements made in FPA tests are also presented: Those include characterising

degradation products using a Fourier Transform Infra-Red (FTIR) spectroscopy, and quantifying the spectral behaviour of pine needles by spectral analysis.

2.3.1 Fire Propagation Apparatus

The combustion of pine needles was studied using the FM Global Fire Propagation Apparatus (FPA). The FPA is a standard (ISO-12136:2011, (ASTM International, 2003)) testing device used to quantify solid material flammability characteristics such as time to ignition, chemical and convective heat release rates, mass loss rate, effective heat of combustion, heat of gasification, smoke generation rate, and smoke yield. It is also designed to obtain the transient response of materials to prescribed heat fluxes in inert or oxidising environments, and to obtain laboratory measurements of generation rates of fire products (CO, CO₂, and total hydrocarbons). All these properties are often used in fire safety engineering and for fire modelling. Compared to the cone calorimeter, the distinguishing features of the FPA are:

- 4 Tungsten-quartz infrared heaters providing a constant or transient radiant flux uniformly distributed on the sample. The imposed heat flux can range from 0 to 100 kW/m², and each heater is supplied with six 500 W lamps, at 120-144 V.
- A prescribed flow of normal air, pure nitrogen, different air mixtures, or even air containing gaseous suppression agents. Pyrolysis tests with a flow of 100 % nitrogen can be used to measure the mass loss rate and to determine the heat of gasification of the material. The use of enhanced oxygen in small-scale fire tests can simulate the flame heat flux occurring in large-scale fires (Tewarson and Pion, 1976; Wu and Bill, 2003). Correlations were developed

between the results from small-scale tests with 40 % oxygen and the results from large-scale tests for a class of materials.

A schematic of the **FPA** is presented in Fig.2.3. A fuel sample sits in a basket, on a load cell inside a cylindrical combustion chamber. A water cooled shield around the sample protects it from the heat before the infrared heaters are ready to provide a steady heat flux. The latter is calibrated so that is is uniformly distributed at the top of the sample. For this study, heat fluxes of 25 and 50 kW/m² were chosen. 25 kW/m² is higher than the critical heat flux necessary for triggering a piloted ignition (**Torero and Simeoni, 2010**), and 50 kW/m² is representative of the heat flux emitted by flames in a wildfire (**Silvani and Morandini, 2009**). The ignition of the sample is performed by means of a premixed ethylene/air pilot flame located 3 cm above the sample. The infrared heaters are kept on after ignition, and remain on during the whole test to be consistent with real fire conditions, mimicking a strong flame feedback from a larger fire surrounding the sample.

Measurements in the FPA

Time to ignition is measured manually between the beginning of the exposure of the samples to the radiative flux (after the shield is dropped) and the first visual observation of a flame. Mass loss is measured using a sensitive load cell (Mettler ToledoTM WMS4002-L) with an accuracy of 0.01 g. Temperature and flow speed are monitored in the exhaust duct, where oxygen, carbon dioxide and carbon monoxide concentrations are measured (using ServomexTM 4100 gas analysers). Oxygen Consumption (**OC**) calorimetry is a convenient and widely used method for measuring the amount of heat released (**Janssens, 1991**). The

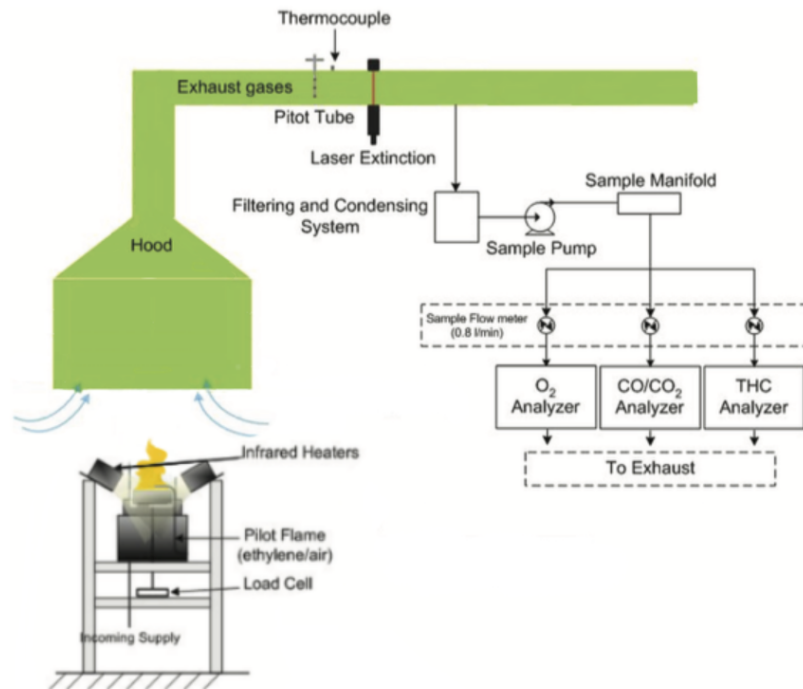
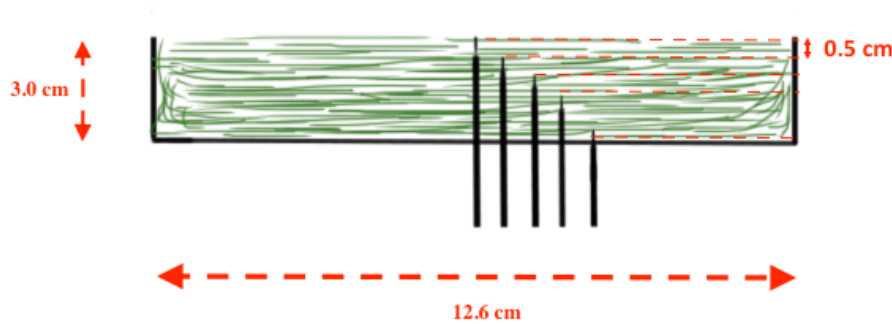


Figure 2.3: Overview of the Fire Propagation Apparatus (FPA). Extracted from Schemel et al. (2008) and modified

Heat Release Rate (HRR) from a fire can be calculated from the amount of oxygen consumed by the combustion process. Chemical heat release rate is then derived from the production rates of carbon dioxide and carbon monoxide. Porous baskets for pine needle samples were specifically designed to allow natural convection and forced gas flow rate to enter through the fuel bed (Schemel et al., 2008). The sample holders are circular baskets (diameter: 12.6 cm, height: 3.1 cm) made of stainless steel, with holes on all the surfaces representing 67 % opening. Airflow can be introduced below the sample (Fig. 2.3) and can pass through and around the porous sample. The used inlet flows are presented in Table 2.4. Hot wire anemometry (Kimo[®] AMI301 with a 0.01 m/s resolution) was used to estimate the averaged velocity of the flow penetrating, and the flow circling around the porous sample by taking measurements on top of the sample and in the gap between the sample and the combustion chamber. These measurements are presented in Chapter 3.

Table 2.4: Flow fluxes supplied by the FPA

Conditions	Symbol	Volumetric flow (L/min)	Corresponding velocity (cm/s)
No Flow	NF	0	0
Low Flow	LF	50	6.67
High Flow	HF	200	26.8

**Figure 2.4:** Experimental setup for temperature measurement (side cut).

Temperature measurements were made on top and inside the porous bed at different depths (5, 10, 15, 30 mm) in the layout presented in Fig. 2.4, using fine K-type exposed junction (ungrounded) thermocouples with a diameter of 0.127 mm (Fig. 2.5).

Samples of four different bulk densities of pine needles were tested: 17, 23, 30, and 40 kg/m³ corresponding to a sample mass of 6.4, 8.7, 11.4, and 15 g, respectively (Fig. 2.6). 15 g corresponds to the maximum amount of pine needles that can fit in the basket without overfilling, compressing, and causing the needles to break.

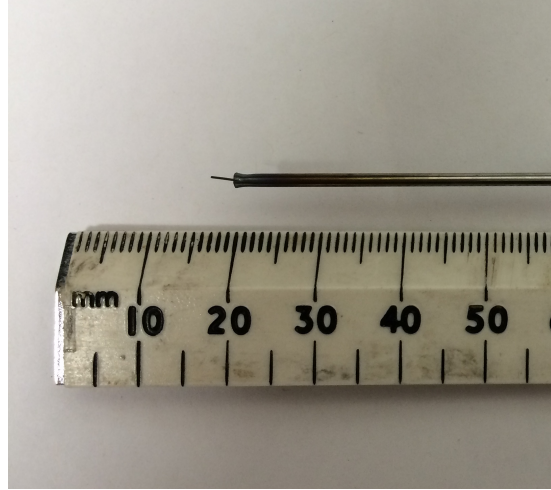


Figure 2.5: K-type thermocouple. Only the sheath and the grounded part can be seen, further zoom is needed to perceive the exposed tip.

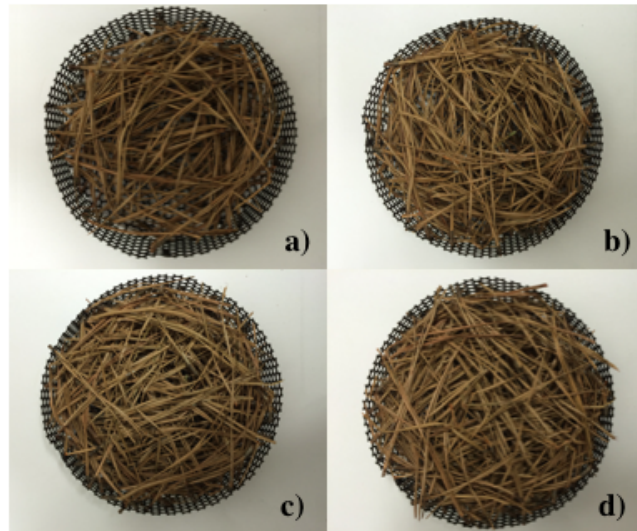


Figure 2.6: Pitch pine needle samples with a) 6.4 g; b) 8.7 g; c) 11.4 g; d) 15 g

The bulk density (ρ_b) is calculated from the ratio of the sample mass to the sample holder volume. The porosity (α_g) is then calculated as:

$$\alpha_g = 1 - \frac{\rho_b}{\rho_s} \quad (2.2)$$

where ρ_s represents the pine needle density (Table 2.1). The porosities and bulk densities are listed in Table 2.5 for the different masses used.

Table 2.5: Summary of bulk densities and porosities

Mass	Bulk density	Porosity
m[g]	ρ_b [kg/m ³]	α_g [-]
6.4	17	0.97
8.7	23	0.96
11.4	30	0.95
15.0	40	0.93

2.3.2 Fourier Transform Infra-Red

A Gasmet DX-4000 Fourier Transform Infra-Red (FTIR) spectrometer was used in a limited number of configurations to analyse pyrolysis gases released by pitch pine needles before ignition. The Gasmet portable sampling system consists of the sampling unit, temperature-controlled sample lines, and temperature-controlled sample probe (all shown in Figure 2.7).

The lines and probes are heated to a temperature of 180°C in order to avoid condensation of the gases after sampling. The Gasmet portable sampling unit

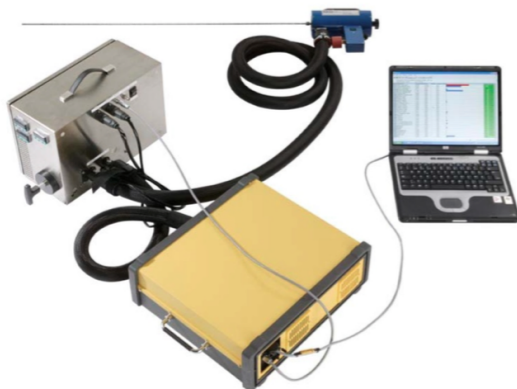


Figure 2.7: Gasmet DX-4000 gas analyser and sampling system

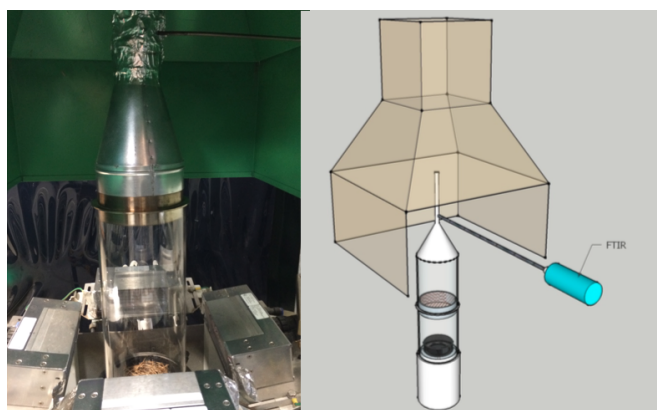


Figure 2.8: FTIR sampling position in the FPA

measures with 5 s sampling intervals. Sampled gases are transmitted through the heated lines and to the digital signal processing electronics of the analyser. The analyser then transmits the information to the CalcmetTM software to data analysis. The FTIR sampling part was mounted at 50 cm above the sample in the FPA, sitting on a funnel above the quartz tube. The quartz tube was used to prevent oxygen dilution of the pyrolysis gases, and the funnel was used to limit the air access above the tube (Fig. 2.8). Initially, tests were made with the FTIR mounted in the exhaust duct (Fig. 2.9). It was found that the dilution reduced the concentration of gases below the detection limit of the analysers.

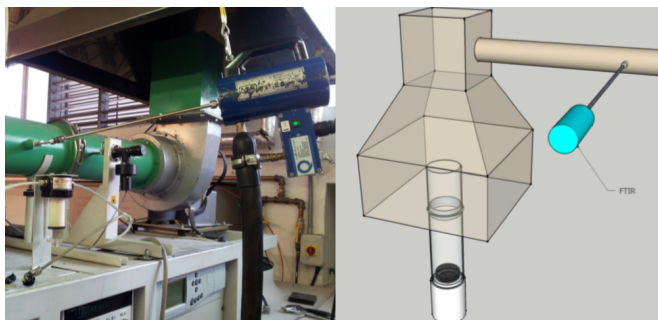


Figure 2.9: Alternative FTIR sampling position in the duct

Further tests were conducted under 100 % nitrogen, providing an inert atmosphere and preventing gases from oxidizing in the air. However, many compounds with nitrogen atoms (NO_x) were detected and perturbed the measurements. Those would not have been produced (or detected) during the preheating phase under air atmosphere. [Fateh et al. \(2016\)](#) detected a small amount of NO only in the preheating phase while analysing gas emission from *Pinus pinaster* in the cone calorimeter under air atmosphere. In that study, only a small peak was detected just before ignition at a low heat flux (15 kW/m^2). However, the study did not indicate if piloted or non-piloted ignition was used for those measurements. Therefore, the measured NO could have resulted from early flash ignitions preceding the main ignition of the fuel bed. To confirm this assumption, [Fateh et al. \(2016\)](#) detected small amounts of NO only after ignition while testing higher heat fluxes ($20, 30, 40$ and 50 kW/m^2). In our configuration, tests were made in a normal air environment, without the use of a pilot flame and with the FTIR sampling 50 cm above the sample. A low heat flux was used (8 kW/m^2), just under critical value reported in [Torero and Simeoni \(2010\)](#) to prevent from ignition and without additional forced flow to limit oxidation. The heat flux was calibrated with the presence of the quartz tube, as it is known to reflect and absorb some of the radiation. The tube was carefully cleaned between repetitions.

2.3.3 Spectral Analysis

It is known that the emissivity and absorptivity of forest material is highly spectrally dependent (Monod et al., 2009). It was also observed that the FPA heaters operate in a very specific spectrum band (Acem et al., 2009; Monod et al., 2009). Hence, it was necessary to evaluate the spectral behaviour of pine needles in the range of the FPA heaters. The spectral reflectivity of pine needle samples was measured at FM Global laboratories over a wide range of wavelengths, from ultraviolet to long infrared (0.25-20 μm) (El Houssami et al., 2016a). This range is similar to those measured in Försth and Roos (2011); Chaos (2014) and much broader than those considered in other studies concerned with the spectral characteristics of vegetation (Kokaly et al., 2003; Acem et al., 2010). With known reflectivity, the emissivity (absorptivity) of the samples can be determined by invoking Kirchhoffs law (Kirchhoff, 1859, 1860), where reflectivity and emissivity/absorptivity are complimentary: Emissivity = Absorptivity = 1 - Reflectivity. This approach assumes a completely opaque surface. The transmissivity of the prepared pine needle samples was measured using the devices described above. The transmissivity was found to be negligible ($< 0.5\%$) over the wavelength range considered, which ensured that the samples were sufficiently thick to be optically opaque. More details about the instrumentation and the configuration are presented in Appendix A.

The aforementioned experimental protocols were necessary to determine physical and chemical properties of pine needles, and their surrounding conditions. They were also essential for providing parameters needed in the numerical model presented hereafter. Since the quality of the input data strongly influence the quality of the simulations, we examined the input parameter quality.

2.4 The Multiphase Approach

A summary of the multiphase approach is presented in this section. This includes the main equations, assumptions, and the manner in which it was implemented in our numerical model. The multiphase approach was implemented in OpenFOAM (OF) and is called ForestFireFOAM. The latter is built following the structure of FireFOAM (FF), a numerical code for fire modelling developed by FM Global. The multiphase approach has the advantage of a great generality, especially when applied to small-scale fires of pine needle beds. It also allows including the process of degradation of the forest fuel by drying, pyrolysis and heterogeneous combustion, and allows to simulate it by assuming a volumetric reaction rate. This approach was not yet implemented neither in OpenFOAM, nor in FireFOAM. Consequently, this section is dedicated to the presentation of the governing equations of the multiphase approach. The equations are presented in the same order as they are solved in ForestFireFOAM. These equations were previously established in (Grishin, 1996; Larini et al., 1998; Morvan and Larini, 2001). The details of the chosen submodels for radiation, convection, combustion and others are not discussed in this section, but will be presented in Chapter 3.

The multiphase approach consists in solving the conservation equations (mass, momentum and energy) averaged in a control volume at an adequate scale that contains a gas phase flowing through N solid phases and considering the strong coupling between phases. Here, only one solid phase is considered, but more phases can easily be added. The solid phase consists of particles of the same geometrical and thermophysical properties, providing the same behaviour. The following assumptions are made for simplicity:

- The fuel bed is considered as a homogeneous distribution of solid particles

whose dimensions and physical properties are evaluated from experimental data.

- Solid particles are motionless and fixed in space.
- Contact between the solid phase is neglected, which is representative to reality because the contact area between two pine needles, and the thermal conductivity of pine are both very small.
- Fuel particles are considered thermally thin, meaning that the temperature throughout any solid particle is uniform at all times.

An illustration of the multiphase formulation is shown in Figure 2.10, where for a small control volume V , one solid phase coexists with the gas phase.

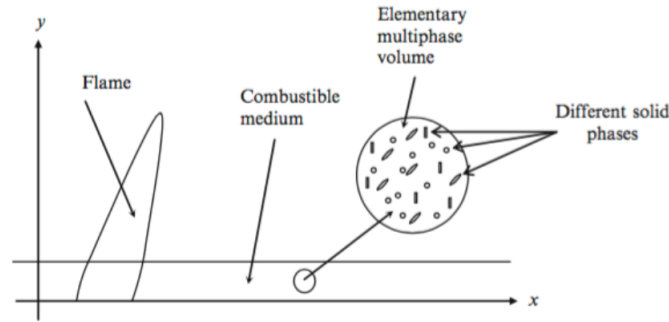


Figure 2.10: Illustration of the multiphase approach

The packing ratio of the solid phase (s) corresponding to the solid volume fraction is defined as:

$$\alpha_s = \frac{V_s}{V} \quad (2.3)$$

Where V_s is the volume occupied by the solid phase in the total volume V . In the same way, the volume fraction of the gas phase (α_g) is defined as:

$$\alpha_g = \frac{V_g}{V} \quad (2.4)$$

By complementarity, we obtain:

$$\alpha_s + \alpha_g = 1 \quad (2.5)$$

The heat and mass transfers between the gas phase and the solid phase are the key concept for the understanding of the fuel ignition and burning processes. These transfers are directly related to S_{gs} the contact surface between the gas phase and the solid phase:

$$\frac{S_{sg}}{V} = \frac{V_s}{V} \frac{S_{sg}}{V_s} = \alpha_s \sigma_s \quad (2.6)$$

with

$$\sigma_s = \frac{S_{gs}}{V_s} \quad (2.7)$$

σ_s being the surface to volume ratio [m^{-1}] of the phase s. The porous media is included using the Leaf Area Density ([LAD](#)), defined as:

$$LAD = \frac{\alpha_s \sigma_s}{2} \quad (2.8)$$

This criteria is important for describing the amount of fuel available in the solid phase in a control volume. As α_s is time dependent, the value of Leaf Area Density ([LAD](#)) is updated at each time step. The density of the solid phase is defined as:

$$\rho_s = \rho_{dry} \alpha_s + (\rho_{H_2O} - \rho_{dry}) \frac{H_u}{\frac{\rho_{H_2O}}{\rho_{dry}} + H_u} \quad (2.9)$$

The complete demonstration of this equation is presented in [Appendix B](#). ρ_{H_2O} the density of water, ρ_{dry} the density of dry pine needle, and H_u the humidity computed from the water mass fraction in the solid phase:

$$H_u = \frac{Y_{H_2O}^{(s)}}{Y_{dry}^{(s)}} \quad (2.10)$$

We also define LAD_{cr} as the critical value for which LAD (representing the solid phase) is considered as completely consumed. In general, for forest fuels, we can consider the following:

$$\frac{LAD_{cr}}{LAD} = \gamma_{ash} \quad (2.11)$$

With γ_{ash} the fraction of ash in the specie considered. This parameter is important to insure numerical stability and the transition from the solid phase to the gas phase, especially for small α_s .

$$\alpha_s = \begin{cases} \alpha_s & \text{if } LAD > LAD_{cr} \\ 0 & \text{else} \end{cases} \quad (2.12)$$

The gas phase is governed by a set of transport equations representing the mass balance equations:

$$\frac{\partial \alpha_g \bar{\rho}}{\partial t} + \frac{\partial \alpha_g \bar{\rho} \tilde{u}_j}{\partial x_j} = (1 - \gamma_{ash}) \dot{\omega}_{char}''' + \dot{\omega}_{vap}''' + (1 - \gamma_{char}) \dot{\omega}_{pyr}''' \quad (2.13)$$

Where \sim is the Favre filter operator, ρ denotes the density of the gas phase, and γ_{char} is the char fraction. Depending on the material property, for forest fuel γ_{char} is usually around 0.2 and 0.3 (Kollman and Côté, 1968). $\dot{\omega}_{vap}'''$, $\dot{\omega}_{pyr}'''$, and $\dot{\omega}_{char}'''$ are the mass production rate of species resulting from the decomposition of the solid fuel: evaporation, pyrolysis, and char oxidation, respectively.

The momentum equation is defined as:

$$\begin{aligned} \frac{\partial \alpha_g \bar{\rho} \tilde{u}_i}{\partial t} + \frac{\partial (\alpha_g \bar{\rho} \tilde{u}_i \tilde{u}_j)}{\partial x_j} = & -\frac{\partial \bar{p}}{\partial x_i} + \frac{\partial}{\partial x_j} \left(\alpha_g \bar{\rho} (\nu + \nu_t) \left(\frac{\partial \tilde{u}_i}{\partial x_j} + \frac{\partial \tilde{u}_j}{\partial x_i} - \frac{2}{3} \frac{\partial \tilde{u}_k}{\partial x_k} \delta_{ij} \right) \right) \\ & + \alpha_g \bar{\rho} g_i - F_D \end{aligned} \quad (2.14)$$

ν_m is the molecular viscosity, ν_t is the sub grid scale viscosity, and p is the pressure. F_D represents the drag force source term resulting from the interaction between the gas flow and the solid phase, and is defined as:

$$F_D = \alpha_g \rho C_D \frac{\alpha_s \sigma_s}{2} |U| u_i \quad (2.15)$$

with C_D the drag force coefficient. The estimation of this coefficient will be expanded in Chapter 3.

Since thermal equilibrium is not assumed between the solid fuel particle and gaseous phase, the temperature in the solid phase is solved separately, in the following equation:

$$C_p^{(s)} \alpha_s \rho_s \frac{dT_s}{dt} = Q_{\pm}^{(s)} - \Delta h_{vap} \dot{\omega}_{vap}''' - \Delta h_{pyr} \dot{\omega}_{pyr}''' - \alpha_{sg} \Delta h_{char} \dot{\omega}_{char}''' \quad (2.16)$$

with $Q_{\pm}^{(s)}$ the energy balance on the solid phase exchanged with the gaseous phase by convection and radiation. Δh_{char} , Δh_{pyr} , Δh_{vap} are the heat of reaction for charring, pyrolysis, and evaporation, respectively. All these parameters will be described in details in Chapter 3. Assuming that 50 % of the heterogeneous combustion is located at the surface of the solid phase, α_{gs} is fixed at 0.5, making 50 % of the combustion energy going in the solid phase and the rest to the gas phase. The specific heat capacity $C_p^{(s)}$ of the solid phase is calculated as:

$$C_p^{(s)} = C_{p_{dry}} Y_{dry} + C_{p_{H_2O}} Y_{H_2O} + C_{p_{char}} Y_{char} \quad (2.17)$$

The time evolution of the fuel is characterized by the variation of its dry, water, and char mass fractions. They can be described by the following three ordinary differential equations:

$$\frac{d\alpha_s \varphi_{H_2O}^{(s)}}{dt} = -\dot{\omega}_{vap}''' \quad (2.18)$$

$$\frac{d\alpha_s \varphi_{dry}^{(s)}}{dt} = -\dot{\omega}_{pyr}''' \quad (2.19)$$

$$\frac{d\alpha_s \varphi_{char}^{(s)}}{dt} = \gamma_{char} \dot{\omega}_{pyr}''' - \left(\frac{\gamma_{ash}}{\gamma_{char}} + 1 \right) \dot{\omega}_{char}''' \quad (2.20)$$

With $\varphi_i^{(s)}$ defined as:

$$\varphi_i^{(s)} = Y_i \rho_s \quad (2.21)$$

The global mass balance equation for the solid phase is:

$$\frac{d\alpha_s \rho_s}{dt} = (\gamma_{char} - 1) \dot{\omega}_{pyr}''' - \dot{\omega}_{char}''' - \dot{\omega}_{vap}''' \quad (2.22)$$

Assuming that the solid consumption is only due to char combustion. The balance equation for the solid fraction is resolved explicitly:

$$\frac{d\alpha_s}{dt} = -\frac{\dot{\omega}_{char}'''}{\rho_s} \quad (2.23)$$

Finally, the energy balance of the gas phase is written as:

$$\begin{aligned} \frac{\partial (\alpha_g \bar{\rho} \tilde{h})}{\partial t} + \frac{\partial (\alpha_g \bar{\rho} \tilde{u}_j \tilde{h})}{\partial x_j} &= \frac{D\bar{p}}{Dt} + \frac{\partial}{\partial x_j} \left(\alpha_g \bar{\rho} \left(a_D + \frac{\nu_t}{Pr_t} \right) \frac{\partial \tilde{h}}{\partial x_j} \right) \\ &+ Q_{comb} + Q_{rad} - Q_{conv}^{(s)} - (1 - \alpha_{gs}) Q_{char}^{(s)} \end{aligned} \quad (2.24)$$

h is the enthalpy, a_D the thermal diffusivity (considering a unity Lewis number approximation). Q_{comb} and Q_{rad} are the source term for the combustion and radiation in the gas phase, respectively.

2.5 Numerical Setup

The above-mentioned model is implemented in the open source libraries of OpenFOAM, and is used to simulate the experiments conducted in the [FPA](#). To do so requires ensuring that the numerical domain is discretised appropriately and that all the equations are solved properly in each cell and at the boundaries, providing fast and accurate solutions.

2.5.1 Turbulence Modelling

In fluid dynamics, a turbulent flow can be represented by a combination of large eddies and small eddies. Large eddies are directly produced from the mean flow. Their size is limited by the geometry of the flow boundaries. They are responsible for effective turbulent transport of mass and energy. The structure of the largest eddies is highly directional (anisotropic) and flow dependent, due to the strong interaction with the mean flow and with other colliding eddies. Large eddies can form larger ones or split into smaller ones. In a similar way, smaller eddies are generated. The small eddies dissipate their rotation and fluctuation energy into heat. The diffusive action of viscosity fades out the directionality, hence the small eddies can be considered independent of the flow direction (isotropic), and dictated by viscosity. Kolmogorov's 1st similarity states that the only factors influencing the behaviour of the small scale motions are the overall kinetic energy production rate (equal to the dissipation rate) and the viscosity ([Kolmogorov, 1941](#)). The difference between small and large scale eddies are listed in Table 2.6.

The Kolmogorov length scale (η) describing the smallest hydrodynamic scale in

Table 2.6: Main differences between large and small scale eddies in a turbulent flow. Extracted from [Troshko and Hassan \(2001\)](#)

Large eddies	Small eddies
Produced by mean flow	Produced by large eddies
Depends on boundaries	Universal
Ordered	Random
Require deterministic description	Can be modelled
Inhomogeneous	Homogeneous
Anisotropic	Isotropic
Long-lived	Short-lived
Diffusive	Dissipative
Difficult to model	Easier to model

turbulent flows is defined as:

$$\eta = \left(\frac{\nu^3}{\epsilon} \right)^{1/4} \quad (2.25)$$

with ϵ the dissipation rate (m^2/s^3) and ν the viscosity (m^2/s). The dissipation rate can be estimated as:

$$\epsilon \sim \frac{U^3}{L} \quad (2.26)$$

By estimating the ratio of the largest (L) to smallest length scales (η) in the flow and by substituting in the previous equation, we get:

$$\frac{L}{\eta} \sim \left(\frac{UL}{\nu} \right)^{3/4} = Re^{3/4} \quad (2.27)$$

Where Re is the Reynolds number based on the large scale flow feature. Notably, the separation of the largest and smallest length scale increases with the Reynolds number. This ratio has important implications for finding the numerical solution of a turbulent flow. For a flow with a high Reynolds number, the ratio L/η

increases, and the number of grid points needed in a computational domain to solve a problem becomes more important.

2.5.2 Direct Numerical Simulation

The most accurate approach for simulating turbulent flows is called Direct Numerical Simulation (DNS), in which the full Navier-Stokes equations are directly solved using very fine meshes to capture all the scales of turbulence, in a given flow from the smallest to the largest eddies (Poinsot and Veynante, 2005). If we consider N as the number of points along one direction in a given mesh, for 3 dimensions:

$$N^3 \geq Re^{9/4} \quad (2.28)$$

This implies that the computational cost of DNS is proportional to $Re^{9/4}$, which makes DNS computationally very expensive for flows with complex geometries, which will often exceed the capacity of most existing computers. Therefore, it can only be applied to low Reynolds number flows over a simple geometry. For instance, Minamoto and Chen (2016) were recently able to simulate a turbulent flame using state of the art supercomputers in a domain of 24 x 12 x 3 mm only. Hence, for fire problems with flames ranging from a few centimetres up to several meters, the use of DNS is not yet possible.

2.5.3 Reynolds Averaged Navier Stokes

In some applications, we are only interested in the average fluid flow (statistically steady). Hence, it is not necessary to simulate the detailed instantaneous flow, meaning computational time is greatly reduced. This is the basis of the Reynolds Averaged Navier Stokes (RANS) approach, in which one solves only for the

averaged quantities while the effect of all the scales of instantaneous turbulent motion is modelled by a turbulence model. This approach has been the backbone of the industrial **CFD** applications. Since **RANS** fails to predict the transient behaviour of the flow, this approach is not appropriate for our case.

2.5.4 Large Eddy Simulation

An alternative approach is Large Eddy Simulation (**LES**), which was proposed by **Smagorinsky (1963)**. The conservation equations are solved on the computational grid and only the Sub-Grid Scale (**SGS**) motions are modelled, resulting in a significant reduction in computational cost compared to **DNS**. **LES** is more accurate than the **RANS** approach since **LES** captures large eddies in full detail whereas they are modelled in the **RANS** approach. For illustration, the effects of the three models are given in Fig. 2.11. Indeed, large eddies contain most of the turbulent energy and are responsible for most of the momentum transfer and turbulent mixing. Furthermore, the small scales tend to be more isotropic and homogeneous than the large ones. Thus, modelling the **SGS** motions is easier than modelling all scales within a single model, as it is done in **RANS**. In our case, **LES** is the most convenient numerical tool, especially because turbulence is coupled with transient reactions.

2.5.5 Mesh Generation

As in any **CFD** simulations, it is important to verify that the size of the mesh does not influence the quality of the results. BlockMesh and snappyHexMesh mesh generators supplied with OpenFOAM (**OpenCFD Ltd.**) are used to create robust

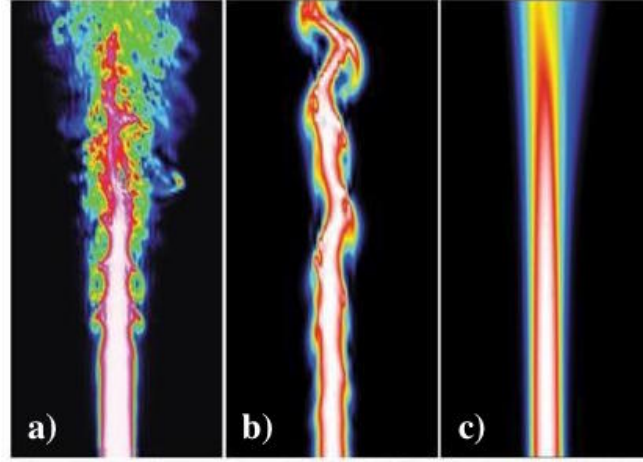


Figure 2.11: Numerical simulation of a turbulent flow using a) DNS; b) LES; and c) RANS. Credit: (Cuenot, 2005)

meshes. Simulations are made in two dimensions in order to reduce computational time. This simplification is acceptable in the **FPA** configuration, since it will be demonstrated (in Chapter 4) that the flow is characterised with a small Reynolds regime. However, it will be important to test the model in three dimensions for other configurations. The overall numerical domain simulating the **FPA** is a rectangle of 1.4 m wide and 1.4 m high. Such a large domain is necessary to ensure that the boundary conditions do not influence the calculations in the zone of interest. The mesh was composed primarily of hexahedral cells. The mesh is stretched beyond the zone of interest until the boundaries, reducing computational time without affecting results, as sketched in Fig. 2.12 and 2.13.

To achieve temporal accuracy and numerical stability, an adaptive time step is used. It is calculated based on the Courant-Fredrichs-Lewy (**CFL**) number, denoted as C_o (Patankar, 1980) and defined as:

$$C_o = \frac{\Delta t |U|}{\Delta x} \quad (2.29)$$

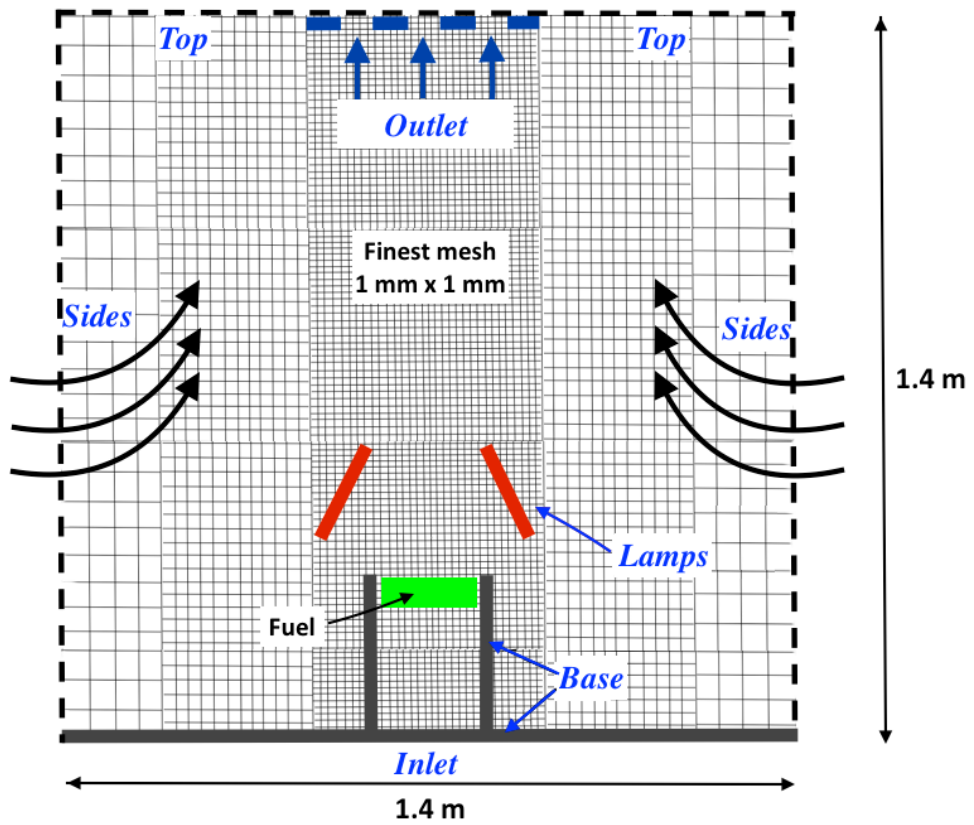


Figure 2.12: Computational domain (not to scale)

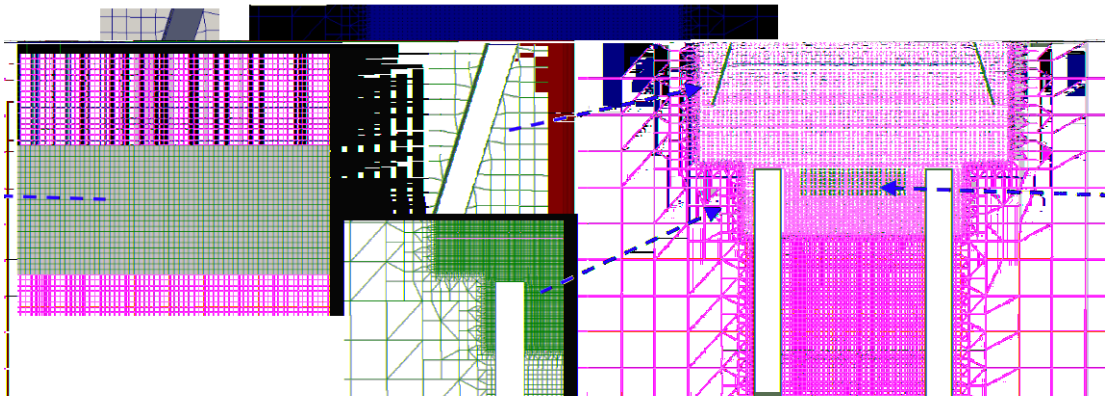


Figure 2.13: Zoom on the computational domain and grid (using Paraview)

where Δt is the time step, $|U|$ is the velocity magnitude and Δx is the cell size. For numerical stability, C_o is bounded by a maximum value of 0.7. Small cell size means more cells in the mesh, hence, greater resolution. However, it also leads to smaller time steps due to the CFL condition, resulting in much longer computational time and more resources needed for each simulation. Therefore, it is important to reach a compromise between computational time and grid resolution (Patankar, 1980).

ForestFireFOAM was developed on the structure of FireFOAM. The latter was written in a compressible form, which means that it should account for the change of density due to pressure, which includes pressure wave formation. However, in FireFOAM (and in ForestFireFOAM) the CFL condition does not include the speed of sound accounting for acoustic waves. As mentioned by Volfeyau (2015), it was excluded in order to prevent the acoustic motion from limiting the time step during low Mach number scenarios, which are found in the case of most fires. Additionally, since a Generalised Geometric-Algebraic Multi-Grid (GAMG) solver is used for the pressure field, acoustic waves cannot appear in coarse meshes, because the wavelength is much smaller than the mesh (Marks, 1991), and for fine meshes, pressure fields converge before any waves are developed in the solution.

The mass in the solid phase and the gas temperature are chosen as criteria for the sensitivity analysis convergence on a simplified test. The evolution of the mass implies that the mass conservation is respected in the solid phase and the evolution of the temperature is representative of the energy conservation in the gas phase. To make sure that the values are independent of the cell size, the evolution of the total mass and the temperature are plotted for different cell sizes, in a specific cell in the fuel region and in the flame region respectively. For clarity, only the results for three tests are shown in Figs. 2.14 and 2.15.

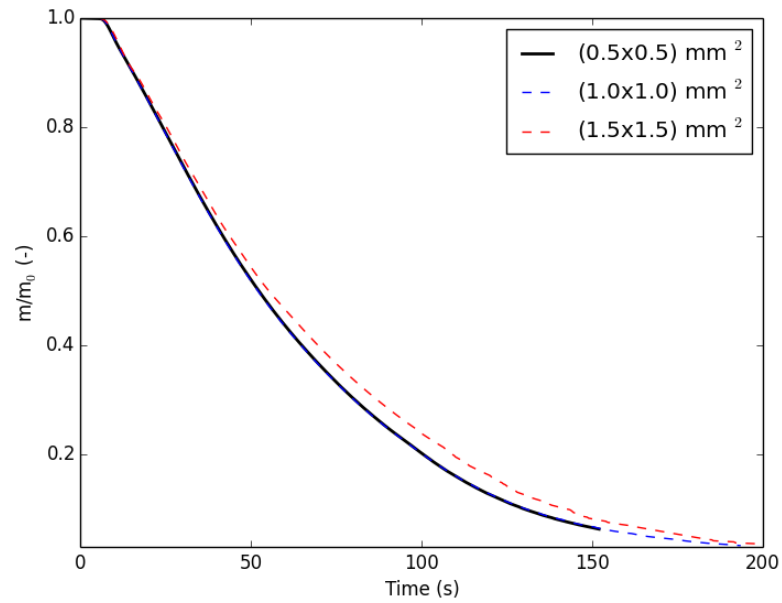


Figure 2.14: Mesh convergence test: time evolution of the mass loss in a cell in the fuel region.

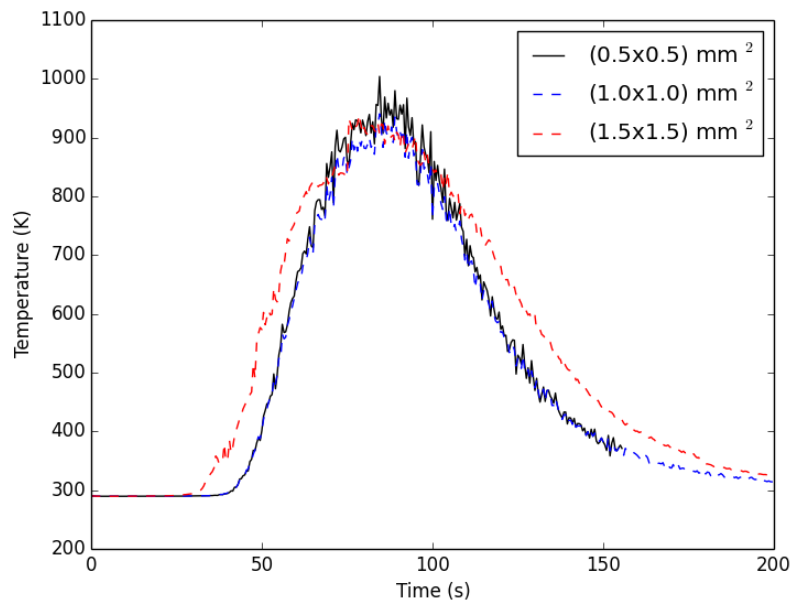


Figure 2.15: Mesh convergence test: time evolution of the gas phase temperature in a cell in the flaming region

In Fig. 2.14, the mass loss in a cell with a size of $(1 \times 1) \text{ mm}^2$ in the fuel region provided the same predictions as the finest mesh of $(0.5 \times 0.5) \text{ mm}^2$ with a relative difference of $(\Delta m/m)_{max} = 2 \%$. However, for a coarser mesh $(1.5 \times 1.5) \text{ mm}^2$ the results were not as accurate $(\Delta m/m)_{max} = 21 \%$. As for the temperature presented in Fig. 2.15, the highest temperature deviation between results of $(1 \times 1) \text{ mm}^2$ and the finest mesh was $(\Delta T/T)_{max} = 6 \%$. For the coarser mesh the difference was much larger, $(\Delta T/T)_{max} = 49 \%$. Therefore, a cell size of $(1 \times 1) \text{ mm}^2$ can be considered acceptable, since it provides converging results in the vicinity of the sample on both the solid and gas phases.

2.5.6 Boundary Conditions

In this section, all used keywords are pre-defined in OpenFOAM libraries (OpenCFD Ltd.). Boundary conditions are very important in LES, especially with significant coupling between phenomena. A poor choice of the boundary conditions can cause instabilities and have a major impact on the results. The physical boundary conditions of the main parameters for walls, inlets, and outlets are illustrated in Fig. 2.12. The left and right sides of the domain are named *Sides*, the top layer is *Top*, and the exhaust above the sample is *Outlet*. *Lamps* are defined as wall boundaries. The combustion chamber and the ground are denoted *Base*. Finally, *Inlet* below the sample is modified for each case, depending if forced flow is injected or not. Hereafter, it will be presented for forced flow conditions. For no flow conditions, *Inlet* is switched to *Base*.

Pressure and velocity boundary conditions

The following boundary conditions in Table 2.7 are chosen for velocity and pressure. Other boundary conditions are listed in Appendix C.

Table 2.7: Chosen boundary conditions for pressure and velocity

	Lamps - Base	Top - Sides	Inlet	Outlet
U	fixedValue	pressureInletOutletVelocity	fixedValue	fixedValue
	uniform (0 0 0)	uniform (0 0 0)	uniform (0 0.267 0)	uniform(0 2.0 0)
p_rgh	buoyantPressure	totalPressure	zeroGradient	zeroGradient

The velocity is set to (fixedValue meaning a Dirichlet condition) at *Lamps* and *Base*, meaning that the velocity is zero. However, *Sides* and *Top* boundaries are free to the atmosphere, and they allow both outflow and inflow according to the internal flow conditions. Hence, they are set to pressureInletOutletVelocity. This boundary condition is a combination of Dirichlet and Neumann that allows representing an open condition. ZeroGradient (Neumann) is applied on all components, except where there is inflow, in which case a fixedValue (Dirichlet) condition is applied to the tangential component. At *Inlet* and *Outlet*, fixed velocities are applied representing the inflow in the combustion chamber and the outflow of the exhaust. Generally, in OpenFOAM the variable p_rgh is the pressure without the hydrostatic pressure as:

$$p_rgh = p - \rho gh \quad (2.30)$$

It is initialized from the pressure field. The pressure equation is solved for the p_rgh, so its corresponding boundary conditions are important for the pressure solution. Once it is solved, the pressure p is calculated as:

$$p = p_rgh + \rho gh \quad (2.31)$$

For *Top* and *Sides*, the pressure is calculated from the internal field. For *Base* and *Lamps*, the buoyantPressure boundary condition is used for the pressure field, which calculates the normal gradient from the local density gradient. Finally, at *Inlet* and *Outlet*, a zeroGradient (Neumann) condition is set.

Radiative boundary conditions

Heaters were modelled by fixing a constant heat flux on specified walls that have equivalent view factor as in the [FPA](#) in two dimensions, and providing the same heat flux required on the sample surface. In order to set a constant heat flux as a boundary condition, we defined a new boundary condition called `greyDiffusiveRadiationHF`, based on the existing `greyDiffusiveRadiation` boundary condition. The former allows imposing a fixed heat flux at a boundary, whereas the latter calculates the equivalent radiation intensity for each solid angle from the temperature field, for a given emissivity. This was necessary to allow inclusion of additional functionalities to the new boundary condition, such as a start time, which allows the flow to establish in the first seconds of the simulation before switching on the lamps. Similarly, transient heat flux can easily be implemented to this boundary condition. The view factor of the [FPA](#) lamps in two dimensions was determined using a crossed string method ([Modest, 2013](#)). This method is applicable for two surfaces, A_1 and A_2 , as shown in Fig. 2.16.

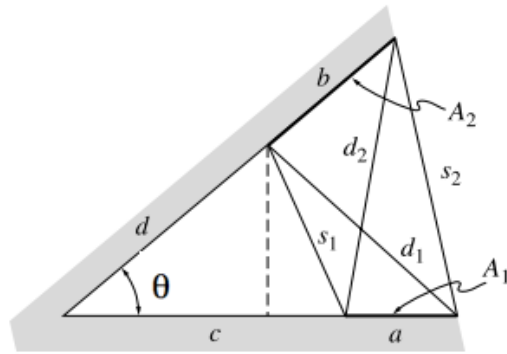


Figure 2.16: View factor calculation for a wedge-shaped groove. Extracted from ([Modest, 2013](#))

The view factor (F_{1-2}) between A_1 and A_2 can be calculated as follows, for known

dimensions a , b , c , d , and θ :

$$F_{1-2} = \frac{d_1 + d_2 - (s_1 + s_2)}{2a} \quad (2.32)$$

From the figure, we have:

$$s_1^2 = (c - d \cos \theta)^2 + d^2 \sin^2 \theta = c^2 + d^2 - 2cd \cos \theta \quad (2.33)$$

Similarly,

$$s_2^2 = (a + c)^2 + (b + d)^2 - 2(a + c)(b + d) \cos \theta \quad (2.34)$$

$$d_1^2 = (a + c)^2 + d^2 - 2(a + c)d \cos \theta \quad (2.35)$$

$$d_2^2 = c^2 + (b + d)^2 - 2c(b + d) \cos \theta \quad (2.36)$$

By knowing the heat flux received at the surface of the sample (q''_{target}), the heat flux that has to be imposed at the lamps (q''_{lamp}) can be written as:

$$q''_{lamp} = \frac{(q''_{target} + \sigma T_\infty^4)}{2F_{1-2}} \quad (2.37)$$

with the factor 2 in the denominator accounting for two lamps; σ , the Stefan-Boltzmann constant; and T_∞ , the ambient temperature.

Radiation intensity is determined by solving the Radiative Transfer Equation ([RTE](#)) for a discrete number of finite solid angles using the finite volume Discrete Ordinate Method ([DOM](#)) available in OpenFOAM. The establishment of the [RTE](#) itself will be discussed in detail in Chapter 3. The [DOM](#) method was first suggested by [Chandrasekhar \(1960\)](#) for one-dimensional astrophysics problems. Later, [Carlson and Lathrop \(1965\)](#) developed the [DOM](#) to solve multi-dimensional neutron transport problems, and over the past decade the method has been applied to solve many radiative heat transfer problems. The finite volume method

for radiative energy transfer is based on the same idea as the finite volume analysis for fluid flows and convective energy transfer. The sphere of solid angles surrounding a control volume is divided into equal solid angles, and by summing over all directions, a total energy balance is written for each control volume, providing a local and overall energy conservation. The accuracy is increased by using a finer discretisation:

$$n_{disc} = 4n_{\phi}n_{\theta} \quad (2.38)$$

where n_{ϕ} and n_{θ} are the number of discretisation in the azimuthal angles in $\pi/2$ and in the polar angles in π , respectively. Since this study is made in two dimensions, n_{θ} is not considered by OpenFOAM ($n_{\theta} = 1$). The discretisation becomes:

$$n_{disc}^{2D} = 4n_{\phi} \quad (2.39)$$

It is important to determine the optimal discretisation number because this method is computationally intensive. A sensitivity analysis is presented in Fig. 2.17, in which $n_{\phi} = 8$ provides a uniform distribution of the radiative heat flux at the top of the fuel sample, as observed in the FPA. The example of $n_{\phi} = 10$ gives slightly better distribution than the former, but it corresponds to 40 solid angles (instead of 32), which slows down the calculation for less than 1 % more precision. This is negligible especially when experimental results can vary by ± 5 %. The effect on computational time is even more apparent for three dimensional calculations ($n \neq 1$). The RTE is solved every 10 iterations, in order to reduce the computational time without affecting results.

It is important to keep in mind that the present simulations are performed in two spatial dimensions but even for an assumed two-dimensional heat transfer geometry, the radiation problem remains in general three-dimensional and cannot

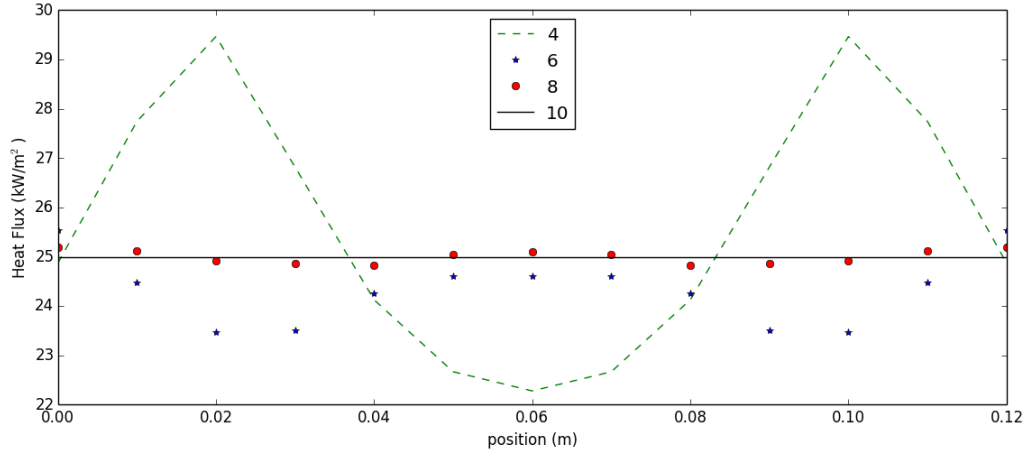


Figure 2.17: Influence of the RTE discretisation on the heat flux received by the sample. Shown labels correspond to values of n_ϕ

be theoretically reduced to a two-dimensional treatment because radiation transport is sensitive to the path length of individual rays and consequently radiation properties depend on both polar angle and azimuthal angle.

2.5.7 Solvers

The set of transport equations in the gas phase are solved using a second order implicit Finite Volume Method (FVM). Total Variation Diminishing (TVD) schemes have been adopted to avoid introduction of false numerical diffusion (Patankar, 1980). The set of Ordinary Differential Equations governing the evolution of the solid fuel was solved using a Crank-Nicolson scheme blended with Euler for better stability (second order implicit) (CFD Direct Ltd, 2015). It is also a pressure based segregated solver, similar to most solvers based in OpenFOAM (OpenCFD Ltd.). Point to point interpolations of values are calculated using a linear interpolation scheme (central differencing). The first time derivative is evaluated with a second order, bounded, implicit method. A blending coefficient is included to improve the stability. Discretisation schemes for the Gradient,

Laplacian and Divergence terms are Gauss linear (second order). TVD schemes (Harten, 1997) are used for the species transport and enthalpy equations.

A description of the solving methods mentioned in this section can be found in OpenFOAM (OpenCFD Ltd.). The solver used for the density equation is a Preconditioned Conjugate Gradient (PCG) linear solver with a Diagonal Incomplete Cholesky (DIC) preconditioning of matrices. The solver stops if the residual falls below the solver tolerance, here set to 10^{-7} , or if the ratio of current to initial residual falls below the solver relative tolerance, set to 0 in order to force the solution to converge to the solver tolerance. The pressure equation is solved using a Generalised GAMG linear solver with a tolerance of 10^{-7} and a relative tolerance set to 0.01, and a Gauss-Seidel smoother. The GAMG generates a quick solution on a mesh with a small number of cells, then maps this solution onto a finer mesh. The approximate mesh size at the coarsest level is set to 10 cells. The cell agglomeration algorithm is performed using a Face Area Pair method.

- Equations for the velocity, the mass fractions and the enthalpy are solved using a Preconditioned Bi-Conjugate Gradient (PBiCG) linear solver for asymmetric matrices with Diagonal Incomplete-LU (DILU) preconditioner and a 10^{-8} tolerance and a relative tolerance set to 0.1.
- Radiation intensity I is solved using GAMG solver with a tolerance of 10^{-4} , the relative tolerance is set to 0 and a DILU smoother is used. The mesh size at the coarser level is set to 10 cells and the Face Area Pair method calculates agglomeration of cells with 10 maximum iterations.
- Incident radiation is solved with PCG solver with a DIC pre-conditioning of matrices.
- The solver tolerance is set to 10^4 and the relative tolerance is set to 0. Finally, the velocity field is corrected and the time pressure is updated using

a PIMPLE algorithm that combines the SIMPLE algorithm (Semi-Implicit Method for Pressure-Linked Equations) (Versteeg and Malalasekera, 1995) with a PISO algorithm (Pressure Implicit with Splitting Operators) (Issa, 1986) to correct the second pressure correction and to correct both velocities and pressure explicitly.

- A momentum predictor is used, as well as one inner corrector and one outer corrector. As for the relaxation factors, they are set to 1 for U and K, to 0.8 for the chemical species, and to 0.5 for the enthalpy. A higher value for the latter can lead to unphysical temperatures, thus to more instabilities.

2.5.8 Parallelisation

ForestFireFOAM allows parallel computation using a Message Passing Interface (MPI) library to facilitate communication between parallel processes in order to reduce computational time. The parallel functionality is implemented in the lower level of the OpenFOAM code hierarchy and uses domain decomposition. Thus, the implementation details are transparent to ForestFireFOAM's main solver. This is an example of the advantage of object oriented programming. Executing parallel simulations results in a speedup (S) curve defined as the ratio of the execution time using one processor (t_1) to the execution time using n processors (t_n):

$$S = \frac{t_1}{t_n} \quad (2.40)$$

By definition, a linear speedup is given for:

$$\frac{t_1}{t_n} = n \quad (2.41)$$

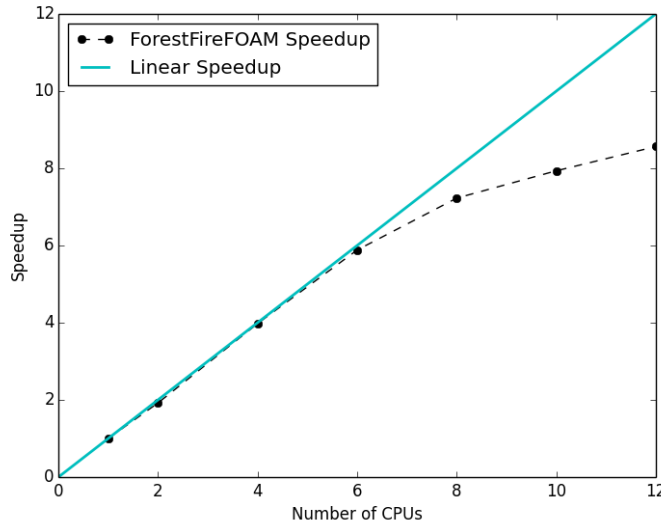


Figure 2.18: ForestFireFOAM scaling on the Mésocentre cluster for a test with 100,000 cells.

Measured speedups are usually smaller than the ideal due to the inter-process communication. However, superlinear speedups can be achieved (values higher than linear) depending on the algorithm used, as observed in (Vilfayeau, 2015). It was necessary to perform a scalability study to achieve good parallel performance and to maintaining a significant work load on every processor. If the problem is too small in size, the parallel performance will deteriorate with the number of processor. For a mesh of 100,000 cells, it was found that using 8 processors presents the optimal use of the MPI capabilities (Fig. 2.18) on the cluster of the Mésocentre of Aix Marseille Université (Equipex Mesocentre, 2016). This leads to using 12,500 cells per processor.

In the future it will be important to profile the code in order to localise the bottlenecks and to optimize the code for further decreasing simulation times.

2.6 Conclusion

In this chapter, we presented the experimental and numerical tools that have been implemented to conduct a thorough investigation of submodelling for physical models applied to wildland fires. First we presented the physical and chemical properties of two distinct North American species: pitch pine and white pine needles. Pine needle beds were used as a reference fuel in this study because they are well characterised in the literature, and they allow repeatable fuel bed properties to be obtained under laboratory settings. The [FPA](#) was used to obtain a controlled experimental environment, and repeatable conditions for burning litters of pine needles. In addition to the [FPA](#) experiments, supplementary tests were used to better describe specific aspects related to the physical and chemical properties of pine needles, such as:

- [DSC](#) measurements to obtain the thermal properties of pine needles.
- Analysing the spectral emissivity of dead pine needles to better describe the radiative heat transfer.
- Including temperature measurements in the [FPA](#) to compare the experimental temperatures with the simulations.
- Pyrolysis gas sampling using [FTIR](#) spectrometry.

Regarding the numerical aspect of the problem, a multiphase approach was implemented in OpenFOAM based on FireFOAM solver, creating ForestFireFOAM solver for porous fuels. Using [LES](#) capabilities, Navier-Stokes conservation equations are solved in a radiative and reactive multiphase medium. In order to perform proper [LES](#), the boundary conditions were established, and the grid sensitivity analysis was conducted. The closure models, or submodels, that are used for degradation, heat transfer, combustion, and radiation are typically applied

to simulate large-scale wildfires in complex environments. Now that numerical simulations can be performed to reproduce the same controlled experimental conditions, the model's behaviour can be assessed with fewer uncertainties compared to larger scale tests. This allows us to identify the limitation of each submodel, couple it with other submodels, and quantify its influence on the physical results.

Chapter 3

Submodelling

In this chapter, the physico-chemical processes of thermal degradation such as pyrolysis, evaporation, and char oxidation occurring in the solid and gas phases are considered. Other phenomena including combustion, radiative and convective heat transfer ([Incropera and Dewitt, 1996](#)) were also studied. These submodels that represent these phenomena are used to close the balance equations, as described below. They are often developed from small-scale experiments under well defined conditions as described in Chapter 2, and have not been fully validated for the multiphase approach ([Morvan et al., 2011](#)). The limitations of the submodels and their improvements are detailed later in the discussion. This type of analysis is necessary because it is the only opportunity to validate the range of applicability of a submodel, to confront it to experimental measurements, and to estimate how it influences the results. Small scale experiments can be well controlled and instrumented, contrarily to field scale experiments (and wildfires) where sources of uncertainty are very large, and sometimes even not quantifiable. Hence, this validation step is necessary before using the model at large scale.

3.1 Heat Transfer in Porous Beds

Pine needles fall from trees and often accumulate forming porous beds (93-97 %) on the forest floor and near structures in the Wildland Urban Interface ([WUI](#)), increasing the fire risk. Such highly porous beds result in a low contact area between each needle. Additionally, the conductivity of pine needle is very small. For instance, the conductivity of wooden material is in the order of 0.04 - 0.12 W.m⁻¹.K⁻¹ ([Young and Sears, 1992](#)), whereas for typical conductive material such as aluminium, copper, or gold, the conductivity is in the order of 200-400 W.m⁻¹K⁻¹. Hence, we can consider that conduction is negligible compared to radiation and convection ([Torero and Simeoni, 2010](#)), and we will exclude the former in our analysis.

3.1.1 Radiative Heat Transfer

The radiative intensity is obtained by solving the multiphase Radiative Transfer Equation ([RTE](#)) ([Larini et al., 1998](#)), which can be written as follows:

$$\frac{d\alpha_g I}{ds} = \alpha_g \sigma_0^{(g)} \left[\frac{\sigma T^4}{\pi} - I \right] + \sigma_0^{(s)} \left[\frac{\sigma T_s^4}{\pi} - I \right] \quad (3.1)$$

In the first term of the right hand side equation, $\frac{\sigma T^4}{\pi}$ represents the intensity increase by gas emission. By subtracting I , we take into account of the intensity attenuation by gas absorption. The second term in the right hand side equation was added to the [RTE](#), (in comparison to the original [RTE](#) in OpenFOAM) to represent the solid to solid radiation exchange. $\sigma_0^{(g)}$ and $\sigma_0^{(s)}$ are the absorption coefficients for the gas and solid phases, respectively. σ is Stefan-Boltzmann constant (5.67×10^{-8} Wm⁻²K⁻⁴). The total irradiance (J) is calculated by

integrating the radiative intensity (I) in every direction:

$$J = \int_0^{4\pi} I d\Omega \quad (3.2)$$

The radiative source term of the solid phase in the energy equation is calculated as:

$$Q_{rad}^{(s)} = \sigma_0^{(s)} \alpha_{eff} (J - 4\sigma T_s^4) \quad (3.3)$$

Where, α_{eff} is the fuel effective absorptivity and $4\sigma T_s^4$ represents the emission from the solid phase. Hence, $(J - 4\sigma T_s^4)$ represents the net radiation reaching a cell. The estimation of the extinction coefficient for the solid phase ($\sigma_0^{(s)}$) can be estimated from the theoretical approximation for spherical particles as mentioned by [De Mestre et al. \(1989\)](#):

$$\sigma_0^{(s)} = \frac{\alpha_s \sigma_s}{4} \quad (3.4)$$

It was shown in [Monod et al. \(2009\)](#) that this estimation of the extinction coefficient is valid for forest fuels but has to be used with a certain correction factor (0.95 to 0.99) depending on the geometrical configuration. This is why further experiments were conducted to estimate the extinction coefficient, or at least to verify if it was well approximated using De Mestre relation in the Fire Propagation Apparatus ([FPA](#)) configuration. A heat flux gauge (Schmidt-Boelter type by Medtherm Corp.) was placed in the [FPA](#) directly under the sample to measure the received heat flux (\dot{q}_r'') through the porous bed of 1, 2, and 3 cm thickness (x). Measurements were taken in the pre-heating phase, during the first 5 seconds before ignition and for initial heat fluxes (\dot{q}_{surf}'') of 30, 40, and 50 kW/m² on the top layer of the sample (i.e. surface) with a precision of 0.1 kW/m². From measurements of (\dot{q}_r''), the extinction coefficient can be estimated as:

$$\sigma_0^{(s)} = \frac{\ln \left(\frac{\dot{q}_{surf}''}{\dot{q}_r''} \right)}{x} \quad (3.5)$$

For pitch pine needle, the theoretical value of the extinction coefficient is

$$\sigma_0^{(s)} = \frac{\alpha_s \sigma_s}{4} = \frac{0.07 \times 7295}{4} = 122.92 m^{-1} \quad (3.6)$$

The measured values are averaged for each heat flux and plotted in Fig. 3.1. On average, the measured extinction coefficients were $147.39 m^{-1}$, which was slightly higher than the theoretical value. Consequently, a correction factor of 1.19 was required for the theoretical estimation in order to match the experimental value. This multiplication factor is higher than what was suggested by [Monod et al. \(2009\)](#), where it was found that De Mestre relation slightly underestimate the real extinction coefficient. The variability of these results is highly sensitive to the sampling preparation, which could explain the different estimations. Moreover, their analysis was made for a medium built with leaves, and not with pine needles.

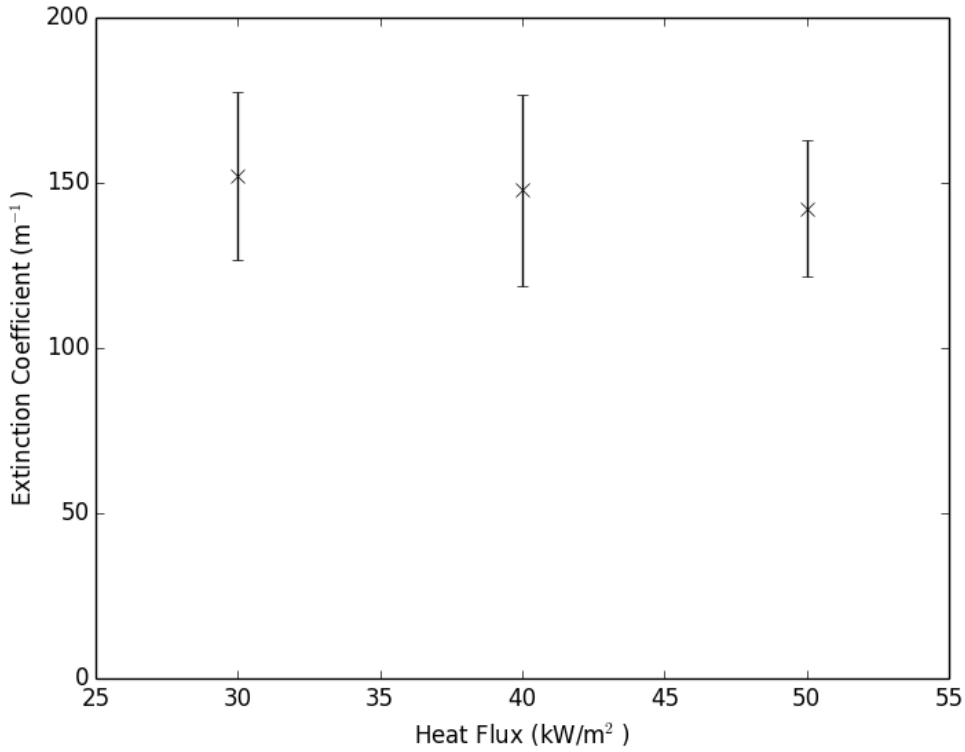


Figure 3.1: Extinction coefficient measurement for different heat fluxes

In order to simulate the experiments performed in the FPA correctly, it is important to estimate the effective absorptivity of the vegetation under the FPA lamps as it was described in Chapter 2. Therefore, the spectral absorptivity of dead pitch pine needles was determined over a wide range of wavelengths, from ultraviolet to long infrared (0.25-20 μm) at FM Global laboratory. The FPA heaters can be considered as greybody radiators and their corresponding spectral intensity I ($\text{kW}/\text{m}^2/\mu\text{m}/\text{sr}$) can be represented using Planck's equation (Chaos, 2014):

$$I(\lambda, T) = \frac{h_p c^2}{\lambda^5} \left[\exp \left(\frac{h_p c}{\lambda k_B T} \right) - 1 \right]^{-1} \quad (3.7)$$

Where λ is the wavelength (μm), h_p is Planck's constant, c is the speed of light, k_B is Boltzmann's constant, and T is a given temperature (K). The spectral radiative intensity curve is normalised and plotted along with the pine needle spectral absorptivity in Fig. 3.2. Highly non-grey spectral distributions are evident. The standard deviation of the six measurements taken for each of the needles is also represented in the figure. There is noted variation of approximately 40 % especially in the near infrared region ($\sim 1\text{-}3 \mu\text{m}$, $3,300\text{-}10,000 \text{ cm}^{-1}$), which indicates that the needles are not perfectly diffuse reflectors, and that directional effects are present. The presented data are also in good agreement with those of Acem et al. (2010); Monod et al. (2009) for Aleppo pine (*Pinus halepensis*) needles, and those of Clark et al. (2007) for lodgepole pine (*Pinus contorta*) needles by showing similar trends.

The average absorptivity is weighted over the black body spectrum at the specific temperature of interest to obtain the effective absorptivity, $\alpha_{eff}(T_r)$. It is dependent on the radiation source temperature, T_r , and is given by:

$$\alpha_{eff}(T_r) = \frac{\int \alpha(\lambda) I(\lambda, T_r) d\lambda}{\int I(\lambda, T_r) d\lambda} \quad (3.8)$$

Figure 3.3 shows the evolution of α_{eff} with temperature. The FPA heaters radiate

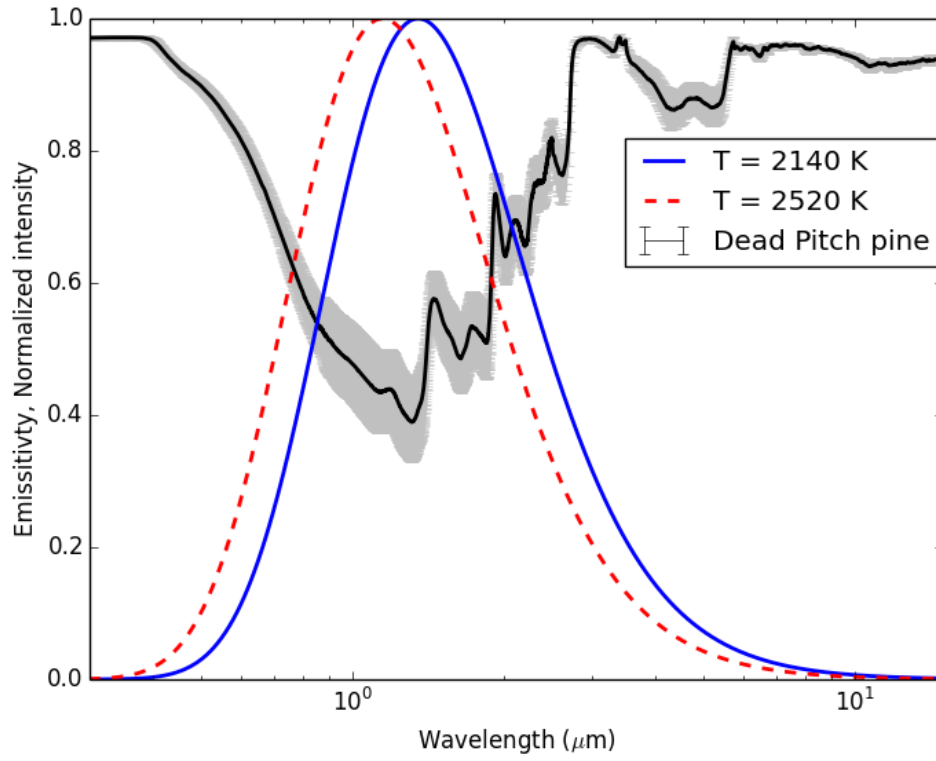


Figure 3.2: Spectral emissivity/absorptivity of dead pitch pine needle, and FPA heaters at 2,140 K and at 2,520 K corresponding to 25 kW/m² and 50 kW/m², respectively (Eq. 3.7).

at temperatures of $2,000 \text{ K} < T_r < 3,000 \text{ K}$ (Chaos, 2014) where the effective absorptivity of dead needles differs by approximately 10 to 15 % (on average, $\alpha_{eff} = 0.64$ for dead needles, over this temperature range). On the other hand, typical surface temperatures are characterised by $300 \text{ K} < T < 1,000 \text{ K}$ for which the effective emissivity of dead needles ($\alpha_{eff} = 0.92$ on average) differs by about 3 %. Naturally, needles start charring around 573 K (Safi et al., 2004). However, char spectrally behaves like a greybody with effective emissivity and absorptivity equal to 0.85 (Försth and Roos, 2011; Chaos, 2014).

As mentioned above, dead needles are highly non-grey absorbers/emitters and differ most notably in the near- and mid-infrared spectral regions. This behaviour

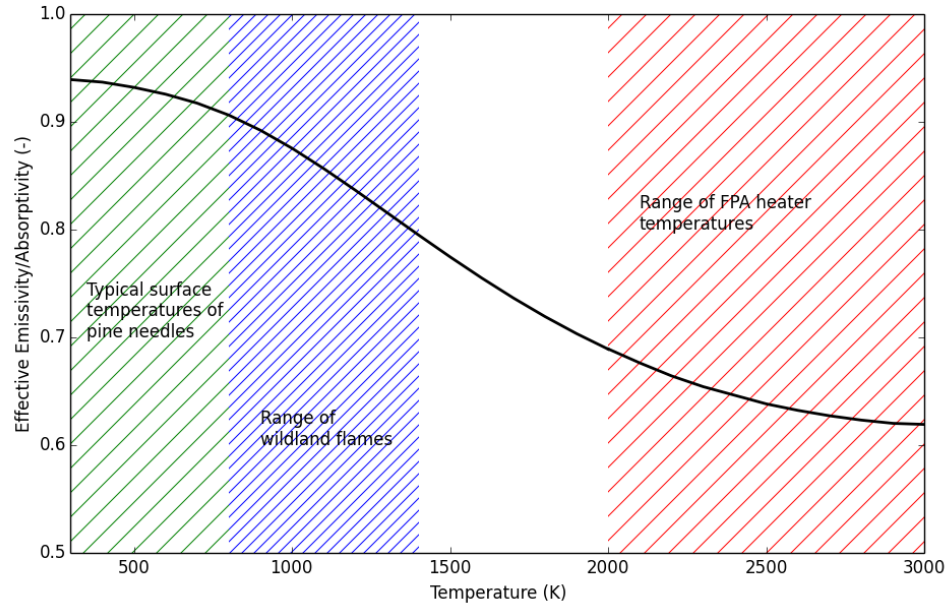


Figure 3.3: Effective emissivity/absorptivity of dead Pitch pine needles for a temperature range

has direct implications on the radiative source term in the energy balance equation and the RTE (Morvan et al., 2009) which requires that the spectral radiation environment interacting with the needles be taken into account. For example, the pine needles considered in the present study would absorb radiation more efficiently from low temperature sources (characterised by longer wavelengths) than from those at higher temperatures (Fig. 3.3). On the other hand, emission of radiation (i.e., re-radiation) from the pine needles would be determined by their surface temperature, which may considerably differ from those of the radiation sources interacting with them. Therefore, the effective emissivity and absorptivity of the pine needles as a function of temperature must be determined.

Typical flame temperatures observed in ventilated conditions are usually much cooler than the operating FPA heater temperatures. Hence, they are better absorbed and the corresponding effective absorptivity is $0.85 < \alpha_{flam} < 0.95$,

which is higher than what is found for the FPA heaters (~ 0.64). As a consequence, pine needles absorb the flame radiation more than the heater radiation. Instead of numerically separating the incoming flame radiation and the FPA heater radiation, and treating both radiations separately, the fuel absorptivity α_{eff} in Eq. 3.3 was set to α_{flam} . The imposed heat flux on the surface (i.e. top layer since there is no real surface) of the fuel was corrected using the effective absorptivity of pine needles under the FPA heaters, as found in the spectral analysis:

$$\dot{q}_{surf}'' = \alpha_{eff} \dot{q}_{FPA}'' \quad (3.9)$$

This simulates the heaters emitting only the fraction that can be absorbed and the fuel absorbs all of it. This simplification allows both radiation sources to be treated the same way in the solid phase. Cellulosic materials have similar spectral distributions (Monod et al., 2009; Acem et al., 2010; Chaos, 2014) and dead pine needle behaviour is comparable to those of hardwood and oak (Chaos, 2014). Differences can be mostly attributed to moisture content in the samples as well as colour differences for shorter wavelengths (i.e. larger wavenumbers). Given these observations, we can safely assume that the spectral emissivity of char from pine needle is very similar to that of other cellulosic materials. Curves of charred materials do not exhibit the strong spectral variations shown by the virgin materials in the FPA (Chaos, 2014). Therefore, these chars are approximated as grey emitters with flat spectral profiles and with an average emissivity value $\alpha_{char} = 0.85$ (Chaos, 2014). Most of char production becomes apparent once the fuel starts burning. Hence, in the model we assume that α_{eff} increases linearly with the produced char fraction until reaching α_{char} .

Planck mean absorption coefficients are used to determine the radiative properties of the gas-phase species such as water vapour, carbon dioxide, and carbon monoxide (Barlow et al., 2001; Smith et al., 2003). The total absorption coefficient

($\sigma_0^{(g)}$ in Eq. 3.1) for the gas is given by:

$$\sigma_0^{(g)} = \sum p_i a_{p,i} \quad (3.10)$$

Where $a_{p,i}$ is the Planck mean absorption coefficient of species i , and p_i is its partial pressure. Suggested expressions for $a_{p,i}$ for the considered gas-phase are given by [Smith et al. \(2003\)](#) as functions of temperature. CO_2 and H_2O are the most important radiating species in vegetation flames ([Boulet et al., 2011](#)). Thus, the inclusion of radiation by CO_2 and H_2O can reduce peak temperature by approximately 50 K in a laminar flame ([Smith et al., 2003](#)). CO radiation contributes much less to the flame temperature reduction than CO_2 and H_2O . The TNF workshop ([Smith et al., 2003](#)) provides curve fits for the pressure-based Planck mean absorption $a_{p,i}$ coefficients for CO_2 , H_2O , CO, and CH_4 based on the results from RADCAL program by [NIST Grosshandler \(1993\)](#) for temperatures between 300 K and 2,500 K.

No soot modelling was attempted in this study. It could be included in the future to better represent the flame. But its absence did not severely influence the burning dynamics of the pine needle bed (which was the focus of this work), as a great amount of the impinging radiation was coming from the lamps. Anecdotal laboratory evidence obtained from a brief study placing a heat flux sensor at the top of the sample during FPA experiments showed that a heat flux $\dot{q}_{lamp}'' = 20 \text{ kW/m}^2$ represents 70 % of the total radiation ($\dot{q}_{lamp}'' + \dot{q}_{flame}''$) reaching the top of the fuel bed and for a heat flux of 50 kW/m^2 , it corresponds to 85 % of the total radiation. As for potential soot models: Syed's model ([Syed et al., 1990](#)), which was originally tested for CH_4 /air diffusion flames ([Kaplan et al., 1996](#)), can be easily implemented. The adaptation of this soot model to the multiphase approach is presented in [Morvan and Larini \(2001\)](#), where the soot formation is

accounted for a mass percentage (3 %) of pyrolysis products, and not from the decomposition of hydrocarbons in the gas phase.

This analysis allowed characterising quantitatively the radiative properties of pine needle under the **FPA** configuration. Further evaluation of the convective mechanism will supplement the heat transfer estimation.

3.1.2 Convective Heat Transfer

The term representing the contribution due to convective heat transfer $Q_{conv}^{(s)}$ between the gas phase and the unburned solid fuel is written as follows in the energy balance equation (i.e. Eq. 2.24):

$$Q_{conv}^{(s)} = \alpha_s \sigma_s h_{conv} (T - T_s) \quad (3.11)$$

Where T and T_s are the gas and solid phase temperatures, respectively. h_{conv} is the convective heat transfer coefficient ($\text{W}/\text{m}^2\cdot\text{K}$). This section aims at evaluating if the models suggested in the literature for estimating the convective heat transfer coefficient are adapted to our experimental configuration. Therefore, two separate models are proposed for natural and forced convection.

Natural convection

Since radiative heat transfer is accurately represented (in the previous section), it is acceptable to chose a convective heat transfer coefficient that best fits the **FPA** setup. When the **FPA** is configured without forced flow, only natural convection occurs, mostly on top of the sample rather than inside the sample, because the configuration of the **FPA** (shield + chamber + basket) blocks the flow through the

sample. Correlations based on Reynolds number were initially used to estimate the convective heat transfer coefficient, such as:

$$h_{conv} = \frac{K}{D}Nu = \frac{K}{D}CRe^mPr^n \quad (3.12)$$

Where Pr is the Prandtl number, a dimensionless number, defined as the ratio of the kinematic viscosity to the thermal diffusivity, K is the air thermal conductivity, D is the equivalent diameter (approximated as $4/\sigma_s$), and C , m , and n are Chilton-Colburn coefficients (Incropera and Dewitt, 1996). These correlations were chosen because they are widely used in physical models using the multiphase approach for simulating wildland fires (Porterie et al., 2005; Mell et al., 2009; Morvan et al., 2009) and even for simulating ignition of forest fuel in no flow conditions (Consalvi et al., 2011). However, using such correlations result in an overestimation of the convective heat transfer coefficient, which is translated in obtaining low temperatures in the fuel bed, as observed in Fig. 3.4.

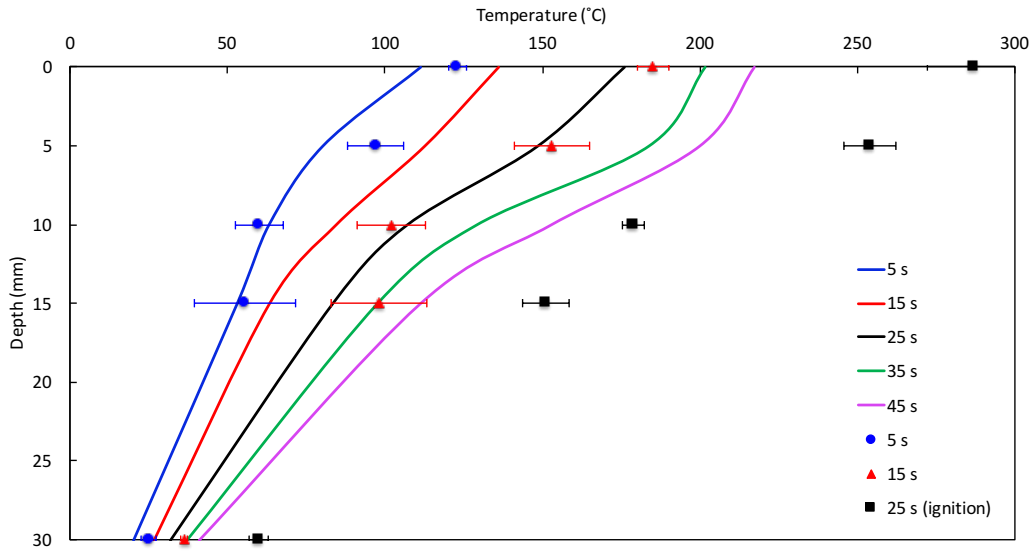


Figure 3.4: Temperature profile before ignition using Eq. 3.12 for pitch pine, bulk density of 40 kg/m^3 , 25 kW/m^2 applied heat flux, and no flow. Symbols: Experiments, lines: Simulation

Regarding the simulation showing in Fig. 3.4, ignition was not observed, even beyond 45 s. This was due to the low solid phase temperature, which was not high enough to trigger the pyrolysis rate, and to reach a flammable mixture in the gas phase for ignition and combustion to occur. Therefore, we propose to implement correlations depending on the Grashof (Gr) number, which are more appropriate than using correlations depending on the Reynolds number for buoyancy problems (Incropera and Dewitt, 1996). The Grashof number is a dimensionless number that represents the ratio of the buoyancy to viscous force acting on a fluid, and is defined from Incropera and Dewitt (1996), as:

$$Gr = \frac{g\beta(T_s - T)D^3}{\nu^2} \quad (3.13)$$

Where β is the coefficient of thermal expansion ($\sim 1/T$ for ideal gases), D is the equivalent diameter (approximated as $4/\sigma_s$), and ν is the kinematic viscosity. The convective heat transfer coefficient becomes:

$$h_{conv} = \frac{K}{D} C' (Gr Pr)^{n'} \quad (3.14)$$

With $C'=0.119$; $n'=0.3$ (Irvine and Hartnett, 1978). This results in $h_{conv} \leq 13$ W/m²K for moderate $Gr \sim 20$, whereas, using correlations based on the Reynolds number (Irvine and Hartnett, 1978) result in $h_{conv} \geq 50$ W/m²K, even for very low values ($Re \sim 5$). The difference between using correlations based on either Re or Gr are non negligible and have direct effect on the energy balance and consequently on the temperature estimation, the degradation rate, ignition time, and the burning dynamics in this configuration.

During the heating process from the start of the test until ignition heat transfer plays an essential role in the temperature evolution, since neither flaming combustion nor significant chemical degradation occurred (for dry needles). Since

no forced flow was applied ($Q_{conv}^{(s)}$ is small), and if we neglect change in properties due to dehydration, we can assume that the gas and the solid phase are close to thermal equilibrium during the heating phase, before ignition, and compare measured and modelled temperatures. For illustration, Table 3.1 presents the absolute value of the difference between the solid and the gas phase temperature ($|\Delta T|$). One can notice that values of $|\Delta T|$ were not significant on average regarding to the maximum temperature, especially towards the bottom of the fuel bed. The maximum values of $|\Delta T|$ are also show in Table 3.1. Larger values were mainly present on the top of the fuel, which were due to local variations and oscillations from buoyancy.

Table 3.1: Difference between solid and gas phase temperatures

Depth (mm)	$ \Delta T _{avg}$ (°C)	$ \Delta T _{max}$ (°C)
0	27	76.5
5	13.6	52.6
10	8.6	39.9
15	5.7	15
30	1.5	4.3

Figures 3.5 and 3.6 show the numerical predictions and experimental results for the temperature evolution in depth, at different positions in the sample (from the top to the back face). Simulated temperatures display a good agreement with the measured ones in the fuel bed, (Figs. 3.5 and 3.6). Only solid phase temperatures are shown for the sake of clarity. The overall prediction has a 31°C maximum deviation from experimental results. The model captures well the trends observed from the experimental data at 25 kW/m² and at 50 kW/m². There is a 5 to 10 s delay between experimental and numerical ignition times. Even if these ignition times are not exactly the same, we have verified that the heating rates are in agreement, and that the temperatures at ignition are matching the experiments

for both heat fluxes. Therefore, the new model for radiation and convection provided improved results.

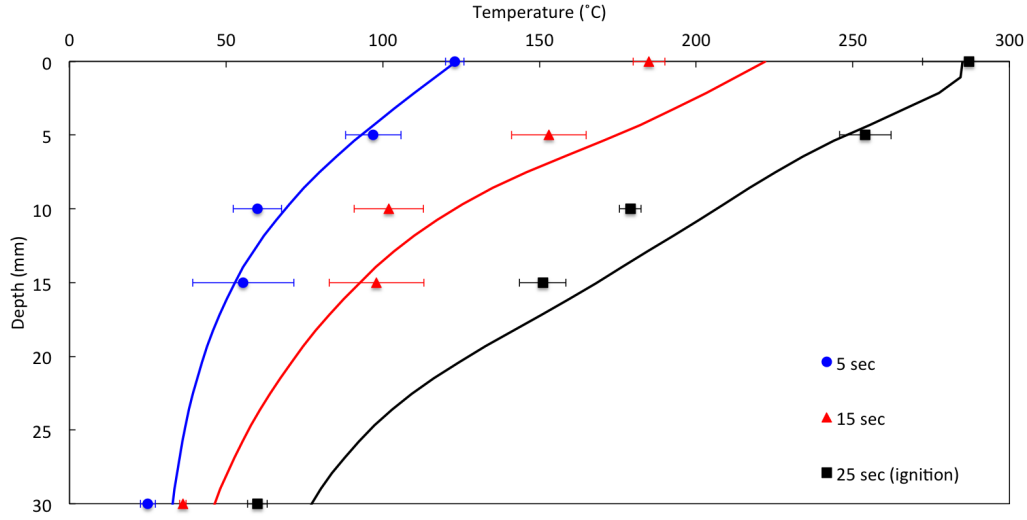


Figure 3.5: Temperature profile before ignition for pitch pine, bulk density of 40 kg/m³, 25 kW/m² applied heat flux, and no flow. Symbols: Experiments, lines: Simulation

Forced flow

When the FPA is configured to provide an inlet flow through the combustion chamber and through the porous sample (i.e. Chapter 2), the heat transfer coefficient h_{conv} can be estimated by using Hilpert correlation (Incropera and Dewitt, 1996) for low Reynolds numbers:

$$h_{conv} = \frac{K}{D} Nu = \frac{K}{D} C Re^m Pr^n \quad (3.15)$$

Despite the complex vegetative structure, a simple correlation based on the Nusselt number such as Eq. 3.15 is appropriate to represent the convective term, as long as the coefficient C, m and n are adapted (Lamorlette et al., 2012). These

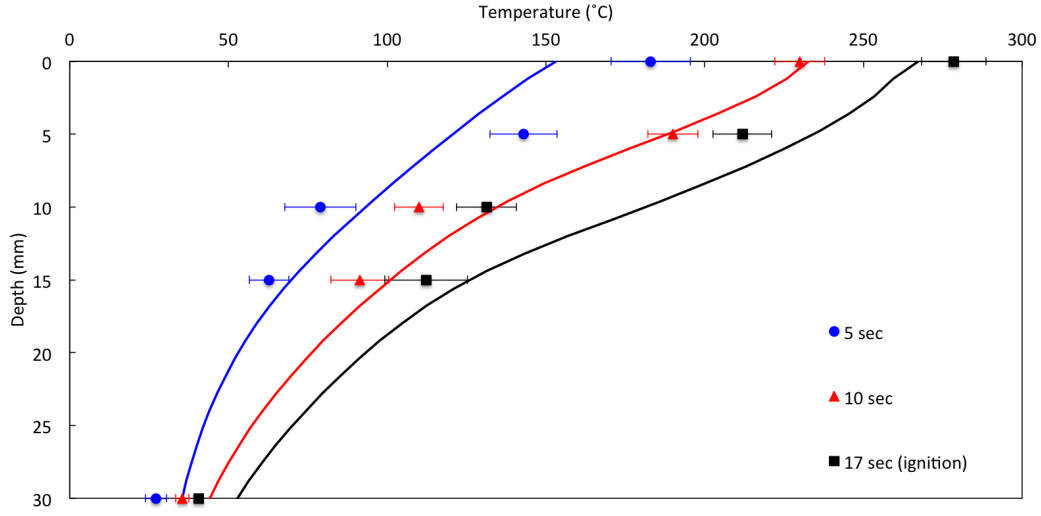


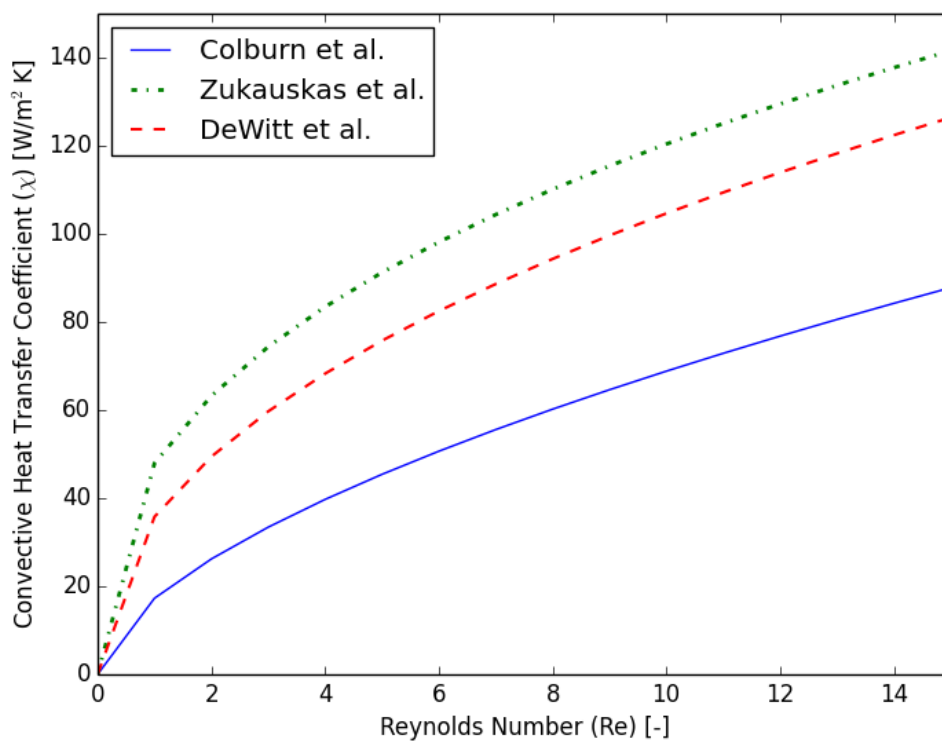
Figure 3.6: Temperature profile before ignition for pitch pine, bulk density of 40 kg/m³, 50 kW/m² applied heat flux, and no flow. Symbols: Experiments, lines: Simulation

values correspond to a convective heat transfer coefficient reduced by the packing effect. Since samples are prepared by stacking pine needles over each other, one can assume that the heat transfer coefficient is similar to the one for array of staggered cylinders in a cross flow. Many correlations are given to represent the Nusselt (Nu) number in these specific conditions or similar ones (Khan et al., 2006). Colburn et al. (Incropera and Dewitt, 1996), Zukauskas (Irvine and Hartnett, 1978), and DeWitt et al. (Incropera and Dewitt, 1996) proposed values for C and m for flow across an isolated cylinder, and across banks of staggered cylinder tubes for 10 or more rows of tubes, and for different Reynolds regimes. All the cited correlations are widely applied in studies that use the multiphase approach (Mell et al., 2009; Morvan et al., 2009; Consalvi et al., 2011). The main correlations are tested in this setup and are listed in Table 3.2 and shown in Fig. 3.7 for typical values of $K = 0.262 \text{ W/(m.K)}$ and $D = 4/\sigma_s^{(pitch)} = 0.0005 \text{ m}$.

The difference between the three correlations presented in Fig. 3.7 is non

Table 3.2: Convective heat transfer coefficients

Correlation	C	m	n
Colburn et al. (Incropera and Dewitt, 1996)	0.33	0.6	1/3
DeWitt et al. (Incropera and Dewitt, 1996)	0.683	0.466	1/3
Zukauskas (Irvine and Hartnett, 1978)	1.04	0.4	0.36

**Figure 3.7:** Convective heat transfer coefficient estimation for forced flow

negligible. Coefficients proposed by Colburn et al. give the lowest heat transfer coefficient values and allow matching better the results. In contrast, the two other models result in very low temperatures, leading to low degradation rates in the solid phase. Figure 3.8 shows the solid phase temperature evolution at the top, middle and backface using Colburn et al. (Incropera and Dewitt, 1996) and Zukauskas coefficients.

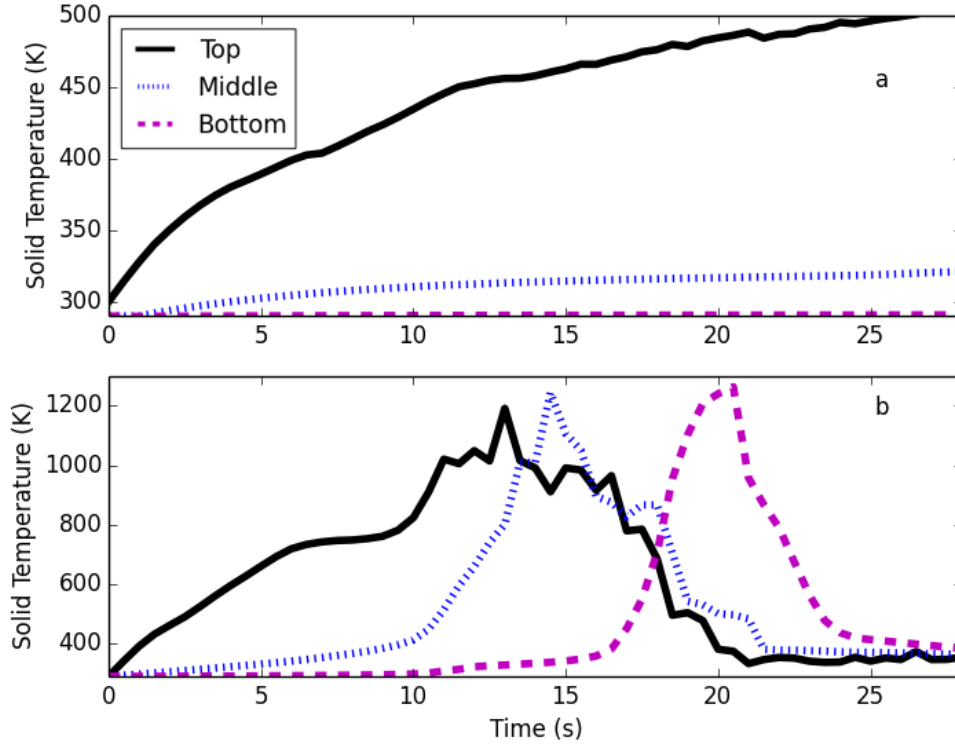


Figure 3.8: Calculated temperature evolution using a) Colburn et al.; b) Zukauskas; based model for convective heat transfer coefficient estimation, for Pitch pine with a bulk density of 40 kg/m^3 , 50 kW/m^2 , and a high flow (HF).

For a High Flow (HF) inlet, the measured flow inside the fuel bed is approximately 0.2 m/s , corresponding to $\text{Re} = 7$. The cited correlations all give convective coefficients $h_{conv} > 40 \text{ W/m}^2\text{K}$. However, this value is high and competes with the radiative heat transfer preventing the solid temperature from rising, degradation to occur, and ultimately ignition to happen. Moreover, these correlations were initially reported for moderate flow temperatures (Irvine and Hartnett, 1978) and were not verified at high temperatures. The coefficients from Colburn et al. corresponded to $h_{conv} \leq 20 \text{ W/m}^2\text{K}$, providing a more moderate convective rate. We can justify that these coefficients are more adapted to account for the sheltering effect produced when elements are close together and act as a bulk

quantity. However, the two other correlations result in a high convective heat loss leading to low temperatures and low degradation rates. The reason why the other correlations work in the cited studies is probably because the energy balance is compensated by an overestimation of the radiative heat transfer through the overestimation of the effective absorptivity of the fuel, for instance. In this study, the radiative heat transfer was specifically examined and quantified (El Houssami et al., 2016b). Using correlations such as Colburn resulted in h_{conv} in the order of 20 W/m²K. This value is relatively low, but it was demonstrated that the packing of needles generally causes the heat transfer coefficient to decrease (Lamorlette et al., 2012).

3.2 Pine Needle Degradation

Under exposure to the intense heat flux coming from the FPA heaters and from the flaming zone, the decomposition of the fuel can be summarised in three steps: evaporation, pyrolysis, and charring.

3.2.1 Evaporation Process

The evaporation rate can be represented using a one-step first-order Arrhenius kinetics law with pre-exponential ($K_{vap} = 6.05 \times 10^5 \text{ K}^{1/2} \cdot \text{s}^{-1}$) and activation energy ($E_{vap}/R = 5956 \text{ K}$) are evaluated for pine foliage and established in Grishin (1981a,b).

$$\dot{\omega}_{vap}''' = \alpha_s \varphi_{H_2O}^{(s)} T_s^{-1/2} K_{vap} \exp \left(\frac{-E_{vap}}{RT_s} \right) \quad (3.16)$$

The sensitivity of this model is more apparent when running simulations with higher initial Fuel Moisture Content (FMC) ($\geq 10\%$). The FMC in dead pine

needles can go up to 30 % when unconditioned (Jolly et al., 2012). Hence, a related analysis on the effect of FMC is presented in Appendix D.

3.2.2 Pyrolysis Process

Pyrolysis gases were analysed using a Fourier Transform Infra-Red (FTIR) device in air and a sampling location above the combustion chamber in the FPA, at low heat flux (10 kW/m²). A such low heat flux was used to avoid ignition and to capture pyrolysis gases only. Pyrolysis gas products are mainly composed of CO, CO₂, CH₄, and of lower amounts of C₂, and C₄ hydrocarbons (Table 3.3). These results are comparable to results for *Pinus halepensis*, *Pinus larcio* and *Erica arborea* with gas chromatography in Tihay et al. (2009b). However, no C₃ hydrocarbons were found in this analysis and H₂O measurement has been excluded due to the FTIR limitations (Smith, 2011).

Table 3.3: Mass fractions of pyrolysis products released from pitch pine needles before ignition

Gas products	Mass fraction
CO	0.199
CO ₂	0.687
CH ₄	0.026
C ₂ H _x	0.027
C ₄ H _y	0.061

The pyrolysis rate ($\dot{\omega}_{pyr}'''$) can be represented using a single-step first order Arrhenius kinetic law, (Grishin, 1996; Di Blasi et al., 2001; Morvan and Larini, 2001) defined as:

$$\dot{\omega}_{pyr}''' = \alpha_s \varphi_{dry}^{(s)} K_{pyr} \exp\left(\frac{-E_{pyr}}{RT_s}\right) \quad (3.17)$$

With $K_{pyr} = 3.64 \times 10^3 \text{ s}^{-1}$ and $E_{pyr}/R = 7,250 \text{ K}$, representing the pre-exponential (frequency) factor and the activation energy, respectively measured for pine foliage (Grishin, 1996; Porterie et al., 2000; Morvan and Larini, 2001; Consalvi et al., 2011).

Pyrolysis rate can also be extended to a two-step equation (Eq. 3.18) bounding the 1st model (Eq. 3.17) by the energy balance exchanged by convection and radiation with the gaseous phase once high temperatures are reached in the solid phase. A similar approach is used in Morvan and Dupuy (2004); Mell et al. (2009).

$$\dot{\omega}_{pyr}''' = \begin{cases} \alpha_s \varphi_{DRY}^{(s)} K_{pyr} e^{\left(\frac{-E_{pyr}}{RT_s}\right)} & T_s \leq 800 \text{ K} \\ \frac{\dot{q}_{net}^{(s)}}{\Delta h_{pyr}} & T_s > 800 \text{ K} \end{cases} \quad (3.18)$$

The transition to the 2nd step limits the reaction, which does not only depend on the kinetics anymore, but on the flux received. One of the main problems using only a 1st order Arrhenius correlation is that the kinetics are not the only involved phenomena, as in Thermogravimetric Analysis (TGA) environment (by design). In fact, the initiation step of preheating is strongly related to the geometrical properties of the samples (thickness, size of leaves and branches) (Cancellieri et al., 2014). Moreover, it is not detailed enough to represent the degradation chemistry accurately. The limiting temperature of 800 K was fitted manually in order to best match experimental data for both pine species and for different heat fluxes and different bulk densities. Usually the transition occurs during the flaming regime (at 800 K).

3.2.3 Charring Process

The exothermic process of pyrolysis is responsible for the formation of char in the solid phase. Generally, char formation is principally due to cellulose and lignin degradation in vegetative fuel (Orfão et al., 1999). The mass balance of char production is described by the following ordinary differential equation (as in Section 2.2) (Grishin, 1996; Morvan et al., 2009):

$$\frac{d\alpha_s \varphi_{char}^{(s)}}{dt} = \gamma_{char} \dot{\omega}_{pyr}''' - \left(\frac{\gamma_{ash}}{\gamma_{char}} + 1 \right) \dot{\omega}_{char}''' \quad (3.19)$$

This means that the char fraction increases once the pyrolysis reaction is activated then is consumed by char oxidation.

In Chapter 4, the complete simulations are presented and compared to the experiments conducted in the FPA. All the above-mentioned degradation models performance is investigated. This includes the time at which the different degradation reactions occur they overlap and how they influence the total mass loss.

3.3 Reactive Flow Modelling

3.3.1 Flow and turbulence

Turbulence in the sub-grid scale is modelled by the one-equation viscosity concept (Schumann, 1975; Shaw and Patton, 2003), which is one of the most frequently used turbulence model in FireFOAM for simulating fire plumes at laboratory scale (Wang et al., 2011; Chatterjee et al., 2012; Ebrahim Zadeh et al., 2016).

The turbulent kinetic energy k , is solved by the transport equation:

$$\frac{\partial \bar{\rho}k}{\partial t} + \nabla(\bar{\rho}\tilde{u}k) = \nabla \left[\left(\mu + \frac{\mu_t}{S_{ct}} \right) \nabla k \right] + P - \bar{\rho}\epsilon - \bar{\rho}C_D \frac{\alpha_s \sigma_s}{2} |U| K \quad (3.20)$$

With an additional sink term representing the contribution of the drag force, with C_D the drag force coefficient (examined later) induced by the solid phase to the turbulent kinetic energy budget, as in [Morvan et al. \(2009\)](#). The production rate P , is calculated as:

$$P = -\frac{2}{3} \left(\bar{\rho}k + \frac{\partial \tilde{u}_k}{\partial x_k} \right) \frac{\partial \tilde{u}_i}{\partial x_i} + 2\mu \frac{\partial \tilde{u}_i}{\partial x_j} \frac{\partial \tilde{u}_j}{\partial x_j} \quad (3.21)$$

and with ϵ the dissipation rate, defined as:

$$\epsilon = C_\epsilon k^{3/2} \Delta^{-1} \quad (3.22)$$

and μ_t , the turbulent viscosity:

$$\mu_t = \bar{\rho}c_k \Delta k^{1/2} \quad (3.23)$$

$\Delta = (\Delta x \Delta y \Delta z)^{1/3}$ represents the sub-grid filter size, and $c_k=0.07$ ([Fureby et al., 1997](#); [Fureby and Tabor, 1997](#)). As the grid is very refined in this study, small turbulent scales comparable to Kolmogorov length scale are resolved, and the influence of the Sub-Grid Scale (SGS) terms is reduced. For instance, for a flow of 1 m/s, a characteristic length of 0.12 m (sample diameter), and a kinematic viscosity of air $1.5 \cdot 10^{-5} \text{m}^2/\text{s}$, the Kolmogorov length scale is in the order of 0.14 mm, which is comparable to the cell size. In [Ren et al.](#), it was demonstrated that the one-equation turbulence model provides high production rate of the subgrid scale turbulent kinetic energy in near-wall regions and that a Wall Adapting Local Eddy (WALE) viscosity model ([Nicoud and Ducros, 1999](#)) can be more adapted ([Ren et al., 2016](#)). However, this issue is negligible in our configuration due

to the small grid size and because the flame region is mostly laminar and not close to a wall condition. As the flow conditions used in this study are relatively low compared to the mean velocities that can be found in wildfires (Fons, 1946; Morvan, 2011), it is important to assess the model's performance under these specific conditions, which could also be found locally during a fire. Following this framework, other flow regimes and more moderate flows could be studied

For a number of tests in the FPA, an airflow was introduced at the inlet below the sample and passed through and around the porous sample. Therefore, it is important to verify if the flow is well represented in the simulation. For illustration, the velocity field and the vectors are presented in Fig. 3.9, showing the flow inside and around the fuel sample using a pseudofluid model that will be introduced later in this section.

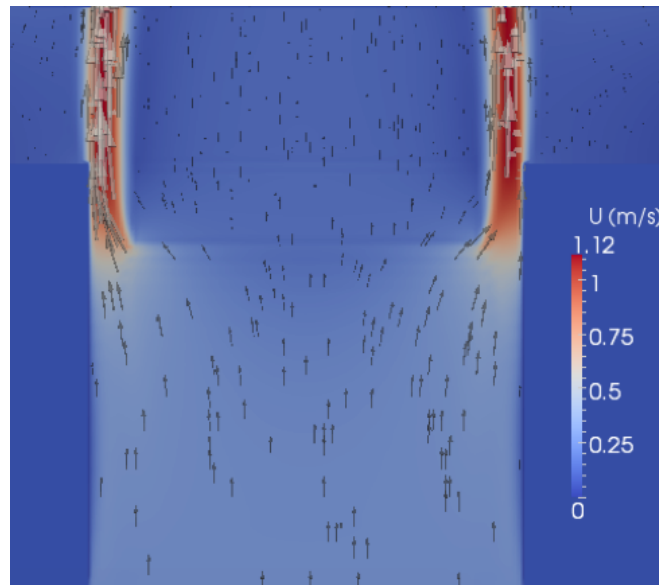


Figure 3.9: Flow field velocity and vectors inside and around the fuel sample (HF - 40 kg/m^3)

The drag forces per unit volume acting on the solid-phase particles are often calculated in studies using the multiphase model (Porterie et al., 2000, 2005; Mell

et al., 2009) from the correlation proposed by Clift et al. (1978) for spheres.

$$C_D = \frac{24(1 + 0.15Re^{0.687})}{Re} \times \frac{3}{8} \quad 1 < Re < 1000 \quad (3.24)$$

We noticed that using this correlation results in predicting high velocity flows penetrating the sample compared to the measurements. This behaviour is shown in Fig. 3.10, where the measured and simulated air velocity around and on top of the fuel sample are presented.

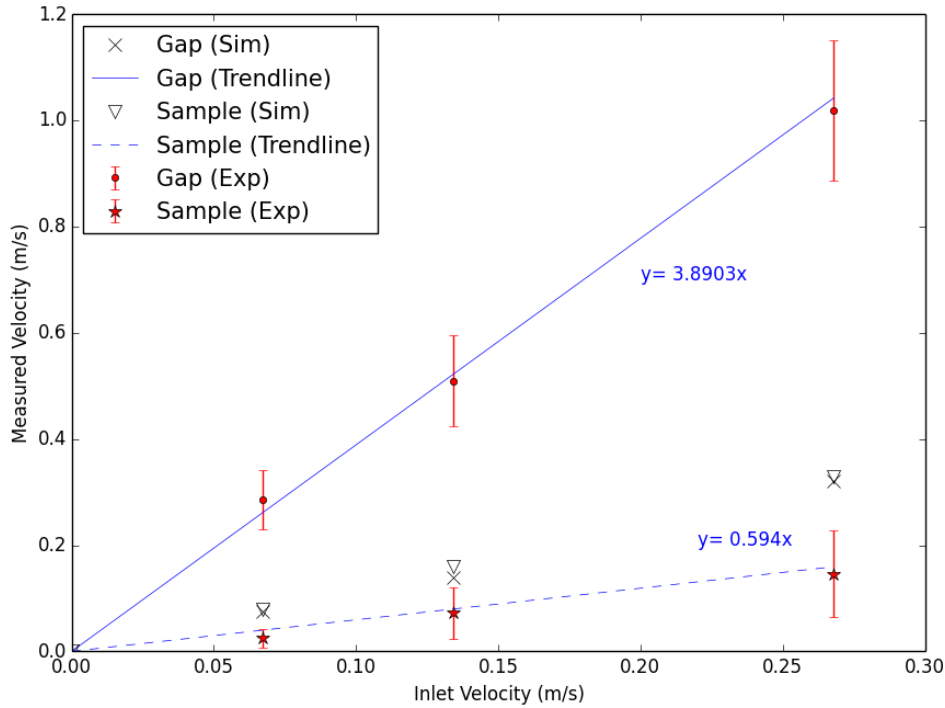


Figure 3.10: Measured and simulated air velocity on the peripheral free space (gap) and on top of the fuel (sample) in the FPA for 40 kg/m³; using drag force estimation for spheres

To more closely represent the cylindrical geometry of the pine needles, the drag coefficient (C_D) was approximated using a pseudo fluid model for arrays of

emerging circular cylinders (Cheng, 2013):

$$C_D = 11Re^{-0.75} + 0.9 \left[1 - \exp\left(\frac{-1000}{Re}\right) \right] + 1.2 \left[1 - \exp\left(\frac{-Re}{4500}\right) \right] \quad (3.25)$$

The use of a correlation for arrays of cylinders is justified by the sheltering effect that diminishes the drag downstream of an element (Raupach, 1992). As element spacing decreases, the bulk drag coefficient decreases (Nepf et al., 1997). Hence, correlations established for isolated elements are no longer effective because of this strong sheltering effect. The outcome of the aforementioned submodels (Eq. 3.24 and 3.25) are presented in Fig. 3.11.

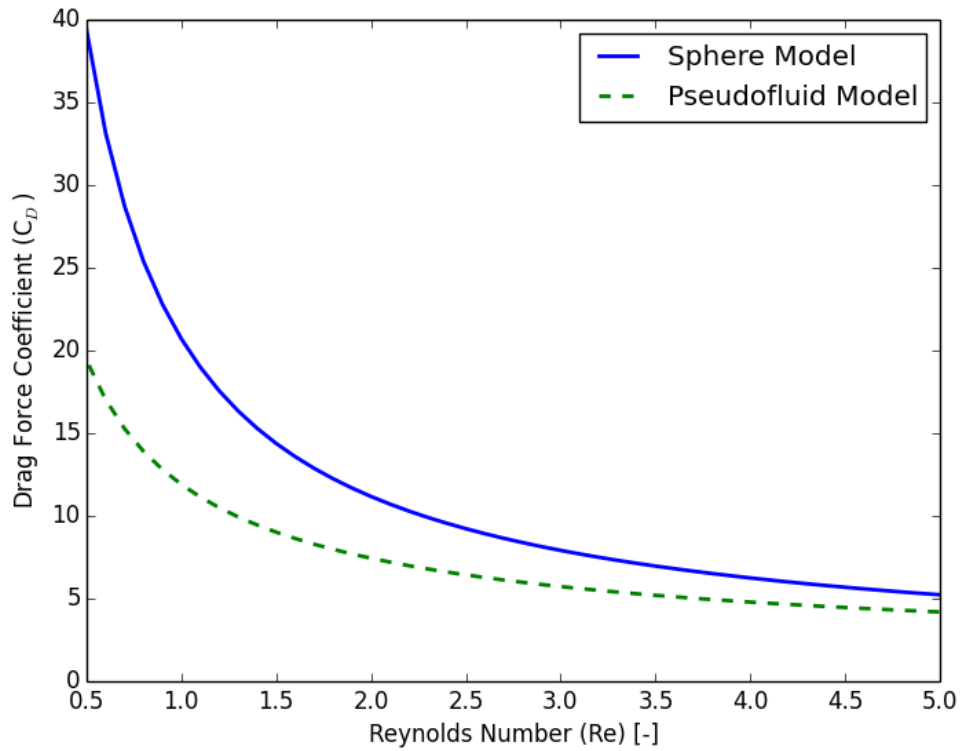


Figure 3.11: Drag force coefficient estimation using different submodels

For $Re > 4$, both submodels provide similar estimations, but for lower Reynolds

numbers ($Re < 4$), corresponding to flows lower than 13.14 cm/s (or $HF/2$), the value of C_D is higher using [Clift et al. \(1978\)](#) model for a sphere. However, flow velocity fields were successfully simulated using the pseudofluid model at both Low Flow (LF) and at High Flow, matching the measured velocities on top and around the sample for tests without combustion for a sample with bulk densities of 23 kg/m³ and 40 kg/m³ shown in Figs. 3.12 and 3.13, respectively.

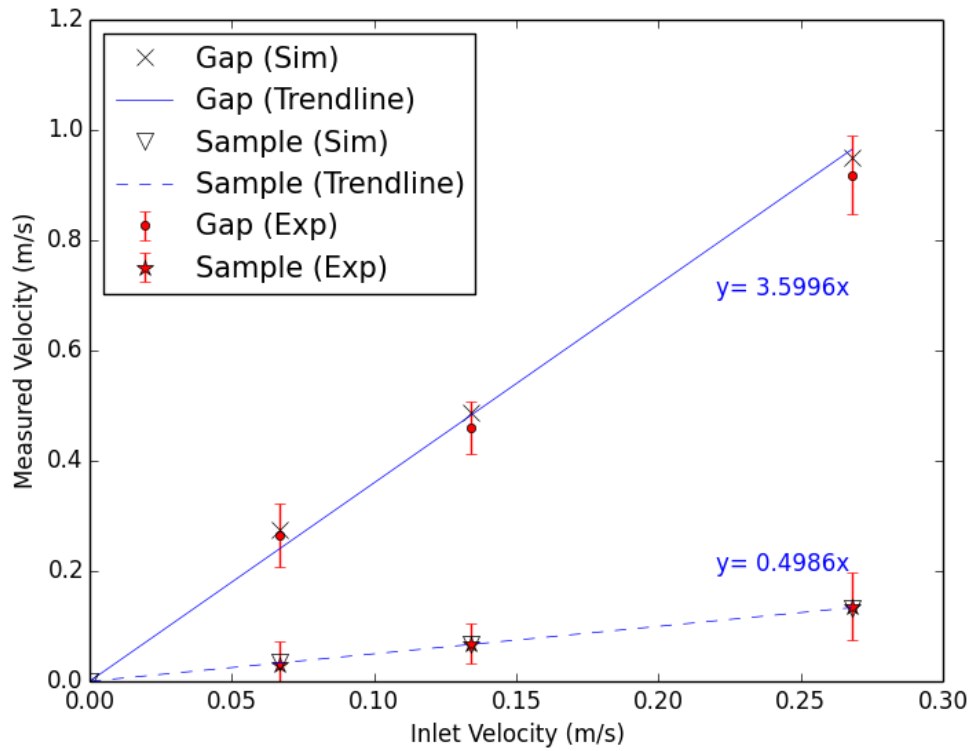


Figure 3.12: Measured and simulated air velocity on the peripheral free space (gap) and on top of the fuel (sample) in the FPA for 23 kg/m³; using pseudofluid model

An overestimation of the drag force leads to an underestimation of the flow in the fuel bed, which affect the burning dynamics through the cooling, air mixing, combustion rate and char oxidation rate, among others. When modeling large scale forest fires, these correlations are usually applied to estimate the mean drag

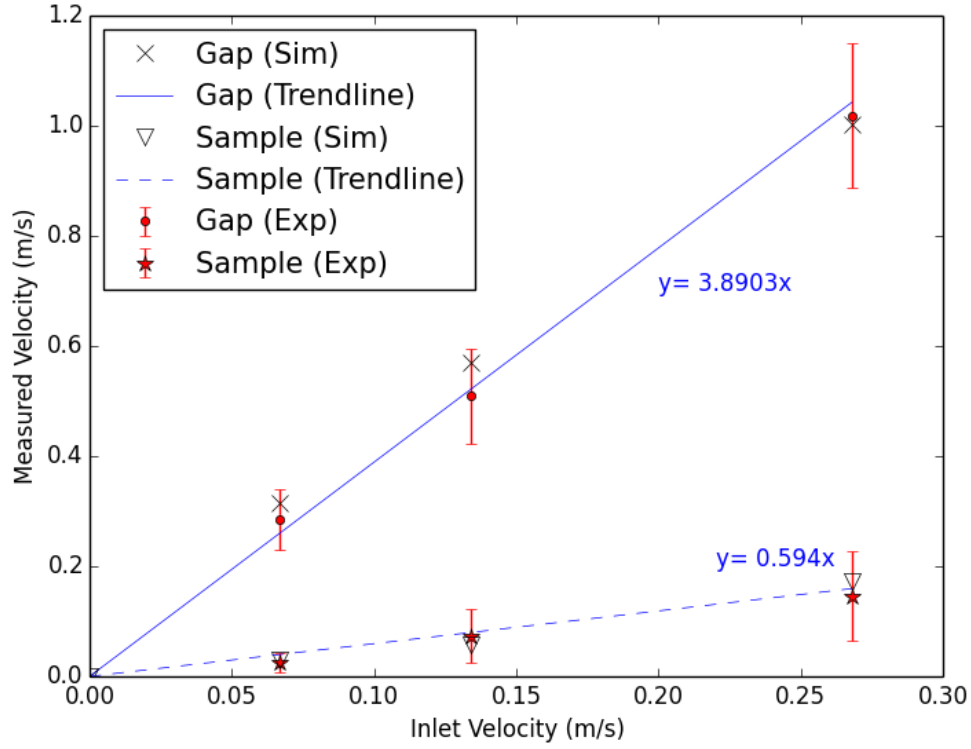


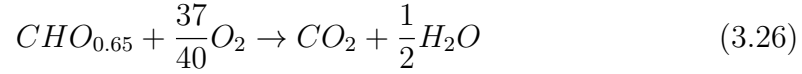
Figure 3.13: Measured and simulated air velocity on the peripheral free space (gap) and on top of the fuel (sample) in the FPA for 40 kg/m^3 ; using pseudofluid model

force generated from both wind/litter and wind/trees interactions in a control volume larger than $1\text{m} \times 1\text{m}$ (Linn et al., 2002; Morvan, 2011). By doing so, variations in the litter and the flow and consequently, the fire behaviour is misrepresented. Hence, vegetation elements producing different drag coefficients have to be separated.

3.3.2 Flaming Combustion

It is assumed that the combustible part of the pyrolysis products can be approximated by mixture of 65 % of CO and 35 % of partially oxidized hydrocarbons

(CHO_x) that includes CH_4 , C_2H_x and C_4H_y . Using the same approach as in [Morvan \(2015\)](#), the combustion of the pyrolysis products in the gas phase can be written as follows using a single step reaction:



This approximation is more realistic than using the oxidation of CO only, as the heat of combustion of $\text{CHO}_{0.65}$ is closer to the heat of combustion of pyrolysis products. Using detailed combustion models (global and skeletal mechanisms) can also achieve better approximation for the flame temperatures ([Tihay et al., 2009c](#)). However, its implementation in OpenFOAM is not trivial and it greatly increases computational time. Moreover, this study focuses more on the solid phase evolution.

The specific heat of the fuel in the gas phase (C_p) is calculated by OpenFOAM libraries from a set of coefficients taken from JANAF interpolation tables of thermodynamics ([Stull and Prophet, 1971](#)). Two sets of 5 coefficients (a_i) are specified, the first set is for temperatures (T_L) between 200 and 1,000 K, and the second for temperatures (T_H) between 1,000 and 6,000 K. The function relating c_p to temperature is:

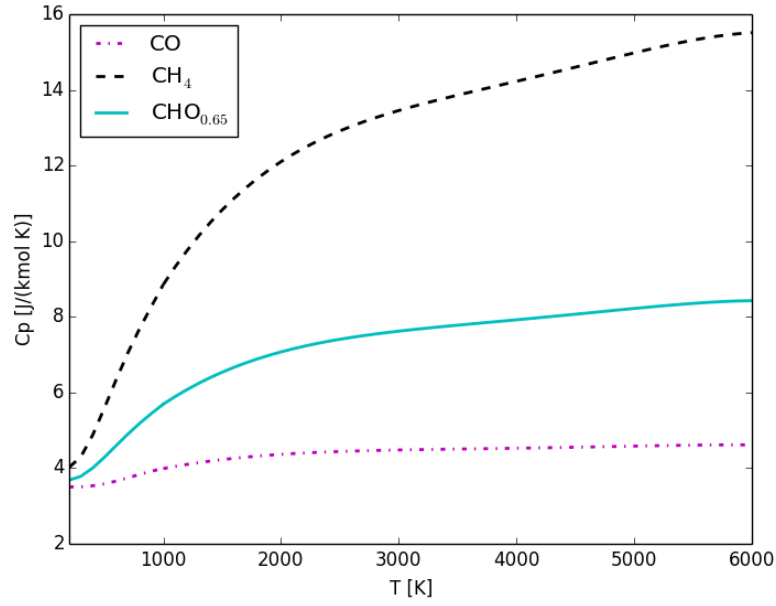
$$C_p = R((((a_4T + a_3)T + a_2)T + a_1)T + a_0) \quad (3.27)$$

With the a_i coefficients found for $\text{CHO}_{0.65}$ listed in [Table 3.4](#), and values of c_p are shown in [Fig. 3.14](#).

Instead of using an Eddy Dissipation Concept ([EDC](#)) for turbulent combustion ([Magnussen and Hjertager, 1977](#)), an extension of the same model is applied, where the characteristic time scale of fuel-air mixing is different under turbulent and laminar flow conditions ([Ren et al., 2016](#)). This combustion model was used

Table 3.4: JANAF coefficients for $\text{CHO}_{0.65}$

	\mathbf{a}_0	\mathbf{a}_1	\mathbf{a}_2	\mathbf{a}_3	\mathbf{a}_4
\mathbf{T}_L	4.13E+00	-5.18E-03	1.79E-05	-1.64E-08	5.25E-12
\mathbf{T}_H	2.55E+00	4.41E-03	-1.50E-06	2.38E-10	-1.41E-14

**Figure 3.14:** Computed specific heat for CO , CH_4 and $\text{CHO}_{0.65}$ using JANAF tables

in a study that focused on fully-developed turbulent region of a wall flame where the diffusion time used for the laminar flow was a placeholder for the near wall region and was not verified. It is recognised that the validity of the modified EDC model for laminar flame studies still needs to be established, but this one was used in the absence of a better and simple model for laminar flames in Large Eddy Simulation (LES). The rate of combustion in the gas phase is expressed as:

$$\bar{\omega}_F''' = \min \left(\frac{\bar{\rho}}{\min \left(\frac{k_{SGS}}{C_{EDC} \epsilon_{SGS}}, \frac{\Delta^2}{C_{DIFF} a_D} \right)}, \min \left(\tilde{Y}_F, \frac{\tilde{Y}_{O_2}}{s} \right) \right) \quad (3.28)$$

\tilde{Y}_F and \tilde{Y}_{O_2} are the fuel and oxygen mass fraction, respectively; a_D is the thermal diffusivity; $C_{EDC} = 4$ and $C_{DIFF} = 10$. The ratio $\frac{k_{SGS}}{\epsilon_{SGS}}$ is the turbulent time scale and the ratio $\frac{\Delta^2}{a_D}$ is the molecular diffusion time scale. The pilot flame was not simulated because in this model, flaming combustion always occurs when the fuel and the oxidizer are mixed, regardless of the available amount of energy required to activate the combustion. In this study, time to ignition is overlooked, since it is known that it depends on the distance between the pilot flame and the sample, on the energy available, and on the flammability of the gases (Fernandez-Pello, 2011). To allow the sample to heat up without having very early local ignitions, and to allow the pyrolysis gases to accumulate before igniting, a Lower Flammability Limit (LFL) (Drysdale, 2011) condition was implemented, considering the lowest flammability limit between CO and CH₄ (representing all CHO hydrocarbons) at 600 K. Since the value of the LFL can decrease with temperature, we assumed that 600 K is in the same order of magnitude of typically measured ignition temperatures (Babrauskas, 2003). This condition also allows obtaining ignition times similar (± 5 s) than the ones found experimentally (Thomas et al., 2013), but ignition time analysis is beyond the scope of this study.

3.3.3 Smouldering Combustion

Char oxidation represents an important source of heat release during smouldering. Hence, it is considered that any material that forms char during its thermal decomposition can potentially sustain a smouldering process (Ohlemiller, 2002). This heterogeneous oxidation is incomplete and emits a higher yield of CO than the gas-phase combustion (Rein et al., 2009). It is represented by the following equation:



Smouldering is a more complex reaction where some oxidation occurs in the gas phase as well. The fraction of energy produced by the char combustion is equally split between the gas and the solid phase ($\alpha_{sg} = 0.5$). This assumption is widely used in different studies (Grishin, 1996; Larini et al., 1998; Mell et al., 2009; Morvan et al., 2009; Consalvi et al., 2011) but has never been validated experimentally. Other parameters in the energy equation (i.e. section 2.4) are sensitive to this value. For instance, if the fraction is higher for the solid phase than for the gas phase, then more energy is retained in the solid phase (increasing T_s), and less energy is released to the gas phase (reducing T). As a consequence, $Q_{conv}^{(s)}$ (Eq. 3.11) is expected to increase, whereas $Q_{rad}^{(s)}$ (Eq. 3.3) should decrease. However, it is very difficult to quantify experimentally the heat flux from the solid alone (excluding gas radiation), and to separate the radiative and the convective heat flux. This is why the assumption that the fraction of energy is equally split between the gas and solid phase was not changed in this study. Instead of using 3-step (Ohlemiller, 2002) or 5-step (Rein, 2005) models to represent smouldering kinetics, it can be simplified to the following single step Arrhenius equation:

$$\dot{\omega}_{char}''' = \frac{\alpha_s \sigma_s}{\gamma_{O_2}} \alpha_g \rho Y_{O_2} K_{char} \exp\left(-\frac{E_{char}}{RT_s}\right) \quad (3.30)$$

where E_{char} is the activation energy of char oxidation and K_{char} is the pre-exponential coefficient, all derived from TGA analysis (Grishin, 1996; Porterie et al., 2000; Morvan and Larini, 2001). This model can underestimate the char oxidation rate ($\dot{\omega}_{char}'''$) when no forced flow is imposed, due to the low mass flux of oxygen induced by buoyancy (in the combustion chamber). Consequently, the char oxidation could not be sustained after flameout, despite the constant lamp radiation. However, additional corrective term can be introduced, depending on the Reynolds number to force the reaction in no flow condition, such as it was introduced

in [Porterie et al. \(2005\)](#) using the multiphase approach:

$$\dot{\omega}_{char}''' = \frac{\alpha_s \sigma_s}{\gamma_{O_2}} \alpha_g \rho Y_{O_2} K_{char} \exp\left(-\frac{E_{char}}{RT_s}\right) \left(1 + \beta_{char} \sqrt{Re}\right) \quad (3.31)$$

Where β_{char} is a constant as suggested by [Porterie et al. \(2005\)](#). Char oxidation represents an important source of heat released during smouldering. Hence, it is considered that any material that forms char during its thermal decomposition can potentially sustain a smouldering process ([Ohlemiller, 2002](#)). By implementing the model of [Evans and Emmons \(1977\)](#) into the ForestFireFOAM, the contribution of char combustion to the energy equation of the solid phase becomes:

$$Q_{char}^{(s)} = \alpha_{sg} [(2\phi - 1)\Delta h_{CO_2} + 2(1 - \phi)\Delta h_{CO}] \dot{\omega}_{char}''' \quad (3.32)$$

This formulation includes the heat of combustion from CO and from CO₂, with ϕ being the split function, defined as:

$$\phi = \frac{2 + CO/CO_2}{2CO/CO_2 + 2} \quad (3.33)$$

and

$$\frac{CO}{CO_2} = 2500 \exp(-6240/T_s) \quad (3.34)$$

The split function (ϕ) allows the prediction of the ratio of CO and CO₂ concentrations produced during smouldering, as a function of the solid phase temperature, as used by [Mendes et al. \(2008\)](#). For temperatures higher than 800K which are typical flaming temperatures, the ratio CO/CO₂ becomes greater than unity, resulting in:

$$\phi \rightarrow 1 \quad Q_{char}^{(s)} = \alpha_{sg} \Delta h_{CO_2} \dot{\omega}_{char}''' \quad (3.35)$$

For temperature below 800K which are obtain after flameout the ratio CO/CO₂ is smaller than unity, leading to:

$$\phi \rightarrow 1/2 \quad Q_{char}^{(s)} = \alpha_{sg} \Delta h_{CO} \dot{\omega}_{char}''' \quad (3.36)$$

The former case allows more CO₂ to be produced, whereas the latter allows more CO to be produced. The insertion of such model can improve the estimation of CO generation during smouldering, as it was observed in similar experiments (Schemel et al., 2008).

The gas phase combustion submodel (EDC) representing flaming combustion, oxidises all fuel in the gas phase, even those produced by smouldering combustion. In reality not all the fuel in the gas phase is oxidized, especially the products originated from smouldering, which are mostly due to their low temperature. To separate between the two types of fuel in the gas phase (the one from pyrolysis products and the one from char combustion), the fuel originated from smouldering product is considered as an "inert" CO phase that does not react with oxygen.

After defining all the submodels used to represent thermal degradation of the solid phase, the transport equation for the chemical species in the gas phase can be written as follows:

$$\begin{aligned} \frac{\partial (\bar{\rho} \tilde{\varphi}_{O_2})}{\partial t} + \frac{\partial (\bar{\rho} \tilde{u}_j \tilde{\varphi}_{O_2})}{\partial x_j} - \frac{\partial}{\partial x_j} \left(\bar{\rho} \left(D_{O_2} + \frac{\nu_t}{Pr} \right) \frac{\partial \tilde{\varphi}_{O_2}}{\partial x_j} \right) \\ = R - \frac{8}{3} \phi \dot{\omega}_{char}''' \end{aligned} \quad (3.37)$$

$$\begin{aligned}
& \frac{\partial (\bar{\rho} \tilde{\varphi}_{H_2O})}{\partial t} + \frac{\partial (\bar{\rho} \tilde{u}_j \tilde{\varphi}_{H_2O})}{\partial x_j} - \frac{\partial}{\partial x_j} \left(\bar{\rho} \left(D_{H_2O} + \frac{\nu_t}{Pr} \right) \frac{\partial \tilde{\varphi}_{H_2O}}{\partial x_j} \right) \\
& = R + \dot{\omega}_{vap}'''
\end{aligned} \tag{3.38}$$

$$\begin{aligned}
& \frac{\partial (\bar{\rho} \tilde{\varphi}_{CO_2})}{\partial t} + \frac{\partial (\bar{\rho} \tilde{u}_j \tilde{\varphi}_{CO_2})}{\partial x_j} - \frac{\partial}{\partial x_j} \left(\bar{\rho} \left(D_{CO_2} + \frac{\nu_t}{Pr} \right) \frac{\partial \tilde{\varphi}_{CO_2}}{\partial x_j} \right) \\
& = R + \left(1 + \frac{8}{3} \right) (2\phi - 1) \dot{\omega}_{char}'''
\end{aligned} \tag{3.39}$$

$$\begin{aligned}
& \frac{\partial (\bar{\rho} \tilde{\varphi}_F)}{\partial t} + \frac{\partial (\bar{\rho} \tilde{u}_j \tilde{\varphi}_F)}{\partial x_j} - \frac{\partial}{\partial x_j} \left(\bar{\rho} \left(D_F + \frac{\nu_t}{Pr} \right) \frac{\partial \tilde{\varphi}_F}{\partial x_j} \right) \\
& = R + (1 - \gamma_{char}) \dot{\omega}_{pyr}'''
\end{aligned} \tag{3.40}$$

$$\begin{aligned}
& \frac{\partial (\bar{\rho} \tilde{\varphi}_{CO})}{\partial t} + \frac{\partial (\bar{\rho} \tilde{u}_j \tilde{\varphi}_{CO})}{\partial x_j} - \frac{\partial}{\partial x_j} \left(\bar{\rho} \left(D_{CO} + \frac{\nu_t}{Pr} \right) \frac{\partial \tilde{\varphi}_{CO}}{\partial x_j} \right) \\
& = R + \left(1 + \left(\frac{1}{2} \right) \frac{11}{3} \right) 2(1 - \phi) \dot{\omega}_{char}'''
\end{aligned} \tag{3.41}$$

$$\begin{aligned}
& \frac{\partial (\bar{\rho} \tilde{\varphi}_{N_2})}{\partial t} + \frac{\partial (\bar{\rho} \tilde{u}_j \tilde{\varphi}_{N_2})}{\partial x_j} - \frac{\partial}{\partial x_j} \left(\bar{\rho} \left(D_{N_2} + \frac{\nu_t}{Pr} \right) \frac{\partial \tilde{\varphi}_{N_2}}{\partial x_j} \right) \\
& = R
\end{aligned} \tag{3.42}$$

Where R is the production/destruction of the chemical species ($\text{CHO}_{0.65}$, CO, O_2 , CO_2 , and H_2O) resulting from the combustion in the gas phase.

Now that the mathematical formulation is completed and that all the chosen

submodels were described, the next chapter will present the simulations of the complete [FPA](#) experiments and their corresponding results.

3.4 Conclusions

All submodels that are needed in ForestFireFOAM were analysed in this chapter to provide an accurate representation of the experiments conducted in the [FPA](#) with pine needle beds. Several experimental and mathematical techniques were necessary to examine the application of each submodel in this context. The main results are:

- Analysing the spectral emissivity of dead pine needles demonstrated that the effective absorptivity of pine needles is lower under the [FPA](#) heaters radiation (~ 0.64) than when submitted to flame radiation (~ 0.92). This analysis allowed a better description of the radiative heat transfer.
- The extinction coefficient was estimated for the specific testing configuration. An additional correction factor (1.15) is required, due to the heterogeneity of the sample that is not considered in the multiphase approach.
- The estimation of the convective heat transfer coefficient needs to be adapted depending on the flow conditions. Different popular models in the multiphase approach were examined. However, it was found that not all of them are appropriate, as they overestimate the heat transfer coefficient. Consequently, the sample heating and the burning dynamics are poorly evaluated. We provided a model that is adequate for natural convection, and a model for forced flow. These models provide temperature estimations of the fuel bed matching the experimental measurements during the heating phase.

- Pyrolysis gases were analysed using a [FTIR](#) to better represent the flammable gases for the gas phase combustion. Measured mass fractions were similar to the ones found for other wildland fuels.
- The drag force resulting from the interaction between the solid and the gas phase has a large influence in the momentum equation and can dramatically change the flow field. Measurements were conducted in the [FPA](#) to quantify the flow velocity on top of the sample and around it. An adapted model was proposed, giving better approximation of the drag force and allowing flow velocities to match the experimental measurements for cold flows.
- An extended [EDC](#) gas phase combustion model was used in this study. It is recognized that the validity of the modified [EDC](#) model for laminar flame studies still needs to be established, but this one was used in the absence of a better and simple model for laminar flames in [LES](#).
- An Arrhenius-type correlation was used for estimating the smouldering combustion rate with a corrective term for low flow, when the rate was underestimated.
- By implementing a split function to the char oxidation rate and an inert CO species that does not oxidise. We propose a model that can generate a fraction of CO and CO₂ depending on whether smouldering combustion is occurring.

Studying the submodels allowed us to ensure that we are properly capturing the physics involved in our [FPA](#) experiments and beyond them, it should increase the model capabilities for accurately simulating wildland fires. Since very fine mesh is used in the computational domain, the influence of the turbulence model was negligible. Therefore, a standard [LES](#) turbulence model was used (the one eddy equation model). However, for tests with coarser meshes we recommend to verify that this submodel is adapted, especially in near wall conditions ([Ren](#)

et al., 2016). Users are also recommended to further investigate the gas phase combustion model, and to verify that the flame geometry and the flame emitted heat flux to a surrounding target are adequately represented. Indeed, it was not the goal of this study, but it will be important for fire spread studies. Now that these submodels were tested individually, the following chapter will present the simulations of the complete FPA experiments.

Chapter 4

Results and Discussions

4.1 Introduction

In this chapter, experimental and numerical results are shown to assess the performance of the submodels presented in the previous chapter. These results include measurements of flaming time, mass loss, heat release rates, and gas emission. They are compared to their corresponding experiments under natural convection for different bulk densities of pitch pine needles. Additionally, tests were conducted on white pine needles to verify that all the submodel behave correctly for a different range of surface to volume ratio. Finally, the results for various forced flows are presented for pitch pine needles.

4.2 Natural Convection

4.2.1 Burning Characteristics

It was shown in Chapter 3 that simulated temperatures (Figs. 3.5 and 3.6) display good agreement with the measured temperatures in the fuel bed before ignition at both 25 kW/m^2 and 50 kW/m^2 . Simulated temperature fields are presented in Fig. 4.1a at the time step before ignition, and in Fig. 4.1b during flaming. The solid phase temperature is shown in the fuel region, whereas the gas phase temperature is shown in the rest of the domain. It can be noticed that the gas temperature under the sample is higher than the ambient temperature. This behaviour was also observed experimentally under the same flow conditions. It is mostly due to the radiation from the fuel and since there is no forced flow injected below, the gas diffusion pushes some gases downward. The temperature field in Figure 4.1b) shows clearly the regression of the solid fuel. Although the sensitivity of the flame model is overlooked in this study, we can confirm that the gas temperature field is comparable to similar experiments conducted with pine needles (Tihay et al., 2009c).

4.2.2 Flaming Time

In the Fire Propagation Apparatus (FPA) experiments, flaming time was measured from the moment flaming ignition occurred until no flames were visually observed. Numerically, it was calculated as the time period during which the gas phase combustion rate was non zero. Flaming times for different bulk densities are presented in Fig. 4.2.

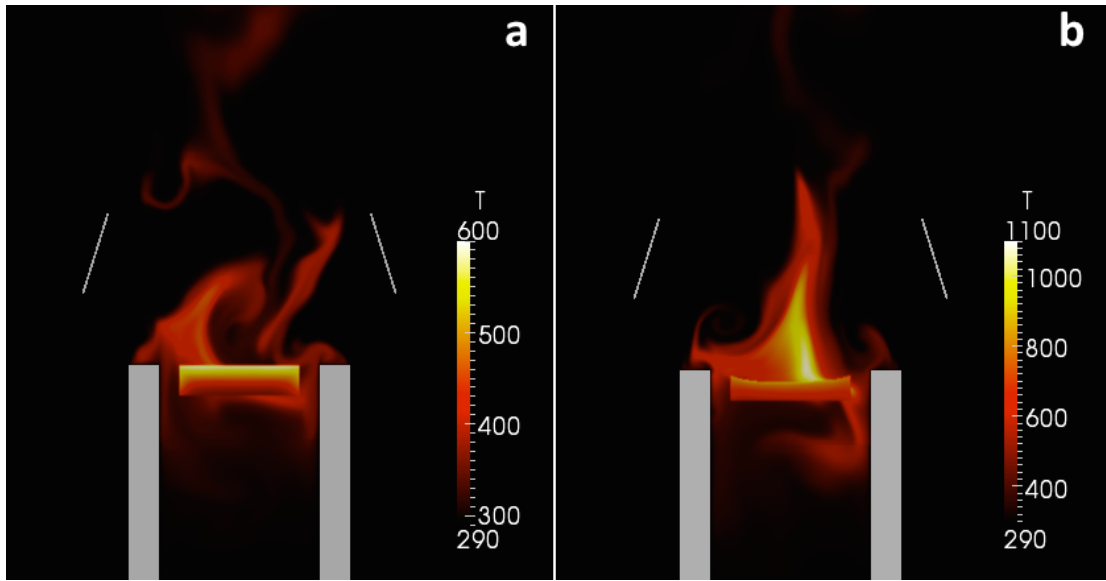


Figure 4.1: Temperature field (in Kelvin) for the gas and solid phases a) just before ignition b) during flaming, for pitch pine with 40 kg/m^3 and 50 kW/m^2

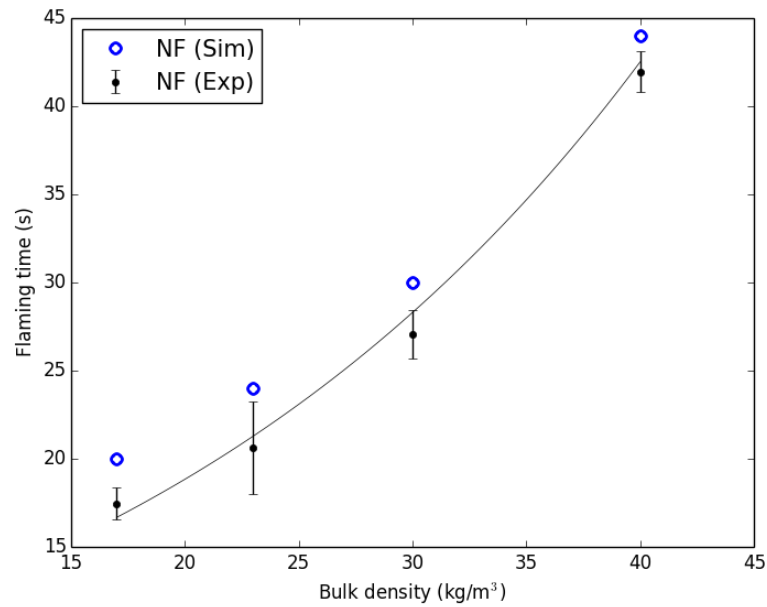


Figure 4.2: Flaming time for different bulk density of pitch pine at 50 kW/m^2 (NF)

Experimental values are averaged over at least three repetitions and error bars correspond to the experimental variability. The mean absolute error is estimated to be ± 1 s. From Fig. 4.2, it can be observed that flaming time increases with the bulk density, since there is more fuel to burn. Similarly, numerical simulations are slightly overpredicting the experimental values (< 5 s), but the overall tendency of increasing times with the bulk density is respected. The relation between flaming time and bulk density is non-linear under natural convection because of the competition between the available fuel affecting the heat transfer on the solid phase and the induced oxygen limiting the combustion rate, especially at high bulk densities.

4.2.3 Mass Loss

One of the main advantages of numerical simulations is the ability of monitoring in detail the evolution of the solid phase, as presented in Fig. 4.3, in which mass loss measurements and simulations are drawn for a bulk density of 40 kg/m^3 and No Flow (NF). The simulated mass loss is split into dry, moisture content, and char fractions. All the curves are shifted by 3 s in order to synchronise the experimental and the simulated ignition times. One can observe that the simulated total mass loss initially agrees with the mean experimental mass loss, despite the slightly steeper simulated curve between 30 and 40 s. However, the simulated curve then slows down and converges to 0.15. Whereas, experimentally, all the mass is consumed (except for 3 % due to ash). This behaviour can be explained by considering the three simulated fractions. All the dry phase and the water content are consumed, but the char fraction produced was not entirely oxidised (0.15 is left), as only half of it was consumed (for $\gamma_{char}=0.3$) .

For better mass loss comparison, the Mass Loss Rate (MLR) are calculated for multiple bulk densities, and are normalised by their initial masses (m_0) in

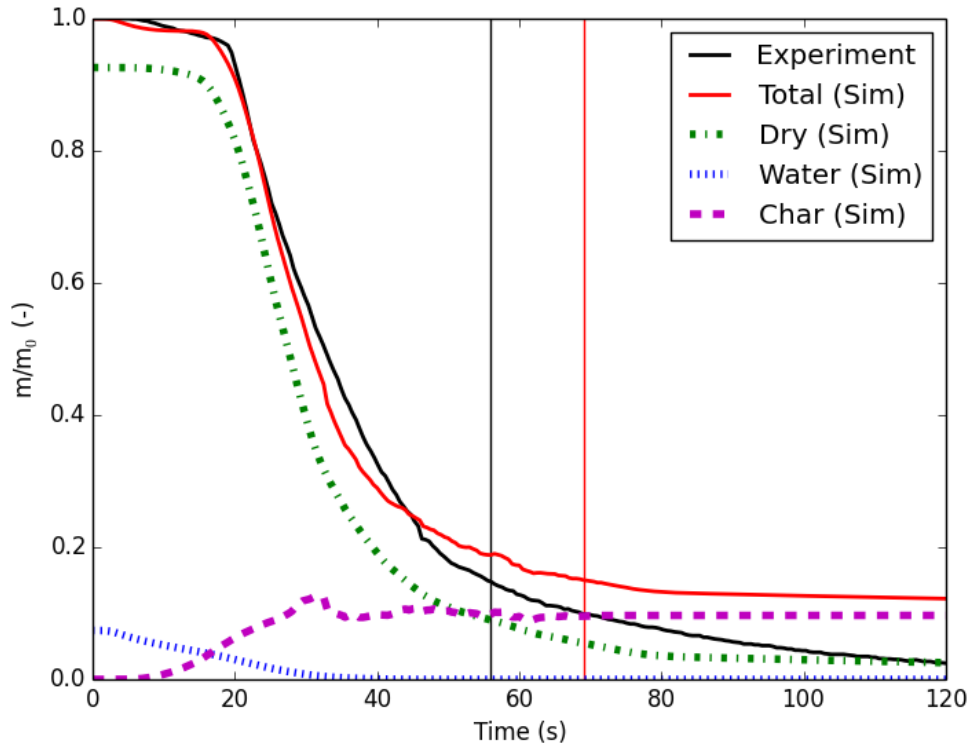


Figure 4.3: Experimental and simulated mass loss, including simulated mass loss of dry, water, and char fractions. Vertical lines correspond to the flameout times. (NF - 40 kg/m³)

Fig. 4.4. A 5 s moving average was used to smooth experimental curves. The experimental results are averaged over three repetitions and the error bars correspond to the experimental variations. The normalisation allows comparing different bulk densities. In general, during the first 10 seconds of the experimental curves, the sample was heating up, losing its moisture content, and its gases through evaporation and pyrolysis respectively. At this stage MLR/m_0 is less than 0.01 s^{-1} . Ignition occurs when there is a sudden growth in MLR/m_0 and reaches the maximum very quickly. At that point, the mass loss is driven by flaming combustion and decreases slowly until the flame extinguishes. Then, char oxidation becomes dominant. Maximum peaks are not only higher for

smaller bulk densities, but the distribution is also narrower and burning times are much shorter for low bulk densities. This indicates that more intense burning occurred and it is due to the increased heat transfer between the gas and the solid phase and the easier penetration of the radiation in the sample body (increased mean free path of radiation). The simulated curves (dotted) were time-shifted so that they coincide with the experimental curves when ignition occurs. One can clearly notice how well the model behaves for 30 and 40 kg/m³ but rather less for smaller bulk densities (17 and 23 kg/m³). For the latter, the mean free path of radiation ($\sim \frac{4}{\alpha_s \sigma_s}$) (Albini, 1985) is of the same order of magnitude as the sample depth. Therefore, the whole fuel bed was fully involved in the radiative heating process. In experiments with lower bulk densities, more radiation is transmitted through the fuel sample, and is reflected by the aluminium basket, which can increase the heating process from below. This phenomenon is a limitation of the experimental setup and it has not been included in the model, leading to the numerical underestimation. As a consequence, for a bulk density of 17 kg/m³ (Fig. 4.4a, the entire sample is heated very quickly and is involved in the burning as soon as ignition occurs. This results in a MLR that has a different shape (2 peaks) from what was found experimentally. It only indicates that the sample was not fully heated following ignition to directly reach its MLR peak. Since the whole sample was thermally involved in the experiments, both peaks merged into one. Nevertheless, the intensity is in the same order of magnitude. This behaviour is less apparent as the bulk density increases (Figs. 4.4b, c, and d) and as the radiation reflected by the basket becomes negligible.

The mass loss evolution is mainly dominated by the pyrolysis model during flaming, followed by the char oxidation. In these simulations, a two-step Arrhenius equation was used for the pyrolysis model, if a one-step Arrhenius equation was used, the peak MLR would have been higher leading to an overestimation of the fire intensity and can underestimate the burning time. By plotting the maximum

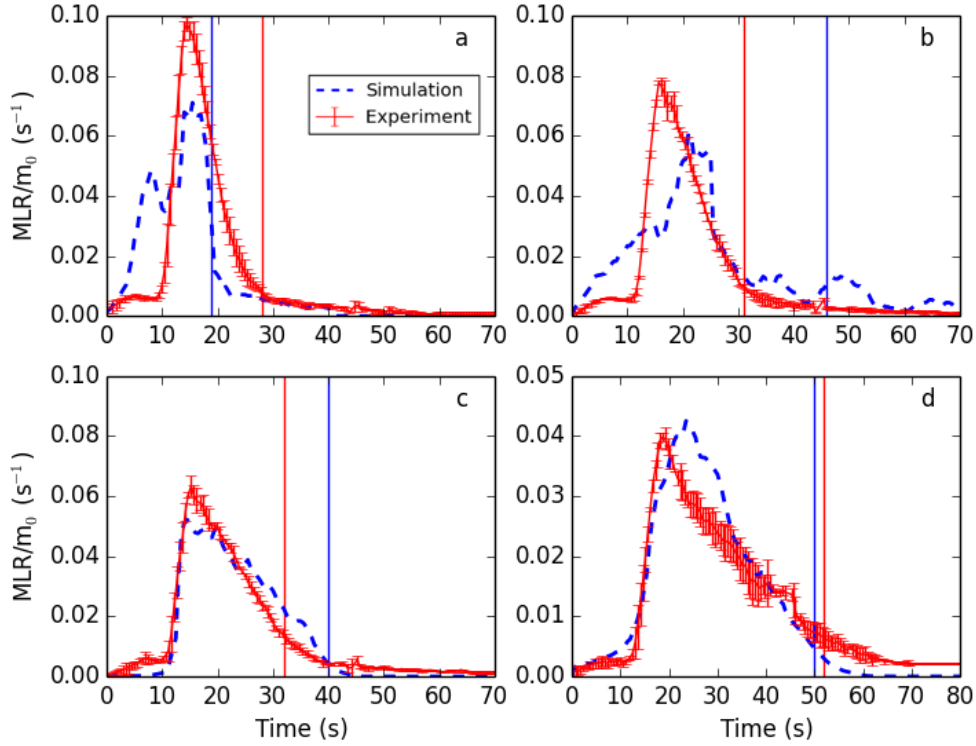


Figure 4.4: Mass loss rates for pitch pine of different bulk densities a) 17 kg/m^3 b) 23 kg/m^3 c) 30 kg/m^3 , and d) 40 kg/m^3 . 50 kW/m^2 applied heat flux. Solid: experiments, dashed: simulations, error bars: standard deviations. Vertical lines: Flameout

values of MLR/m_0 for different bulk densities in Fig. 4.5, it can be noticed that values decrease linearly with increasing bulk densities. For this range of packing ratio (α_s), the optical thickness defined as the ratio between the depth of the sample (0.03 m) and the extinction length ($\frac{4}{\alpha_s \sigma_s}$), varied from 1.3 for the lower bulk density to 3.1 for the higher. This means that the totality of the sample is thermally affected by the radiation for low bulk density. Whereas, only the upper layer of the sample absorbed the radiation for the high bulk density. Because pyrolysis is a temperature-driven process, the entire sample pyrolysed at once in the former case. In the latter case, due to the temperature gradient

observed before ignition (see chapter 3, Fig. 3.6), only the upper part of the sample burned in the beginning, then the lower part was gradually heated as the fire propagated downwards. This downward propagation was also observed experimentally. However, the thermally heated mass (m_{TH}) can be estimated as:

$$m_{TH} = \alpha_s \rho_s \frac{4}{\alpha_s \sigma_s} S \quad (4.1)$$

with S the surface of the fuel sample and $(\frac{4}{\alpha_s \sigma_s})$ the extinction length. m_{TH} is independent of the solid fraction (since it appears in the numerator and denominator), meaning that the mass increased through the increase of the bulk density is compensated by the decline of the extinction length, keeping the heated mass constant. This is why the peak **MLR** is not affected by the packing ratio and consequently by the initial mass of solid fuel in the basket.

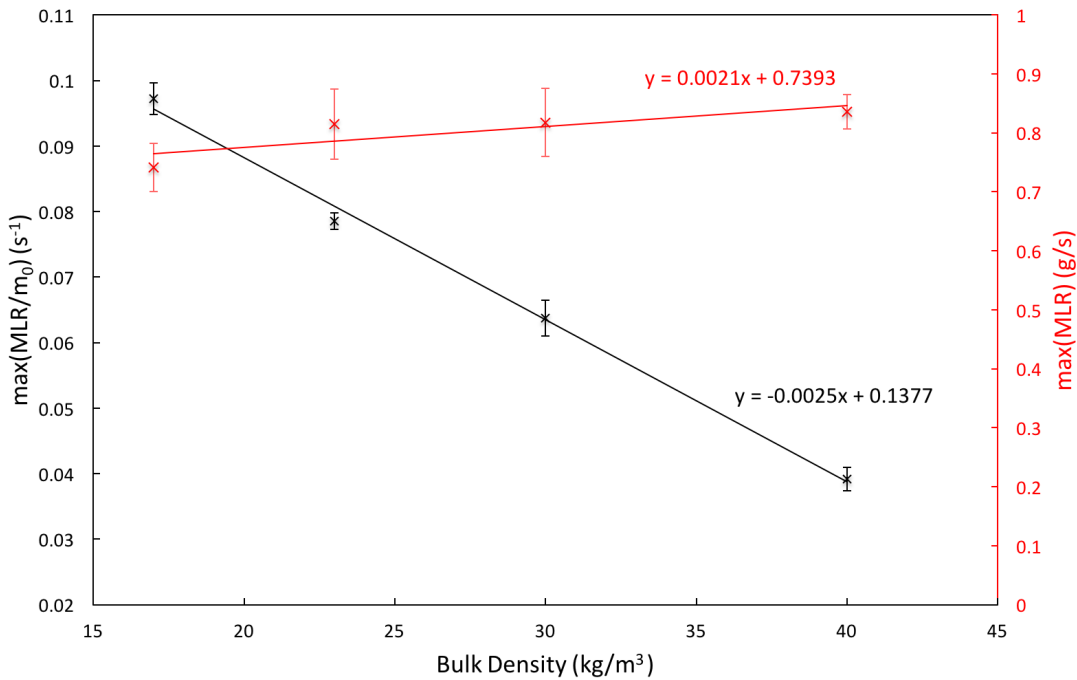


Figure 4.5: Measured maximum values of mass loss rates and normalised mass loss rates for pitch pine at 50 kW/m² for different bulk densities and their corresponding trendlines. Error bars: standard deviations

This result is confirmed by analysing the evolution of MLR/m_0 that decreases with the increase of the initial solid fuel mass m_0 (Fig. 4.5). When it is not normalised (in red), these peaks are rather constant for the bulk densities tested. Indeed, they increase very slowly, keeping a linear trend with increasing bulk densities. This means that the intensities are similar regardless of the bulk densities tested.

4.2.4 Heat Release Rate

Only the burning duration increases with bulk density, as it is presented in Fig. 4.6, where the corresponding Heat Release Rate (**HRR**) are plotted. Similarly to the **MLR** behaviour, the **HRR** is averaged for three repetitions. The variability of the experimental measurements is illustrated by the error bars added to the mean values. **HRR** was determined by Oxygen Consumption (**OC**) calorimetry as described in Schemel et al. (2008). As with the numerical **MLR**, acceptable predictions only occur for higher bulk densities. The peak **HRR** increases with the bulk density experimentally and in the model. It can also be noticed that the experimental peaks are wider as the bulk density increases, meaning that the burning times including flaming and smouldering become longer. The peak **HRR** at 40 kg/m^3 (Fig. 4.6d) is at approximately 8 kW, which is comparable to what was found in Schemel et al. (2008) for Aleppo pine (*Pinus halepensis*) tested in the same condition.

For low bulk densities (17 and 23 kg/m^3) the quantity of flammable gases released during pyrolysis could affect the conditions of ignition and the sustainability of the flame and consequently the **HRR**, via the amount of gaseous fuel effectively burned and the retroaction (by radiation of soot particles) of the flame toward the solid fuel. From the vertical lines, representing flameout times, one can observe that smouldering (post flameout) times increase with the bulk densities. This is due to the geometrical or the packing effect that limits fresh air from reaching

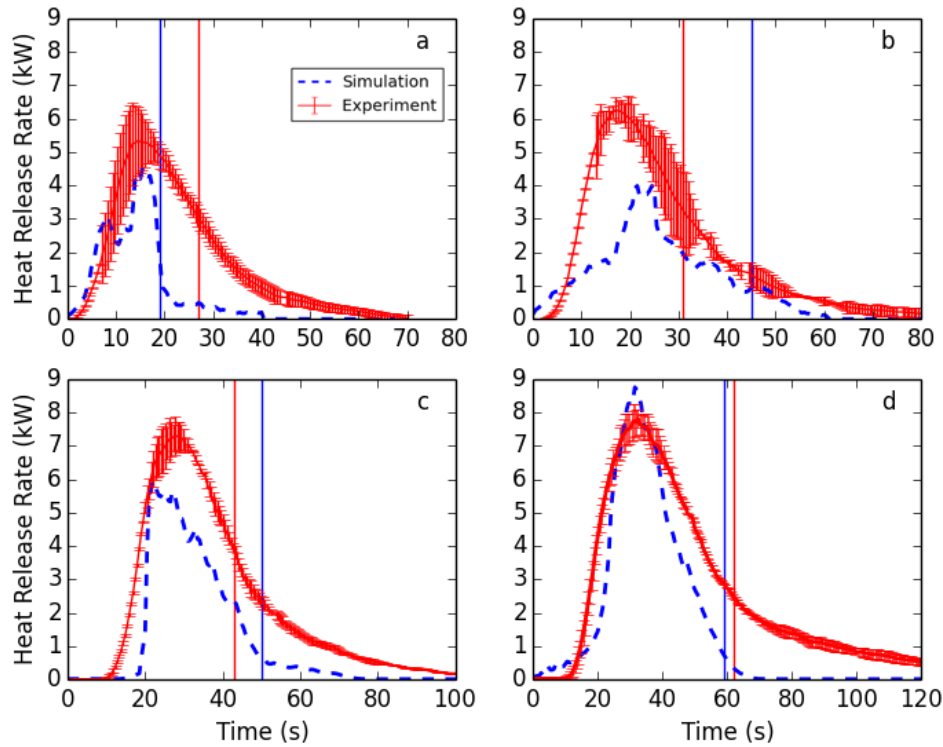


Figure 4.6: Heat release rates of pitch pine for different bulk densities: a) 17 kg/m^3 b) 23 kg/m^3 c) 30 kg/m^3 ,and d) 40 kg/m^3 . 50 kW/m^2 applied heat flux. Solid: experiments, dashed: simulation. Vertical lines correspond to the flameout times.

the fuel, hence slows down smouldering combustion. In consequence, the total burning time also increases with the bulk density. The HRR after flameout is underestimated for most cases presented in Fig. 4.6. It is because the char oxidation rate was not maintained after flame out as the temperature dropped, resulting in a total heat released smaller than it should be. Therefore, a single step model is not enough to represent this complex phenomenon in the tested conditions.

By separating the percentage of energy released during flaming and after flameout (due to smouldering) in Table 4.1, it was found that on average 73.3 % of the

energy is released during flaming and 26.7 % after flameout. These values are similar regardless of the bulk density. However, the simulations resulted in 92.4 % of the energy released during flaming, against only 7.6 % after flame out. The percentage of energy released after flameout decreased with the bulk density in both cases (experiments and simulations), indicating that more char combustion occurred for low bulk densities due to the better air ventilation.

Table 4.1: Percentage of energy released by flaming and smouldering during experiments and simulations for all bulk densities

Bulk density (kg/m ³)	Experiments		Simulations	
	Flaming (%)	Smouldering (%)	Flaming (%)	Smouldering (%)
17	73.6	26.4	86.1	13.9
23	71	29	91.5	8.5
30	72.7	27.3	93.5	6.5
40	75.8	24.2	98.3	1.7
Average	73.3	26.7	92.4	7.6

4.2.5 Low Heat Flux

Further tests were performed at 25 kW/m² for pitch pine needles and are presented in Fig. 4.7 to evaluate the models accuracy at low heat flux. The experimental MLR is slightly higher for higher heat fluxes (Fig. 4.4d) during smouldering (after 40 s) that is due to the external heat flux sustaining the oxidation of the char. Concerning the numerical predictions, they are in agreement with the experiments. The main tendencies are found, except at the end of the curve (after flameout), where char oxidation drops again for the same reason as for high heat flux.

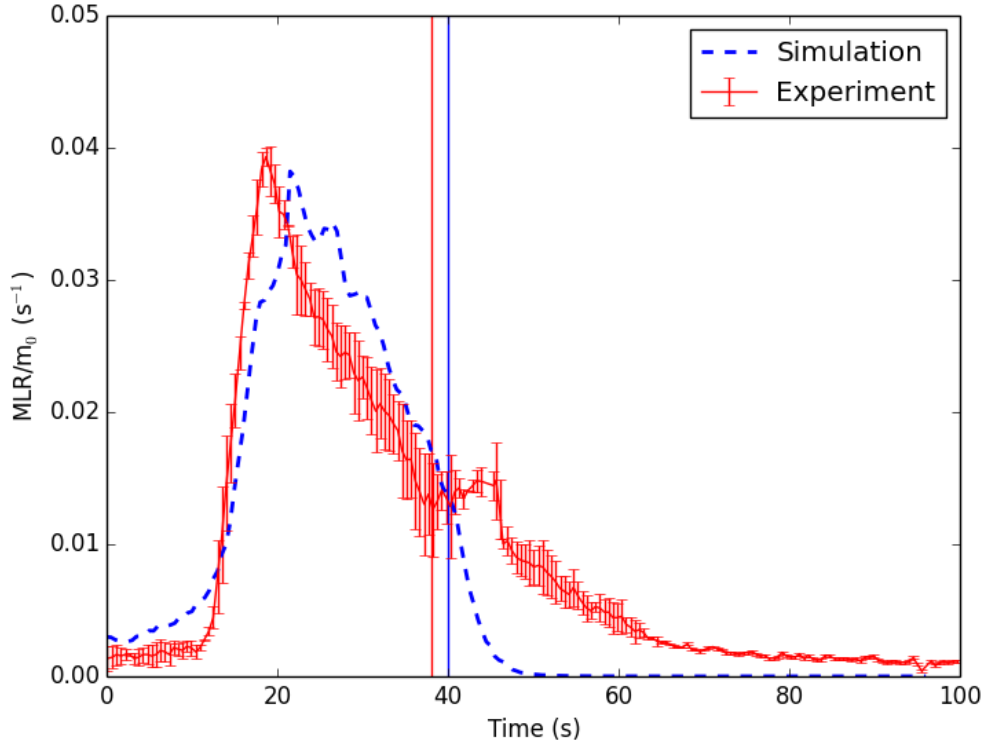


Figure 4.7: Normalised mass loss rates of pitch pine at 25 kW/m², bulk density of 40 kg/m³. Solid: experiments, dashed: simulations. Vertical lines correspond to the flameout times

The radiative Biot number (Bi_{Rad}) can be defined as (Benkoussas et al., 2007):

$$Bi_{Rad} = \frac{\alpha_{eff} q''_{surf}}{\lambda_s \sigma_s \Delta T} \quad (4.2)$$

With $\lambda_s = 0.12$ W/m.K being the fuel conductivity, $\Delta T = 300$ K, and $\alpha_{eff} = 0.64$. For a radiative heat flux $q''_{surf} = 25$ kW/m², $Bi_{Rad} = 0.06$, which is below the limit of the thermally thin hypothesis $Bi_{Rad} < 0.1$ (Benkoussas et al., 2007; Lamorlette et al., 2015). Whereas, for $q''_{surf} = 50$ kW/m², the radiative Biot number ($Bi_{Rad} = 0.12$) is in the thermally intermediate regime. Nevertheless, numerical results show good agreement with experiments, which means that the

temperature gradient inside a needle is not large enough to conflict with the thermally thin assumption stated in Chapter 2. Furthermore, the estimation of the Fourier number (F_o) give insights on the transient heat transfer. The Fourier number can be regarded a dimensionless time variable taking into account the thermal properties and characteristic thickness of the body (Drysdales, 2011), such as:

$$F_o = \frac{\alpha t_{max(MLR)}}{L^2} \quad (4.3)$$

with α the thermal diffusivity ($\alpha = \frac{K}{\rho_s c_{ps}}$), L a characteristic length scale, equivalent to the diameter of a pine needle ($L = \frac{4}{\sigma_s}$), and $t_{max(MLR)}$ the time to reach max(MLR). For both cases (25 and 50 kW/m²), $F_o = 0.012$ because $t_{max(MLR)}$ was the same. Hence, it can be commented that the change in the initial heat flux did not affect the heating time from ignition until reaching the maximum mass loss rate, which is why both MLR were similar.

4.2.6 Pitch Pine vs White Pine

The same tests were conducted on white pine needles (*Pinus strobus*) to highlight the effect of the Surface to Volume Ratio (SVR) and providing MLR and HRR presented in Figs. 4.8 and 4.9, respectively. As stated in Chapter 2, the SVR of white pine is 1,4173 m⁻¹, almost the double of the SVR of pitch pine (7,295 m⁻¹). Hence, the extinction length scale is reduced by a factor two, compared to pitch pine needles. Tests were made only for a bulk density of 40 kg/m³, because it was able to provide the best results for pitch pine. Computed curves were time-shifted so that they coincide with experimental curves when ignition occurs (17 s). The time shift is between 5 and 10 s, but it is not consistent between different simulations and experiments. Therefore, time to ignition is not successfully predicted. This is not surprising because piloted ignition is such a marginal event that any small variation in the experiment or in the numerical

condition can influence it. Additionally, the experimental uncertainty for ignition is very high (Thomas et al., 2013).

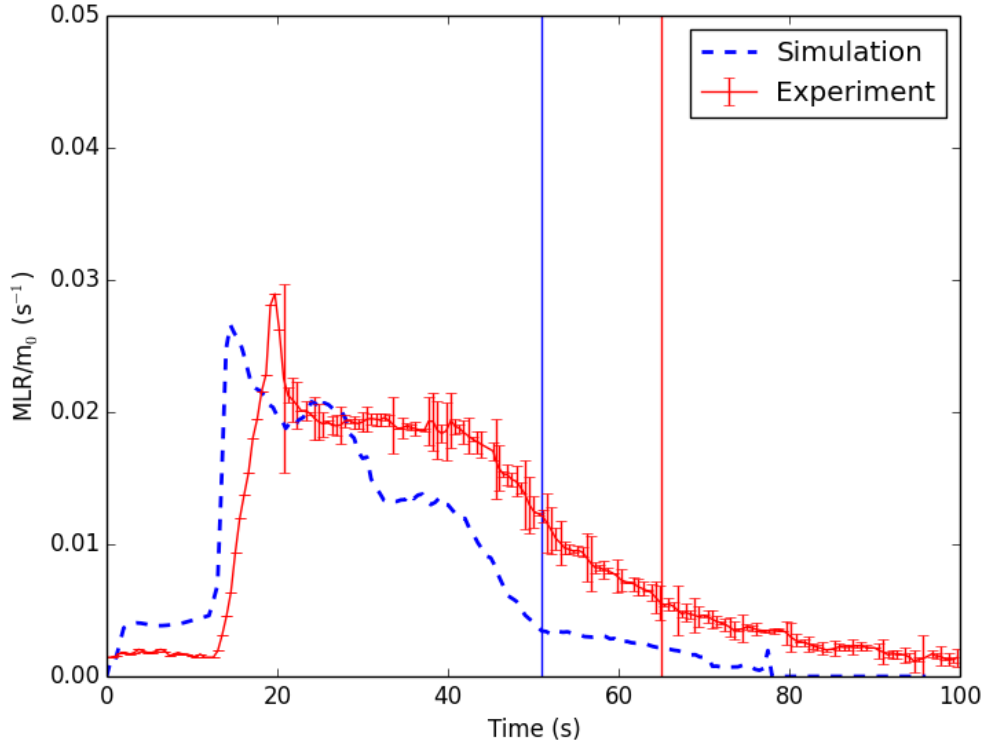


Figure 4.8: Normalised mass loss rate for white pine at 50 kW/m^2 , bulk density of 40 kg/m^3 . Solid: experiments, dashed: simulation. Vertical lines correspond to the flameout times

In Fig. 4.8, during the first 17 s a higher amount of mass was lost in the simulation due to evaporation and pyrolysis that occurred before ignition, resulting in an increase in the HRR that is not observed experimentally (Fig. 4.9). This is because the combustion model allowed local ignitions as soon as pyrolysis gases were mixed with air, which did not occur experimentally. These local ignitions occurred despite the Lower Flammability Limit (LFL) condition added to the combustion model, which is underestimating in this case. The other two humps around 30 and 40 s correspond to a combination of the smouldering reaction taking

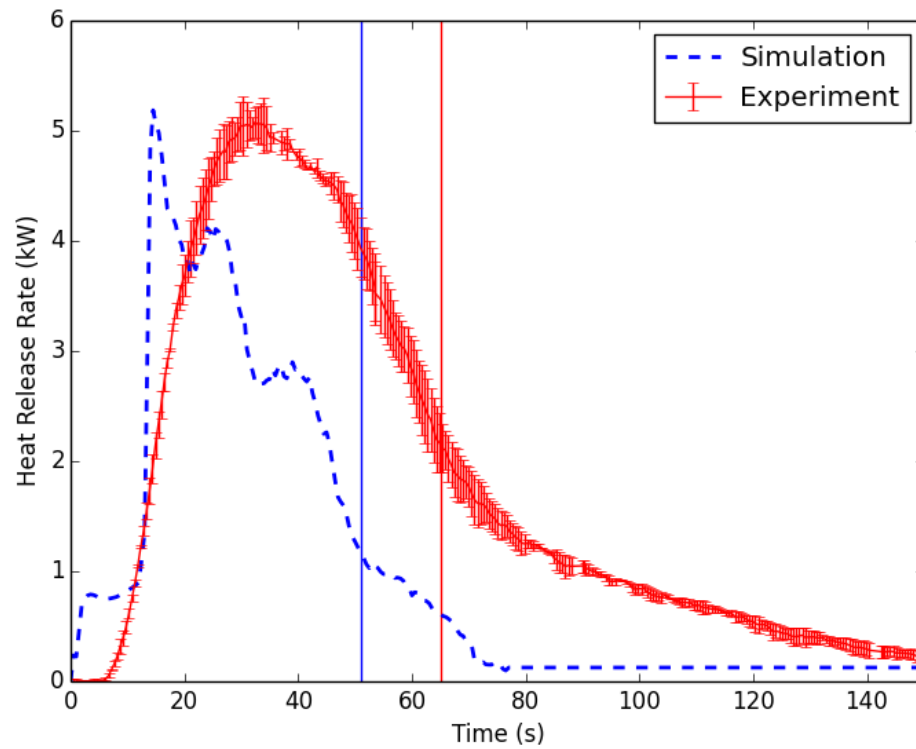


Figure 4.9: Heat release rate for white pine at 50 kW/m^2 , bulk density of 40 kg/m^3 . Solid: experiments, dashed: simulation. Vertical lines correspond to the flameout times

over and the fire (heat wave) reaching the bottom boundary of the sample. Despite all that, the peak [HRR](#) and peak [MLR](#) show good agreement with experimental measurements. However, burning times are underestimated again because of the low char oxidation, resulting in less total heat released.

- Pitch pine beds are less compact than those of white pine, due to the geometrical properties of the specie [SVR](#), inducing bigger gaps inside the bed and allowing oxygen to pass through more efficiently. Hence, pitch pine releases more energy than white pine during flaming (Fig. [4.6d](#) and Fig. [4.9](#)). These results are in agreement with the experiments conducted by [Bartoli et al. \(2011\)](#) with different pine species.

- Burning time of pitch pine is longer than for white pine. This agrees with [Anderson \(1969\)](#) observations on the statement that residence time in a fire spread increases with particle thickness.
- For white pine needles, the examination of the Fourier number (F_o , $\frac{\alpha t_{max(MLR)}}{L^2} = 6.7$) reveals that the characteristic time to reach the maximum mass loss rate is larger than the characteristic time of pine properties, unlike for pitch pine. Hence, the change in the thermal condition of the environment is slower than the temperature change in the sample, which is similar to the conditions used in Thermogravimetric Analysis ([TGA](#)) (and with a small Bi), from which the pyrolysis models were developed. This explains why the better numerical results were found for white pine than for pitch pine.

4.3 Forced Flow

4.3.1 Burning Characteristics

The observed flame was mostly laminar especially at the base, as shown in [Fig. 4.10](#). Unsteady and transient behaviour was also observed, but only in the intermittent zone of the flame, which was mostly due to the entrained air. [Figure 4.11](#) illustrates the predicted temperature field of the corresponding experiment during flaming (pitch pine, High Flow ([HF](#)), 40 kg/m³). Temperature ranges were in the same order of magnitude as other flames from wildland fuels ([Dupuy et al., 2003](#); [Tihay et al., 2009c](#)). The shape of the simulated flame is consistent with the experimental one ([Figs. 4.10a and b](#)).

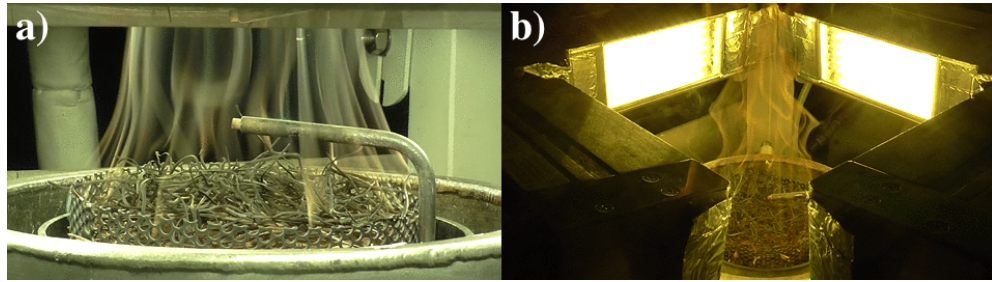


Figure 4.10: Pitch pine needles burning in the FPA a) low view angle, b) high view angle

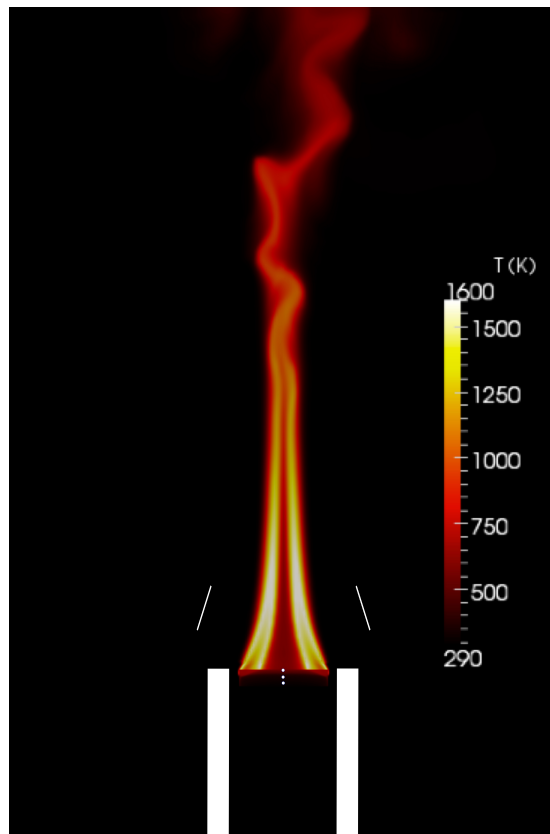


Figure 4.11: Temperature field during flaming for HF and 40 kg/m^3 . Three white points correspond to sampling points in the fuel bed

The evolution of the temperature in the solid phase is presented in Fig. 4.12 at the top of the sample, the middle, and the backface using the coefficients proposed by Colburn et al. (Incropera and Dewitt, 1996) for estimating the convective heat

transfer coefficient. The temperature on top, in the middle, and in the backface increased at a slower rate than observed in NF conditions before ignition. As the flame propagated downwards, the backface temperature increased until it was fully involved in the flame. This temperature evolution is consistent with temperature measurements conducted for 15 g of white pine in the FPA under similar testing conditions (heat flux of 50 kW/m^2 and 100 L/min inlet flow equivalent to HF/2) (Simeoni et al., 2012). The temperature rise in the fuel is steeper on top of the sample than on the bottom, because the latter is less exposed to radiation than the former and because it is more influenced by the convective cooling coming from the inlet.

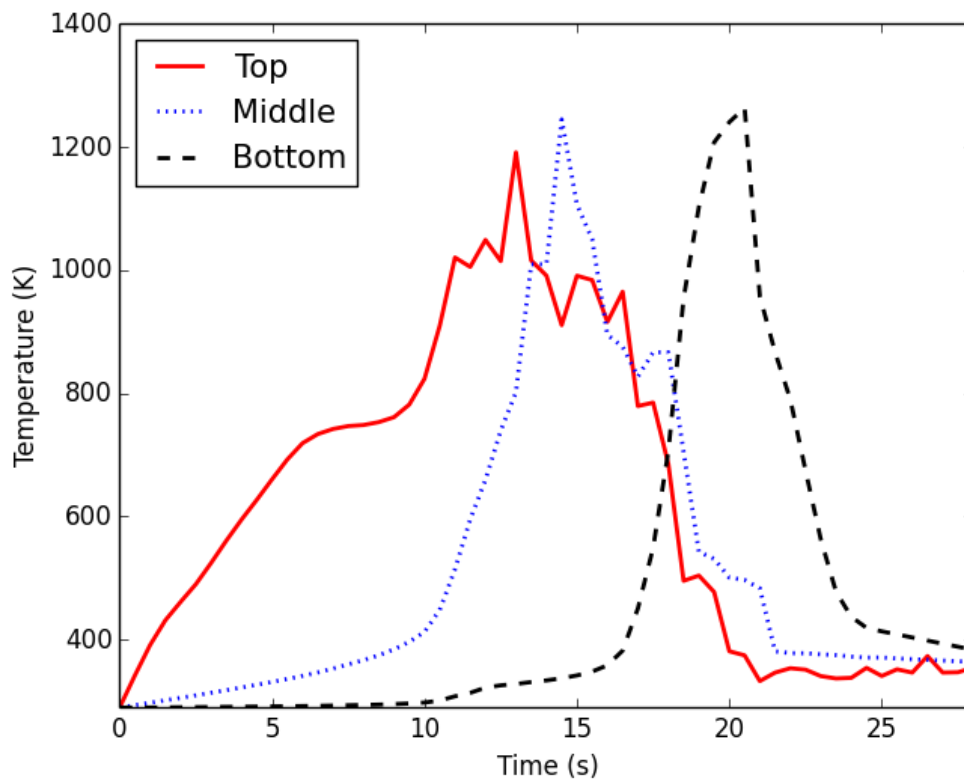


Figure 4.12: Simulated solid temperatures at the top, middle and bottom of the sample (corresponding to three sampling points in Fig. 4.11 for HF and 40 kg/m^3).

4.3.2 Flaming Time

Measured and simulated flaming times are plotted in Fig. 4.13 for different bulk densities and inlet flows. Overall, flaming time increases with bulk density, as there is more fuel to burn for higher bulk densities. It also increases with decreasing flow velocity, and the flames are maintained the longest (45 s) under natural convection at maximum bulk density. The forced flow enhances the mixing pyrolysis gases with air and makes the burning faster. For lower bulk densities, the influence of the forced flow is not as dominant as for higher bulk densities. For all flow conditions, flaming times varies between 13 and 17 s. Since the sample is very porous (96 %), the induced air easily penetrates and provides enough oxygen to obtain well-ventilated combustion conditions, even for NF and Low Flow (LF) conditions (Table 2.4). The increase in the flaming time is more significant for higher flow rates because the air contribution is related to an increase in the combustion rate, as the latter becomes limited by the fuel available. Whereas, under natural convection the combustion rate is limited by both the available fuel and the oxygen, especially for high bulk densities (92 %). In a natural convection regime, it is more likely that the combustion is limited by oxygen supply than by pyrolysis. The simulations slightly overpredicts the flaming time. It is a consequence of using a highly efficient gas phase combustion model (EDC), where all the available fuel or oxygen is consumed when they mix. In reality, the combustion efficiency is not maximum due to air dilution and cooling.

Figures 4.14a, b, and c describe the evolution of the fuel and oxygen mass fractions inside the fuel bed under HF conditions at ignition, 5 s and 15 s after ignition, respectively. It can be noted that the propagation occurs from top to bottom, which is in agreement with the experimental observations. Moreover, the evolution of the mass fractions (step) are representative of a typical diffusion flame, meaning that no partial mixing is involved. It is clear that the oxygen is

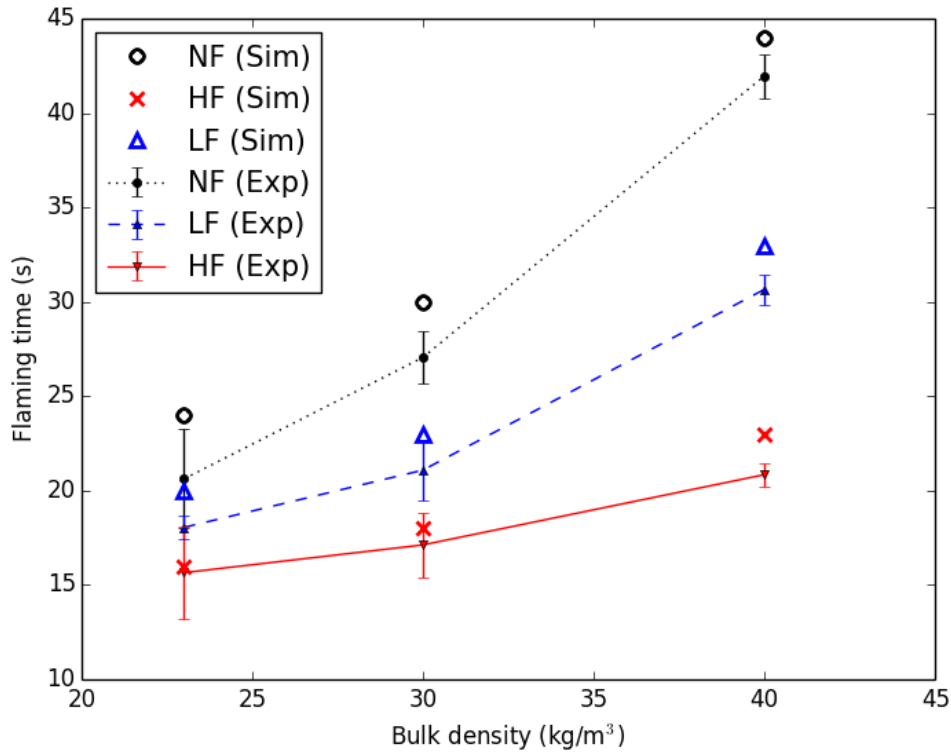


Figure 4.13: Measured and simulated flaming time for different bulk densities and inlet flows. Filled markers: experiments, empty markers: simulations, error bars: standard deviations for experiments

completely consumed in the first cell of the reaction zone. Figures 4.14d, e, and f represent the evolution of the mass fraction in NF conditions. In Fig. 4.14d, the conditions at ignition are similar to those encountered with HF (Fig. 4.14a). As the flame propagates slower in NF, Figs. 4.14e and 4.14f show the mass fractions 20 and 40 s after ignition. It appears that the entire fuel sample is embedded in the fuel rich zone and that there is no sufficient oxygen inside it to ensure flaming combustion. Anecdotal observations of experiments using pine needles in the cone calorimeter under natural convection allowed to see the flame burning below the sample, which is characteristic of the behaviour of a fuel rich diffusion flame and confirms the prediction from Figs. 4.14e and f. This behaviour was also observed

in the FPA in natural convection but it was harder to see because of the light of the heaters.

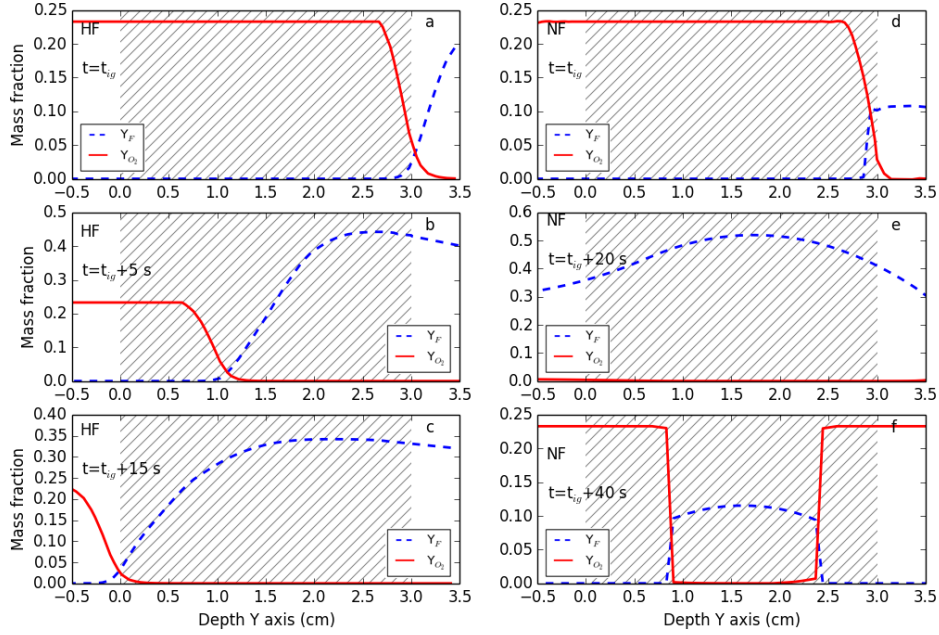


Figure 4.14: Fuel and oxygen mass fractions along the vertical and at the center of the sample (hatched area) during flaming. Figures a, b, and c correspond to distributions at ignition, 5 s and 15 s, respectively for HF conditions. Figures d, e, and f correspond to distributions at ignition, 20 s and 40 s, respectively for NF conditions

4.3.3 Mass Loss

Similarly to the mass loss presented previously in NF, mass loss measurements and simulations are presented in Fig. 4.15 for pitch pine at HF with a bulk density of 40 kg/m^3 . The experimental curves are shifted by 7 s to synchronise both experimental and simulated ignition times. The simulated mass losses are split into dry, moisture content, and char fractions, giving more insight on the

mass loss mechanisms. In the beginning, the mass fraction was only composed of moisture content and of dry material. Then the moisture content evaporated during the first 13 s of the simulation. More dry material was lost via pyrolysis when ignition occurred, during which the dry fraction decreased steeply, and the char fraction formed (corresponding to flaming).

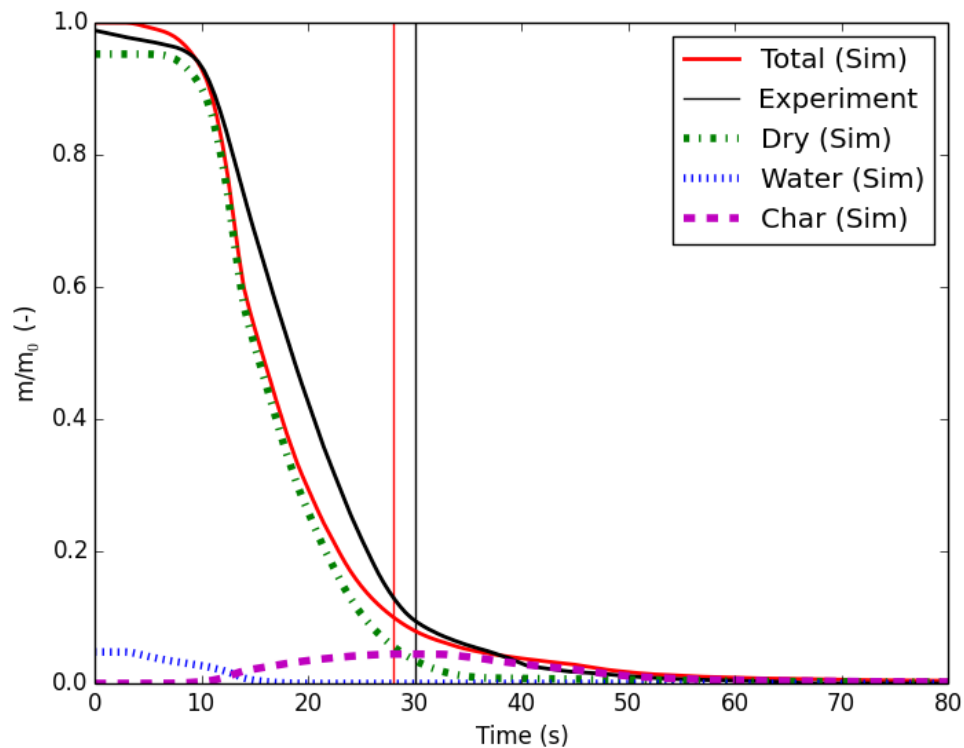


Figure 4.15: Experimental and simulated mass loss, including simulated mass loss of dry, water, and char fractions. Vertical lines correspond to the flameout times. (HF - 40 Kg/m³)

The transition between flaming and smouldering combustion occurred 5 s prior to flameout, during which pyrolysis and char oxidation rates were overlapping. This observation is confirmed in Fig. 4.16 by observing the pyrolysis and char oxidation rates overlapping near flameout time. This behaviour is also consistent with the observations made in Schemel et al. (2008).

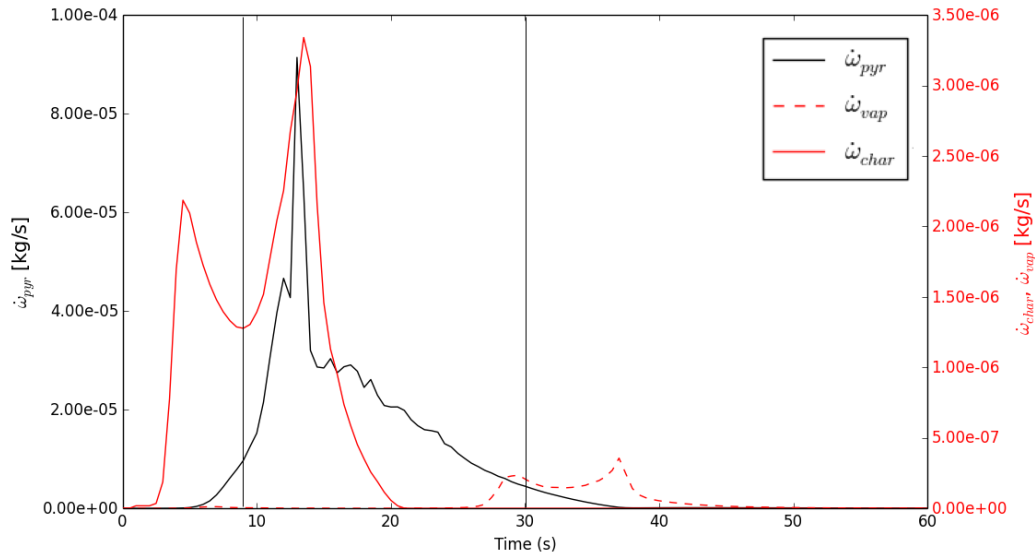


Figure 4.16: Simulated rate of evaporation, pyrolysis, and char oxidation, integrated over sample volume. Vertical lines correspond to ignition and flameout times. (HF - 40 kg/m³)

Mass Loss Rate are calculated from experimental and numerical mass losses and are shown in Fig. 4.17 for two bulk densities: 23 kg/m³ (Fig. 4.17a) and 40 kg/m³ (Fig. 4.7b) at HF. In the first 10 s of both cases, the smaller slope corresponds to pyrolysis and evaporation before ignition. When ignition occurred, the slope increased steeply. The subsequent slowing down corresponds to flameout (vertical line around 30 s), where mainly char oxidation remained. The numerical predictions overpredicted the maximum value by around 20 %, but followed the same trend as in the experiments in both condition. This can be due to the radiation attenuation coefficient that can drastically change the distribution of the mass loss rate. As the mean free path of radiation becomes higher, it increases the solid temperature along the fuel sample depth and causes more solid degradation in depth. Since, the thermally heated mass (m_{TH}) in Eq. 4.1 is independent of the solid fraction, the oxygen supply is strongly responsible for affecting the combustion rate.

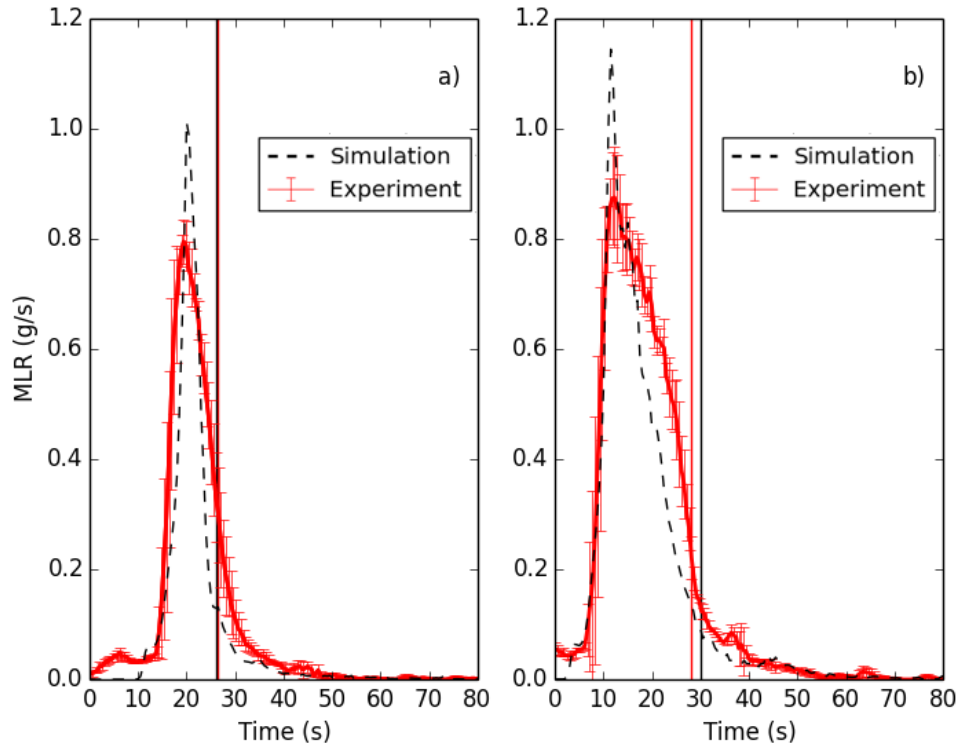


Figure 4.17: Mass loss rates (MLR) for different bulk densities a) 23 kg/m^3 and b) 40 kg/m^3 , all at HF. Solid line: experiments, dashed line: simulations, error bars: standard deviation. Vertical lines correspond to the flameout times

For a better comparison between the different bulk densities and flow conditions, MLR were averaged for each configuration, and are presented separately during flaming in Fig. 4.18. One can observe that the average MLR increases with an increasing inlet flow for all tested conditions. As the flow enhances the mixing of pyrolysis gases with air, the combustion rate is increased. Overall, simulations are consistent with measurements, regardless of the peak values that are slightly overestimated numerically, as shown in Fig. 4.18. The following observations are made:

- Under HF conditions, the average value increases with the bulk density. This is a result of the direct influence of the airflow on the combustion rate.

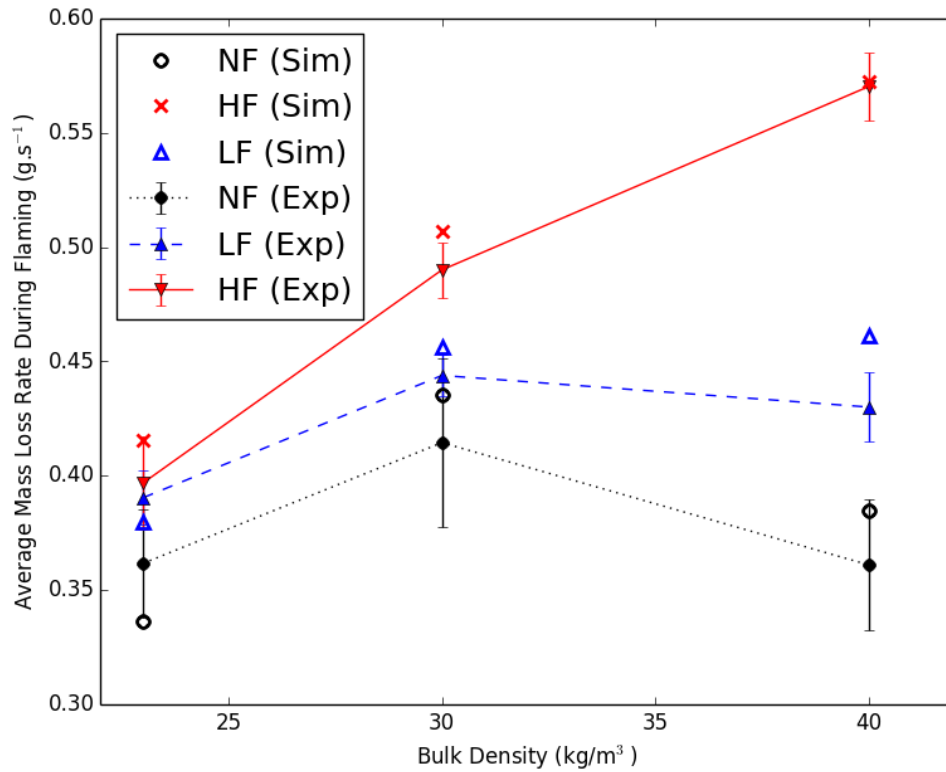


Figure 4.18: Averaged values for measured and simulated mass loss rates during flaming

- For **NF** conditions, the average **MLR** increases at 30 kg/m³, as there more fuel to burn. However, it decreases at the highest bulk density, due to the low ventilation conditions induced by natural convection, which slows down the reaction.
- As for **LF** condition, the evolution of the mean **MLR** illustrates the competition between radiation heating the solid phase with increasing bulk density (and increasing α_s) and the decreasing oxygen available to sustain the reaction.
- At the lowest bulk density (23 kg/m³), which corresponds to the highest porosity, the mean **MLR** is similar for **LF** and **HF**, because air is able to

penetrate easily, providing well-ventilated combustion conditions, which are similar even in **NF** conditions.

- For higher bulk densities, the sample is more compact, causing more contact between pine needles, and more shadowing effect from the drag forces. Therefore, there is less contact with the gas phase.
- As the extinction length ($\sim \frac{4}{\alpha_s \sigma_s}$) (Albini, 1985) changes from 13.7 mm to 7.8 mm, between 23 and 40 kg/m³, respectively, radiation cannot penetrate deeper in the sample body. The optical thickness defined as the ratio between the depth of the sample (3 cm) and the extinction length shows that the sample is optically thick (2.19 and 3.84 for 23 and 40 kg/m³, respectively). This means that radiation is able to penetrate only 45 % and 26 % of the bed layer. When the total amount of radiation is distributed on a shallow layer, the limiting factor is the amount of fuel available for pyrolysis. Whereas, when the same amount of energy is distributed deeper in the fuel (i.e. low bulk density), the limiting factor is the heat transferred downwards.
- Between experiments and simulations with and without flow, the existence of two regimes is highlighted. The oxygen limited oxygen regime (**NF**) and the fuel limited regime (**LF** and **HF**). Because the mean **MLR** is not a monotonic function of the density in **NF** condition, the combustion is limited by oxygen supply (via saturation).

The average **MLR** is also calculated after flameout and is presented in Fig 4.19.

It can be safely assumed that the mass loss is driven by smouldering. Since the latter occurs at a very slow reaction rate, the average **MLR** is one order of magnitude smaller than for flaming, which makes it difficult to distinguish tendencies. Globally, the average **MLR** increased with bulk density and with

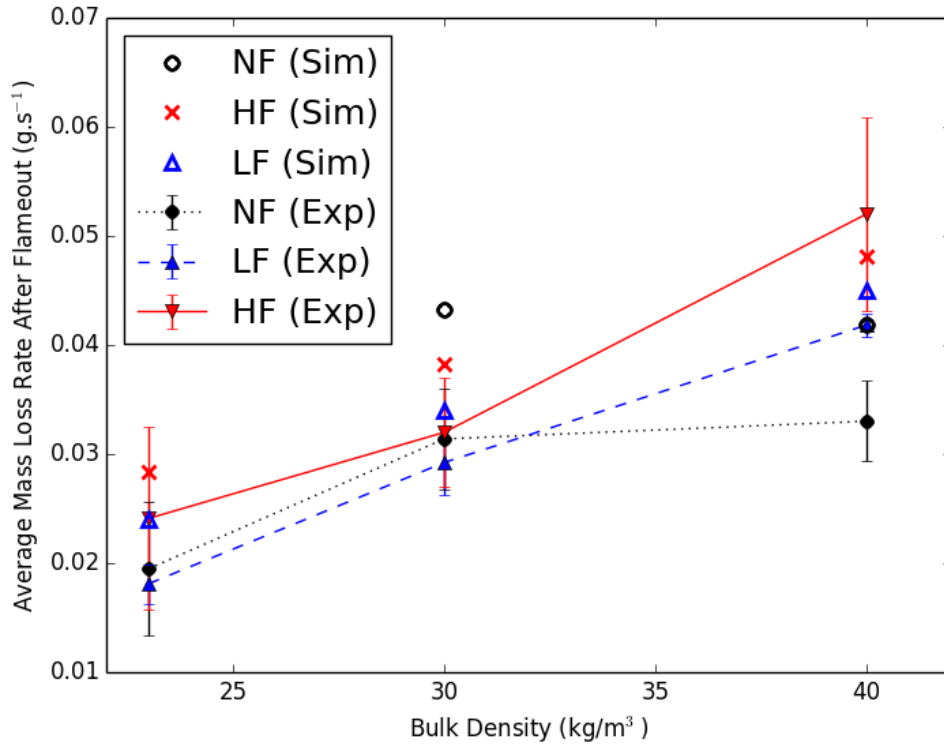


Figure 4.19: Averaged values for measured and simulated mass loss rates after flameout

the flow, because more fuel and more air were available, respectively. This is consistent with Eq. 3.31 in Chapter 3, in which the char oxidation rate is proportional to the oxygen concentration and to the bulk density. The numerical predictions in LF and HF compares well with measurements, as a result of the proper flow and heat transfer estimation. However, numerical results in NF conditions do not match the experimental results because the char oxidation was not sustained due to the low air supply in natural convection. Hence, the reaction only occurred during the few seconds after flameout then dropped, resulting in a high average MLR compared to the experiments, which lasted longer. Smouldering time for NF could be enhanced by using a more comprehensive model for estimating the char combustion rate. This can be accomplished by accounting for a diffusion-controlled regime, as proposed by Boonmee and Quintiere (2005),

in addition to the kinetic-controlled regime. Alternatively, the char oxidation rate can be improved by accounting for the increase of the surface to volume ratio in the solid phase (which is kept constant in this study) representing the char pores that are formed in the fuel. The implementation of such model is detailed in Appendix E, in which preliminary tests display better estimation of the mass loss in NF conditions.

4.3.4 Heat Release rate

The measured and simulated HRR are presented in Fig. 4.20 for two bulk densities at HF. Computed curves are time-shifted so that they coincide with experimental curves when ignition occurred. The peak HRR are slightly over estimated in both cases, a resultant of the high MLR peaks. Nevertheless, the overall trend is matched and the total heat released is similar. The peak HRR at 40 kg/m³ (Fig. 4.20b) is at approximately 11 kW, which is comparable to what was found in Bartoli et al. (2011); Simeoni et al. (2012) for Aleppo pine tested in comparable conditions. The transition between flaming and smouldering (at flameout) is better predicted numerically for the higher bulk density (Fig. 4.20b). Whereas, for the lower bulk density (Fig. 4.20a), an abrupt transition is noticed only in the simulation (at 35 s). The transition is smoother for higher bulk density than for lower bulk density because there was more solid fraction available to burn, increasing the heat transfer from solid to solid and better sustaining char oxidation after flameout.

By calculating the experimental and simulated percentage of energy released during flaming and after flameout, it can be noticed that on average two third of the energy was released during flaming at HF, compared to 73 % for NF. This is due to the decreasing flaming time with increasing flow velocity observed in Fig.

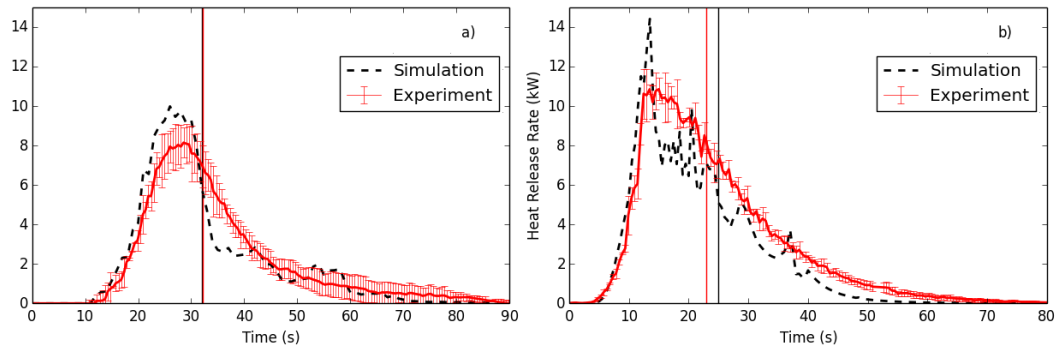


Figure 4.20: Measured and simulated Heat Release Rates for a) 23 kg/m³ b) 40 kg/m³, all at HF. Solid line: experiments, dashed line: simulations, error bars: standard deviation. Vertical lines correspond to the flameout times

4.13. As for the simulations in Table 4.2, they are in agreement with experimental observations for all cases.

Table 4.2: Percentage of energy released by flaming and smouldering during experiments and simulations for all bulk densities at HF

Bulk density (kg/m ³)	Experiments		Simulations	
	Flaming (%)	Smouldering (%)	Flaming (%)	Smouldering (%)
23	64.2	35.8	65.5	34.5
30	65.2	34.8	66.7	33.3
40	64.8	35.2	68	32
Average	64.7	35.3	66.7	33.3

For better illustration of the influence of the porosity in the \overline{HRR} , averaged values for measured and simulated \overline{HRR} are normalised over their corresponding initial fuel mass (\overline{HRR}/m_0) and are presented during flaming and after flameout, in Fig. 4.21 and 4.22, respectively. The normalisation allows better comparison of the energy rate released between different bulk densities. In Fig. 4.21, \overline{HRR}/m_0 globally increases with the flow. This is consistent with the observed

MLR (Fig. 4.13) and with the shorter flaming times for higher flow conditions. Essentially, higher HRR is reached for shorter flaming times due to the better mixing, and consequently the enhanced combustion rates. The observed \overline{HRR}/m_0 trends to decrease with an increasing bulk density, which is consistent with the aforementioned observations regarding the competition between radiation penetration and oxygen available. As for the numerical predictions, these tendencies are well matched at HF and LF but cannot be obtained in NF conditions, due to the underestimated combustion rate.

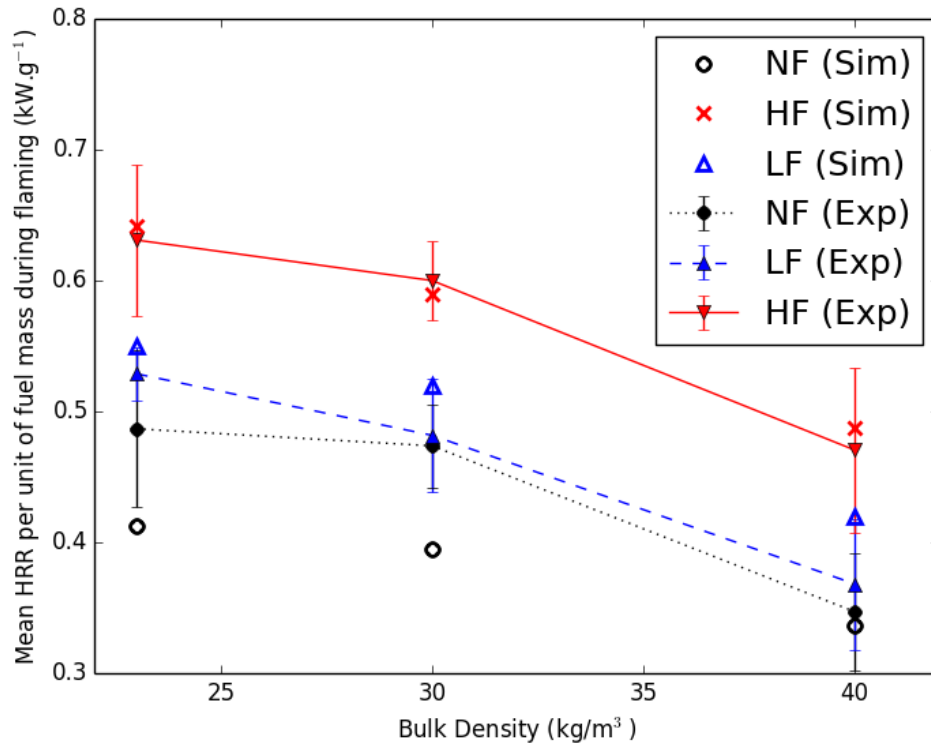


Figure 4.21: Averaged values for measured and simulated heat release rates during flaming

Regarding \overline{HRR}/m_0 after flameout (Fig. 4.22), the measured values are an order of magnitude lower than during flaming. They decrease with an increasing bulk density, since more air can reach the reacting solid phase at lower bulk densities. \overline{HRR}/m_0 is consistently slightly higher at HF, especially for the

higher bulk density. Simulations at HF conditions matched the measurements. However, a high average MLR was found after flameout at NF condition, (Fig. 4.19). Consequently, the calculated \overline{HRR}/m_0 is overestimated compared to measurements as a higher HRR was released over a short period of time. However, the calculated total energy released is smaller than the experimental one, since not all the char is oxidised in the simulations in NF.

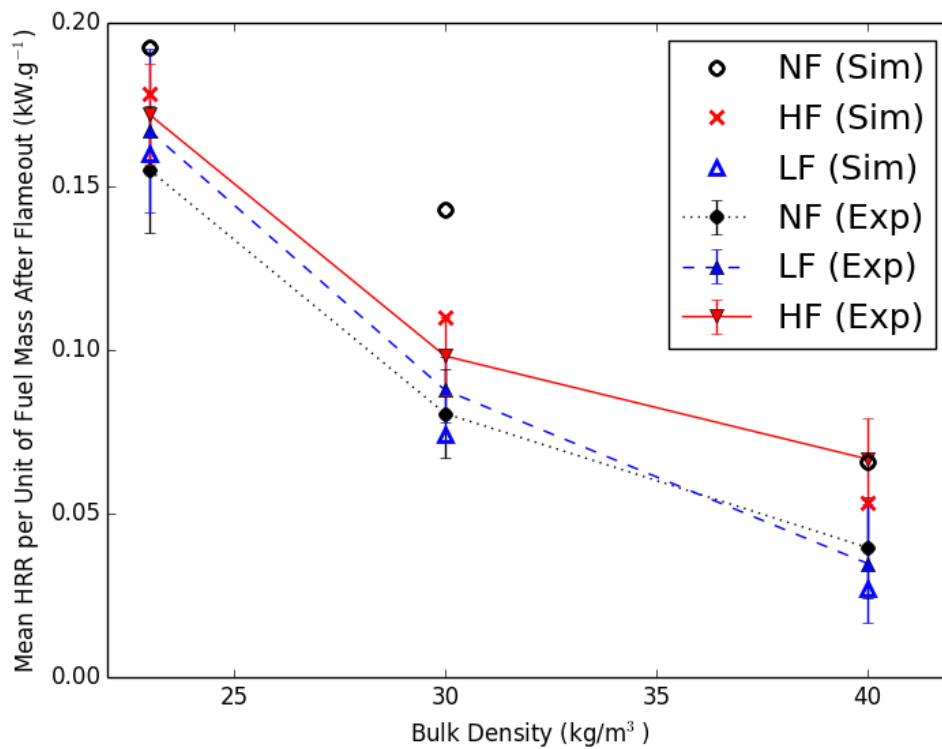


Figure 4.22: Averaged values for measured and simulated heat release rates after flameout

In summary, we were able to quantify the behaviour of the model by comparing simulations to experiments under different conditions. More importantly, we were able to assess the submodel performances despite the strong coupling between the different dynamics.

4.3.5 Gas Emission

It is necessary to verify the predicted gas emissions resulting from the split function presented in Chapter 3, for estimating the amount of CO and CO₂ in the simulation. The experimental and simulated time evolution of CO and CO₂ are presented in Fig. 4.23 for a fuel bulk density of 40 kg/m³ and HF. The experimental values were measured in the gas analysers. Similarly, the simulated values were obtained at the outlet boundary. It can be observed that a large amount of CO₂ was produced during flaming, then dropped after flameout. The simulation overestimated the CO₂ production during flaming because the entire CO was consumed in the gas phase due to the high efficiency of the combustion model. As a direct result, no CO was produced in the simulation during flaming time (<18 s). In reality, not all CO was consumed, due to dilution with air and cooling. Indeed, the concentration of measured CO increased as the flame was dying and as more smouldering occurred. An extinction model could be added to account for the unburned gases and better represent the incomplete combustion in the flame, especially at a larger scale (Vilfayeau et al., 2015). But its absence did not severely influence the representation of the burning dynamics of the pine needle bed (which was the focus of this work) as most of the impinging radiation was coming from the FPA heaters. The peak value for experimental CO was 25 ppm, whereas for the simulation, the peak was at 35 ppm. Once again it was due to the combustion efficiency that was overestimated in the gas phase and had little influence on the burning dynamics. More importantly, the transition in the gas emission between flaming and smouldering combustion is in agreement with experiments conducted by Schemel et al. (2008) using pine needle beds in the FPA. However, an adjustment will be needed for very large fires, where extinction is likely to play a role, especially if the model is used to estimate fire emissions (Vilfayeau et al., 2015).

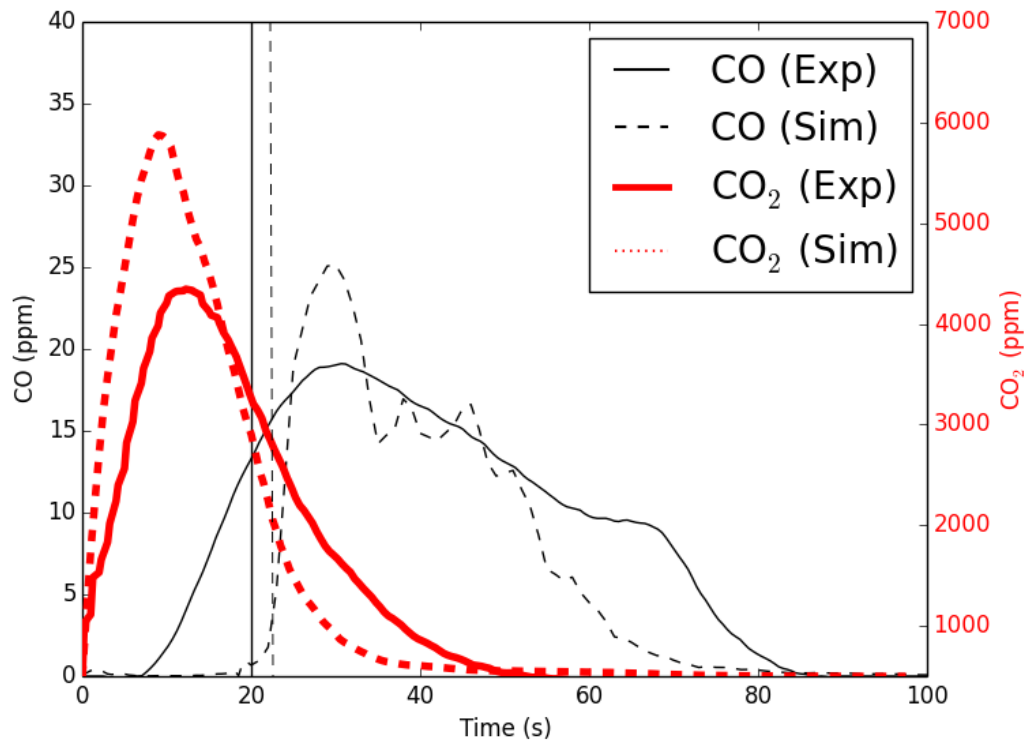


Figure 4.23: Measured and simulated CO and CO₂ production (HF - 40 kg/m³). Solid lines are experiments; dashed lines are simulations. Vertical lines correspond to the flameout times. Plots are shifted to have ignition at 0 s

4.4 Conclusion

The approach presented in this chapter assessed the relevance and the performance of the submodels that are used to close Computational Fluid Dynamics (CFD) models, particularly when the multiphase approach is used. Some submodels were successfully adapted in a specific range of conditions, and allowed improving burning rate estimations by better describing the underlying physics. Moreover, the importance of using appropriate submodels were also demonstrated. It was shown which submodels needed to be appropriately refined

in order to provide acceptable predictions. This was done by comparing simulations to experiments with various fuel surface to volume ratios, bulk densities, inlet flows, and applied heat fluxes. Because of the strong coupling between the different submodels, the framework of using controlled experiments and matching simulations at a small scale is necessary for choosing the adequate submodels. This framework is common in combustion, but its application in wildland fires is novel. The main results are summarised as follows:

- The selected gas-phase combustion model was not sufficient for estimating unburned gases during flaming. However it did not affect the quality of the result and the general trends for predicting the burning dynamics of the solid phase and the relevance of the submodel improvements. This aspect needs further investigations, especially for supporting emission estimations.
- Overall, the model performs well as flaming time, average mass loss rates, and average heat release rates were successfully modelled in the chosen range of conditions but is still very sensible to each submodel.

For Natural Convection

- A two-step Arrhenius correlation is appropriate to represent pyrolysis rate, giving quantitatively similar **MLR** and **HRR** for high bulk densities (30 and 40 kg/m³).
- Findings are comparable for a very low bulk density (17 kg/m³) in terms of order of magnitude, but different behaviours are found due to the easier penetration of the radiation in the sample body that increases the heating rate. It was not attempted to adapt the model because it is only a limitation of the experimental setup and does not reflect the applicability of the multiphase model.

- It was shown that underestimating the contribution of the char oxidation leads to underestimating [MLR](#) and [HRR](#). In fact, the char oxidation rate was not sustained after flame out. Therefore, a single step model does not represent this complex phenomenon efficiently in natural convection. We deliberately chose to show that one-step models for char oxidation are not appropriate. Indeed, the use of this model is often assumed to be correct without further justifications ([Porterie et al., 2000](#); [Séro-Guillaume and Margerit, 2002](#); [Margerit and Sero-Guillaume, 2002](#); [Mell et al., 2009](#); [Morvan, 2011](#)). In consequence, burning times and zones can be misjudged when simulating larger fires. Since this model gave good predictions in forced flow conditions, it indicates that the issue in natural convection does not originate from the energy activation, but perhaps with the 50/50 % assumption of the heat released between the solid phase and the gas phase. A sensitivity analysis to this parameter should be further investigated.

For Forced flow

- The estimation of the drag force coefficient directly affects the flow field inside and around the porous fuel. Consequently, it affects the associated burning dynamics in both flaming, and smouldering combustion. The proposed simulations can be used for subgrid modelling and included in large scale simulations to represent the drag force through litter beds separately from the one for trees using the multiphase approach.
- Similarly, for the convective heat transfer coefficient we have verified that Colburn coefficients are appropriate for our experimental conditions. Whereas, other cited coefficients can prevent the fuel from igniting.
- The char oxidation model based on a single step Arrhenius equation is

sufficient for characterising smouldering combustion, and especially mass loss after flameout.

- The additional split function in the char oxidation based on [Evans and Emmons \(1977\)](#) model allowed predicting an acceptable gas emission and adequately modelling the transition between flaming and smouldering emission.

Chapter 5

Conclusion

Summary of the developed work

In this study, a systematic approach was developed to assess the performance of submodels and to better understand how a set of physical phenomena contributes to the wildfire dynamics. This study focused on understanding the burning behaviour of forest fuels, which has not been fully described in wildland fires. We developed a framework that consists of testing submodels by comparing numerical predictions to experimental measurement in a controlled environment using the FM Global Fire Propagation Apparatus ([FPA](#)). In order to support a detailed analysis, the physical and chemical properties of pitch pine needles were characterised. To capture the relevant physical processes, the following experiments needed to be undertaken:

- Differential Scanning Calorimetry ([DSC](#)) experiments to obtain the specific heat capacity of pine needles.
- Analysis of the spectral emissivity of dead pine needles to allow full

description of the radiative heat transfer under the FPA heaters and the flame radiation.

- Measurements of the fuel bed temperature in the FPA to test the model's temperature predictions.
- Including some gas phase species measurements (e.g. by Fourier Transform Infra-Red (FTIR) spectrometry) to measure pyrolysis gas products and to simulate an equivalent fuel in the gas phase.

A multiphase approach was implemented in OpenFOAM (OpenCFD Ltd.) and based on the FireFOAM solver (Wang et al., 2011), creating ForestFireFOAM solver. Using Large Eddy Simulation (LES) capabilities, Navier-Stokes conservation equations are solved in a radiative and reactive multiphase medium. To perform proper LES, the boundary conditions were verified and a grid sensitivity analysis was conducted. The multiphase formulation was used to provide an accurate representation of the experimental setup and to represent the porous nature of the fuel.

Submodels representing thermal degradation, heat transfer, and combustion were implemented in ForestFireFOAM and analysed to ensure that an accurate representation of the physical processes was achieved. Necessary modifications were successfully implemented improving each phenomenon affecting the burning rate estimation. The importance and the implications of using appropriate submodels were shown in this framework. This is necessary to improve our understanding of the burning dynamics of forest fuels before developing further predictive tools in wildfires. Due to the strong coupling between the different submodels, the framework of using controlled experiments and matching simulations at a small scale is necessary to adequately refining each submodel. This methodology can also be applied to explore the burning dynamics of other fuels with different characteristics. Overall, temperatures, flaming time, mass loss rates, and heat release

rates were successfully simulated in the chosen range of conditions which include varying the heat flux, the flow conditions, the surface to volume ratio, and bulk density. These variations influenced the radiation penetration, the heating and cooling rates, as well as the degradation and the combustion of the fuel. On the basis of the results presented in this thesis, the following conclusions can be drawn:

- The spectral emissivity analysis allowed a better description of the radiative heat transfer, as the effective absorptivity of pine needles was relatively lower (~ 0.64) in the near infrared band (typical of FPA heaters radiation) than when submitted to flame radiation (~ 0.92). The results found in this studies illustrate the importance of characterising the spectral properties of the fuels subjected to distinctive radiation of the FPA and to flame radiation. This is an important aspect to consider while using this apparatus, even for different fuels.
- The extinction coefficient was estimated for the specific testing configuration, which is representative of pine needle litters in their natural state. An additional correction factor of 1.15 was required, due to the heterogeneity of the sample and the non-spherical shape that was not considered in the multiphase approach. This parameter has an important impact on the heat in depth distribution and should not be neglected.
- The estimation of the convective heat transfer coefficient required adaptation depending on the flow conditions. Different models that are often used in the multiphase approach were examined. However, we found that they were not adapted to our experimental conditions, as some overestimated the heat transfer coefficient and prevented the fuel from igniting. We provided two models, one for natural convection, and another one for forced flow conditions. These models provide suitable temperature estimations,

matching experimental measurements during the heating phase. In general, if radiative and convective heat transfers are poorly represented, the sample heating and the burning dynamics will be poorly predicted.

- A two-step Arrhenius model was determined to be adequate to represent the experimental conditions with no forced flow and giving similar tendencies and magnitudes for the Mass Loss Rate ([MLR](#)) and Heat Release Rate ([HRR](#)) with different bulk densities. In these models, the magnitude of the pyrolysis rate estimation can be affected by the provided kinetic coefficients. However, the general tendency of the pyrolysis rate and the [MLR](#) are strongly driven by the heat transfer estimation and the energy balance. Thus, it is more important to verify that the heat transfer is correctly represented before evaluating the degradation rates.
- In forced flow conditions, the char oxidation model based on a single step Arrhenius equation was proved sufficient and needs no further improvements. However, the model requires enhancement in natural convection because of the low oxygen concentrations. This can be accomplished by either using a more comprehensive model or by accounting for the increase of the surface to volume ratio in the solid phase as a result of the char pores forming in the fuel. The latter suggestion provided better mass loss estimations after flameout, but it needs to be tested for more configurations.
- By implementing a split function to the char oxidation rate and an inert CO species that does not oxidise. We proposed a model based on [Evans and Emmons \(1977\)](#) that can generate a fraction of CO and CO₂ depending on whether smouldering combustion is occurring. This improved the previous implementation that oxidised all available CO in the gas phase, and that only considered CO₂ production due to char oxidation. Results showed that

this model can successfully reproduce the experimental tendencies qualitatively. However, this aspect will need further investigations, especially for supporting emission estimations.

- The estimation of the drag force coefficient directly affected the flow field inside and around the porous fuel sample. Consequently, it affected the associated burning dynamics for both flaming, and smouldering combustion. The proposed simulations can be used for subgrid modelling in large scale simulations to represent the drag force through litter beds separately from the one for trees, as both are very different.
- An extended Eddy Dissipation Concept (EDC) gas phase combustion model was used in this study. It has the advantage of considering both laminar and turbulent flow characteristics, and the transition between both, which can occur in the FPA configuration and in wildfires. The combustion model was not sufficient for estimating unburned pyrolysis products during flaming. However, it did not affect the quality of the result and the general trends for predicting the burning dynamics of the solid phase and the relevance of the submodel improvements.

Recommendation for future work

The analysis presented in this thesis allowed verifying if the different submodels realated to the fuel are adapted and allowed to pinpoint how they influence the results, by being a source of error, and most importantly by misrepresenting the physical phenomena involved in the process. This study ensures that the physics involved in the burning of the fuel are correctly represented. This step has to be perceived as a preliminary step before predicting fire spread at a larger scale, where the sources of uncertainty are very large due to the complex conditions.

Finally, the following recommendations are proposed to use this model at a larger scale:

- Since very fine mesh was used in the computational domain, the influence of the turbulence model was negligible. Therefore, a One eddy equation ([LES](#)) turbulence model was used. However, for tests with coarser meshes we recommend to verify that this submodel is adapted, especially near the ground ([Ren et al., 2016](#)). Furthermore, it is important to test the model with three dimensional simulations, especially with turbulent flows.
- Future users are also recommended to further investigate the gas phase combustion model, and to verify that the flame geometry and the flame radiation are adequately represented. Indeed, it was not the goal of this study, but it will be necessary for propagation studies.

Overall, fire science is relatively new compared to other disciplines and its application to wildfires appeared even more recently. Despite being a major and recurrent issue in the world, research in wildfire remains minor compared to other research fields. Historically, wildfires were studied by land managers, foresters, and environmentalist, which is why most existing studies relied on observations, phenomenological descriptions, or statistics. From an engineering point of view, understanding the physical and chemical phenomena driving and influencing a fire are important before predicting the fire spread rate, its intensity as well as its occurrence. The knowledge developed in this study proves that when it comes to understanding such complex problems, each aspect (submodel) needs to be evaluated in a controlled and repeatable way, before adding layers of complexity. This approach of using a building block method has been successfully applied in various fields. Additionally, with the computational capabilities available nowadays and with the diagnostic tools constantly improving, it is possible to conduct more measurements with better precision in a fire test to evaluate the

range of validity of a model, and improve our understanding of the subject. As Computational Fluid Dynamics (CFD) still presents a bottleneck for providing fast and operational results, the improved knowledge extracted from the physical approach should be used to develop simplified physical models that can deliver faster results at a larger scale.

Appendix A

Spectral Analysis Configuration

The experimental configurations of the spectral analysis conducted at FM Global Laboratory measuring the radiative properties of pitch pine needles are described hereafter*. It is noted that other studies that have investigated the spectral characteristics of pine needles ([Daughtry et al., 1989](#); [Mesarch et al., 1999](#); [Acem et al., 2010](#)) used samples consisting of a single layer of needles. In this case, corrections were needed to take into account the effect of void spaces between the needles; no such correction techniques are employed herein. However, it is necessary to ensure that the fraction of blackbody emissive power contained within the spectral band is as high as possible. This allows characterising the radiation of temperatures typical of fires and bench-scale tests such as those conducted in the Fire Propagation Apparatus ([FPA](#)), which are very dominant in the near infrared ([Chaos, 2014](#)). Two instruments were used to cover this spectral range:

*Extracted from: [Chaos \(2015\)](#) Spectral analysis of pitch pine needles. Personal Communication

- Ultraviolet, visible, and near infrared spectra (0.25-2.5 μm) were collected by a double-beam Shimadzu UV-3600 UV-Vis-NIR spectrophotometer equipped with a 6-cm diameter integrating sphere coated with barium sulfate (BaSO_4) and fitted with lead selenide and photomultiplier detectors.
- Mid- and long-infrared spectra (2-20 μm) were obtained with a Nicolet iS10 Fourier Transform Infra-Red (FTIR) spectrometer coupled with a 7.6 cm diameter gold-coated integrating sphere (Pike Technologies IntegratIRTM) fitted with a mercury cadmium telluride (HgCdTe) detector.

For measurements in the ultraviolet, visible, and near infrared spectral regions, a substitution method was employed where the reflectivity of the samples was compared to that of a calibrated reference (Fig. A.1a). Measured values were corrected for substitution errors (Jacquez and Kuppenheim, 1955). For measurements in the mid- and long-infrared regions a flipper mirror could be switched to illuminate a calibrated reference or the sample so that no substitution was needed (Taylor, 1920), see Fig. A.1b.

All reflectivity measurements were performed by illuminating the samples at 8° from their surface normal and collecting the total hemispherical reflectivity (directional-hemispherical measurement). It is noted that no attempt was made to separate the measured reflectivity into diffuse and specular components. All surfaces are assumed to be Lambertian (diffuse) so that specularly reflected light is negligible compared to the total hemispherical value. Two sets of scans were taken for each measurement: one for the calibrated reference (the background reading) immediately followed by the sample scan. The calibrated reference used for the ultraviolet, visible, and near infrared measurements was a NIST traceable Labsphere Spectralon[®]. certified diffuse reflectance standard (component SRS-99-010, serial 7A37B-4165); for the mid- and long-infrared measurements a NPL (National Physics Laboratory, UK) traceable Avian gold certified diffuse

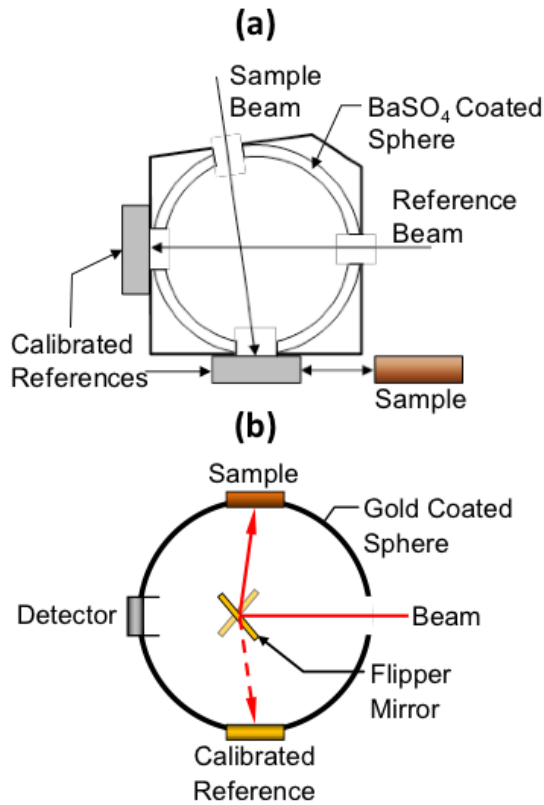


Figure A.1: Spectral reflectivity measurement systems: a) integrating sphere for measurements in the ultraviolet, visible, and near infrared; b) integrating sphere for measurements in the mid- and long-infrared.

reflectance standard (model RS-Au-02c, calibration AT-20121201-IR1) was used. The uncertainty in the calibration values of the references is 2 %; the uncertainty in the spectral measurements reported herein is estimated to be 5 % due to photometric accuracy of the detectors used.

The moisture content, on a dry mass basis, was 13.3 ± 0.7 %, based on five repeat measurements performed on an A & DMX-50 Moisture Analyser. Needles were placed on sample holders with 25.4 mm diameter apertures (Fig. A.2); this aperture size ensured that the needles filled the sample ports of the integrating spheres used. Samples were prepared by arranging needles either in structured side-by-side (Fig. A.2a) or random (Fig. A.2b) orientations). Three samples of

each orientation were assembled. As mentioned above, sufficient needle layers were used to generate optically opaque samples. On average the thickness of the samples tested was 10 mm, approximately.

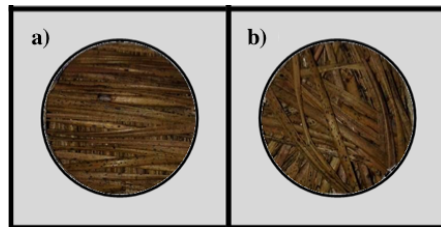


Figure A.2: Pitch pine needle samples prepared for spectral analysis a) arranged in structured b) random orientations.

Appendix B

Mathematical demonstration for density equation in the solid phase

The humidity (H_u) is computed from the water mass fraction in the solid phase such as:

$$H_u = \frac{Y_{H_2O}^{(s)}}{Y_{dry}^{(s)}} \quad (B.1)$$

$$H_u = \frac{\rho_{H_2O}}{\rho_{dry}} \frac{X_{H_2O}}{X_{dry}} \quad (B.2)$$

With X representing the mole fraction in the solid phase.

$$X_{dry} + X_{H_2O} = 1 \quad (B.3)$$

H_u can also be expressed in the following way:

$$H_u = \frac{\rho_{H_2O}}{\rho_{dry}} \frac{X_{H_2O}}{(1 - X_{H_2O})} \quad (B.4)$$

This formulation leads to

$$H_u - H_u X_{H_2O} = \frac{\rho_{H_2O}}{\rho_{dry}} X_{H_2O} \quad (\text{B.5})$$

$$H_u = X_{H_2O} \left[\frac{\rho_{H_2O}}{\rho_{dry}} + H_u \right] \quad (\text{B.6})$$

$$X_{H_2O} = \frac{H_u}{\frac{\rho_{H_2O}}{\rho_{dry}} + H_u} \quad (\text{B.7})$$

The density of the solid phase is defined as:

$$\rho_s = \rho_{dry} X_{dry} + \rho_{H_2O} X_{H_2O} \quad (\text{B.8})$$

$$\rho_s = \rho_{dry} (1 - X_{H_2O}) + \rho_{H_2O} X_{H_2O} \quad (\text{B.9})$$

$$\rho_s = X_{H_2O} (\rho_{H_2O} - \rho_{dry}) + \rho_{dry} \quad (\text{B.10})$$

By introducing Eq. [B.7](#) into Eq. [B.10](#), ρ_s becomes*:

$$\rho_s = \rho_{dry} \alpha_s + (\rho_{H_2O} - \rho_{dry}) \frac{H_u}{\frac{\rho_{H_2O}}{\rho_{dry}} + H_u} \quad (\text{B.11})$$

*Extracted from: Lamorlette, A. (2012) Calcul des propriétés de ρ_s et Cp_s . Personal Communication.

Appendix C

Boundary Conditions

WALL			PATCH		
	Base	Lamps	Top	Outlet	Sides
	Calculated;	Calculated;	Calculated;	Calculated;	Calculated;
p	InternalField uniform 101325;	InternalField; buoyantPressure;	InternalField; type totalPressure;	InternalField; type totalPressure;	InternalField; type totalPressure;
p_rgh	InternalField uniform 101325;	InternalField;	p0 U; phi; rho; psi; gamma 0;	p0 U; phi; rho; psi; gamma 0;	p0 U; phi; rho; psi; gamma 0;
U	InternalField uniform (0 0 0);	type fixedValue; value uniform (0 0 0);	InternalField; type inletOutlet; value \$InternalField; type pressureInletOutletVelocity;	InternalField; type pressureInletOutletVelocity; value \$InternalField; type pressureInletOutletVelocity;	InternalField; type pressureInletOutletVelocity; value \$InternalField; type pressureInletOutletVelocity;
k	InternalField uniform 1e-4;	type zeroGradient;	InternalField; type inletOutlet; inletValue uniform 1e-4; type zeroGradient;	InternalField; type inletOutlet; inletValue uniform 1e-4; type zeroGradient;	InternalField; type inletOutlet; inletValue uniform 1e-4; type zeroGradient;
mu_sgs	InternalField uniform 0;	type fixedValue; value uniform 0.0;	InternalField; type inletOutlet; inletValue uniform 1e-4; type zeroGradient;	InternalField; type inletOutlet; inletValue uniform 1e-4; type zeroGradient;	InternalField; type inletOutlet; inletValue uniform 1e-4; type zeroGradient;
alpha_sgs	InternalField uniform 0;	type alphaSgsWallFunction; value uniform 0;	InternalField; type inletOutlet; inletValue uniform 1e-4; type zeroGradient;	InternalField; type inletOutlet; inletValue uniform 1e-4; type zeroGradient;	InternalField; type inletOutlet; inletValue uniform 1e-4; type zeroGradient;
T	InternalField uniform 0;	fixedValue; value uniform 290;	InternalField; type inletOutlet; value uniform 290;	InternalField; type inletOutlet; value uniform 290;	InternalField; type inletOutlet; value uniform 290;
ldDefault	InternalField uniform 0;	type greyDiffusiveRadiation; T T; emissivityMode lookup; emissivity uniform 1; value uniform 0;	type greyDiffusiveRadiation; T T; emissivityMode lookup; emissivity uniform 1.0; value uniform 0;	type greyDiffusiveRadiation; T T; emissivityMode lookup; emissivity uniform 1.0; value uniform 0;	type greyDiffusiveRadiation; T T; emissivityMode lookup; emissivity uniform 1.0; value uniform 0;
G	InternalField uniform 0;	type MarshakRadiation; T T; emissivity 1; value uniform 0;	type MarshakRadiation; T T; emissivity 1; value uniform 0;	type MarshakRadiation; T T; emissivity 1; value uniform 0;	type MarshakRadiation; T T; emissivity 1; value uniform 0;
N2	InternalField uniform 0.76699;	InternalField; fixedValue; value \$InternalField;	InternalField; fixedValue; value \$InternalField;	InternalField; fixedValue; value \$InternalField;	InternalField; fixedValue; value \$InternalField;
O2	InternalField uniform 0.23301;	InternalField; fixedValue; value \$InternalField;	InternalField; fixedValue; value \$InternalField;	InternalField; fixedValue; value \$InternalField;	InternalField; fixedValue; value \$InternalField;

Figure C.1: Boundary conditions

Appendix D

Extension to Live Needles

In order to test the models performance for more complex fuel, we attempted to simulate the combustion of live pine needles in the [FPA](#), following the same experimental configuration, using the [FPA](#). In this way, only the fuel properties were modified, and all the other experimental conditions remained the same. The main differences between live and dead needles are the values for the density and the fuel moisture content Fuel Moisture Content ([FMC](#)). In these tests, full grown (one-year-old) pitch pine needles were selected, all belonging from the same generation of foliage (season). Fully grown needles were chosen because their moisture is usually constant compared to new growth needles. The latter which may exceed to 250 % then drops rapidly to 120 %, as they grow in size from the spring until midsummer until they match the moisture content of the older foliage near the end of their growth ([Jolly et al., 2014](#)).

Experimental conditions

For convenience, the amount of water in the fuel is expressed in percentage, computed from the weight of contained water divided by the dry weight of the fuel. Moisture content ranges from 40 to 120 % in live needles, and from 5 to 30 % for dead needles (Jolly et al., 2012). The tested needles were conditioned in an oven for specific durations in order to reach the FMC wanted, as shown in Table D.1. These experimental data are extracted from Thomas (2017).

Table D.1: Conditioning and properties of live needles

FMC (%)	Oven time (h)	Total mass (g)	Porosity (%)
7	24	13.95	95.3
25	5.5	17.14	94.5
50	3	21.50	93.5
110	0	29.44	91.8

Prior to the oven conditioning, the FMC ranged between 90 and 120 %. All others FMC were artificially achieved by drying them in an oven at 60°C for a specific duration (Table D.1). The dry mass of material was kept constant in the samples for all tests (13.9 g). After completely drying needles, they naturally absorb water available in air by extracting water vapour from the atmosphere, until the vapour pressure of the outer surface of the bound water is equivalent to the surrounding vapour pressure. This is equivalent to 4-7 % of FMC on dry basis.

Additionally, a spectral analysis was conducted (described in Chapters 2 and 3) for live needles with a FMC of 134.7 ± 6 %. As the FPA heaters radiate at temperatures of $2,000 \text{ K} < T_r < 3,000 \text{ K}$ (Chaos, 2014), the effective absorptivity of live needles was on average, $\alpha_{eff} = 0.72$, over this temperature range. This value is higher than for dead needles (0.67). The difference in the measured absorptivity is due to the difference in the colour pigments, internal cell structure

of the needles, and especially water content that increase the absorptivity (Rock et al., 1986).

Results and discussion

Mass loss

The detailed mass loss evolution is presented in Fig. D.1 for a sample with 100 % FMC. One can notice that ignition occurred when half of the initial FMC evaporated. However, the evolution of the mass loss in one cell in the sample (Fig. D.2) indicates that all the water was evaporated before ignition of the cell. These results are in agreement with the observations reported by Pickett et al. (2010) on the ignition of various live leaf samples. They found that ignition did not occur at the end of global evaporation, but at the end of local evaporation. They also found that a 30 to 60 % of moisture remained in the sample at ignition time.

Heat release rate

The evolution of the heat release rate is presented in Fig. D.3a for tests performed with live needles with 7 % FMC, corresponding to the driest conditions that can be achieved. The results are also compared to simulations and to experiments performed with dead needles with the same conditions (7 % FMC). Average values from three repetitions are shown, for clarity, experimental variations are not included. The maximum variations were 1.7 kW and 0.6 kW for live and dead fuel, respectively. Differences are observed between the Heat Release Rate (HRR)

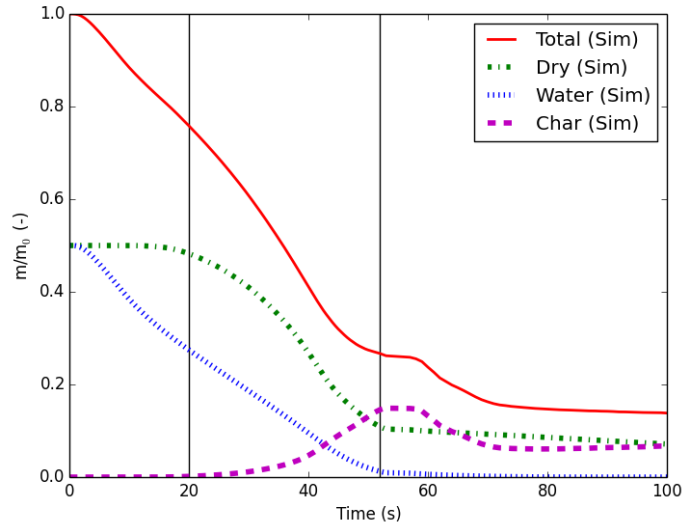


Figure D.1: Simulated mass loss, including dry, water, and char fractions. Vertical lines: ignition and flameout times; FMC 50 %, NF, 40 kg/m³.

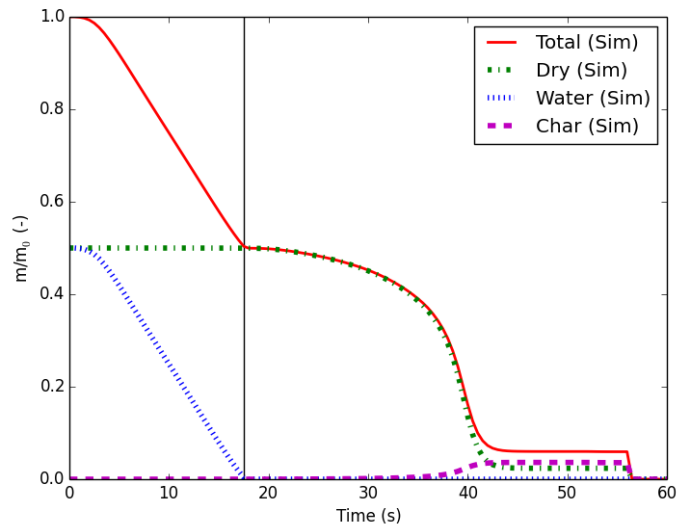


Figure D.2: Simulated mass loss in one cell, including dry, water, and char fractions. Vertical lines: ignition; FMC 50 %, NF, 40 kg/m³.

curves of live and dead fuels. The maximum value is slightly higher for live needles (9 kW) than for dead needles (8 kW).

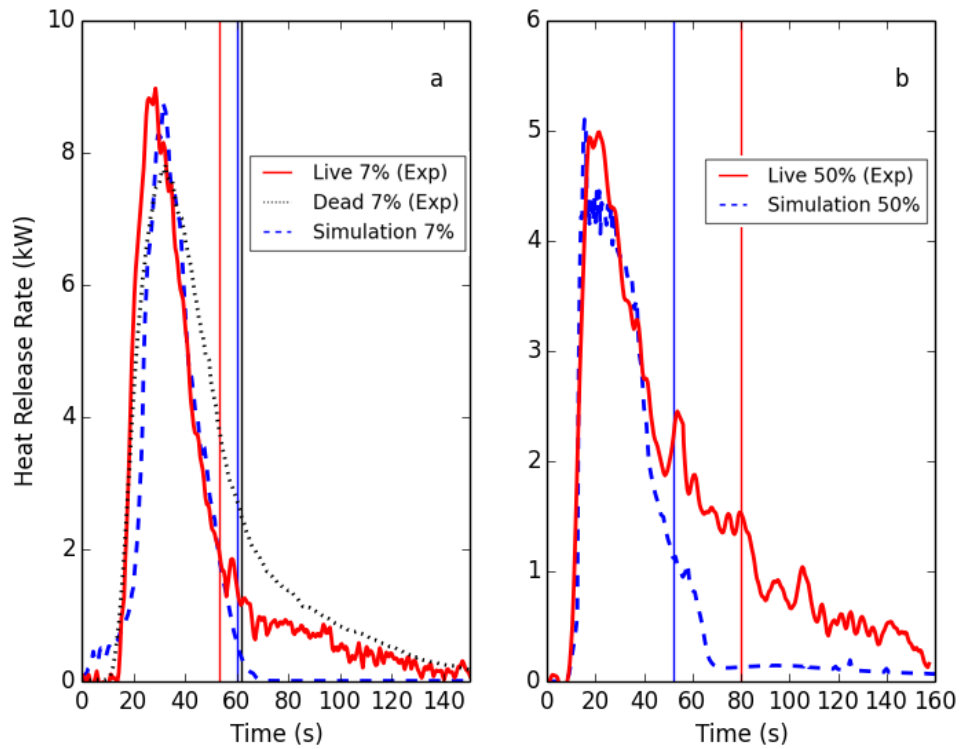


Figure D.3: Measured and simulated heat release rates for a) 7 %; b) 50 % fuel moisture content.

Grishin (1996) reported that chemical composition of live pine foliage and dead pine litter is different. Thus, the physical and chemical processes that occur during the growth and decay of pine needles lead to substantial changes in the flammable properties of the fuel (Grishin, 1996). Concerning the simulation, as the model does not discern between live and dead fuel, the computed HRR during the first 60 s provides a tendency that fits between both measured ones. However, after flameout (60 s), smouldering is not well predicted as the char combustion rate is low, again due to the fact that low oxygen concentration is available in no flow condition, as explained earlier. Concerning the water loss mechanism, it is reduced to consider only a solid to gas phase change through an Arrhenius equation that triggers around 100°C (Chapter 3), where in reality, the mechanism

is more complex, and is related to an evapo-transpiration mechanism that occurs at much lower temperatures (Nobel, 2009).

The computed and measured heat release rates of live needles with 50 % FMC are presented in Fig. D.3b. The measured HRR peaked at 5 kW, instead of 9 kW for 7 %, because water vapour dilutes the gas mixture, making it more difficult to generate a flammable mixture. This is in agreement with the numerical analysis provided in Ferguson et al. (2013) where water vapour was introduced into a gas mixture of a diffusion flame. Similar behaviour was also observed by Morvan (2013). However, the total heat realised was 15 % higher for 50 % FMC than for the dry one. Since the dry mass is the same for both cases, this endorses the observations made in Fig. D.3a. Here for instance, less heat is generated during flaming but it is compensated during smouldering (more intense and longer time). Finally, the simulation is able to well predict the tendencies and the peak HRR from ignition until flameout time. However, the char combustion model does not work for the same reasons as for dry needles, as mentioned earlier.

The average values of the HRR were calculated during flaming time and are presented in Fig. D.4 for all the tested FMC. Similarly, the values of the peak HRR are presented in Fig. D.5.

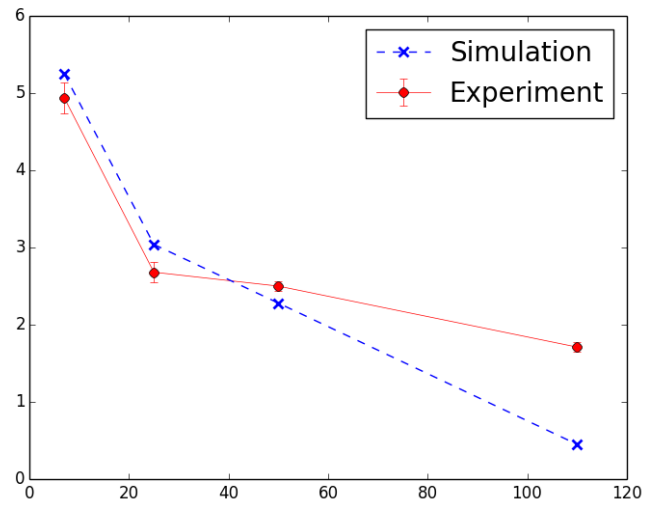


Figure D.4: Measured and simulated average heat release rates for different fuel moisture content.

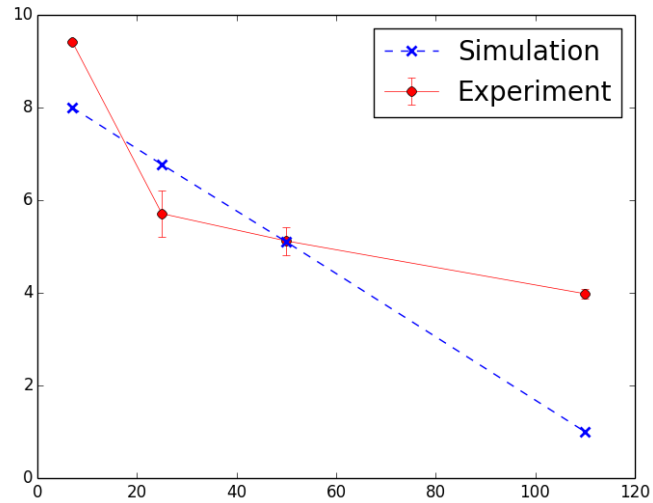


Figure D.5: Measured and simulated peak heat release rates for different fuel moisture content.

A steep drop in the average HRR is observed as the FMC increases from 7 to 25 %, then the curve reaches 2 kW at 110 %. At high FMC, flaming and smouldering

overlapped and they were difficult to discern because of the large amount of water vapour released in the air. Tendencies observed in Fig. D.4 and D.5 indicate that live fuel released more energy than what was predicted, especially at high FMC. Moreover, the predicted evolution of the peak HRR is almost linear. Whereas, experimentally the evolution denotes two different regimes for low FMC and for high FMC. All these indications show that until ~ 50 % FMC, burning dead or live pine needles can be modelled in the same way, but for higher FMC, the current evaporation model is not sufficient. This is due to two main causes:

- First, char combustion was not well represented because of no flow conditions and as smouldering and low efficiency flaming combustion were overlapping for high FMC, the mean and peak HRR were underestimated.
- Second, and more importantly, in the simulations the high amount of water prevented most of the fuel from igniting. This was not observed experimentally. This means that less energy is required to eliminate water from a cell than what was considered.

The simulations can be improved by adding a transpiration model which usually occurs at a lower temperature than for evaporation. Such model would require to calculate the partial pressure of water vapour in the environment, the atmospheric vapour pressure, and the air relative humidity.

Conclusion

In order to test the models performance for more complex fuel, preliminary results obtained for live needles were tested in ForestFireFOAM. Measurements of the peak HRR and the average HRR were compared to numerical prediction at different FMC. Two main regimes were observed for high (>20 %) and low FMC

(< 20 %) on dry basis. The model was successfully able to predict the tendencies from 7 to 50 %. For higher values, above this value, other submodels are needed, especially to represent the evaporation of bound and free water, which is a main characteristic of live fuel.

Appendix E

Charring Effect on the Surface to Volume Ratio

It was demonstrated in Chapter 4 that a single-step Arrhenius equation was not sufficient to model the evolution of char combustion in no flow (NF) conditions. It was found that this underestimation was mainly due to the low oxygen available to sustain the char combustion. In order to improve this issue, the low combustion rate can be enhanced by considering an increase in the surface to volume ratio (SVR) as a function of the charring rate*. This change in the SVR, is physically justified by the formation of pores on the surface of a needles due to char formation, as illustrated in Fig. E.1.

By considering the density of graphite ($\rho_c = 1800 \text{ kg/m}^3$) and the density of char ($\rho_{char} = 200 \text{ kg/m}^3$) (Grishin, 1996), we define a unit-less variable γ as:

$$\rho_{char} = (1 - \gamma)\rho_c \quad (\text{E.1})$$

*Extracted from: Morvan, D. (2015) Surface to volume ratio of a porous cylindrical particle. Personal Communication.

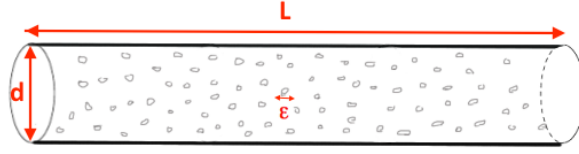


Figure E.1: pine needle approximated as a cylinder with char pores on the surface

$$\gamma = 1 - \frac{\rho_{char}}{\rho_c} = 0.88 \quad (\text{E.2})$$

d_γ and n_γ are defined as the pore diameter ($\sim 50 \mu\text{m}$ (Morvan and Dupuy, 2001)) and the number of pores per unit volume, respectively. The pore surface per unit volume can be calculated the following way:

$$n_\gamma \times 4\pi \left(\frac{d_\gamma}{2} \right)^2 = n_\gamma \pi d_\gamma^2 \quad (\text{E.3})$$

The new surface to volume ratio (σ_s^*) becomes:

$$\sigma_s^* = \frac{\text{surface particle} + \text{surface pores}}{\text{volume}} \quad (\text{E.4})$$

$$\sigma_s^* = \frac{\pi d L + n_\gamma \pi d_\gamma^2 \times \frac{\pi d^2 L}{4} Y_{char}^{(s)}}{\frac{\pi d^2}{4} L} \quad (\text{E.5})$$

$$\sigma_s^* = \frac{4}{d} \left[1 + n_\gamma \frac{\pi}{4} d_\gamma^2 d Y_{char}^{(s)} \right] \quad (\text{E.6})$$

with $Y_{char}^{(s)}$ the char mass fraction in the solid phase. γ can be re-written as:

$$\gamma = n_\gamma \times \frac{4}{3} \pi \left(\frac{d_\gamma}{2} \right)^3 = n_\gamma \frac{\pi d_\gamma^3}{6} \quad (\text{E.7})$$

Eq. E.3 becomes:

$$n_\gamma \pi d_\gamma^2 = \frac{6\pi}{d_\gamma} \quad (\text{E.8})$$

By introducing Eq. E.8 into Eq. E.6, σ_s^* becomes:

$$\sigma_s^* = \frac{4}{d} \left[1 + \frac{3}{2} \gamma \frac{d}{d_\gamma} Y_{char}^{(s)} \right] \quad (\text{E.9})$$

For a cylindrical needle, the diameter can be approximated as a function of the surface to volume ratio:

$$\sigma_s = \frac{\pi d L}{\pi \frac{d^2}{4} L} = \frac{4}{d} \quad (\text{E.10})$$

Finally, σ_s^* becomes:

$$\sigma_s^* = \sigma_s \left[1 + \frac{3}{2} \gamma \frac{d}{d_\gamma} Y_{char}^{(s)} \right] \quad (\text{E.11})$$

Using Eq. E.11, the surface to volume ratio can only increase with char production. By including σ_s^* to the char oxidation model (Chapter 3) in NF conditions, the mass loss after flameout is improved, as observed in Fig. E.2. However, this model is limited to NF conditions, because its inclusion highly

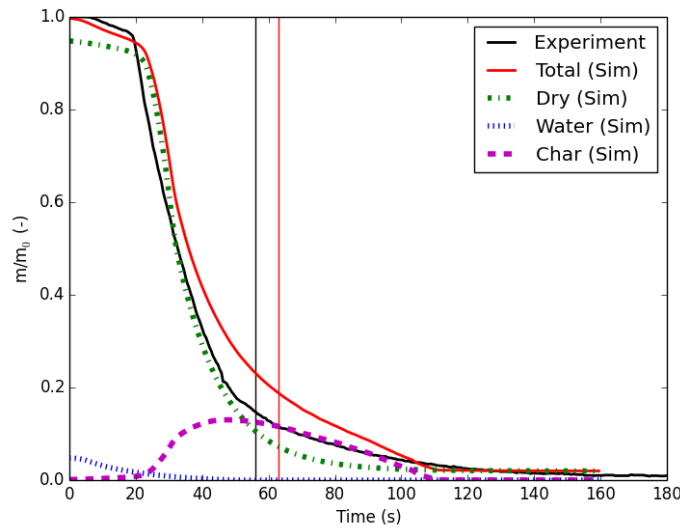


Figure E.2: Simulated mass loss, including dry, water, and char fractions. Vertical lines: flameout times; Pitch pine, NF, 40 kg/m³.

affects the char combustion rate (and numerical stability) especially if a forced flow is introduced. Therefore, further development of this submodel are promising.

References

- B. Abdalhaq, A. Cortés, T. Margalef, and E. Luque. *Optimization of Fire Propagation Model Inputs: A Grand Challenge Application on Metacomputers*, chapter Optimizati, pages 447–451. Springer, Berlin, 2002. doi: 10.1007/3-540-45706-2_60.
- Z. Acem, A. Lamorlette, A. Collin, and P. Boulet. Analytical determination and numerical computation of extinction coefficients for vegetation with given leaf distribution. *International Journal of Thermal Sciences*, 48(8):1501–1509, 2009. doi: 10.1016/j.ijthermalsci.2009.01.009.
- Z. Acem, G. Parent, B. Monod, G. Jeandel, and P. Boulet. Experimental study in the infrared of the radiative properties of pine needles. *Experimental Thermal and Fluid Science*, 34(7):893–899, 2010. doi: 10.1016/j.expthermflusci.2010.02.003.
- A. Águas, A. Ferreira, P. Maia, P.M. Fernandes, L. Roxo, J. Keizer, J.S. Silva, F.C. Rego, and F. Moreira. Natural establishment of Eucalyptus globulus Labill. in burnt stands in Portugal. *Forest Ecology and Management*, 323:47–56, Jul 2014. doi: 10.1016/j.foreco.2014.03.012.
- F.A. Albini. Spot fire distance from burning trees - a predictive model. Technical report, USDA Forest Service, Intermountain Forest and Range Experiment Station, Ogden, Utah, 1979.
- F.A. Albini. Wildland Fire Spread by Radiation: a Model Including Fuel Cooling by Convection. *Combustion Science and Technology*, 45:101–113, 1985.
- M.E. Alexander and M.G. Cruz. Evaluating a model for predicting active crown fire rate of spread using wildfire observations. *Canadian Journal of Forest Research*, 36(11):3015–3028, Nov 2006. doi: 10.1139/x06-174.
- A. Anca-Couce, N. Zobel, A. Berger, and F. Behrendt. Smouldering of pine wood: Kinetics and reaction heats. *Combustion and Flame*, 159(4):1708–1719, Apr 2012. doi: 10.1016/j.combustflame.2011.11.015.

- D.H. Anderson, E.A. Catchpole, N.J. De Mestre, and T. Parkes. Modelling the spread of grass fires. *The Journal of the Australian Mathematical Society. Series B. Applied Mathematics*, 23(04):451, Apr 1982. doi: 10.1017/S0334270000000394.
- H.E. Anderson. *Heat transfer and fire spread*. Intermountain Forest and Range Experiment Station, Forest Service, U.S. Dept. of Agriculture, Ogden, Utah, 1969. doi: 10.5962/bhl.title.69024.
- H.E. Anderson. Forest fuel ignitibility. *Fire Technology*, 6(4):312–319, Nov 1970. doi: 10.1007/BF02588932.
- X. Arnan, A. Rodrigo, and J. Retana. Post-fire recovery of Mediterranean ground ant communities follows vegetation and dryness gradients. *Journal of Biogeography*, 33(7):1246–1258, Jul 2006. doi: 10.1111/j.1365-2699.2006.01506.x.
- S. Arrhenius. On the influence of carbonic acid in the air upon the temperature of the ground. *Philosophical Magazine and Journal of Science*, 41(5):237–276, 1896.
- ASTM International. ASTM E2058-03, Standard Test Methods for Measurement of Synthetic Polymer Material Flammability Using a Fire Propagation Apparatus (FPA), 2003.
- V. Babrauskas. *Ignition handbook*. Fire Science Publishers/Society of Fire Protection Engineers, Issaquah, WA, 2003. ISBN 0972811133.
- M.J. Baeza, A. Valdecantos, J.A. Alloza, and V.R. Vallejo. Human disturbance and environmental factors as drivers of long-term post-fire regeneration patterns in Mediterranean forests. *Journal of Vegetation Science*, 18(2):243, 2007. doi: 10.1658/1100-9233(2007)18[243:HDAEFA]2.0.CO;2.
- R. S. Barlow, A. N. Karpetis, J. H. Frank, and J. Y. Chen. Scalar profiles and NO formation in laminar opposed-flow partially premixed methane/air flames. *Combustion and Flame*, 127(3):2102–2118, 2001. doi: 10.1016/S0010-2180(01)00313-3.
- P. Bartoli, A. Simeoni, J. L. Torero, and P.A. Santoni. Experimental study on the combustion dynamics of forest floor fuel beds. In *6th International Conference on Forest Fire Research*, page 151, 2010.
- P. Bartoli, A. Simeoni, H. Biteau, J.L. Torero, and P.A. Santoni. Determination of the main parameters influencing forest fuel combustion dynamics. *Fire Safety Journal*, 46(1-2):27–33, Jan 2011. doi: 10.1016/j.firesaf.2010.05.002.
- T. Beer. The interaction of wind and fire. *Boundary-Layer Meteorology*, 54(3):287–308, Feb 1991. doi: 10.1007/BF00183958.

- C.M. Belcher, J.M. Yearsley, R.M. Hadden, J.C. McElwain, and G. Rein. Baseline intrinsic flammability of Earth's ecosystems estimated from paleoatmospheric oxygen over the past 350 million years. *Proceedings of the National Academy of Sciences*, 107(52):22448–22453, Dec 2010. doi: 10.1073/pnas.1011974107.
- B. Benkoussas, J. L. Consalvi, B. Porterie, N. Sardoy, and J. C. Loraud. Modelling Thermal Degradation of Woody Fuel Particles. *International Journal of Thermal Sciences*, 46(4):319–327, 2007. doi: 10.1016/j.ijthermalsci.2006.06.016.
- B.S. Beshty. A mathematical model for the combustion of a porous carbon particle. *Combustion and Flame*, 32:295–311, Jan 1978. doi: 10.1016/0010-2180(78)90104-9.
- H. Biteau, T. Steinhaus, C. Schemel, A. Simeoni, G. Marlair, N. Bal, and J. Torero. Calculation Methods for the Heat Release Rate of Materials of Unknown Composition. *Fire Safety Science*, 9:1165–1176, 2008. doi: 10.3801/IAFSS.FSS.9-1165.
- W.J. Bond, F.I. Woodward, and G.F. Midgley. The global distribution of ecosystems in a world without fire. *New Phytologist*, 165(2):525–538, Nov 2004. doi: 10.1111/j.1469-8137.2004.01252.x.
- N. Boonmee and J.G. Quintiere. Glowing ignition of wood: the onset of surface combustion. *Proceedings of the Combustion Institute*, 30(2):2303–2310, Jan 2005.
- P. Boulet, G. Parent, Z. Acem, a. Collin, and O. Séro-Guillaume. On the emission of radiation by flames and corresponding absorption by vegetation in forest fires. *Fire Safety Journal*, 46(1-2):21–26, 2011. doi: 10.1016/j.firesaf.2010.03.006.
- G.M. Byram. Combustion of forest fuels. In K.P. Davis, editor, *Forest fire: control and use*, pages 61–89. McGraw and Hill, New York, 1959a.
- G.M. Byram. Forest fire behaviour. In K.P. Davis, editor, *Forest fire: control and use*, pages 90–123. McGraw and Hill, New York, 1959b.
- D. Cancellieri, E. Leoni, and J.L. Rossi. Kinetics of the thermal degradation of *Erica arborea* by DSC: Hybrid kinetic method. *Thermochimica Acta*, 438(1-2): 41–50, Nov 2005. doi: 10.1016/j.tca.2005.07.013.
- D. Cancellieri, V. Leroy-Cancellieri, E. Leoni, A. Simeoni, A.Y. Kuzin, .I. Filkov, and G. Rein. Kinetic investigation on the smouldering combustion of boreal peat. *Fuel*, 93:479–485, Mar 2012. doi: 10.1016/j.fuel.2011.09.052.
- D. Cancellieri, V. Leroy-Cancellieri, and E. Leoni. Multi-scale kinetic model for forest fuel degradation. In *Advances in forest fire research*, pages 360–370.

- Imprensa da Universidade de Coimbra, Coimbra, 2014. doi: 10.14195/978-989-26-0884-6_40.
- B.G. Carlson and K.D. Lathrop. *Transport Theory: The Method of Discrete Ordinates*. U.S Atomic Energy and Laboratory, Los Alamos Scientific Commission, 1965.
- CFD Direct Ltd. OpenFOAM User Guide: 4.4 Numerical schemes, 2015. URL <http://cfd.direct/openfoam/user-guide/fvschemes/>.
- S. Chandrasekhar. *Radiative Transfer*. 1960. doi: 10.1007/SpringerReference_221860.
- M. Chaos. Spectral Aspects of Bench-Scale Flammability Testing: Application to Hardwood Pyrolysis. *Fire Safety Science*, 11:165–178, 2014. doi: 10.3801/IAFSS.FSS.11-165.
- M. Chaos. Determination of Separation Distances Inside Large Buildings. *Fire Technology*, 2015. doi: 10.1007/s10694-015-0548-0.
- P. Chatterjee, J.L. De Ris, Y. Wang, N. Krishnamoorthy, and S.B. Dorofeev. Laminar Smoke Point Based Subgrid Soot Radiation Modeling Applied to LES of Buoyant Turbulent Diffusion Flames. *Journal of Physics: Conference Series*, 369:10, 2012. doi: 10.1088/1742-6596/369/1/012009.
- N.P. Cheney and J.S. Gould. Fire Growth in Grassland Fuels. *International Journal of Wildland Fire*, 5(4):237–247, 1995.
- N.P. Cheney, J.S. Gould, and W.R. Catchpole. The Influence of Fuel, Weather and Fire Shape Variables on Fire-Spread in Grasslands. *International Journal of Wildland Fire*, 3(1):31–44, 1993.
- N.P. Cheney, J.S. Gould, and W.R. Catchpole. Prediction of Fire Spread in Grasslands. *International Journal of Wildland Fire*, 8(1):1, 1998. doi: 10.1071/WF9980001.
- N.S. Cheng. Calculation of Drag Coefficient for Arrays of Emergent Circular Cylinders with Pseudofluid Model. *Journal of Hydraulic Engineering*, 139(6): 602–611, 2013. doi: 10.1061/(ASCE)HY.1943-7900.0000722.
- R.N. Clark, G.A. Swayze, R. Wise, E. Livo, T. Hoefen, R. Kokaly, and S.J. Sutley. USGS Digital Spectral Library splib06a: U.S. Geological Survey, Digital Data Series 231, 2007.
- T.L. Clark, J. Coen, and D. Latham. Description of a coupled atmosphere-fire model. *International Journal of Wildland Fire*, 13(1):49–63, 2004.

- R. Clift, J.R. Grace, and M.E. Weber. *Bubbles, Drops and Particles*. Academic Press New York, 1978.
- J.L. Coen, M. Cameron, J. Michalakes, E.G. Patton, P.J. Riggan, and K.M. Yedinak. WRF-Fire: Coupled Weather/Wildland Fire Modeling with the Weather Research and Forecasting Model. *Journal of Applied Meteorology and Climatology*, 52(1):16–38, Jan 2013. doi: 10.1175/JAMC-D-12-023.1.
- J.L. Consalvi, F. Nmira, A. Fuentes, P. Mindykowski, and B. Porterie. Numerical Study of Piloted Ignition of Forest Fuel Layer. *Proceedings of the Combustion Institute*, 33:2641–2648, 2011.
- M.G. Cruz, A.L. Sullivan, J.S. Gould, N.C. Sims, A.J. Bannister, J.J. Hollis, and R.J. Hurley. Anatomy of a catastrophic wildfire: The Black Saturday Kilmore East fire in Victoria, Australia. *Forest Ecology and Management*, 284:269–285, 2012. ISSN 03781127. doi: 10.1016/j.foreco.2012.02.035.
- M.G. Cruz, J.S. Gould, S. Kidnie, R. Bessell, D. Nichols, and A. Slijepcevic. Effects of curing on grassfires: II. Effect of grass senescence on the rate of fire spread. *International Journal of Wildland Fire*, 24(6):838, 2015. doi: 10.1071/WF14146.
- B. Cuenot. Introduction à la modélisation de la combustion turbulente CER-FACS/CFD Toulouse - France: Cours de Combustion Turbulente de D. Veynante, ECP et L. Vervisch, INSA Rouen, 2005.
- C.S.T. Daughtry, L.L. Biehl, and K.J. Ranson. A new technique to measure the spectral properties of conifer needles. *Remote Sensing of Environment*, 27(1): 81–91, Jan 1989. doi: 10.1016/0034-4257(89)90039-4.
- D. Davies, S. Kumar, and J. Descloitres. Global Fire Monitoring Using MODIS Near-Real-Time Satellite Data. *GIM International*, 18(4):41–43, 2004.
- N.J. De Mestre, E.A. Catchpole, D.H. Anderson, and R.C. Rothermel. Uniform Propagation of a Planar Fire Front without Wind. *Combustion Science and Technology*, 65(4-6):231–244, 1989.
- C. Di Blasi. Comparison of semi-global mechanisms for primary pyrolysis of lignocellulosic fuels. *Journal of Analytical and Applied Pyrolysis*, 47(1):43–64, 1998. doi: 10.1016/S0165-2370(98)00079-5.
- C. Di Blasi, C. Branca, A. Santoro, and E. Gonzalez Hernandez. Pyrolytic Behavior and Products of Some Wood Varieties. *Combustion and Flame*, 124(1-2):165–177, 2001. doi: 10.1016/S0010-2180(00)00191-7.
- A.P. Dimitrakopoulos and K.K. Papaioannou. Flammability Assessment of Mediterranean Forest Fuels. *Fire Technology*, 37(2):143–152, 2001.

- K. Dmitrieva. Alberta Wildfires Set for Largest Canadian Disaster for Insurers, 2016. URL <http://www.bloomberg.com/news/articles/2016-05-05/alberta-wildfires-set-for-largest-canadian-disaster-for-insurers>.
- D. Drysdale. *An Introduction to Fire Dynamics*. John Wiley & Sons, Ltd, Chichester, UK, 3rd edition, 2011.
- J.L. Dupuy. Slope and Fuel Load Effects on Fire Behavior: Laboratory Experiments in Pine Needles Fuel Beds. *International Journal of Wildland Fire*, 5(3): 153, 1995. doi: 10.1071/WF9950153.
- J.L. Dupuy, J. Maréchal, and D. Morvan. Fires from a cylindrical forest fuel burner: Combustion dynamics and flame properties. *Combustion and Flame*, 135(1-2):65–76, 2003. doi: 10.1016/S0010-2180(03)00147-0.
- J.L. Dupuy, J. Maréchal, D. Portier, and J.C. Valette. The effects of slope and fuel bed width on laboratory fire behaviour. *International Journal of Wildland Fire*, 20(2):272, 2011. doi: 10.1071/WF09075.
- S. Ebrahim Zadeh, G. Maragkos, T. Beji, and B. Merci. Large Eddy Simulations of the Ceiling Jet Induced by the Impingement of a Turbulent Air Plume. *Fire Technology*, Jan 2016. doi: 10.1007/s10694-015-0561-3.
- M. El Houssami, E. Mueller, A. Filkov, J.C. Thomas, N. Skowronski, M.R. Gallagher, K. Clark, R. Kremens, and A. Simeoni. Experimental Procedures Characterising Firebrand Generation in Wildland Fires. *Fire Technology*, 52(3):731–751, 2016a. doi: 10.1007/s10694-015-0492-z.
- M. El Houssami, J.C. Thomas, A. Lamorlette, D. Morvan, M. Chaos, R. Hadden, and A. Simeoni. Experimental and numerical studies characterizing the burning dynamics of wildland fuels. *Combustion and Flame*, 168:113–126, Jun 2016b. doi: 10.1016/j.combustflame.2016.04.004.
- H.W. Emmons. Fire in the forest. *Fire Research Abstracts and Reviews*, 5:163, 1963.
- H.W. Emmons. Fundamental problems of the free burning fire. *Symposium (International) on Combustion*, 10(1):951–964, Jan 1965. doi: 10.1016/S0082-0784(65)80238-7.
- Equipex Mesocentre. Mésocentre Aix Marseille Université, 2016. URL <https://equipex-mesocentre.univ-amu.fr>.
- D. Evans and H. Emmons. Combustion of Wood Charcoal. *Fire Research*, 1(1): 57–66, 1977.

- P.G. Falkowski. The Rise of Oxygen over the Past 205 Million Years and the Evolution of Large Placental Mammals. *Science*, 309(5744):2202–2204, Sep 2005. doi: 10.1126/science.1116047.
- FAO. Global Forest Resources Assessment 2010. Technical report, Food and Agriculture Organization of the United Nations, Rome, 2010.
- T. Fateh, F. Richard, B. Batiot, T. Rogaume, J. Luche, and J. Zaida. Characterization of the burning behavior and gaseous emissions of pine needles in a cone calorimeter FTIR apparatus. *Fire Safety Journal*, 82:91–100, May 2016. doi: 10.1016/j.firesaf.2016.03.008.
- S.C. Ferguson, A. Dahale, B. Shotorban, S. Mahalingam, and D.R. Weise. The Role of Moisture on Combustion of Pyrolysis Gases in Wildland Fires. *Combustion Science and Technology*, 185(3):435–453, Mar 2013. doi: 10.1080/00102202.2012.726666.
- P.M. Fernandes, H.S. Botelho, and C. Loureiro. Models for the sustained ignition and behaviour of low-to-moderately intense fires in maritime pine stands. In *Proceedings of the IV International Conference on Forest Fire Research, Luso, Portugal*, page 98, 2002.
- P.M. Fernandes, H.S. Botelho, F.C. Rego, and C. Loureiro. Empirical modelling of surface fire behaviour in maritime pine stands. *International Journal of Wildland Fire*, 18(6):698–710, 2009. doi: 10.1071/WF08023.
- A. Fernandez-Pello. On Fire Ignition. *Fire Safety Science*, 10:25–42, 2011. doi: 10.3801/IAFSS.FSS.10-25.
- M.A. Finney. FARSITE: Fire Area Simulator: Model Development and Evaluation. *Research Paper RMRS-RP-4 Revised, USDA Forest Service, Rocky Mountain Research Station, Fort Collins, CO*, 1998.
- M.D. Flannigan, B.J. Stocks, and B.M. Wotton. Climate change and forest fires. *Science of The Total Environment*, 262:221–229, 2000.
- M.D. Flannigan, B.J. Stocks, M. Turetsky, and B.M. Wotton. Impacts of climate change on fire activity and fire management in the circumboreal forest. *Global Change Biology*, 15(3):549–560, Mar 2009. doi: 10.1111/j.1365-2486.2008.01660.x.
- W.L. Fons. Analysis of fire spread in light forest fuels. *Journal of Agricultural Research*, 72(3):93–121, 1946.
- R. Font, J.A. Conesa, J. Moltó, and M. Muñoz. Kinetics of Pyrolysis and Combustion of Pine Needles and Cones. *Journal of Analytical and Applied Pyrolysis*, 85(1-2):276–286, 2009. doi: 10.1016/j.jaap.2008.11.015.

- M. Försth and A. Roos. Absorptivity and Its Dependence on Heat Source Temperature and Degree of Thermal Breakdown. *Fire and Materials*, 35(5): 285–301, Aug 2011. doi: 10.1002/fam.1053.
- J.S. Fried, M.S. Torn, and E. Mills. The Impact of Climate Change on Wildfire Severity: A Regional Forecast for Northern California. *Climatic Change*, 64 (1/2):169–191, May 2004. doi: 10.1023/B:CLIM.0000024667.89579.ed.
- C. Fureby and G. Tabor. Mathematical and Physical Constraints on Large-Eddy Simulations. *Theoretical and Computational Fluid Dynamics*, 9(2):85–102, 1997. doi: 10.1007/s001620050034.
- C. Fureby, G. Tabor, G. Weller, and D. Gosman. A comparative study of subgrid scale models in homogeneous isotropic turbulence. *Physics of Fluids*, 9(5): 1416–1429, 1997.
- L. Giglio, J. Descloitres, C.O. Justice, and Y.J. Kaufman. An enhanced contextual fire detection algorithm for MODIS. *Remote Sensing of Environment*, 87(2-3): 273–282, 2003. doi: 10.1016/S0034-4257(03)00184-6.
- H.T. Gisborne. The Importance of Duff Moisture Content in the Forest Fire Problem. *Journal of Forestry*, 21(8):807–809, 1923.
- H.T. Gisborne. The Objectives of Forest Fire-Weather Research. *Journal of Forestry*, 25(4):452–456, 1927.
- H.T. Gisborne. Early and Modern American Fire Studies. *Journal of Forestry*, 26(1):128–129, 1928.
- I.J. Glasspool and A.C. Scott. Phanerozoic concentrations of atmospheric oxygen reconstructed from sedimentary charcoal. *Nature Geoscience*, 3(9):627–630, Sep 2010. doi: 10.1038/ngeo923.
- GOC. Canadian Forest Fire Weather Index (FWI) System, 2016. URL <http://cwfis.cfs.nrcan.gc.ca/background/summary/fwi>.
- J.S. Gould, W.L. McCaw, N.P. Cheney, P.F. Ellis, I.K. Knight, and A.L. Sullivan. Project Vesta Fire in Dry Eucalypt Forest: Fuel Structure, Dynamics and Fire Behaviour. Technical report, (CSIRO Ensis and Department of Environment and Conservation: Canberra, ACT), 2007.
- A.M. Grishin. Kinetics of non-equilibrium drying of certain forest fuels. In *Fizika Goreniya I Metody Ego Issledovaniya (Physics of combustion and methods of study it)*, pages 11–17, Cheboksary, 1981a. Chuvash University.
- A.M. Grishin. *Matematicheskiye modeli lesnykh pozharov (Mathematical models of forest fires)*. Tomsk University, Tomsk, 1981b.

- A.M. Grishin. *A Mathematical Modelling of Forest Fires and New Methods of Fighting Them*. Publishing House of the Tomsk University, Tomsk, 1996. ISBN 5-7511-0840-X.
- A.M. Grishin, A.N. Golovanov, and S.V. Rusakov. Evaporation of Free Water and Water Bound with Forest Combustibles under Isothermal Conditions. *Journal of Engineering Physics and Thermophysics*, 76(5):1166–1172, Sep 2003. doi: 10.1023/B:JOEP.0000003236.10238.0b.
- P. Groffman, P. Kareiva, S. Carter, N.B. Grimm, J. Lawler, M. Mack, V. Matzek, and H. Tallis. Ecosystems, biodiversity, and ecosystem services. In *Climate change impacts in the United States: The third national climate assessment.*, chapter Ch. 8: Eco, pages 195–219. U.S. Global Change Research Program, 2014. doi: 10.7930/J0TD9V7H.On.
- W. L. Grosshandler. RADCAL: A Narrow-Band Model for Radiation Calculations in a Combustion Environment, NIST technical note 1402. Technical report, 1993.
- R.M. Hadden. *Smouldering and self-sustaining reactions in solids: an experimental approach*. PhD thesis, University of Edinburgh, 2011. URL <http://hdl.handle.net/1842/5587>.
- R.M. Hadden, A. Alkatib, G. Rein, and J.L. Torero. Radiant Ignition of Polyurethane Foam: The Effect of Sample Size. *Fire Technology*, 50(3):673–691, May 2014. doi: 10.1007/s10694-012-0257-x.
- R.B. Hammer, V.C. Radeloff, J.S. Fried, and S.I. Stewart. Wildland-Urban Interface housing growth during the 1990s in California, Oregon, and Washington. *International Journal of Wildland Fire*, 16(3):255–265, 2007. doi: 10.1071/WF05077.
- J. Han, Z. Shen, L. Ying, G. Li, and A. Chen. Early post-fire regeneration of a fire-prone subtropical mixed Yunnan pine forest in Southwest China: Effects of pre-fire vegetation, fire severity and topographic factors. *Forest Ecology and Management*, 356(2015):31–40, 2015. doi: 10.1016/j.foreco.2015.06.016.
- A. Harten. High Resolution Schemes for Hyperbolic Conservation Laws. *Journal of Computational Physics*, 135(2):260–278, Aug 1997. doi: 10.1006/jcph.1997.5713.
- T. Hasan, J.I. Gerhard, R. Hadden, and G. Rein. Self-sustaining smouldering combustion of coal tar for the remediation of contaminated sand: Two-dimensional experiments and computational simulations. *Fuel*, 150:288–297, 2015. doi: 10.1016/j.fuel.2015.02.014.

- C.M. Hoffman, R.R. Linn, R. Parsons, C. Sieg, and J. Winterkamp. Modeling spatial and temporal dynamics of wind flow and potential fire behavior following a mountain pine beetle outbreak in a lodgepole pine forest. *Agricultural and Forest Meteorology*, 204:79–93, 2015. doi: 10.1016/j.agrformet.2015.01.018.
- J.V. Hofmann. Meteorological factors and forest fires. *Monthly Weather Review*, 51(11):569, 1923.
- F.S. Hu, P.E. Higuera, J.E. Walsh, W.L. Chapman, P.A. Duffy, L.B. Brubaker, and M.L. Chipman. Tundra burning in Alaska: Linkages to climatic change and sea ice retreat. *Journal of Geophysical Research: Biogeosciences*, 115:1–8, 2010. doi: 10.1029/2009JG001270.
- ICNF. Instituto da Conservacao da Natureza e das Florestas. IFN6 Areas dos usos do solo e das especies florestais de Portugal continental. Resultados preliminares. Technical report, Lisboa, 2013.
- III. Wildfires, 2016. URL <http://www.iii.org/fact-statistic/wildfires>.
- F. P. Incropera and D P Dewitt. *Introduction to Heat Transfer*. Wiley, New York, 3rd edition, 1996.
- T.F. Irvine and J.P. Hartnett. *Advances in Heat Transfer*, volume 4. Academic Press, 1978.
- R.I. Issa. Solution of the implicitly discretised fluid flow equations by operator-splitting. *Journal of Computational Physics*, 62(1):40–65, Jan 1986. doi: 10.1016/0021-9991(86)90099-9.
- J.A. Jacquez and H.F. Kuppenheim. Theory of the Integrating Sphere. *Journal of the Optical Society of America*, 45(6):460, Jun 1955. doi: 10.1364/JOSA.45.000460.
- M. L. Janssens and W. Parker. *Oxygen Consumption Calorimetry*. Elsevier, New York, 1992.
- M.L. Janssens. Measuring rate of heat release by oxygen consumption. *Fire Technology*, 27(3):234–249, 1991.
- F.X. Jervis, G. Rein, A. Simeoni, and J.L. Torero. Burning Behaviour of Live and Dead Pinus Halepensis Needles using Small Scale Calorimetry Experiments. *The Sixth International Seminar on Fire & Explosion Hazards (FEH6)*, pages 978–981, 2011. doi: 10.3850/978-981-08-7724-8.
- W.M. Jolly, R.A. Parsons, A.M. Hadlow, G.M. Cohn, S.S. McAllister, J.B. Popp, R.M. Hubbard, and J.F. Negron. Relationships between moisture, chemistry, and ignition of Pinus contorta needles during the early stages of mountain pine

- beetle attack. *Forest Ecology and Management*, 269:52–59, Apr 2012. doi: 10.1016/j.foreco.2011.12.022.
- W.M. Jolly, J. Hintz, R.C. Kropp, and E.T. Conrad. Physiological drivers of the live foliar moisture content spring dip in *Pinus resinosa* and *Pinus banksiana* and their relationship to foliar flammability. In *Advances in forest fire research*, pages 401–408. Imprensa da Universidade de Coimbra, 2014. doi: 10.14195/978-989-26-0884-6_44.
- JRC. Forest fires in Europe Middle East and North Africa 2011. Technical report, Joint Research Centre, Ispra, 2012.
- C.R. Kaplan, C.R. Shaddix, and K.C. Smith. Computations of Enhanced Soot Production in Time-Varying CH₄/Air Diffusion Flames. *Combustion and Flame*, 106:392–405, 1996.
- R.E. Keane, K.C. Ryan, T.T. Veblen, C.D. Allen, J. Logan, and B. Hawkes. Cascading effects of fire exclusion in Rocky mountain ecosystems: a literature review. RMRS-GTR-91. Technical report, USDA Forest Service, Rocky Mountain Research Station, Fort Collins, 2002. URL <http://www.fs.fed.us/rm/pubs/rmrs{-}gtr091.pdf>.
- W.A. Khan, R.J. Culham, and M.M. Yovanovich. Analytical Model for Convection Heat Transfer from Tube Banks, 2006.
- G. Kirchhoff. Über Den Zusammenhang Zwischen Emission Und Absorption Von Licht Und Wärme. In *Monatsberichte der Akademie der Wissenschaften zu Berlin*, pages 783–787, Berlin, 1859.
- G. Kirchhoff. I. On the Relation Between the Radiating and Absorbing Powers of Different Bodies for Light and Heat. *The London, Edinburgh, and Dublin Philosophical Magazine and Journal of Science*, 20(130):1–21, 1860.
- T. Kitzberger, T.W. Swetnam, and T.T. Veblen. Inter-hemispheric synchrony of forest fires and the El Nino-Southern Oscillation. *Global Ecology and Biogeography*, 10(3):315–326, May 2001. doi: 10.1046/j.1466-822X.2001.00234.x.
- A.K. Kochanski, M.A. Jenkins, J. Mandel, J.D. Beezley, and S.K. Krueger. Real time simulation of 2007 Santa Ana fires. *Forest Ecology and Management*, 294: 136–149, Apr 2013. doi: 10.1016/j.foreco.2012.12.014.
- R.F. Kokaly, D.G. Despain, R.N. Clark, and K.E. Livo. Mapping Vegetation in Yellowstone National Park Using Spectral Feature Analysis of AVIRIS Data. *Remote Sensing of Environment*, 84(3):437–456, Mar 2003. doi: 10.1016/S0034-4257(02)00133-5.

- F.F.P. Kollman and W.A. Côté. *Principles of Wood Science and Technology, 1. Solid Wood*. 1968. doi: 10.1007/978-3-642-87931-9.
- A.N. Kolmogorov. The local structure of turbulence in incompressible viscous fluid for very large Reynolds numbers. *Doklady Akademii Nauk SSSR*, 30(1890): 301–305, 1941. ISSN 13645021. doi: 10.1098/rspa.1991.0075.
- E. Koo, P.J. Pagni, D.R. Weise, and J.P. Woycheese. Firebrands and spotting ignition in large-scale fires. *International Journal of Wildland Fire*, 19:818–843, 2010.
- R. Koppmann, K. Von Czapiewski, and J. S. Reid. A review of biomass burning emissions, part I: gaseous emissions of carbon monoxide, methane, volatile organic compounds, and nitrogen containing compounds. *Atmospheric Chemistry and Physics Discussions*, 5(5):10455–10516, 2005. ISSN 16807375. doi: 10.5194/acpd-5-10455-2005.
- A. Lamorlette and F. Candelier. Thermal behavior of solid particles at ignition: Theoretical limit between thermally thick and thin solids. *International Journal of Heat and Mass Transfer*, 82:117–122, 2015. doi: 10.1016/j.ijheatmasstransfer.2014.11.037.
- A. Lamorlette, A. Collin, and O. Sero-Guillaume. Characterization of heat transfer between phases inside a porous medium as applied to vegetal set representations. *International Journal of Heat and Mass Transfer*, 55(4):607–617, 2012. doi: DOI10.1016/j.ijheatmasstransfer.2011.10.051.
- A. Lamorlette, M. EL Houssami, J. C. Thomas, A. Simeoni, and D. Morvan. A dimensional analysis of forest fuel layer ignition model: Application to the ignition of pine needle litters. *Journal of Fire Sciences*, 33(4):320–335, 2015. doi: 10.1177/0734904115591177.
- M. Larini, F. Giroud, B. Porterie, and J.C. Loraud. A multiphase formulation for fire propagation in heterogeneous combustible media. *International Journal of Heat and Mass Transfer*, 41:881–897, 1998.
- C.W. Lautenberger. *A generalized pyrolysis model for combustible solids*. PhD thesis, University of California, Berkeley, 2007. URL <http://escholarship.org/uc/item/7wz5m7dg>.
- E. Leoni, D. Cancellieri, N. Balbi, P. Tomi, and A.F. Bernardini. Thermal Degradation of Pinus Pinaster Needles by DSC , Part 2: Kinetics of Exothermic Phenomena. *Journal of Fire Sciences*, 21(March):117–130, 2003. doi: 10.1177/073490402032834.

- V. Leroy. *Contribution à la modélisation des feux de forêt: Cinétique de dégradation thermique et cinétique de combustion des végétaux*. PhD thesis, Université Pascal Paoli, 2007. URL <https://tel.archives-ouvertes.fr/tel-00343986>.
- V. Leroy, D. Cancellieri, and E. Leoni. Thermal degradation of ligno-cellulosic fuels: DSC and TGA studies. *Thermochimica Acta*, 451(1-2):131–138, Dec 2006. doi: 10.1016/j.tca.2006.09.017.
- V. Leroy, D. Cancellieri, E. Leoni, and J.L. Rossi. Kinetic study of forest fuels by TGA: Model-free kinetic approach for the prediction of phenomena. *Thermochimica Acta*, 497(1-2):1–6, Jan 2010. doi: 10.1016/j.tca.2009.08.001.
- R.R. Linn. *A Transport Model for Prediction of Wildfire Behavior*. PhD thesis, Thesis LA-1334-T, Los Alamos National Laboratory, Albuquerque, NM, 1997.
- R.R. Linn, J. Reisner, J.J. Colman, and J. Winterkamp. Studying wildfire behavior using FIRETEC. *International Journal of Wildland Fire*, 11(4):233, 2002. doi: 10.1071/WF02007.
- R.R. Linn, J. Winterkamp, J.J. Colman, C. Edminster, and J.D. Bailey. Modeling interactions between fire and atmosphere in discrete element fuel beds. *International Journal of Wildland Fire*, 14(1):37, 2005. doi: 10.1071/WF04043.
- R.T. Long, J.L. Torero, J.G. Quintiere, and A.C. Fernandez-Pello. Scale and transport considerations on piloted ignition of PMMA. In *Sixth International Symposium on Fire Safety Science*, Poitiers, France, 1999.
- A.V. Luikov. *Heat and Mass Transfer: Handbook [in Russian]*. Moscow, 1978.
- A.V. Lykov. *Teoriya sushki (Theory of drying) [in Russian]*. Energiya, Moscow, 1968.
- B.F. Magnussen and B.H. Hjertager. On mathematical modeling of turbulent combustion with special emphasis on soot formation and combustion. *Symposium (International) on Combustion*, 16(1):719–729, Jan 1977. doi: 10.1016/S0082-0784(77)80366-4.
- J. Mandel, J.D. Beezley, and A.K. Kochanski. Coupled atmosphere-wildland fire modeling with WRF 3.3 and SFIRE 2011. *Geoscientific Model Development*, 4(3):591–610, Jul 2011. doi: 10.5194/gmd-4-591-2011.
- S.L. Manzello and E.I.D. Foote. Characterizing Firebrand Exposure from Wildland-Urban Interface (WUI) Fires: Results from the 2007 Angora Fire. *Fire Technology*, 50:105–124, 2014.

- A. Maranghides and W. Mell. Framework for Addressing the National Wildland Urban Interface Fire Problem - Determining Fire and Ember Exposure Zones Using a WUI Hazard Scale. Technical Note 1748. Technical report, NIST, Gaithersburg, MD, 2012.
- J. Margerit and O. Sero-Guillaume. Modelling Forest Fires. Part II: Reduction to Two-Dimensional Models and Simulation of Propagation. *International Journal of Heat and Mass Transfer*, 45:1723–1737, 2002. doi: 10.1016/S0017-9310(01)00249-6.
- R.J. Marks. *Introduction to Shannon Sampling and Interpolation Theory*. Springer Texts in Electrical Engineering. Springer New York, New York, NY, 1991. doi: 10.1007/978-1-4613-9708-3.
- J.B. Marsdens-Smedley and W.R. Catchpole. Fire Behaviour Modelling in Tasmanian Buttongrass Moorlands - II. Fire Behaviour. *International Journal of Wildland Fire*, 5(4):215, 1995.
- S. McAllister, I. Grenfell, A. Hadlow, W.M. Jolly, M. Finney, and J. Cohen. Piloted ignition of live forest fuels. *Fire Safety Journal*, 51:133–142, Jul 2012. doi: 10.1016/j.firesaf.2012.04.001.
- A.G. McArthur. Weather and grassland fire behaviour. Commonwealth Department of National Development, Forestry and Timber Bureau Leaflet 100. (Canberra). Technical report, 1966.
- A.G. McArthur. Fire behaviour in eucalypt forests. Technical report, Commonwealth Department of National Development, Forestry and Timber Bureau Leaflet 107, Canberra, 1967.
- W. Mell. WFDS Preliminary Users Guide, 2010. URL http://www.fs.fed.us/pnw/fera/research/wfds/wfds_user_guide.pdf.
- W. Mell, J.J. Charney, and M.A. Jenkins. Numerical Simulations of Grassland Fire Behavior from the LANL-FIRETEC and NIST-WFDS Models. In *East-FIRE Conference, May 11- 13, 2005, George Mason University, Fairfax, VA*, pages 1–10, 2005.
- W. Mell, M.A. Jenkins, J. Gould, and P. Cheney. A Physics-Based Approach to Modelling Grassland Fires. *International Journal of Wildland Fire*, 16(1):1–22, 2007.
- W. Mell, A. Maranghides, R. McDermott, and S.L. Manzello. Numerical simulation and experiments of burning douglas fir trees. *Combustion and Flame*, 156(10):2023–2041, 2009. doi: 10.1016/j.combustflame.2009.06.015.

- A. Mendes, A. Dollet, C. Ablitzer, C. Perrais, and G. Flamant. Numerical simulation of reactive transfers in spouted beds at high temperature: Application to coal gasification. *Journal of Analytical and Applied Pyrolysis*, 82(1):117–128, 2008. doi: 10.1016/j.jaap.2008.02.001.
- J.M.C. Mendes-Lopes, J.M.P. Ventura, and J.M.P. Amaral. Flame characteristics, temperature-time curves, and rate of spread in fires propagating in a bed of Pinus pinaster needles. *International Journal of Wildland Fire*, 12(1):67–84, 2003.
- S. Meradji, G. Accary, D. Morvan, O. Bessonov, and D. Fougère. Numerical Simulation of Grassland-Fires Behavior Using Firestar 3D Model. In *Topical Problems of Fluid Mechanics 2016*, 2016. doi: 10.14311/TPFM.2016.018.
- M.A. Mesarch, E.A. Walter-Shea, G.P. Asner, E.M. Middleton, and S.S. Chan. A Revised Measurement Methodology for Conifer Needles Spectral Optical Properties. *Remote Sensing of Environment*, 68(2):177–192, May 1999. doi: 10.1016/S0034-4257(98)00124-2.
- P. Methacanon, O. Chaikumpollert, P. Thavorniti, and K. Suchiva. Hemicellulosic polymer from Vetiver grass and its physicochemical properties. *Carbohydrate Polymers*, 54(3):335–342, 2003. doi: 10.1016/S0144-8617(03)00182-6.
- Y. Minamoto and J.H. Chen. DNS of a turbulent lifted DME jet flame. *Combustion and Flame*, 169:38–50, Jul 2016. doi: 10.1016/j.combustflame.2016.04.007.
- M.F. Modest. *Radiative heat transfer*. Mechanical Engineering Series. Mc Graw-Hill International Editions, 1993.
- M.F. Modest. View Factors. In *Radiative Heat Transfer*, pages 129–159. Elsevier, 2013. doi: 10.1016/B978-0-12-386944-9.50004-2.
- B. Monod, A. Collin, G. Parent, and P. Boulet. Infrared Radiative Properties of Vegetation Involved in Forest Fires. *Fire Safety Journal*, 44(1):88–95, 2009.
- F. Morandini and X. Silvani. Experimental Investigation of the Physical Mechanisms Governing the Spread of Fire. *International Journal of Wildland Fire*, 19:570–582, 2010.
- F. Morandini, Y. Perez-Ramirez, V. Tihay, P.A. Santoni, and T. Barboni. Radiant, convective and heat release characterization of vegetation fire. *International Journal of Thermal Sciences*, 70:83–91, Aug 2013. doi: 10.1016/j.ijthermalsci.2013.03.011.
- C. Moro. Détermination des caractéristiques physiques de particules de quelques espèces forestières méditerranéennes, Rap. Tech, PIF2006-06. Technical report, INRA, Avignon, 2006.

- D. Morvan. Physical Phenomena and Length Scales Governing the Behaviour of Wildfires: A Case for Physical Modelling. *Fire Technology*, 47(2):437–460, Apr 2011. doi: 10.1007/s10694-010-0160-2.
- D. Morvan. Numerical study of the effect of fuel moisture content (FMC) upon the propagation of a surface fire on a flat terrain. *Fire Safety Journal*, 58: 121–131, May 2013. doi: 10.1016/j.firesaf.2013.01.010.
- D. Morvan. Numerical Study of the Behaviour of a Surface Fire Propagating Through a Firebreak Built in a Mediterranean Shrub Layer. *Fire Safety Journal*, 71:34–48, 2015. doi: 10.1016/j.firesaf.2014.11.012.
- D. Morvan and J.L. Dupuy. Modeling of fire spread through a forest fuel bed using a multiphase formulation. *Combustion and Flame*, 127(1-2):1981–1994, 2001. doi: 10.1016/S0010-2180(01)00302-9.
- D. Morvan and J.L. Dupuy. Modeling the Propagation of a Wildfire Through a Mediterranean Shrub Using a Multiphase Formulation. *Combustion and Flame*, 138(3):199–210, 2004. doi: 10.1016/j.combustflame.2004.05.001.
- D. Morvan and M. Larini. Modeling of One Dimensional Fire Spread in Pine Needles with Opposing Air Flow. *Combustion Science and Technology*, 164(1): 37–64, 2001. doi: 10.1080/00102200108952161.
- D. Morvan, J.L. Dupuy, E. Rigolot, and J.C. Valette. FIRESTAR: A Physically based model to study wildfire behaviour. *Forest Ecology and Management*, 234: S114, Nov 2006. doi: 10.1016/j.foreco.2006.08.155.
- D. Morvan, S. Méradji, and G. Accary. Physical modelling of fire spread in Grasslands. *Fire Safety Journal*, 44(1):50–61, Jan 2009. doi: 10.1016/j.firesaf.2008.03.004.
- D. Morvan, C. Hoffman, F. Rego, and W. Mell. Numerical simulation of the interaction between two fire fronts in grassland and shrubland. *Fire Safety Journal*, 46(8):469–479, Nov 2011. doi: 10.1016/j.firesaf.2011.07.008.
- N.A. Moussa, T.Y. Toong, and C.A. Garriss. Mechanism of smoldering of cellulosic materials. *Symposium (International) on Combustion*, 16(1):1447–1457, Jan 1977. doi: 10.1016/S0082-0784(77)80427-X.
- E. Mueller. *LES Modeling of Flow Through Vegetation with Applications to Wildland Fires*. Degree of master of science, Worcester Polytechnic Institute, 2012. URL [http://wpi.summon.serialssolutions.com/search?s.cmd=addFacetValueFilters\(Library,WPI+Project+Reports\)&s.fvf=Library,WPI+Theses+%26+Dissertations,&s.pn=1{%&}s.q=mueller](http://wpi.summon.serialssolutions.com/search?s.cmd=addFacetValueFilters(Library,WPI+Project+Reports)&s.fvf=Library,WPI+Theses+%26+Dissertations,&s.pn=1{%&}s.q=mueller).

- E. Mueller, N. Skowronski, K. Clark, R. Kremens, M. Gallagher, J. Thomas, M. El Houssami, A. Filkov, B. Butler, J. Hom, W. Mell, and A. Simeoni. An experimental approach to the evaluation of prescribed fire behavior. In *Advances in forest fire research*, pages 41–53. Imprensa da Universidade de Coimbra, 2014. doi: 10.14195/978-989-26-0884-6{_}4.
- NAS. US. National Academy of Science, Committee on Fire Research. Technical Report, National Research Council Publications, vol. 949. Technical report, 1961.
- NASA. Goddard Institute for Space Studies. URL <http://data.giss.nasa.gov>.
- G. Ne’eman, S. Goubitz, and R. Nathan. Reproductive traits of *Pinus halepensis* in the light of fire a critical review. *Plant Ecology (formerly Vegetatio)*, 171 (1/2):69–79, 2004. doi: 10.1023/B:VEGE.0000029380.04821.99.
- H.M. Nepf, J.A. Sullivan, and R.A. Zavitoski. A model for diffusion within an emergent plant canopy. *Limnology and Oceanography*, 42(8):85–95, 1997.
- F. Nicoud and F. Ducros. Subgrid-scale stress modelling based on the square of the velocity gradient tensor. *Flow, Turbulence and Combustion*, 62(3):183–200, 1999. doi: 10.1023/A:1009995426001.
- NIFC. National Significant Wildland Fire Potential Outlook: Outlook Period May, June and July through August, 2016. Technical report, National Interagency Fire Center, 2016. URL http://www.predictiveservices.nifc.gov/outlooks/monthly_seasonal_outlook.pdf.
- M. Nijhuis. Forest fires: Burn out. *Nature*, 489(7416):352–354, Sep 2012. doi: 10.1038/489352a.
- R.Y. Niu and P.M. Zhai. Study on forest fire danger over Northern China during the recent 50 years. *Climatic Change*, 111(3-4):723–736, 2012. doi: DOI10.1007/s10584-011-0198-2.
- NOAA. El Niño & La Niña (El Niño-Southern Oscillation), 2016. URL <https://www.climate.gov/enso>.
- P.S. Nobel. *Physicochemical and Environmental Plant Physiology*. 2009. doi: 10.1016/B978-0-12-374143-1.00003-X.
- I.R. Noble, A.M. Gill, and G.A.V. Bary. McArthur’s Fire-Danger Meters Expressed As Equations. *Austral Ecology*, 5(2):201–203, 1980. doi: doi: 10.1111/j.1442-9993.1980.tb01243.x.
- T.J. Ohlemiller. Smoldering Combustion. In *SFPE Handbook of Fire Protection Engineering (3rd Ed.) Chapter 2*, pages 201–210. National Fire Protection

- Association, Quincy, MA, 2002. ISBN 978-1-4939-2564-3. doi: 10.1007/978-1-4939-2565-0.
- OpenCFD Ltd. OpenFOAM: The Open Source CFD Toolbox. URL <http://www.openfoam.org>.
- J.J.M. Orfão, F.J.a. Antunes, and J.L. Figueiredo. Pyrolysis kinetics of lignocellulosic materialsthree independent reactions model. *Fuel*, 78(3):349–358, 1999. doi: 10.1016/S0016-2361(98)00156-2.
- E. Ormeño, B. Céspedes, I. Sánchez, A. Velasco-García, J.M. Moreno, C. Fernandez, and V. Baldy. The relationship between terpenes and flammability of leaf litter. *Forest Ecology and Management*, 257(2):471–482, Jan 2009. doi: 10.1016/j.foreco.2008.09.019.
- Oxford Dictionary. Oxford English Dictionary Online, 2010. URL <http://dictionary.oed.com>.
- P.J. Pagni and T.G. Peterson. Flame spread through porous fuels. *Symposium (International) on Combustion*, 14:1099–1107, 1973.
- G. Parent, Z. Acem, S. Lechêne, and P. Boulet. Measurement of Infrared Radiation Emitted by the Flame of a Vegetation Fire. *International Journal of Thermal Sciences*, 49(3):555–562, 2010. doi: 10.1016/j.ijthermalsci.2009.08.006.
- E. Pastor. Mathematical models and calculation systems for the study of wildland fire behaviour. *Progress in Energy and Combustion Science*, 29(2):139–153, 2003. doi: 10.1016/S0360-1285(03)00017-0.
- S.V. Patankar. *Numerical Heat Transfer and Fluid Flow*. McGraw-Hill, New York, 1980.
- J.G. Pausas, C. Bladé, A. Valdecantos, J.P. Seva, D. Fuentes, J.A. Alloza, A. Vilagrosa, S. Bautista, J. Cortina, and R. Vallejo. Pines and oaks in the restoration of Mediterranean landscapes of Spain: New perspectives for an old practice a review. *Plant Ecology (formerly Vegetatio)*, 171(1/2):209–220, 2004. doi: 10.1023/B:VEGE.0000029381.63336.20.
- J.G. Pausas, J. Llovet, R. Anselm, and R. Vallejo. Are wildfires a disaster in the Mediterranean basin ? A review Vegetation changes Shrublands dominated by resprouting species. *International Journal of Wildland Fire*, pages 1–22, 2008.
- B.M. Pickett, C. Isackson, R. Wunder, T.H. Fletcher, B.W. Butler, and D.R. Weise. Experimental measurements during combustion of moist individual foliage samples. *International Journal of Wildland Fire*, 19(2):153, 2010. doi: 10.1071/WF07121.

- P. Pironi. *Smouldering Combustion of Organic Liquids in Porous Media for Remediating NAPL-contaminated Soils*. PhD thesis, University of Edinburgh, 2009. URL <http://hdl.handle.net/1842/3222>.
- P. Pironi, C. Switzer, G. Rein, A. Fuentes, J.I. Gerhard, and J.L. Torero. Small-scale forward smouldering experiments for remediation of coal tar in inert media. *Proceedings of the Combustion Institute*, 32(2):1957–1964, 2009. doi: 10.1016/j.proci.2008.06.184.
- T. Poinso and D. Veynante. *Theoretical and Numerical Combustion*. Philadelphia, 2nd edition, 2005.
- B. Porterie, D. Morvan, J. C. Loraud, and M. Larini. Firespread Through Fuel Beds: Modeling of Wind-Aided Fires and Induced Hydrodynamics. *Physics of Fluids*, 12(7):1762–1782, 2000. doi: 10.1063/1.870426.
- B. Porterie, J.L. Consalvi, A. Kaiss, and J.C. Loraud. Predicting Wildland Fire Behavior and Emissions Using a Fine-Scale Physical Model. *Numerical Heat Transfer, Part A: Applications*, 47(6):571–591, 2005. doi: 10.1080/10407780590891362.
- A. Pratap, T. Lilly Shanker Rao, K.N. Lad, and Heena D. Dhurandhar. Isoconversional vs. Model fitting methods. *Journal of Thermal Analysis and Calorimetry*, 89(2):399–405, Aug 2007. doi: 10.1007/s10973-006-8160-7.
- S. Pyne. *Year of the fires: the story of the great fires of 1910*. Mountain Press Publishing Company, New York, 2008.
- J.G. Quintiere. A simplified theory for generalizing results from a radiant panel rate of flame spread apparatus. *Fire and Materials*, 5(2):52–60, 1981.
- J.G. Quintiere. *Fundamentals of Fire Phenomena*. 2006. ISBN 978-0-470-09113-5.
- J.G. Quintiere and M.T. Harkleroad. New Concepts for Measuring Flame Spread Properties. In *Fire Safety: Science and Engineering*, pages 239–239–29. ASTM International, West Conshohocken, PA, 1984. doi: 10.1520/STP35300S.
- M.C. Radich. Introdução e expansão do eucalipto em Portugal. In J.S. Silva, editor, *Pinhais e Eucaliptais, a Floresta Cultivada.*, pages 151–165. Lisbon, 2007.
- G.D. Raithby and E.H. Chui. A Finite-Volume Method for Predicting a Radiant Heat Transfer in Enclosures With Participating Media. *Journal of Heat Transfer*, 112(2):415, 1990. doi: 10.1115/1.2910394.
- M.R. Raupach. Drag and drag partition on rough surfaces. *Boundary-Layer Meteorology*, 60(4):375–395, 1992. doi: 10.1007/BF00155203.

- R.G. Rehm and H.R. Baum. The equations of motion for thermally driven buoyant flows. *Journal of Research of the National Bureau of Standards*, 83(3):297–308, 1978.
- G Rein. *Computational Model of Forward and Opposed Smoldering Combustion with Improved Chemical Kinetics*. PhD thesis, University of California, Berkeley, 2005.
- G. Rein, S. Cohen, and A. Simeoni. Carbon emissions from smouldering peat in shallow and strong fronts. *Proceedings of the Combustion Institute*, 32(2): 2489–2496, 2009. doi: 10.1016/j.proci.2008.07.008.
- J. Reisner, S. Wynne, L. Margolin, and R.R. Linn. Coupled Atmospheric Fire Modeling Employing the Method of Averages. *Monthly Weather Review*, 128(10):3683–3691, Oct 2000. doi: 10.1175/1520-0493(2001)129<3683:CAFMET>2.0.CO;2.
- N. Ren, Y. Wang, S. Valfayeau, and A. Trouvé. Large Eddy Simulation of turbulent vertical wall fires supplied with gaseous fuel through porous burners. *Combustion and Flame*, 169:194–208, 2016. doi: 10.1016/j.combustflame.2015.12.008.
- M. Rochoux. *Vers une meilleure prévision de la propagation d'incendies de forêt: évaluation de modèles et assimilation de données*. PhD thesis, École Centrale Paris, France, 2014.
- M.C. Rochoux, B. Cuenot, S. Ricci, A. Trouvé, B. Delmotte, S. Massart, R. Paoli, and R. Paugam. Data assimilation applied to combustion. *Comptes Rendus Mécanique*, 341(1-2):266–276, Jan 2013a. doi: 10.1016/j.crme.2012.10.011.
- M.C. Rochoux, B. Delmotte, B. Cuenot, S. Ricci, and A. Trouvé. Regional-scale simulations of wildland fire spread informed by real-time flame front observations. *Proceedings of the Combustion Institute*, 34(2):2641–2647, Jan 2013b. doi: 10.1016/j.proci.2012.06.090.
- B.N. Rock, J.E. Vogelmann, D.L. Williams, A.F. Vogelmann, and T. Hoshizaki. Remote Detection of Forest Damage. *BioScience*, 36(7):439–445, Jul 1986. doi: 10.2307/1310339.
- A. Rodrigo, J. Retana, and F.X. Picó. Direct Regeneration is not the only response of Mediterranean forests to large fires. *Ecology*, 85(3):716–729, Mar 2004. doi: 10.1890/02-0492.
- F.E. Rogers and T.J. Ohlertiller. Cellulosic Insulation Material: I. Overall Degradation Kinetics and Reaction Heats. *Combustion Science and Technology*, 24:129–137, 1980.

- S. G. Romanovskii. *Processes of Thermal Treatment of Moist Materials [in Russian]*. Moscow, 1976.
- E. Rosenfeld. Top 10 Devastating Wildfires, Jun 2011. URL http://content.time.com/time/specials/packages/article/0,28804,2076476_2076484_2076504,00.html.
- M. Rossi, P. Bardin, E. Cateau, and D. Vallauri. Forêts anciennes de Méditerranée et des montagnes limitrophes Références pour la naturalité régionale. Technical report, Marseille, 2013. URL <http://www.foretsanciennes.fr/wp-content/uploads/Rossi-et-al-2013.pdf>.
- R.C. Rothermel. A Mathematical Model for Predicting Fire Spread in Wildland Fuels. Technical Report Research Paper INT-115, 1972.
- M. Saâdaoui, N. Mahjoub Saïd, H. Mhiri, P. Caminat, G. Le Palec, and P. Bournot. Study of the behaviour of a flame resulting from the combustion of pine needles in a cylindrical basket. *International Journal of Thermal Sciences*, 47(3):293–305, Mar 2008. doi: 10.1016/j.ijthermalsci.2007.01.021.
- M.J. Safi, I.M. Mishra, and B. Prasad. Global Degradation Kinetics of Pine Needles in Air. *Thermochimica Acta*, 412(1-2):155–162, Mar 2004. doi: 10.1016/j.tca.2003.09.017.
- P.A. Santoni, A. Simeoni, J.L. Rossi, F. Bosseur, F. Morandini, X. Silvani, J.H. Balbi, D. Cancellieri, and L. Rossi. Instrumentation of Wildland Fire: Characterisation of a Fire Spreading Through a Mediterranean Shrub. *Fire Safety Journal*, 41(3):171–184, 2006.
- C.F. Schemel, A. Simeoni, H. Biteau, J.D. Rivera, and J.L. Torero. A Calorimetric Study of Wildland Fuels. *Experimental Thermal and Fluid Science*, 32(7):1381–1389, 2008.
- U. Schumann. Subgrid-scale model for finite-difference simulations of turbulent flows in plane channels and annuli. *Journal Computational Physics*, 18(4):376–404, 1975.
- O. Séro-Guillaume and J. Margerit. Modelling Forest Fires. Part I: a complete set of equations derived by extended irreversible thermodynamics. *International Journal of Heat and Mass Transfer*, 45:1705–1722, 2002.
- D. Seto and C.B. Clements. Fire Whirl Evolution Observed during a Valley Wind-Sea Breeze Reversal. *Journal of Combustion*, 2011:1–12, 2011. doi: 10.1155/2011/569475.
- R.H. Shaw and E.G. Patton. Canopy Element Influences on Resolved- and Sub-Grid-Scale Energy Within a Large-Eddy Simulation. *Agricultural and Forest Meteorology*, 115:5–17, 2003.

- S.B. Show. Climate and forest fires in northern California. *Journal of Forestry*, 17:965–79, 1919.
- F. Siegert, G. Ruecker, A. Hinrichs, and A. Hoffmann. Increased damage from fires in logged forests during droughts caused by El Niño. *Nature*, 414(6862): 437–440, Nov 2001. doi: 10.1038/35106547.
- X. Silvani and F. Morandini. Fire Spread Experiments in the Field: Temperature and Heat Fluxes Measurements. *Fire Safety Journal*, 44(2):279–285, 2009.
- S. Simard. Fire Severity, Changing Scales, and How Things Hang Together. *International Journal of Wildland Fire*, 1(1):23, 1991. doi: 10.1071/WF9910023.
- A. Simeoni. Experimental Understanding of Wildland Fires. In *Fire Phenomena and the Earth System*, pages 35–52. John Wiley & Sons, Oxford, Apr 2013. doi: 10.1002/9781118529539.ch3.
- A. Simeoni. Wildland Fires. In *SFPE Handbook of Fire Protection Engineering*, pages 3283–3302. Springer, New York, NY, 2016. doi: 10.1007/978-1-4939-2565-0.
- A. Simeoni, J.C. Thomas, P. Bartoli, P. Borowieck, P. Reszka, F. Colella, P.A. Santoni, and J.L. Torero. Flammability studies for wildland and wildlandurban interface fires applied to pine needles and solid polymers. *Fire Safety Journal*, 54(0):203–217, Nov 2012. doi: 10.1016/j.firesaf.2012.08.005.
- N.S. Skowronski, K.L. Clark, M. Duveneck, and J. Hom. Three-dimensional canopy fuel loading predicted using upward and downward sensing LiDAR systems. *Remote Sensing of Environment*, 115:703–714, 2011. doi: 10.1016/j.rse.2010.10.012.
- J. Smagorinsky. General circulation experiments wiht the primitive equations I. The basic experiment. *Monthly Weather Review*, 91(3):99–164, 1963. doi: 10.1126/science.27.693.594.
- B. Smith. Introduction to Infrared Spectroscopy. In *Fundamentals of Fourier Transform Infrared Spectroscopy, Second Edition*, pages 1–17. CRC Press, Mar 2011. doi: 10.1201/b10777-2.
- N. Smith, J. Gore, JM. Kim, and Q. Tang. International workshop on measurement and computation of turbulent nonpremixed flames, 2003. URL <http://www.ca.sandia.gov/TNF/radiation.html>.
- W.T. Sommers, S.G. Coloff, and S.G. Conard. Synthesis of Knowledge: Fire History and Climate Change. Technical report, 2011. URL http://www.firescience.gov/JFSP_fire_history.cfm.

- S.M. Stein, S.J. Comas, J.P. Menakis, M.A. Carr, S.I. Stewart, H. Cleveland, L. Bramwell, and V.C. Radeloff. Wildfire, wildlands, and people: understanding and preparing for wildfire in the Wildland-Urban Interface - a forests on the edge report. General Technical Report RMRS-GTR-299. Fort Collins, CO. U.S. Department of Agriculture, Forest Service, Rocky Mountain Research. Technical report, 2013.
- B.J. Stocks, J.A. Mason, J.B. Todd, E.M. Bosch, B. M. Wotton, B.D. Amiro, M.D. Flannigan, K.G. Hirsch, K.A. Logan, D.L. Martell, and W.R. Skinner. Large forest fires in Canada, 1959–1997. *Journal of Geophysical Research*, 108 (D1), Dec 2002. ISSN 0148-0227. doi: 10.1029/2001JD000484.
- B.J. Stocks, M.E. Alexander, and R.A. Lanoville. Overview of the International Crown Fire Modelling Experiment (ICFME). *Canadian Journal of Forest Research*, 34(8):1543–1547, Aug 2004. doi: 10.1139/x04-905.
- D.R. Stull and H. Prophet. JANAF Thermochemical Tables. Technical report, National Bureau of Standards, 1971.
- A.L. Sullivan. Wildland surface fire spread modelling, 19902007. 2: Empirical and quasi-empirical models. *International Journal of Wildland Fire*, 18(4):369, 2009a. doi: 10.1071/WF06142.
- A.L. Sullivan. Wildland surface fire spread modelling, 19902007. 3: Simulation and mathematical analogue models. *International Journal of Wildland Fire*, 18(4):387, 2009b. doi: 10.1071/WF06144.
- A.L. Sullivan. Wildland surface fire spread modelling, 19902007. 1: Physical and quasi-physical models. *International Journal of Wildland Fire*, 18(4):349, 2009c. doi: 10.1071/WF06143.
- J. Swann, J. Hartman, and C. Beyler. Study of Radiant Smoldering Ignition of Plywood Subjected to Prolonged Heating Using the Cone Calorimeter, TGA, and DSC. *Fire Safety Science*, 9:155–166, 2008. doi: 10.3801/IAFSS.FSS.9-155.
- K.J. Syed, C.D. Stewart, and J.B. Moss. Modelling Soot Formation and Thermal Radiation in Buoyant Turbulent Diffusion Flames. *Proceedings of the Combustion Institute*, 23:1533–1541, 1990. ISSN 00820784. doi: 10.1016/S0082-0784(06)80423-6.
- K. Tansey, J.M. Grégoire, P. Defourny, R. Leigh, J.F. Pekel, E. Van Bogaert, and E. Bartholomé. A new, global, multi-annual (20002007) burnt area product at 1 km resolution. *Geophysical Research Letters*, 35(1):L01401, 2008. doi: 10.1029/2007GL031567.
- C.S. Tarifa, P.P. Del Notario, and F.G. Moreno. On the flight paths and lifetimes of burning particles of wood. *Symposium (International) on Combustion*, 10 (1):1021–1037, 1965. doi: 10.1016/S0082-0784(65)80244-2.

- A. H. Taylor. The Measurement of Diffuse Reflection Factors and a New Absolute Reflectometer. *Journal of the Optical Society of America*, 4(1):9, Jan 1920. doi: 10.1364/JOSA.4.000009.
- B. Teague, R. Mcleod, and S. Pascoe. Final Report. 2009 Victorian Bushfires Royal Commission Summary and Volume 1: The Fires and the Fire-Related Deaths . Technical report, 2010.
- A. Tewarson. Combustion efficiency and its radiative component. *Fire Safety Journal*, 39(2):131–141, 2004. doi: 10.1016/j.firesaf.2003.07.004.
- A. Tewarson and R.F. Pion. Flammability of plasticsI. Burning intensity. *Combustion and Flame*, 26:85–103, Feb 1976. doi: 10.1016/0010-2180(76)90059-6.
- J.C. Thomas. *Improving the understanding of fundamental mechanisms that influence ignition and burning behaviour of porous wildland fuel beds*. PhD thesis, The University of Edinburgh, UK, 2017.
- J.C. Thomas, A. Simeoni, J.L. Torero, and F. Colella. Piloted Ignition Regimes of Wildland Fuel Beds. In *Fall Technical Meeting of the Eastern States Section of the Combustion Institute; Storrs; CT; October 9-12*, 2011.
- J.C. Thomas, J.N. Everett, A. Simeoni, N. Skowronski, and J.L. Torero. Flammability Study of Pine Needle Beds. In *Proc. of the Seventh International Seminar on Fire & Explosion Hazards (ISFEH7)*, 2013. doi: 10.3850/978-981-08-7724-8.
- J.C. Thomas, A. Simeoni, M. Gallagher, and N. Skowronski. An Experimental Study Evaluating the Burning Dynamics of Pitch Pine Needle Beds Using the FPA. *Fire Safety Science*, 11:1406–1419, 2014. doi: 10.3801/IAFSS.FSS.11-1406.
- P.H. Thomas. Some Aspects of the Growth and Spread of Fire in the Open. *Forestry*, 40(2):139–164, 1967.
- V. Tihay. *Contribution experimentale et theorique pour la modelisation de la combustion dans les feux de foret*. PhD thesis, Universite de Corse, 2007. URL <https://tel.archives-ouvertes.fr/tel-00376628>.
- V. Tihay and P. Gillard. Pyrolysis gases released during the thermal decomposition of three Mediterranean species. *Journal of Analytical and Applied Pyrolysis*, 88(2):168–174, 2010. doi: 10.1016/j.jaap.2010.04.002.
- V. Tihay, P.A. Santoni, A. Simeoni, J.P. Garo, and J.P. Vantelon. Skeletal and global mechanisms for the combustion of gases released by crushed forest fuels. *Combustion and Flame*, 156(8):1565–1575, Aug 2009a. doi: 10.1016/j.combustflame.2009.05.004.

- V. Tihay, A. Simeoni, P.A. Santoni, J.P. Garo, and J.P. Vantelon. A global model for the combustion of gas mixtures released from forest fuels. *Proceedings of the Combustion Institute*, 32(2):2575–2582, 2009b. doi: 10.1016/j.proci.2008.06.095.
- V. Tihay, A. Simeoni, P.A. Santoni, L. Rossi, J.P. Garo, and J.P. Vantelon. Experimental study of laminar flames obtained by the homogenization of three forest fuels. *International Journal of Thermal Sciences*, 48(3):488–501, Mar 2009c. ISSN 12900729. doi: 10.1016/j.ijthermalsci.2008.03.018. URL <http://linkinghub.elsevier.com/retrieve/pii/S1290072908000756>.
- V. Tihay, F. Morandini, P.A. Santoni, Y. Perez-Ramirez, and T. Barboni. Combustion of forest litters under slope conditions: Burning rate, heat release rate, convective and radiant fractions for different loads. *Combustion and Flame*, 161(12):3237–3248, 2014. doi: 10.1016/j.combustflame.2014.06.003.
- Z. Todd. Fort McMurray wildfire - by the numbers, May 2016. URL <http://www.cbc.ca/news/canada/edmonton/fort-mcmurray-wildfire-by-the-numbers-1.3572193>.
- J.L. Torero. *Buoyancy Effects on Smoldering of Polyurethane Foam*. PhD thesis, University of California at Berkeley, 1991.
- J.L. Torero. Flaming Ignition of Solid Fuels. *SFPE Handbook of Fire Protection Engineering*, pages 2.260–2.278, 2008. doi: 10.1007/978-1-4939-2565-0_21.
- J.L. Torero and A. Simeoni. Heat and Mass Transfer in Fires: Scaling Laws, Ignition of Solid Fuels and Application to Forest Fires. *The Open Thermodynamics Journal*, 4(1):145–155, Jan 2010. doi: 10.2174/1874396X01004010145.
- A.A. Troshko and Y.A. Hassan. A two-equation turbulence model of turbulent bubbly flows. *International Journal of Multiphase Flow*, 27(11):1965–2000, 2001. doi: 10.1016/S0301-9322(01)00043-X.
- C.E. Van Wagner. Development and structure of the Canadian Forest Fire Weather Index System . Technical report, 1987.
- J.A. Vega, P. Cuiñas, P. Fonturbel, and C. Perez-Gorostiaga, P. Fernandez. Predicting fire behaviour in Galician (NW Spain) shrubland fuel complexes. In *In Viegas, D.X. (ed.), 3rd International Conference on Forest Fire Research & 14th Fire and Forest Meteorology Conference*, pages 713–28, Luso, Portugal, 1998.
- H.K. Versteeg and W. Malalasekera. An Introduction to Computational Fluid Dynamics - The Finite Volume Method, 1995.
- D.X. Viegas. Slope and wind effects on fire propagation. *International Journal of Wildland Fire*, 13(2):143, 2004. doi: 10.1071/WF03046.

- D.X. Viegas. A Mathematical Model For Forest Fires Blowup. *Combustion Science and Technology*, 177(1):27–51, 2005. doi: 10.1080/00102200590883624.
- D.X. Viegas. Parametric study of an eruptive fire behaviour model. *International Journal of Wildland Fire*, 15(2):169, 2006. doi: 10.1071/WF05050.
- D.X. Viegas, M.G. Cruz, L.M. Ribeiro, A.J. Silva, A. Ollero, B. Arrue, R. Dios, F. Gómez-Rodríguez, L. Merino, A.I. Miranda, and P. Santos. Gestosa fire spread experiments. In *IV International Conference on Forest Fire Research*, pages 1–13, Luso, 2002. ISBN 9077017720.
- S. Vilfayeau. *Large Eddy Simulation of Fire Extinction Phenomena*. PhD thesis, University of Maryland, 2015. URL <http://hdl.handle.net/1903/17356>.
- S. Vilfayeau, N. Ren, Y. Wang, and A. Trouvé. Numerical simulation of under-ventilated liquid-fueled compartment fires with flame extinction and thermally-driven fuel evaporation. *Proceedings of the Combustion Institute*, 35(3):2563–2571, 2015. doi: 10.1016/j.proci.2014.05.072.
- Y. Wang, P. Chatterjee, and J.L. De Ris. Large eddy simulation of fire plumes. *Proceedings of the Combustion Institute*, 33(2):2473–2480, Jan 2011. doi: 10.1016/j.proci.2010.07.031.
- R.O. Weber. Modelling fire spread through fuel beds. *Progress in Energy and Combustion Science*, 17(1):67–82, Jan 1991. doi: 10.1016/0360-1285(91)90003-6.
- R.W. Wells. *Fire at Peshtigo*. Englewood Cliffs, New Jersey, prentice edition, 1968.
- G.W. Wendel. Eastern white pine. In *Forest cover types of the United States and Canada*, pages 25–26. Washington DC, 1980.
- P.A. Werth, B.E. Potter, C.B. Clements, M.A. Finney, S.L. Goodrick, M.E. Alexander, M.G. Cruz, J.A. Forthofer, and S.S. McAllister. Synthesis of Knowledge of Extreme Fire Behavior: Volume I for Fire Managers PNW-GTR-854. Technical report, USDA Forest Service, Pacific Northwest Research Station, Portland (Oregon), 2011.
- A.L. Westerling, H.G. Hidalgo, D.R. Cayan, and T.W. Swetnam. Warming and earlier spring increase western U.S. forest wildfire activity. *Science*, 313(5789):940–3, 2006. doi: 10.1126/science.1128834.
- I. S. Wickman. Theory of opposed-flow flame spread. *Progress in Energy and Combustion Science*, 18(6):553–593, 1992.

- U. Wickström and U. Göransson. Full-scale/Bench-Scale correlations of wall and ceiling linings. *Fire and Materials*, 16(1):15–22, Jan 1992. doi: 10.1002/fam.810160103.
- F.A. Williams. Urban and wildland fire phenomenology. *Progress in Energy and Combustion Science*, 8(4):317–354, Jan 1982. doi: 10.1016/0360-1285(82)90004-1.
- WNA. World Nuclear Power Reactors database, 2016. URL <http://www.world-nuclear.org/information-library/facts-and-figures>.
- B.M. Wotton, C.A. Nock, and M.D. Flannigan. Forest fire occurrence and climate change in Canada. *International Journal of Wildland Fire*, 19(3):253, 2010. doi: 10.1071/WF09002.
- B.M. Wotton, J.S. Gould, W.L. McCaw, N.P. Cheney, and S.W. Taylor. Flame temperature and residence time of fires in dry eucalypt forest. *International Journal of Wildland Fire*, 21(3):270–281, 2012. doi: 10.1071/WF10127.
- J.G. Wright. Forest fire hazard research as developed and conducted at the Petawawa Forest Experiment Station. Technical report, Forestry Service of the Department of the Interior, 1932.
- P.K. Wu and R.G. Bill. Laboratory tests for flammability using enhanced oxygen. *Fire Safety Journal*, 38(3):203–217, 2003. doi: 10.1016/S0379-7112(02)00083-8.
- G. Xanthopoulos, C. Calfapietra, and P. Fernandes. Fire Hazard and Flammability of European Forest Types. In Francisco Moreira, Margarita Arianoutsou, Piermaria Corona, and Jorge De las Heras, editors, *Post-Fire Management and Restoration of Southern European Forests*, chapter 4, pages 79–92. 2012. doi: 10.1007/978-94-007-2208-8_4.
- H.D. Young and F.W. Sears. *University Physics*. Addison-Wesley, Boston, 7th edition, 1992.
- X.Y. Zhou and J.C.F. Pereira. A multidimensional model for simulating vegetation fire spread using a porous media sub-model. *Fire and Materials*, 24(1):37–43, Jan 2000. doi: 10.1002/(SICI)1099-1018(200001/02)24:1<37::AID-FAM718>3.0.CO;2-Q.
-